Synthesis, Structural and Property Studies of Bismuth Containing Perovskites

Wei-tin Chen

For the degree of Doctor of Philosophy
School of Chemistry
University of Edinburgh

February 2009

Declaration

I hereby declare the work described in this thesis was carried out at the School of Chemistry and Centre for Science at Extreme Conditions, University of Edinburgh, during the period September 2005 to December 2008. This thesis was composed by myself and the work detailed herein is my own, expect where otherwise stated, and no part of it has been submitted for any other degree or professional qualification.

Wei-tin Chen

Acknowledgements

First and foremost, I would like to express my deep and sincere gratitude to my supervisor Prof. J. Paul Attfield for his assistance, inspiring guidance, enthusiasm and optimism during this work. I am grateful to Prof. R. S. Liu at National Taiwan University, for providing the opportunity to study at University of Edinburgh.

I am thankful to past and present members of Attfield group, in particular Tony for teaching me GSAS, Luis for useful discussion and suggestions, Jenny for answering my questions and Jan-Willem for advices and inspiration. I especially thank Luis, Jenny and Mark for their great help for proofreading my thesis. I sincerely thank Sandra, Simon, George, Minghui, Shigeto, Mark, Anna, Andrea, and also Elizabeth, Sophia and Congling, for the enjoyable atmosphere in office and outings. I appreciate CSEC members Javier, Komatsu, Somchai, Gaétan, Kostas, Lindsay, Adrian, Artur, Miriam and everyone else for their help in science and life.

I am thankful to the collaborators Drs. W. Zhou, D. Sinclair and M. Li; Drs. F. Sher, N. Mathur and F. Morrison; Profs. Y. Shimakawa, M. Azuma, T. Saito, and Dr. O. Smirnova for the projects on $Bi_xCa_{1-x}FeO_3$, $Bi_xLa_{1-x}MnO_3$, and $BiNiO_3$ and $BiCu_3Mn_4O_{12}$, respectively. I thank Drs. A. Hewat, P. Henry and E. Suard; Drs. M. Brunelli, I. Margiolaki, and W. van Beek; Drs. M. Tucker and W. Kockelmann; and Mr. R. Blackley for assistance with data collection at ILL, ESRF, ISIS and the University of St. Andrews EM facility, respectively. I acknowledge EPSRC for provision of these facilities and for financial support.

I heartily thank my dear friends in Taiwan, Julian Su for always being there for me; and Miriam Wu for always supporting me. I also thank my friends in Edinburgh, Chen-Yen, Ching-Wen, Bor-Ran, Li-Wen, Hsin-Yi, Liang-Ping and Nan-Wei and others, without you I cannot have such wonderful memories these years.

Last but most importantly, I am most grateful to my parents Mr. Ming-Liao Chen and Mrs. Yi-Chun Kuo and my sister Liang-Tsu Chen for their love and care, without their incredible support I certainly will not have this achievement. And I am most thankful to my dear love Hsin-Hua Nien, for all her encouragement and support during these years not only for me to pursue this Ph.D. but everything in life!

Abstract

Several bismuth-containing transition metal perovskites that are of interest as potential multiferroic materials have been synthesised and studied. These materials have been structurally characterised and their physical properties have been examined at varying temperatures and pressures.

The new series of substituted bismuth ferrite perovskites $Bi_xCa_{1-x}FeO_3$, where x = 0.4 - 1.0, has been prepared. A disordered cubic phase (x = 0.4 - 0.67) and the coexistence of rhombohedral and cubic phases (x = 0.8 and 0.9) have been observed. The x = 0.8 sample is located at the phase boundary and shows a transformation from cubic to rhombohedral symmetry at 473 - 573 K. All samples are antiferromagnets at room temperature and have Néel temperature of 623 - 643 K. Ferroelectric order is suppressed in the disordered cubic phase.

$Bi_xLa_{1-x}MnO_3$ materials with x = 0.8, 0.9 and 1.0 were synthesised at 3 - 6 GPa. For x = 1.0 and 0.9 samples a highly distorted perovskite structure with monoclinic space group *C*2/*c* was adopted and ferromagnetic behaviour was observed with Curie temperatures of 101 and 94 K, respectively. $Bi_{0.8}La_{0.2}MnO_3$ shows an *O′*-type orthorhombic *Pnma* structure and canted *A*-type antiferromagnetic ordering below 80 K.

A new phase of $BiNiO_3$ has been discovered at 4 - 5 GPa below 200 K, in which a *Pb*11 symmetry has been revealed with $a = 5.2515(2)$ Å, $b = 5.6012(3)$ Å, $c = 7.6202(4)$ Å and $\beta = 90.20(1)$ ° at 4.3 GPa and 100 K. This new Phase Id is derived from the ambient Phase I $Bi^{3+}_{0.5}Bi^{5+}_{0.5}Ni^{2+}O_3$, where the charge disproportionated Bi^{3+}/Bi^{5+} cations become disordered. The updated P-T phase diagram of $BiNiO_3$ is presented.

$BiCu_3Mn_4O_{12}$ has been studied by neutron diffraction from 5 to 400 K. The incorporation of Mn^{3+} into the Cu site has been observed, showing that the true composition is $BiCu_{2.5}Mn_{4.5}O_{12}$. The ordering of Mn and Cu moments below transition temperature 320 K is found to be ferromagnetic rather than ferrimagnetic as proposed previously.

Contents

Chapter 1
Introduction

Perovskite-type transition metal oxides are of great interest due to their magnetic, dielectric and transport properties that emerge from the coupling of spin, charge and orbital degrees of freedom. Many fascinating properties can be exhibited in the transition metal perovskites, such as ferromagnetism, ferroelectricity and ferroelesticity, showing switchable orientation states. The multiferroism, which arises when a material simultaneously possesses more than two ferroic properties, has attracted much attention recently not only because of its interesting character but also for potential practical applications. Bismuth-containing perovskites are one of the most extensively studied families, since the multiferroism may be observed as a consequence of the presence of $6s^2$ lone pair electrons of Bi^{3+} combining with the magnetism from transition metal cations. In this work, several bismuth-containing transition metal perovskites have been synthesised, structurally characterised, and their physical properties have been examined at varying temperatures and pressures. An overview of the studied materials, structures and properties are given in this chapter, while more detailed discussion about the material studied in this thesis can be found in each resultant chapters.

1.1 Transition Metal Oxides

Transition metal oxides are one of most widely studied group of inorganic solid materials, which provides a remarkable variety of chemical and physical properties. Examples of magnetic and electronic properties are high temperature superconductivity (*e.g.* layered cuprates $La_{2-x}Sr_xCuO_4$[1]), colossal magnetoresistance (CMR, *e.g.* $R_{1-x}A_xMnO_3$, R = rare earth, A = alkali earth[2,3]), ferroelectricity (*e.g.* $BaTiO_3$, described later) or multiferroism (*e.g.* $BiFeO_3$ and $BiMnO_3$, described later). The exceptional characteristics of the materials are due to the unique nature of

transition metal's outer *d* electrons, which give cations with several oxidation states and vary the metal-oxygen bonding from nearly ionic to metallic. The properties strongly depend on the structure of the transition metal oxides, which can adopt a wide diversity, for example, perovskite, spinel and pyrochlore. With changes in temperature, pressure, or chemical composition, the transition metal oxide structures may be altered, hence the properties can traverse from one to another regime.

1.2 Perovskites

The ABO_3 structure is a very common and large family in transition metal oxides that adopts the name of mineral Perovskite, $CaTiO_3$. The mineral was discovered in Russia by Gustav Rose in 1839 and named after Russian mineralogist, L. A. Perovski. From the coupling of spin, charge and orbital ordering, perovskite-type transition metal oxides attract much attention due to the wide range of magnetic and transport properties[4]. Typical useful properties of perovskites are ferromagnetism and ferroelectricity which do not usually appear simultaneously in the same material phase.

The ideal structure of perovskite is primitive cubic structure ABO_3 (space group $Pm\bar{3}m$) with the lattice parameter $a \approx 4$ Å. In the centre of the unit cell there is a large twelve coordinate *A* cation, surrounded by eight corner-sharing BO_6 octahedra. The octahedra consist of a *B* cation, normally this is a transition metal, in eight corners of the unit cell and oxygen in the middle of the twelve edges, as shown in Figure 1.1. For the ideal perovskite, the relationship between the ionic radii r_A, r_B and r_O (of *A*, *B* and O ions, respectively) is generally defined as

$$r_A + r_O = \sqrt{2}(r_B + r_O) \qquad \textbf{(1.1)}$$

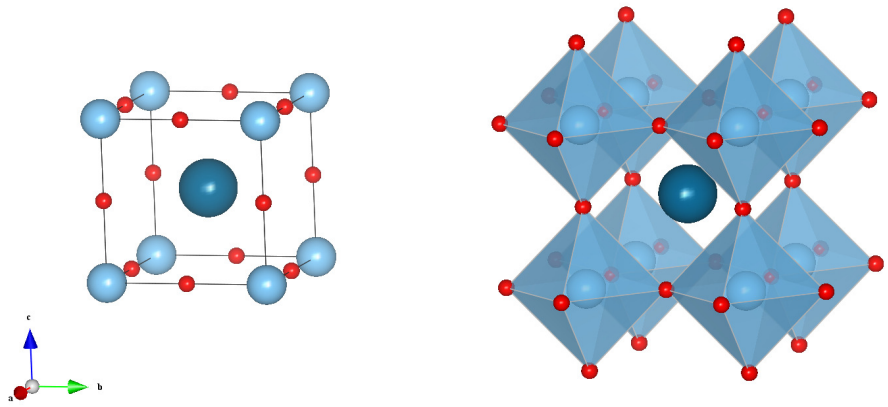

Figure 1.1 The schematic diagram of the structure of ABO_3 perovskites, where the darker, the lighter and red spheres represent *A*, *B* cations and oxygen, respectively.

The symmetry of the simple perovskite structure can be lowered as low as triclinic due to the sizes of *A* and *B* cations which can make the framework of octaheda twisted or distorted. For such perovskite structures the tolerance factor, *t*, was introduced by Goldschmidt[5]:

$$r_A + r_O = t\sqrt{2}(r_B + r_O) \qquad \textbf{(1.2)}$$

where $t = 1$ for the ideal cubic perovskite, but in practice there is some flexibility and the cubic structure can form with $0.9 < t < 1.0$. The BO_6 octahedra can be tilted, rotated or distorted to compensate for the non-ideal cation sizes and hence alter the unit cell forming a superstructure. The tilting classification scheme by Glazer can be used to systematically characterise the resultant superstructures[6]. For the tilting of octahedra, the component tilts from the pseudocubic axes [100], [010] and [001] are considered. Unequal tilts to the axes can be shown as *abc* as a general case, while repeating the appropriate letter indicating the equality of tilts, *e.g. aac*. The superscripts +, – and 0 represent the same tilt, opposite tilt and no tilt to the axes. $GdFeO_3$ is a classic example, in which $t < 1$ and the *A* cation is too small for the space between the octahedra[7]. The tilting of octahedra leads to an enlarged orthorhombic *Pbnm* unit cell with the Glazer notation $a^-b^+a^-$[6]. This structure is commonly adopted by many perovskites, which consists of four ABO_3 formula units. For $t > 1$, the perovskite structure will be distorted because of the space available for *B* cation in the octahedron is larger than required. This is the origin of the ferroelectricity in $BaTiO_3$ which has $t = 1.06$.

In addition to the simple perovskite ABO_3, an expanded unit cell may occur when more than two types of cation are present in one phase. The *A*- or *B*-site ordered double or triple perovskites can arise, where the ordering of the cations strongly depends on the differences of their charges and sizes. With the general formula double perovskites $AA'B_2O_6$, 1:1 *A*-site ordering can be found in different manners as shown in $CaFeTi_2O_6$[8] and $NdAgTi_2O_6$[9]. $CaCu_3Mn_4O_{12}$[10] belongs to $AA'_3B_4O_{12}$, in which the 1:3 ordering of *A*-cations is a common form of *A*-site ordering perovskite. On the other hand, distinct types of 1:1 *B*-site ordering can be observed in $A_2BB'O_6$ double perovskites (*e.g.* Ba_2YRuO_6[11], La_2LiRuO_6[12] and La_2CuSnO_6[13]). The 1:2 and 1:3 *B*-site ordering $A_3BB'_2O_9$ and $A_4BB'_3O_{12}$ materials also have been reported, such as $Ba_3ZnTa_2O_9$[14] and $Ba_4LiSb_3O_{12}$[15], respectively. Moreover, the combination of *A*- and *B*-site ordering give rise to unusual $AA'BB'O_6$ and $AA'_3B_2B'_2O_{12}$ materials, which can be represented by $NaLaMgWO_6$[16] and $CaCu_3Ga_2Sb_2O_{12}$[17], respectively.

Apart from above mentioned double or triple perovskites, doping or substitution of *A* or *B* cations are also commonly adopted, giving the perovskite solid solutions. The substitution may alter the structure due to different sizes of the cations, while the substitution with non-isovalent cations gives rise to mixed-valence in the materials. Therefore different properties from the parent compounds and novel characteristics may take place with the substitution, for example, the exhibited (colossal magnetoresistance) CMR effects in $R_{1-x}A_xMnO_3$ (*R* = rare earth, *A* = alkali earth)[2,3] materials and the variation of the magnetic ordering across the $Bi_xLa_{1-x}MnO_3$ solid solution[18].

1.3 Charge, Orbital and Spin Ordering

In a transition metal oxide material, the presence of mixed-velent cations may give rise to charge ordering, where the cations with different charges are ordered on specific crystallography sites in the material. Spin ordering can exist from the arrangement of unpaired *d* electrons of transition metal cations, which result in various magnetic properties. Both charge and spin ordering are associated with

orbital ordering, and fascinating properties can be observed due to the interaction between charge, spin and orbital ordering.

1.3.1 Charge Ordering

Charge ordering in solids was first envisaged by Eugene Wigner in the late 1930s[19]. The phenomena of charge ordering and the formation of modulated structures is one of the most studied research topics in mixed-valence transition metal oxides. When charge ordering occurs below the transition temperature T_{CO}, the electron hopping between cations is suppressed hence the electrical resistivity of the material is increased. Magnetite (Fe_3O_4) is a classic charge ordering example which adopts an AB_2O_4 inverse spinel structure $Fe^{3+}(Fe^{2+}Fe^{3+})O_4$. The material is a ferrimagnet with moderate electrical conductivity. A first order transition occurs showing significant increase of the resistivity on cooling below 120 K[20]. It was proposed that the first order transition, so called Verwey transition, is owing to the charge ordering of Fe^{2+} and Fe^{3+} at *B* sites[21].

The studies on doped manganite perovskites have been widely extended due to the exhibited charge ordering character and subsequently different ground states and colossal magnetoresistance[22,23]. For instance, the delocalised electrons of Mn cations in half doped $(La^{3+}_{0.5}Ca^{2+}_{0.5})Mn^{3.5+}O_3$ material become localised showing a

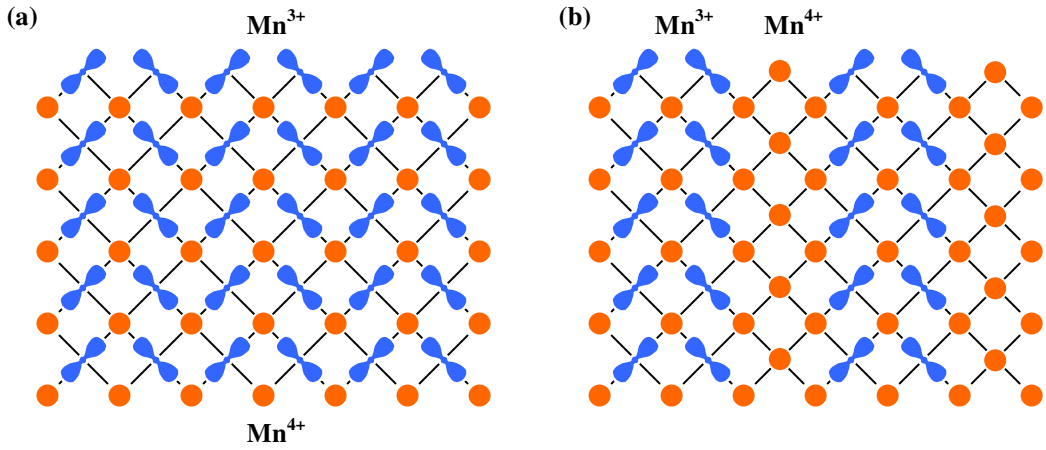

Figure 1.2 The *striped* model of charge ordered $La_{1-x}Ca_xMnO_3$ where (a) x = 0.5 and (b) x = ⅔, showing the ordering of localised Mn^{3+} and Mn^{4+} cations[24].

charge ordered $(La^{3+}_{0.5}Ca^{2+}_{0.5})(Mn^{3+}_{0.5}Mn^{4+}_{0.5})O_3$ phase below T_{CO}[25,26]. Such charge ordered Mn^{3+} and Mn^{4+} layers can be represented by a *striped* model[24,26]. With different doping levels in $La_{1-x}Ca_xMnO_3$, the *striped* model was also observed but with different periodicity, as shown in Figure 1.2.

In some undoped perovskite materials that have cations in unstable oxidation states, charge disproportionation can be observed showing ordering of the two more stable cations. Unlike the layered ordering demonstrated above, a different fashion of ordering was shown in the materials with charge disproportionation. A typical example is $Ba^{2+}Bi^{4+}O_3$, which becomes $Ba^{2+}(Bi^{3+}_{0.5}Bi^{5+}_{0.5})O_3$ below the charge ordering transition temperature[27] (Figure 1.3). Charge disproportionation can be also observed in $CaFeO_3$ showing ordered cations with different charges $Ca^{2+}(Fe^{3+}_{0.5}Fe^{5+}_{0.5})O_3$[28], in rare earth nickelates $RNiO_3$ which can be represented as $R^{3+}(Ni^{2+}_{0.5}Ni^{4+}_{0.5})O_3$[29-32].

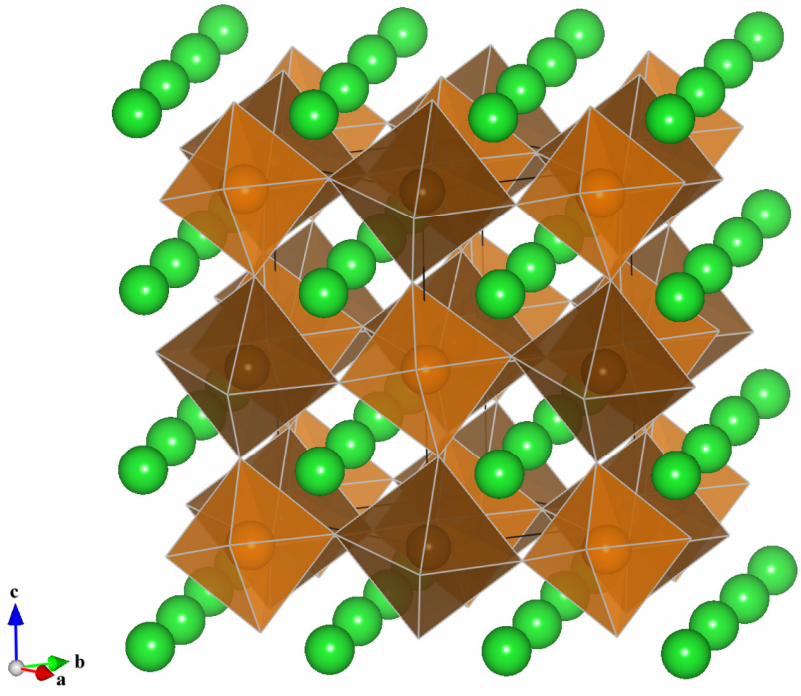

Figure 1.3 The ordering in the charge disproportionation material $BaBiO_3$, where the darker and lighter octahedra represent $Bi^{3+}O_6$ and $Bi^{5+}O_6$, respectively.

1.3.2 Orbital Ordering

In transition metal perovskites ABO_3, the transition metal forms a BO_6 octahedra configuration, in which its d orbitals split into t_{2g} (d_{xy}, d_{yz}, d_{xz}) and e_g ($d_{x^2-y^2}$, d_{z^2}) orbital groups. The t_{2g} orbitals are lower in energy while the e_g orbitals are higher in energy and point directly toward the ligands. This gives rise to two possible configurations of the d electron filling, the low spin (LS) and high spin (HS) states. In perovskite materials mainly the high spin configuration is observed for 3d transition metals. When the t_{2g} or e_g orbitals are partially occupied, the elongation of the octahedra occurs usually giving two long and four short BO bonds, which is known as a Jahn-Teller (JT) distortion[33]. Typical examples of transition metal cations with strong Jahn-Teller effects are Mn^{3+} (d^4) and Cu^{2+} (d^9). The JT distortions can also be observed in Ti^{3+} (d^1) and V^{3+} (d^2) cations and other $t_{2g}^{\ n}$ ions, however these distortions are more difficult to detect.

The arrangement of the distortion orientation in solid materials leads to so called cooperative Jahn-Teller distortions and long range orbital ordering, as shown in $LaMnO_3$ perovskite[25] (Figure 1.4). The orbital ordering is also exhibited in charge ordered materials such as $La_{0.5}Ca_{0.5}MnO_3$[26] and $Pr_{0.5}Ca_{0..5}MnO_3$[34]. The manner of the ordered orbitals may affect the magnetic ordering of a material, which is described by the Goodenough-Kanamori rules[35].

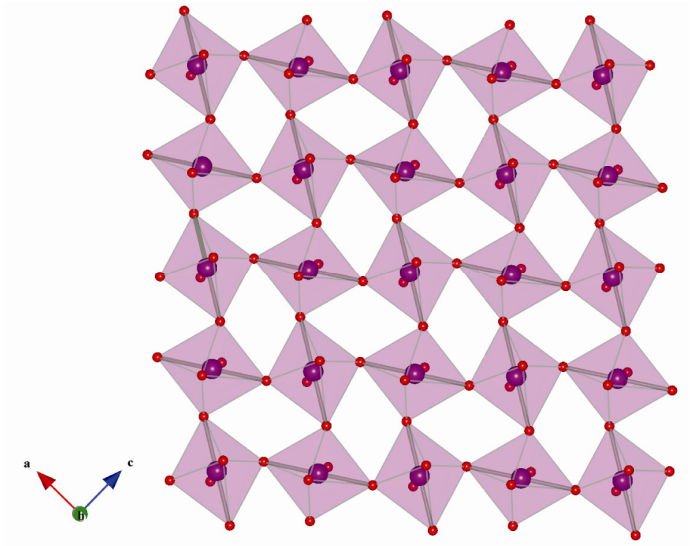

Figure 1.4 The orbital ordering of $LaMnO_3$, showing the arrangement of d_{z^2} orbitals.

1.3.3 Spin (magnetic) Ordering

Apart from diamagnetism which arises in all substances with the application of an external magnetic field, the magnetic behaviour of a material results from the presence of unpaired electrons. Magnetic properties are mainly exhibited by materials containing transition metals or lanthanides, owing to their partially filled *d* and *f* orbitals, respectively. When the moments in the material are oriented randomly, it is known as a paramagnet, in which the alignment of the moments can be achieved through the application of a magnetic field. A spontaneous magnetic ordering can be observed, however, when the interaction between unpaired electrons lead to alignments of electron spins. Three main classes of magnetic behaviours are given below and schematic diagrams of the alignments are shown in Figure 1.5 (a) - (c). When the spins are oriented parallel to each other and giving an overall magnetic moment, the material is a ferromagnet (Figure 1.5 (a)). If the moments on the neighbouring atoms are aligned antiparallel and the magnetic moments are cancelled by each other, the ordering is antiferromagnetic (Figure 1.5 (b)). A ferrimagnet possesses multiple types of magnetic ions and their magnetic moments may be aligned antiparallel, but a net magnetic moment occurs due to the unequal magnitudes (Figure 1.5 (c)). Similar to simple ferrimagnetism, a residual magnetic moment exists in a canted antiferromagnet, which shows the almost antiparallel arrangement of the spins but with a canting angle (Figure 1.5 (d)). The material is also called a weak ferromagnet owing to the net magnetic components.

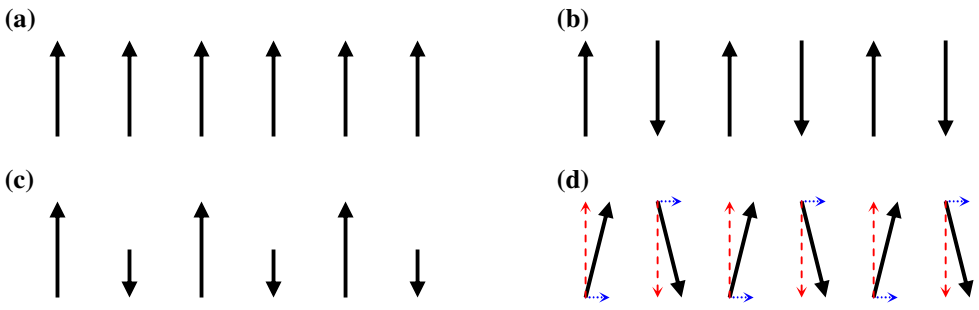

Figure 1.5 Schematic diagrams showing the spins of (a) ferromagnet, (b) antiferromagnet, (c) ferrimagnet and (d) canted antiferromagnetic, where the magnetic components in different directions are represented by dashed arrows.

In an antiferromagnetic material, equal amounts of two spin states are aligned antiparallelly in the lattice. The spins can be aligned with several different arrangements as described in the classification by Wollan *et al.*[36]. Three common examples of these antiferromagnetic ordering types are shown in Figure 1.6. *A*-type antiferromagnetic ordering has the spins aligned ferromagnetically in the *ab* plane, and each layer is antiferromagnetically to one another. This can be observed in $LaMnO_3$ perovskite[36], which is resulted from the Jahn-Teller distortion of Mn^{3+} cations. In *C*-type ordering the magnetic moments are aligned antiferromagnetically in the *ab* plane, and the *ab* layers stack ferromagnetically along the *c* axis, which can be found in $BiCoO_3$ perovskite[37]. *G*-type ordering is commonly adopted in simple cubic perovskites, in which the spins on all nearest neighbouring atoms are aligned antiferromagnetically by the superexchange interactions, as shown in $LaFeO_3$[38] and $LaCrO_3$[39].

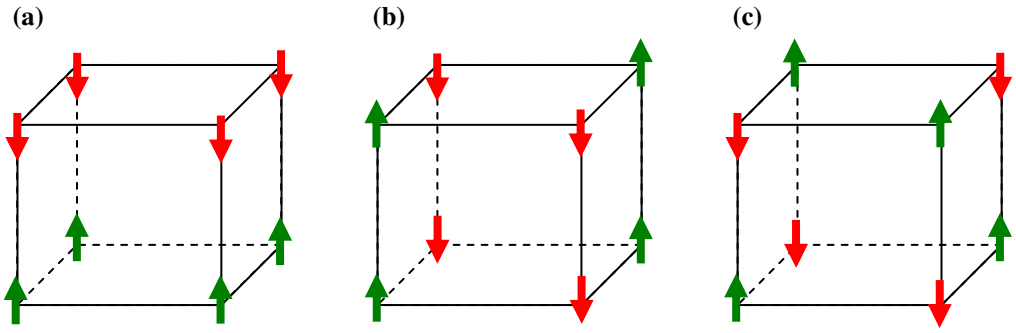

Figure 1.6 Schematic diagram showing the spin arrangements in (a) *A*-type, (b) *C*-type and (c) *G*-type antiferromagnetic ordering.

1.3.3.1 Behaviour under a magnetic field

When the magnetic field H is applied to substance, a linear magnetisation response M is induced, and the magnetic susceptibility χ can be defined as:

$$\chi = \frac{M}{H} \qquad (1.3)$$

The magnetic susceptibility χ represents the response of a substance to an applied magnetic field and is temperature dependent. Many paramagnetic substances, in which there is no interaction between moments, follow the Curie law,

$$\chi = \frac{C}{T} \quad \textbf{(1.4)}$$

where T is temperature in K, and C is the Curie constant which is defined as

$$C = \frac{N_A \mu_{eff}^2 \mu_B^2}{3k_B} \approx \frac{1}{8}\mu_{eff}^2 \quad \textbf{(1.5)}$$

where N_A is Avogrado's number, k_B is Boltzmann constant, μ_B is the Bohr magneton, and μ_{eff} is spin only effective magnetic moment

$$\mu_{eff} = g\sqrt{S(S+1)} \quad \textbf{(1.6)}$$

where g is the gyromagnetic ratio and is approximately 2, and S is the total spin quantum number. It should be noted that the contribution of orbital angular momentum is ignored since there is normally quenched by crystal field effects for the first row transition metals[40].

When the spontaneous interaction between neighbouring unpaired electrons exists, the magnetic properties of the material are more complex and the Curie law is no longer valid. For ferromagnetic materials, all the spins are aligned parallel and hence show a sharp increase in the susceptibility below a transition temperature, which is called the Curie temperature, T_C. Similarly, the magnetic moments become aligned antiparallel and lead to a decrease of susceptibility in antiferromagnets below a transition temperature, which is known as the Néel temperature, T_N. Above the transition temperature, the paramagnetic behaviour of ferro- and antiferromagnetic materials can be described with the Curie-Weiss law

$$\chi = \frac{C}{T-\theta} \quad \textbf{(1.7)}$$

where θ is the Weiss constant, which is positive for ferromagnets and negative for antiferromagnets. The typical temperature-dependent susceptibility and inverse

susceptibility curves of paramagnetic, ferro- and antiferromagnetic materials are shown in Figure 1.7[41].

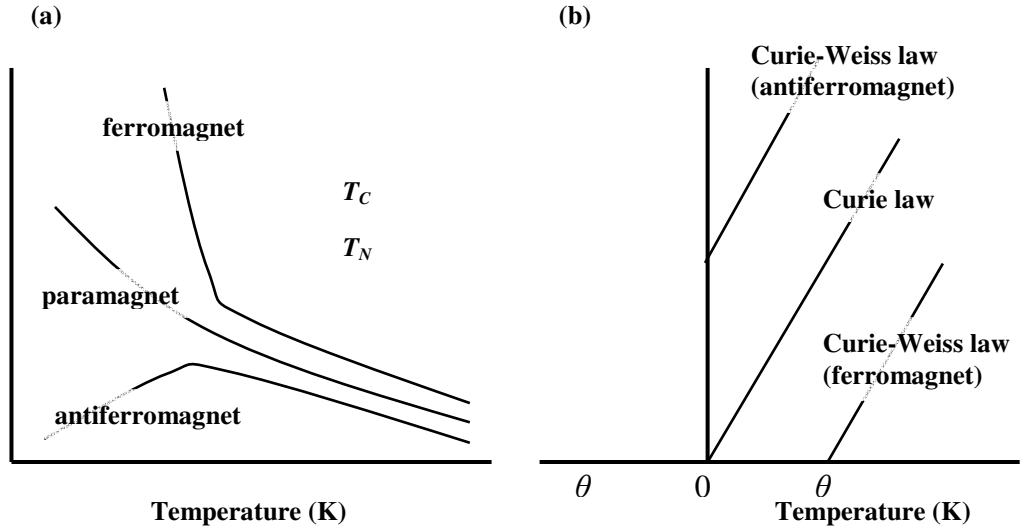

Figure 1.7 Temperature-dependent behaviour of (a) susceptibility and (b) inverse susceptibility[41] of paramagnet, ferro- and antiferromagnet.

For ferromagnetic materials, a characteristic hysteresis loop can be observed, which shows the relationship between M and H (Figure 1.8[41]). Considering a ferromagnetic material which is magnetised in one direction with an increasing field, the saturated magnetisation (M_s) can be found when the magnetisation reaches a maximum. The magnetisation will not relax to zero when the field is removed and the application of an opposite direction field is necessary to relax the magnetisation. If a cyclic magnetic field is applied, the magnetisation of the material will trace out a loop. The hysteresis loop results from the existence of magnetic domains in the material. With the application of the opposite field, a remnant magnetisation (M_r) occurs showing the remaining magnetisation at zero field, while the coercive field (H_c) is the opposite field applied when the magnetisation is relaxed to zero. A large hysteresis area is the property of a hard magnetic material, while a small area indicates a soft magnetic material.

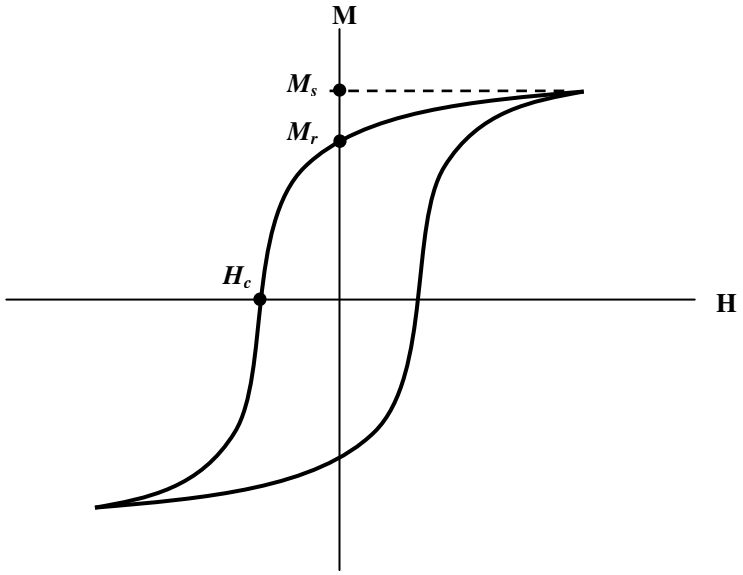

Figure 1.8 Typical hysteresis loop of a ferromagnet, showing the saturated magnetisation (M_s), remnant magnetisation (M_r) and coercive field (H_c).

1.3.3.2 Exchange mechanisms

The interaction between magnetic moments in a material at low temperatures which may lead to long range magnetic ordering, can be expressed as

$$\hat{H} = -2J_{ij}\hat{S}_i \cdot \hat{S}_j \qquad \textbf{(1.8)}$$

where J_{ij} is the exchange constant and S_i and S_j represent two coupled spins. The exchange constant is related to the interaction energy, and is positive for a ferromagnetic interaction and negative for an antiferromagnetic interaction.

Direct exchange, a direct dipole-dipole interaction between magnetic moments, may occur when the cation *d* orbitals overlap sufficiently[42]. A critical distance is required for the overlap between cations, and in non-metallic transition metal materials the cations are too distant from each other for the direct exchange to occur. Long range magnetic ordering can arise via a superexchange mechanism[43] instead, in which an indirect interaction takes place depending on the covalent bonding of the metal cations and their bridging anion.

Consider a linear M^{n+}-O-M^{n+} pathway with a bond angle 180 º. The strongest interactions between the metal cations are predicted to be antiferromagnetic, as shown in Figure 1.9. The strength of the interaction is highly dependent on the M-O-M angle, as the superexchange is weakened if the bond angle decreases.

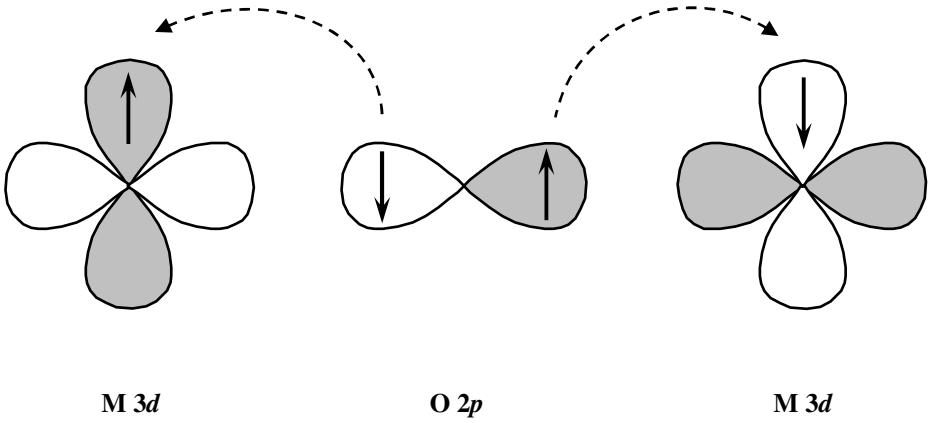

Figure 1.9 The M-O-M linear pathway giving antiferromagnetic coupling.

When the M-O-M angle is 90 º, the superexchange via the overlap of metal *d* orbitals and two different *p* orbitals of oxygen anion can give rise to ferromagnetic coupling, as shown in Figure 1.10. Therefore by superexchange the different M-O-M angles can lead to anti- or ferromagnetic coupling between cations.

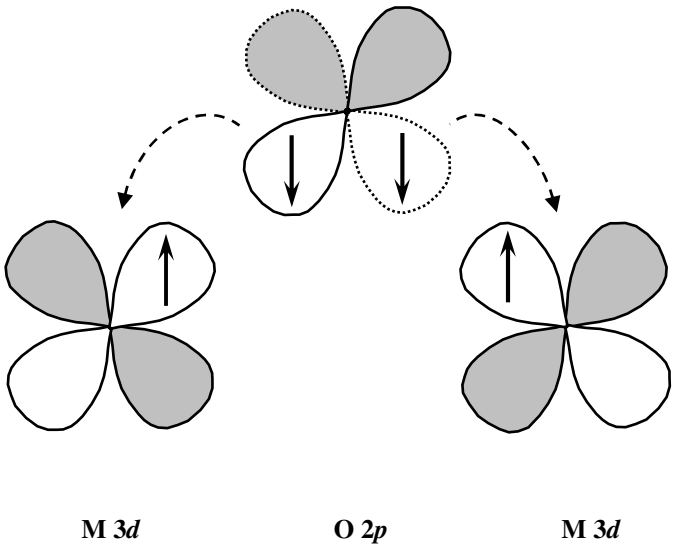

Figure 1.10 The superexchange interaction of 90º M-O-M giving ferromagnetic coupling.

A ferromagnetic coupling of a linear M-O-M array can also exist via superexchange with the presence of cooperative Jahn-Teller distortions. The interaction can occur between the bridging ligand, with a half filled *d* orbital on one metal cation and an empty *d* orbital on the other, as shown in Figure 1.11. These superexchange pathways and the resultant interactions are summarised in the Goodenough-Kanamori rules[35].

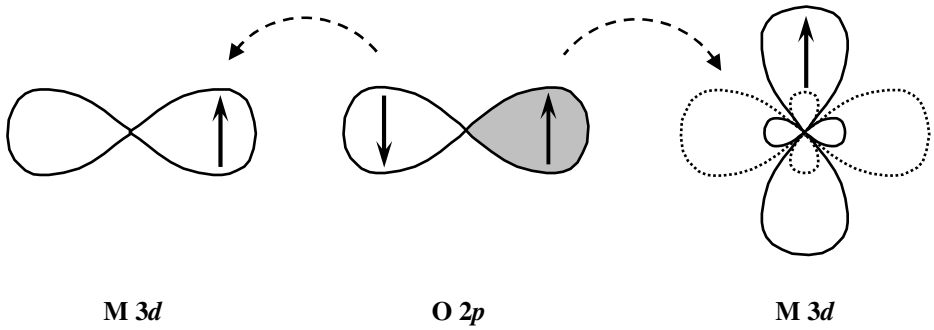

Figure 1.11 The superexchange of linear M-O-M with cooperative Jahn-Teller distortion leads to ferromagnetic coupling between cations.

Other exchange mechanisms can arise in metallic materials. For mixed-valence materials, which have cations with different oxidation states, a double exchange[22,44] mechanism can predict the movement of the electron, as shown in Figure 1.12. The delocalisation of electrons between adjacent cations reduces the kinetic energy and therefore favours a ferromagnetic coupling of the magnetic moments. This interaction can be seen between Mn^{3+} and Mn^{4+} cations in the mixed-valent manganites[45,46].

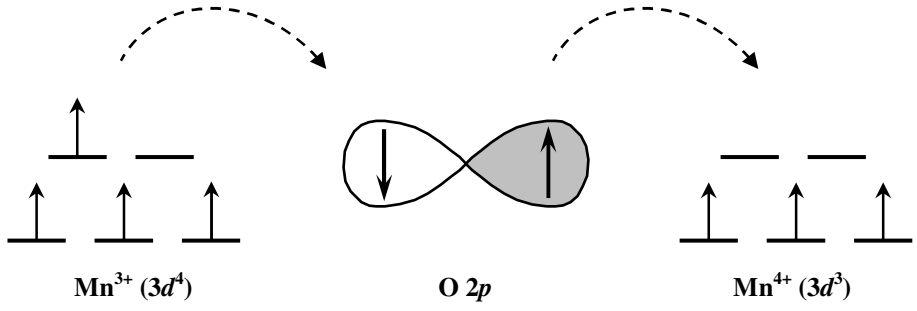

Figure 1.12 Schematic diagram of double exchange mechanism in Mn^{3+}-O-Mn^{4+}.

1.4 Ferroic Properties

A ferroic can be defined as a material that possess two or more orientation states or domains, which can be transformed from one to another when an appropriate force is applied[47]. In general, the spontaneous characteristic physical properties of ferroic materials occur below a transition temperature, while a non-ferroic state exists above such temperature. The main classes of magnetic materials and the properties of ferro- and ferrimagnetic materials that show spontaneous magnetisation are discussed earlier. Ferroelectric materials exhibit reversible spontaneous electric polarisation and ferroelasticity is the mechanical analogue of ferroelectricity and ferromagnetism. Materials that possess ferroic properties are extensively studied for fundamental research and also applications, *e.g.* as memories.

1.4.1 Ferroelectricity

Ferroelectric materials are generally defined by the exhibited reversible spontaneous electric polarisation without an external electric field. The spontaneous polarisation is due to the absence of centrosymmetry in the material, which produces an electric dipole moment. A schematic polarisation of the typical ferroelectric material $BaTiO_3$ is shown in Figure 1.13. Antiferroelectric properties can be found

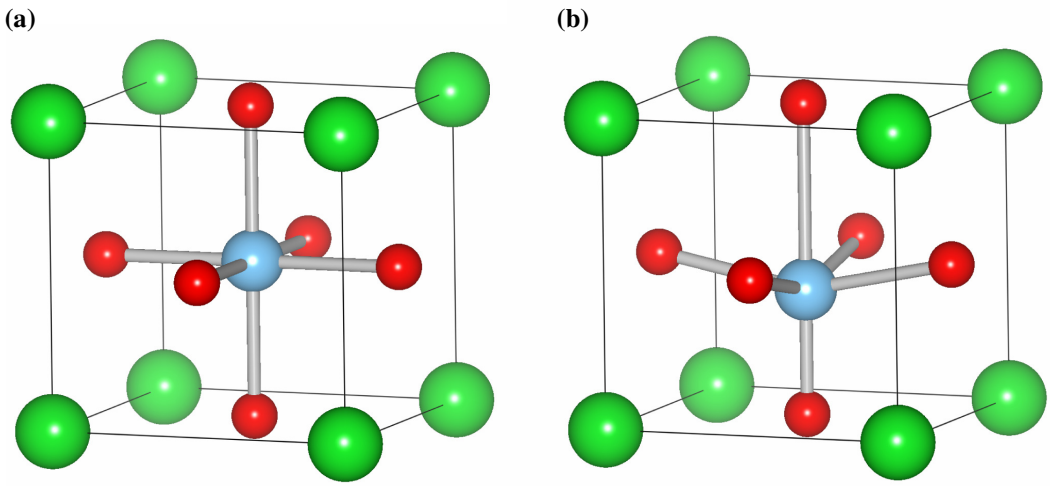

Figure 1.13 The schematic (a) non-polarised and (b) polarised $BaTiO_3$, where the ferroelectric effect is due to the displacement of the central atom.

if the material favours an antiparallel arrangement of the dipole moments. The ferroelectric and antiferroelectric materials transform to the paraelectric phase (where the dipoles are oriented randomly) above the transition temperature, which is similar to the transformation of ferromagnetic and antiferromagnetic materials to the paramagnetic state. At the transition temperature, a dielectric constant anomaly occurs for both ferroelectric and antiferroelectric materials.

As discussed earlier, an M-H hysteresis loop can be observed for the ferromagnetic materials. A ferroelectric exhibits the analogous characteristic hysteresis loop between polarisation (P) and electric field (E). Thus the orientation state of the polarisation can be altered by the application of an electric field. When an electric field is applied to the ferroelectric material, the saturated polarisation will be reached. This is due to the displacement of the material structure that generates a dipole moment. When the applied electric field is removed, the displacement remains and shows a residual polarisation in the absence of applied electric field. In order to reverse the direction of the polarisation, a coercive electric field is needed.

1.4.2 Multiferroics

The attempts to combine ferromagnetic and ferroelectric properties into one phase started in the 1960s. Although ferromagnetism or ferroelectricity can be found in numerous systems, the multiferroic materials, which show simultaneously magnetic and electric ordering in a single phase, are relatively rare. In addition to the fascinating physics resulting from the independent existence of two or more ferroic order parameters in one material, the coupling between magnetic and electric properties gives rise to additional phenomena. It can result in magnetoelectric effects in which the magnetisation can be tuned by an applied electric field and vice versa. This kind of material has a large application potential for new devices, taking advantage of these couplings based on local off-centred distortions and electron spins. For example, it is expected to form a new type of memory by a combination of ferroelectric and ferromagnetic properties. The coexistence of ferroelectricity and

ferromagnetism and their coupling with elasticity provide an extra degree of freedom in the design of new functional sensors and multi-state memory devices[48].

However the driving forces for ferromagnetism and ferroelectricity are generally incompatible hence it is difficult to have intrinsic multiferroic materials. The single phase multiferroic materials can be divided into two main groups[49]. In *Type-I* materials the ferroelectricity and the magnetic ordering are due to different active sublattices which coexist in one phase. The ferroelectricity in the conventional ferroelectric perovskites can arise from the off-centre displacement of small transition metal cations with d^0 configuration. The empty *d*-orbitals of the transition metal ion, for instance Ti^{4+} in $BaTiO_3$[48], tend to hybridise with 2*p* orbitals of the surrounding oxygens. The established strong covalency stabilises the off-centring of the *B* cation. This tendency, however, is removed with the presence of *d* electrons, which are essential for magnetic properties. Examples of *Type-I* materials based on d^0 and d^n cations are $PbFe^{3+}_{½}Nb^{5+}_{½}O_3$[50] or $PbFe^{3+}_{⅔}W^{6+}_{⅓}O_3$[51]. In these materials, the coupling between the sublattices is not strong.

The well-known *Type-I* multiferroic perovskites $BiFeO_3$[52] and $BiMnO_3$[53] contain magnetic Fe^{3+} (d^5) and Mn^{3+} (d^4). The polarisation in these materials results from the *A*-cation lone pairs of Bi^{3+} or Pb^{2+} cations (another example is $PbVO_3$[54]) rather than transition metal d^0 cations. In hexagonal perovskites (*e.g.* $RMnO_3$, *R* = Y[55] or small rare earth), geometric ferroelectricity is observed, which results from rotation of the MnO_5 trigonal biprisms in the material. Such tilting generates dipole moments of Y-O pairs and hence leads to ferroelectricity. In $LuFe_2O_4$[56], the frustration of Fe^{2+}/Fe^{3+} charge ordering in the double triangular FeO_2 layers forms electric polarisation and hence induces ferroelectricity.

In *Type-II* multiferroic materials the ferroelectricity occurs only in the magnetically ordered phase[57]. *Type-II* multiferroic materials include $TbMnO_3$[58], $TbMn_2O_5$[59] and $Ni_3V_2O_8$[60], in which the ferroelectricity is observed with spiral or helicoidal magnetic structures that result from spin frustration. $HoMnO_3$[61] is also a *type-II* multiferroic due to exchange striction within its unusual *E*-type magnetic structure[62].

1.5 Bismuth-Containing Perovskites

Bismuth-containing perovskites have attracted much attention due to their potential multiferroism and as lead-free ferroelectric materials. The presence of the off-centre Bi^{3+} displacement often leads to polar superstructures with appreciable ferroelectricity. Ferro/antiferromagnetic ordering is expected as a result of the coupling of the transition metal cations' spins.

BiMO$_3$ perovskites have been investigated where $M = 3d$ transition metals Sc, Cr, Mn, Fe, Co and Ni. The $BiScO_3$ and $BiCrO_3$ perovskites are synthesised with high-pressure techniques and adopt a *C2/c* monoclinic structure[63,64], which is the same as $BiMnO_3$. $BiCrO_3$ was further investigated recently due to its potential multiferroism[65,66], and was found to exhibit a structural transition at 420 K from the monoclinic structure to a $GdFeO_3$-type orthorhombic structure at increasing high temperatures[67,68]. The long range *G*-type antiferromagnetic ordering was observed below $T_N = 109$ K[68] and antiferroelectric properties were shown in thin film samples[69], which is in agreement with theoretical studies[65,70]. $BiMnO_3$ and $BiFeO_3$ are well-known bismuth-containing transition metal perovskites which show both magnetic and dielectric properties[63,71-73]. $BiMnO_3$ is a heavily distorted perovskite with a structural phase transition at 760 K[53], and is ferroelectric with Curie temperature $T_{C\text{-}FE} = 450$ K[74]. The ferroelectricity remains to low temperatures through the ferromagnetic transition at $T_{C\text{-}FM} = 105$ K[63,75,76]. $BiFeO_3$ has a rhombohedrally distorted structure. It shows *G*-type antiferromagnetic order with a long-periodicity spiral below the Néel temperature $T_N = 643$ K[77] and ferroelectricity below $T_{C\text{-}FE} = 1103$ K[78]. The ferroelectricity of $BiFeO_3$ is due to the Bi^{3+} $6s^2$ lone pair while the weak ferromagnetism results from the residual moment of the canted Fe^{3+} spin structure[72]. $BiCoO_3$ shows a tetragonal *P*4*mm* structure from 520 to 5 K, while a *C*-type antiferromagnetic behaviour with $T_N = 470$ K and the pyroelectric properties were revealed[37]. $BiNiO_3$ remains a $P\bar{1}$ triclinic structure down to 5 K at ambient pressure and displays a G-type antiferromagnetism below $T_N = 300$ K[79,80]. High pressure studies of $BiNiO_3$ have been conducted, showing a pressure induced structural transition from triclinic to an orthorhombic *Pbnm* structure at approximately 3 GPa[81].

A designed bismuth-containing double perovskite $Bi_2BB'O_6$, where *B* and *B′* are respectively Ni and Mn, has been prepared by high-pressure synthesis[82]. The material is heavily distorted with a monoclinic *C*2 structure, in which the Ni^{2+} and Mn^{4+} cations ordered in a rock-salt configuration[82]. The ferromagnetic ordering below $T_{C\text{-}FM} = 140$ K and the ferroelectric properties below $T_{C\text{-}FE} = 485$ K were reported for Bi_2NiMnO_6[82]. Other $Bi_2BB'O_6$ double perovskites, such as Bi_2CrFeO_6 and Bi_2CrCuO_6, have been explored theoretically[70,83,84] and the studies of Bi_2CrFeO_6 have been reported[85-88]. The multiferroism is shown in Bi_2CrFeO_6 thin films[79,81,82], while the $BiFeO_3$-like structure and the absence of *B*-site ordering was revealed by the bulk material[86].

The properties of perovskite materials are strongly dependent on their structures and the valence states of their cations. The structures can be distorted not only due to different cation sizes, but also by the introduced mixed-valence of the cations. This can be achieved by either non-stoichiometry of oxygen or *A* and/or *B*-cation substitutions, which are widely investigated to tune the properties of the materials. For instance, $BiMnO_3$ with strontium[76,89] and calcium[90,91] *A*-site substitutions have been studied extensively for the their spin, charge and orbital ordering. In $BiFeO_3$, trivalent[92-97] or divalent[98-101] cations substitution for Bi^{3+}, and dopings at *B*-sublattice[86,102-106] have recently been investigated in order to improve the magnetoelectric properties.

1.6 References

1. R. J. Cava, R. B. van Dover, B. Batlogg, and E. A. Rietman, *Phys. Rev. Lett.,* **58**, 408 (1987).
2. R. von Helmolt, J. Wecker, B. Holzapfel, L. Schultz, and K. Samwer, *Phys. Rev. Lett.,* **71**, 2331 (1993).
3. S. Jin, T. H. Tiefel, M. McCormack, R. A. Fastnacht, R. Ramesh, and L. H. Chen, *Science,* **264**, 413 (1994).
4. J. B. Goodenough, *Rep. Prog. Phys.,* **67**, 1915 (2004).
5. V. M. Goldschmidt, *Skr. Nor. Vidensk.-Akad. Oslo I, Mat.-Nat. Kl,* **8**, 7 (1926).

6. A. Glazer, *Acta Crystallogr. B,* **28**, 3384 (1972).
7. S. Geller, *J. Chem. Phys.,* **24**, 1236 (1956).
8. K. Leinenweber and J. Parise, *J. Solid State Chem.,* **114**, 277 (1995).
9. J.-H. Park, P. M. Woodward, and J. B. Parise, *Chem. Mater.,* **10**, 3092 (1998).
10. J. Chenavas, J. C. Joubert, M. Marezio, and B. Bochu, *J. Solid State Chem.,* **14**, 25 (1975).
11. P. D. Battle and C. W. Jones, *J. Solid State Chem.,* **78**, 108 (1989).
12. P. D. Battle, C. P. Grey, M. Hervieu, C. Martin, C. A. Moore, and Y. Paik, *J. Solid State Chem.,* **175**, 20 (2003).
13. M. T. Anderson and K. R. Poeppelmeier, *Chem. Mater.,* **3**, 476 (1991).
14. A. J. Jacobson, B. M. Collins, and B. E. F. Fender, *Acta Crystallogr. B,* **32**, 1083 (1976).
15. A. J. Jacobson, B. M. Collins, and B. E. F. Fender, *Acta Crystallogr. B,* **30**, 1705 (1974).
16. T. Sekiya, T. Yamamoto, and Y. Torii, *Bull. Chem. Soc. Jpn.,* **57**, 1859 (1984).
17. S.-H. Byeon, M. W. Lufaso, J. B. Parise, P. M. Woodward, and T. Hansen, *Chem. Mater.,* **15**, 3798 (2003).
18. I. O. Troyanchuk, O. S. Mantytskaja, H. Szymczak, and M. Y. Shvedun, *Low Temp. Phys.,* **28**, 569 (2002).
19. E. P. Wigner, *Trans. Faraday Soc.,* **34**, 678 (1938).
20. E. J. W. Verwey, *Nature,* **144**, 327 (1939).
21. E. J. W. Verwey and P. W. Haayman, *Physica,* **8**, 979 (1941).
22. C. Zener, *Phys. Rev.,* **82**, 403 (1951).
23. M. Uehara, S. Mori, C. H. Chen, and S. W. Cheong, *Nature,* **399**, 560 (1999).
24. S. Mori, C. H. Chen, and S. W. Cheong, *Nature,* **392**, 473 (1998).
25. J. B. Goodenough, *Phys. Rev.,* **100**, 564 (1955).
26. P. G. Radaelli, D. E. Cox, M. Marezio, and S. W. Cheong, *Phys. Rev. B,* **55**, 3015 (1997).
27. D. E. Cox and A. W. Sleight, *Acta Crystallogr. B,* **35**, 1 (1979).
28. P. M. Woodward, D. E. Cox, E. Moshopoulou, A. W. Sleight, and S. Morimoto, *Phys. Rev. B,* **62**, 844 (2000).
29. J. B. Torrance, P. Lacorre, A. I. Nazzal, E. J. Ansaldo, and C. Niedermayer, *Phys. Rev. B,* **45**, 8209 (1992).
30. J. A. Alonso, J. L. García-Muñoz, M. T. Fernandez-Díaz, M. A. G. Aranda, M. J. Martínez-Lope, and M. T. Casais, *Phys. Rev. Lett.,* **82**, 3871 (1999).

31. J. A. Alonso, M. J. Martínez-Lope, M. T. Casais, J. L. García-Muñoz, and M. T. Fernández-Díaz, *Phys. Rev. B,* **61**, 1756 (2000).
32. T. Saito, M. Azuma, E. Nishibori, M. Takata, M. Sakata, N. Nakayama, T. Arima, T. Kimura, C. Urano, and M. Takano, *Phys. B: Condens. Matter,* **329-333**, 866 (2003).
33. H. A. Jahn and E. Teller, *Proc. R. Soc. London, A,* **161**, 220 (1937).
34. J. P. Attfield, *Solid State Sci.,* **8**, 861 (2006).
35. J. B. Goodenough,"*Magnetism and the Chemical Bond*", John Wiley & Sons, (1963).
36. E. O. Wollan and W. C. Koehler, *Phys. Rev.,* **100**, 545 (1955).
37. A. A. Belik, S. Iikubo, K. Kodama, N. Igawa, S.-i. Shamoto, S. Niitaka, M. Azuma, Y. Shimakawa, M. Takano, F. Izumi, and E. Takayama-Muromachi, *Chem. Mater.,* **18**, 798 (2006).
38. W. C. Koehler, E. O. Wollan, and M. K. Wilkinson, *Phys. Rev.,* **118**, 58 (1960).
39. M. Gilleo, *Acta Crystallogr.,* **10**, 161 (1957).
40. S. Elliott,"*The Physics and Chemistry of Solids*", John Wiley & Sons, (1998).
41. A. R. West,"*Basic Solid State Chemistry*", John Wiley & Sons, (2000).
42. J. B. Goodenough, *Phys. Rev.,* **117**, 1442 (1960).
43. P. W. Anderson, *Phys. Rev.,* **79**, 350 (1950).
44. P. G. de Gennes, *Phys. Rev.,* **118**, 141 (1960).
45. A. J. Millis, P. B. Littlewood, and B. I. Shraiman, *Phys. Rev. Lett.,* **74**, 5144 (1995).
46. A. P. Ramirez, *J. Phys.: Condens. Matter,* **9**, 8171 (1997).
47. R. E. Newnham and L. E. Cross, pp. in *Preparation and Characterization of materials***.** Edited by J. M. Honig and C. N. R. Rao. Academic Press, New York, (1981).
48. N. A. Hill, *J. Phys. Chem. B,* **104**, 6694 (2000).
49. J. v. d. Brink and D. I. Khomskii, *J. Phys.: Condens. Matter,* **20**, 434217 (2008).
50. G. A. Smolenskiĭ and I. E. Chupis, *Soviet physics : Uspekhi.,* **25**, 1553 (1982).
51. Z.-G. Ye and H. Schmid, *Ferroelectrics,* **162**, 119 (1994).
52. F. Kubel and H. Schmid, *Acta Crystallogr. B,* **46**, 698 (1990).
53. H. Faqir, H. Chiba, M. Kikuchi, Y. Syono, M. Mansori, P. Satre, and A. Sebaoun, *J. Solid State Chem.,* **142**, 113 (1999).
54. A. A. Belik, M. Azuma, T. Saito, Y. Shimakawa, and M. Takano, *Chem. Mater.,* **17**, 269 (2005).
55. B. B. V. Aken, T. T. M. Palstra, A. Filippetti, and N. A. Spaldin, *Nat. Mater.,* **3**, 164 (2004).
56. N. Ikeda, K. Kohn, N. Myouga, E. Takahashi, Kit, ocirc, H. h, and S. Takekawa, *J. Phys. Soc. Jpn.,* **69**, 1526 (2000).

57. M. Mostovoy, *Phys. Rev. Lett.,* **96**, 067601 (2006).
58. T. Kimura, T. Goto, H. Shintani, K. Ishizaka, T. Arima, and Y. Tokura, *Nature,* **426**, 55 (2003).
59. N. Hur, S. Park, P. A. Sharma, J. S. Ahn, S. Guha, and S. W. Cheong, *Nature,* **429**, 392 (2004).
60. G. Lawes, A. B. Harris, T. Kimura, N. Rogado, R. J. Cava, A. Aharony, O. Entin-Wohlman, T. Yildirim, M. Kenzelmann, C. Broholm, and A. P. Ramirez, *Phys. Rev. Lett.,* **95**, 087205 (2005).
61. A. Muñoz, M. T. Casáis, J. A. Alonso, M. J. Martínez-Lope, J. L. Martínez, and M. T. Fernández-Díaz, *Inorg. Chem.,* **40**, 1020 (2001).
62. I. A. Sergienko, C. Sen, and E. Dagotto, *Phys. Rev. Lett.,* **97**, 227204 (2006).
63. F. Sugawara, S. Iiida, Y. Syono, and S.-i. Akimoto, *J. Phys. Soc. Jpn.,* **25**, 1553 (1968).
64. A. A. Belik, S. Iikubo, K. Kodama, N. Igawa, S. Shamoto, M. Maie, T. Nagai, Y. Matsui, S. Y. Stefanovich, B. I. Lazoryak, and E. Takayama-Muromachi, *J. Am. Chem. Soc.,* **128**, 706 (2006).
65. N. A. Hill, P. Battig, and C. Daul, *J. Phys. Chem. B,* **106**, 3383 (2002).
66. C. Goujon, C. Darie, M. Bacia, H. Klein, L. Ortega, and P. Bordet, *J. Phys. Conf.,* **121**, 022009 (2008).
67. T. Yokosawa, A. A. Belik, T. Asaka, K. Kimoto, E. Takayama-Muromachi, and Y. Matsui, *Phys. Rev. B,* **77**, 024111 (2008).
68. A. A. Belik, S. Iikubo, K. Kodama, N. Igawa, S. Shamoto, and E. Takayama-Muromachi, *Chem. Mater.,* **20**, (2008).
69. D. H. Kim, H. N. Lee, M. Varela, and H. M. Christen, *Appl. Phys. Lett.,* **89**, 162904 (2006).
70. P. Baettig, C. Ederer, and N. A. Spaldin, *Phys. Rev. B,* **72**, 214105 (2005).
71. C. Blaauw and F. v. d. Woude, *J. Phys. C: Solid State Phys.,* **6**, 1422 (1973).
72. P. Fischer, M. Polomska, I. Sosnowska, and M. Szymanski, *J. Phys. C: Solid State Phys.,* **13**, 1931 (1980).
73. I. Sosnowska, T. P. Neumaier, and E. Steichele, *J. Phys. C: Solid State Phys.,* **15**, 4835 (1982).
74. A. Moreira dos Santos, S. Parashar, A. R. Raju, Y. S. Zhao, A. K. Cheetham, and C. N. R. Rao, *Solid State Commun.,* **122**, 49 (2002).
75. V. A. Bokov, I. E. Myl'nikova, S. A. Kizhaev, M. F. Bryzhina, and N. A. Grigoryan, *Sov. Phys. Solid State,* **7**, 2993 (1966).
76. H. Chiba, T. Atou, and Y. Syono, *J. Solid State Chem.,* **132**, 139 (1997).

77. G. A. Smolenskii and V. M. Yudin, *Sov. Phys. Solid State,* **6**, 2936 (1965).
78. Y. E. Roginskaya, Tomashpo.Yy, Venevtse.Yn, V. M. Petrov, and G. S. Zhdanov, *Sov. Phys. Jetp,* **23**, 47 (1966).
79. S. Ishiwata, M. Azuma, M. Takano, E. Nishibori, M. Takata, M. Sakata, and K. Kato, *J. Mater. Chem.,* **12**, 3733 (2002).
80. S. J. E. Carlsson, M. Azuma, Y. Shimakawa, M. Takano, A. Hewat, and J. P. Attfield, *J. Solid State Chem.,* **181**, 611 (2008).
81. M. Azuma, S. Carlsson, J. Rodgers, M. G. Tucker, M. Tsujimoto, S. Ishiwata, S. Isoda, Y. Shimakawa, M. Takano, and J. P. Attfield, *J. Am. Chem. Soc.,* **129**, 14433 (2007).
82. M. Azuma, K. Takata, T. Saito, S. Ishiwata, Y. Shimakawa, and M. Takano, *J. Am. Chem. Soc.,* **127**, 8889 (2005).
83. Y. Uratani, T. Shishidou, F. Ishii, and T. Oguchi, *Phys. B: Condens. Matter,* **383**, 9 (2006).
84. F. Fajardo, R. Cardona, D. A. Landínez Téllez, J. Arbey Rodríguez M, and J. Roa-Rojas, *J. Magn. Magn. Mater.,* **320**, e111 (2008).
85. R. Nechache, C. Harnagea, A. Pignolet, F. Normandin, T. Veres, L.-P. Carignan, and D. Menard, *Appl. Phys. Lett.,* **89**, 102902 (2006).
86. M. R. Suchomel, C. I. Thomas, M. Allix, M. J. Rosseinsky, A. M. Fogg, and M. F. Thomas, *Appl. Phys. Lett.,* **90**, 112909 (2007).
87. N. Ichikawa, M. Arai, Y. Imai, K. Hagiwara, H. Sakama, M. Azuma, Y. Shimakawa, M. Takano, Y. Kotaka, M. Yonetani, H. Fujisawa, M. Shimizu, K. Ishikawa, and Y. Cho, *Appl. Phys. Express,* **1**, 101302 (2008).
88. D. H. Kim, H. N. Lee, M. D. Biegalski, and H. M. Christen, *Appl. Phys. Lett.,* **91**, 042906 (2007).
89. R. J. Goff and J. P. Attfield, *J. Solid State Chem.,* **179**, 1369 (2006).
90. H. Chiba, M. Kikuchi, K. Kusaba, Y. Muraoka, and Y. Syono, *Solid State Commun.,* **99**, 499 (1996).
91. I. O. Troyanchuk, O. S. Mantytskaya, and A. N. Chobot, *Phys. Solid State,* **44**, 2266 (2002).
92. S.-T. Zhang, L.-H. Pang, Y. Zhang, M.-H. Lu, and Y.-F. Chen, *J. Appl. Phys.,* **100**, 114108 (2006).
93. G. L. Yuan, S. W. Or, and H. L. W. Chan, *J. Phys. D: Appl. Phys.,* **40**, 1196 (2007).
94. V. L. Mathe, K. K. Patankar, R. N. Patil, and C. D. Lokhande, *J. Magn. Magn. Mater.,* **270**, 380 (2004).
95. G. L. Yuan, S. W. Or, J. M. Liu, and Z. G. Liu, *Appl. Phys. Lett.,* **89**, 052905 (2006).

96. V. L. Mathe, *J. Magn. Magn. Mater.,* **263**, 344 (2003).
97. G. L. Yuan and S. W. Or, *J. Appl. Phys.,* **100**, 024109 (2006).
98. D. H. Wang, W. C. Goh, M. Ning, and C. K. Ong, *Appl. Phys. Lett.,* **88**, 212907 (2006).
99. J. Li, Y. Duan, H. He, and D. Song, *J. Alloys Compd.,* **315**, 259 (2001).
100. V. A. Khomchenko, D. A. Kiselev, J. M. Vieira, A. L. Kholkin, M. A. Sa, and Y. G. Pogorelov, *Appl. Phys. Lett.,* **90**, 242901 (2007).
101. D. Kothari, V. R. Reddy, A. Gupta, V. Sathe, A. Banerjee, S. M. Gupta, and A. M. Awasthi, *Appl. Phys. Lett.,* **91**, 202505 (2007).
102. B. Yu, M. Li, J. Liu, D. Guo, L. Pei, and X. Zhao, *J. Phys. D: Appl. Phys.,* **41**, 065003 (2008).
103. Y.-K. Jun, W.-T. Moon, C.-M. Chang, H.-S. Kim, H. S. Ryu, J. W. Kim, K. H. Kim, and S.-H. Hong, *Solid State Commun.,* **135**, 133 (2005).
104. C. H. Yang, T. Y. Koo, and Y. H. Jeong, *Solid State Commun.,* **134**, 299 (2005).
105. I. A. Santos, H. L. C. Grande, V. F. Freitas, S. N. de Medeiros, J. A. Paesano, L. F. Cótica, and E. Radovanovic, *J. Non-Cryst. Solids,* **352**, 3721 (2006).
106. X. Qi, J. Dho, R. Tomov, M. G. Blamire, and J. L. MacManus-Driscoll, *Appl. Phys. Lett.,* **86**, 062903 (2005).

Chapter 2
Theoretical Considerations and Experimental Techniques

2.1 Sample Preparation

To prepare the samples studied in this thesis both conventional and high-pressure high-temperature (HPHT) solid state synthesis was used. Details of the synthesis methods are described below and different conditions of sample preparation will be discussed in the following chapters.

2.1.1 Conventional Ceramic Synthesis

Transition metal perovskites are typically prepared by the so-called standard ceramic method from stoichiometric amounts of required elements in their oxide or carbonate forms. The high-purity starting materials are ground using an agate pestle and mortar until a homogeneous mixture is obtained, then the mixture is pressed into pellets in order to improve particle contact. The prepared pellets are heated in an alumina boat within a high temperature furnace, usually between 800 and 1400 °C, to overcome the slow kinetics of ion diffusion across particle boundaries. After a certain period of heating treatment, the products are quenched from high temperature in order to ensure homogeneity. The progress of reaction is monitored with laboratory X-ray powder diffractometer (XRD) after each firing stage. Several intermediate regrinds and repelletings are applied in the synthesis to ensure the homogeneity of the required material and the completeness of reaction. The repetition is halted when a single phase is confirmed by XRD.

2.1.2 High Pressure Synthesis

For the synthesis of perovskites, the tolerance factor can be used to estimate the stability of desired materials. The materials with tolerance factor $0.85 < t < 1$ are usually stable, while poor perovskite phase stability is expected by lower *t*. High-pressure (1 to 10 GPa) high-temperature (~1000 °C) techniques have been used since *ca.* 1970 to prepare perovskites[1], with lower *t* that can be stabilised and recovered to ambient condition. The rates of the high-temperature solid state reactions can also be increased under high pressure treatments, where the perovskite phases are formed by ionic diffusion between component oxides.

A multi-anvil Walker-module press[2,3] manufactured by Max Voggenreiter GmbH was used to prepare samples with the high pressure synthesis method. Initial oxide reagents are weighed carefully in stoichiometric amounts for target products and ground thoroughly. The pressure cell assembly is then adopted as shown in Figure 2.1 (a). The well mixed reactants are loaded into a gold foil capsule then placed in a BN container, which electrically insulates the gold from the surrounding graphite sleeves furnace. A cylindrical ZrO_2 sleeve surrounds the furnace in order to provide thermal insulation. The cell is contacted by the Mo disks, which enable electric current to pass through the graphite resistance heater. This cylindrical assembly sits in a pressure transmitting MgO octahedron, which is surrounded by eight tungsten carbide cube anvils (Figure 2.1(b)). The prepared pressure cell and assembled WC anvils are placed into a cube-shaped cavity formed by 6 steel wedges, which are placed in a containment ring. High pressure is applied by a hydraulic press, which provides the force uniaxially through a pressure distribution plate on top of the steel wedges (Figure 2.1(c)). The desired sample temperature is controlled by applied electric power according to a power-temperature plot from previous temperature calibrations. After the heating stage the samples are quenched to room temperature and the applied pressure is released slowly. Each synthesis experiment can produce a bulk cylindrical product of ~ 20 mg in weight. A laboratory X-ray powder diffractometer is used to characterise the products.

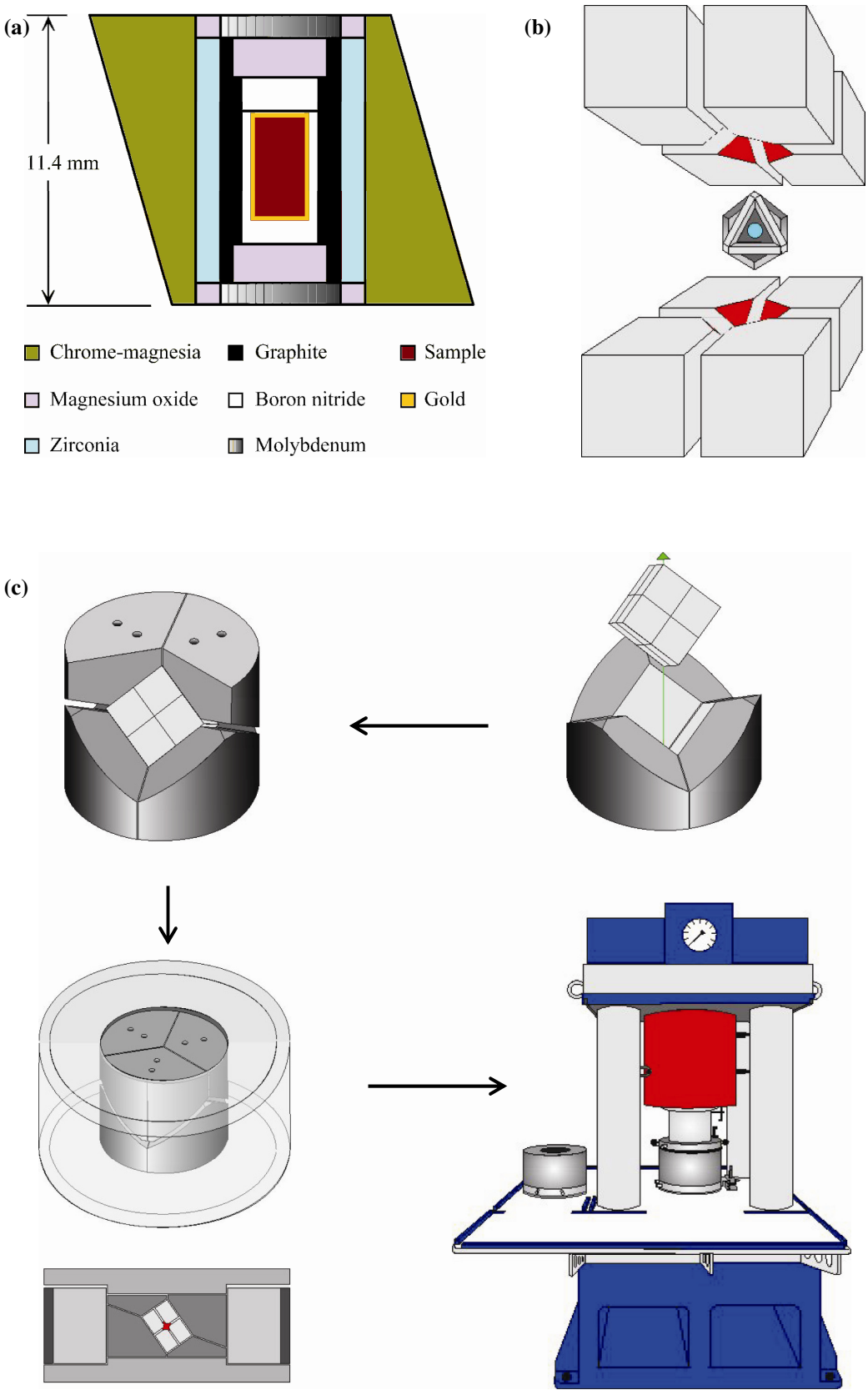

Figure 2.1 The schematic diagram of (a) the pressure cell assembly, (b) the octahedron in the WC cubic anvils and (c) the configuration of anvils in the Walker-module press[3,4].

2.2 Structural Determination

2.2.1 Diffraction Methods

Diffraction is a phenomenon that has been widely used to develop many useful and powerful techniques for the purposes of determination and characterisation of crystalline material structures. A crystalline solid consists of a three-dimensional periodic array of atoms which can be considered as extended from its unit cell. When the wavelength of an incident beam is comparable to the inter-atomic spacing in the crystal, the atoms can scatter and reflect the incident radiation so a diffraction pattern can be generated. X-ray, neutron and electron beams have a range of different wavelengths which are suitable to perform diffraction experiments for structure determination.

A crystalline material can be considered as consisting of layered parallel lattice planes which behave like semi-transparent mirrors. The constructive interference from the incident beam occurs when Bragg's Law is satisfied

$$n\lambda = 2d\sin\theta \qquad \textbf{(2.1)}$$

where n is an integer determined by diffraction order, d is the separating distance between parallel planes, λ is the wavelength of incident beams and θ is the angle of incidence, as shown in Figure 2.2. From Bragg's Law the symmetry and lattice parameters of the unit cell of a material can be obtained from analysing the positions of Bragg peaks, whereas positions of the atoms within the cell are related to the peak intensities.

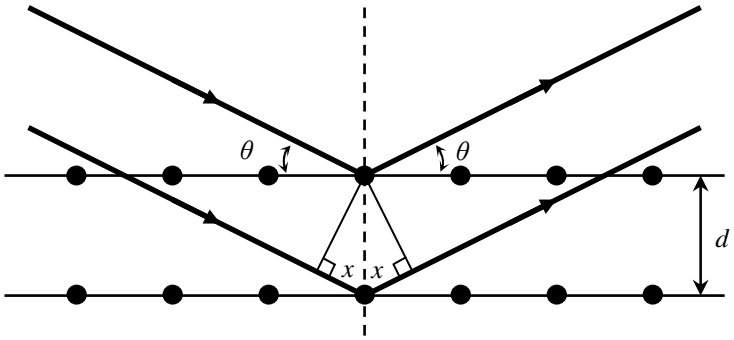

Figure 2.2 Diffraction of a beam from a set of lattice planes, separated by a distance, *d*.

To relate the atomic planes to the unit cell lattice parameters of a given crystalline material, the Miller indices are used. The Miller indices of a plane are commonly written (*hkl*), given by $h = a / x$, $k = b / y$ and $l = c / z$ where a, b, and c are lattice parameters of the unit cell and x, y, and z are the points where the plane intersects the crystallographic axes. Thus the distance between a family of (*hkl*) planes can be considered using Bragg's Law $\lambda = 2d_{hkl} \sin\theta_{hkl}$. From this consideration the position of the reflections can be predicted for a given periodic solid, and for an unknown solid the periodicity can be obtained from observed reflection positions.

The relative intensities of the observed reflections, I_{hkl}, are proportional to $|F_{hkl}|^2$, where F_{hkl} is the structure factor for the (*hkl*) reflection and is defined as

$$F_{hkl} = \sum_{j=1}^{N} f_j \exp\left[2\pi i\left(hx_j + ky_j + lz_j\right)\right]\exp\left[-B_j\left(\sin^2\theta\right)/\lambda^2\right] \qquad \textbf{(2.2)}$$

where F_{hkl} is the summation over all the atoms within the unit cell, f_j is the scattering factor or form factor for X-rays (scattering length b_j for neutrons) of atom j, x_j, y_j, and z_j are the fractional coordinates of atom j in the unit cell. The thermal motion of atoms is taken into account by the Debye-Waller factor where B_j is the atomic temperature factor which is related to the mean square thermal displacement factor U_j by $B = 8\pi^2 U$.

In this way, the observed diffraction pattern can provide information about not only the symmetry and lattice parameters of a particular crystalline material, but also the atomic contents and positions within its unit cell.

2.2.1.1 Powder Diffraction

For many materials it is impossible or extremely difficult to produce sufficiently large single crystals for single crystal diffraction experiments. In contrast, crystalline powders are relatively easy to synthesise. A crystalline powder sample consists of a large number of randomly orientated crystallites. For any given lattice plane there will be crystals in the material oriented with appropriate Bragg angle θ for diffraction

to occur. These crystals will take up every possible angular position with respect to the incident beam and therefore the diffracted beams will be emitted as cones of radiation, as shown in Figure 2.3. Although the three-dimensional nature of single crystal diffraction is compressed into one-dimensional data, a powder diffraction pattern can still provide information to derive the lattice parameters from diffraction peak positions and contents within the unit cell from peak intensities.

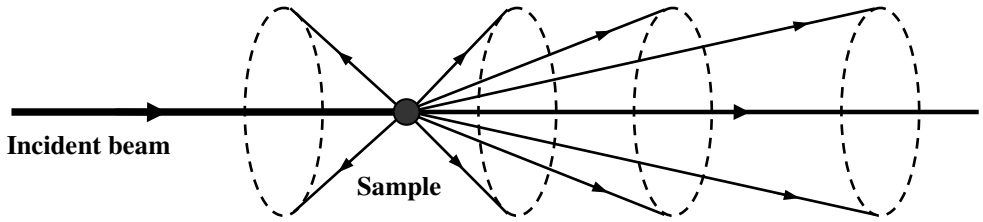

Figure 2.3 Cones of the diffracted radiation from the incident beam for a powder sample.

2.2.1.2 Rietveld Refinement

The Rietveld method, which was developed in the late 1960s[5], is widely used to refine crystal and magnetic structures from obtained X-ray or neutron powder diffraction patterns. For most powder diffraction patterns, overlaps happen between Bragg reflections especially for lower-symmetry materials due to the polycrystalline nature of a powder sample. Instead of analysing each individual reflection or resolving the reflection overlaps, the Rietveld method is performing a curve fitting procedure by considering the observed intensity $y_{i(obs)}$ of each equally spaced steps i over the entire pattern including the background intensity and the sum of the contribution of reflections close to the i powder pattern step:

$$y_{i(obs)} = y_{i(background)} + \sum_{i} y_{i(Bragg)}^{(i)} \qquad \textbf{(2.3)}$$

The Rietveld method is a refinement technique to minimise the residual S_y between the observed intensity $y_{i(obs)}$ and the calculated intensity $y_{i(calc)}$ by the best least-square fits to all the steps:

$$S_y = \sum_i \frac{(y_{i(obs)} - y_{i(calc)})^2}{y_{i(obs)}} = \sum_i w_i (y_{i(obs)} - y_{i(calc)})^2 \quad \textbf{(2.4)}$$

where w_i is statistical weight that equals $1/y_{i(obs)}$, and $y_{i(calc)}$ is the intensity of each step which can be calculated by a mathematical expression that includes the factors related to both the structure and the non-diffraction terms. Therefore a good initial structure model is required including information about space group, unit cell lattice parameters, atomic positions and instrumental details, where $y_{i(calc)}$ is expressed:

$$y_{i(calc)} = s\sum_{hkl} L_{hkl} \left|F_{hkl}\right|^2 \phi(2\theta_i - 2\theta_{hkl}) P_{hkl} A + y_{i(background)} \quad \textbf{(2.5)}$$

where s is the scale factor, L_{hkl} contains the Lorentz, polarisation and multiplicity factors, F_{hkl} is the structure factor which includes nuclear and magnetic structure factors if applicable, $\phi(2\theta_i - 2\theta_{hkl})$ is the peak shape function which describes the effects of the instrument and the sample on the reflection profile, P_{hkl} is the preferred orientation function, A is the absorption factor and $y_{i(background)}$ is the background intensity at the step i of the diffraction pattern. During the refinement cycles, each of these terms and its parameters may be varied to improve the match between observed and calculated diffraction patterns, *i.e.* to minimise the S_y value.

The fitting results can be estimated by examining a plot of the difference between observed and calculated patterns. On the other hand, several numerical terms can be used to estimate the goodness of the least-square refinements. These residual values are defined as:

$$R_p = \frac{\sum \left|(y_{i(obs)}) - (y_{i(calc)})\right|}{\sum (y_{i(obs)})} \quad \textbf{\textit{R-pattern}} \quad \textbf{(2.6)}$$

$$R_{wp} = \left| \frac{\sum w_i (y_{i(obs)} - y_{i(calc)})^2}{\sum w_i (y_{i(obs)})^2} \right|^{1/2} \quad \textbf{\textit{R-weight pattern}} \quad \textbf{(2.7)}$$

$$\chi^2 = \sum \frac{w_i (y_{i(obs)} - y_{i(calc)})^2}{n - p + c} \quad \textbf{\textit{Goodness of fit}} \quad \textbf{(2.8)}$$

where n is the number of observations, p is the number of parameters and c is the number of constrains in the definition of goodness of fit. A good fit with the refined

structure model will accompany with a low residual value. The R_{wp} is commonly considered since it contains S_y which quantity to be minimised by the least-square refinements. The goodness of fit, χ^2, which is directly proportional to S_y, is also typically regarded and is ideally to be unity.

All refinements of nuclear structures and magnetic orderings from X-rays and neutrons powder diffraction patterns in this thesis were carried out with Rietveld method using the General Structure Analysis System (GSAS) developed by A. C. Larson and R. B. Von Dreele[6].

2.2.1.3 X-ray Diffraction

In order to satisfy Bragg's Law (Equation 2.1), the incident radiation with a comparable wavelength to the interatomic spacings in a given crystalline material is required. This corresponds to the X-ray region of the electromagnetic spectrum, thus X-rays are ideal and commonly used for conducting diffraction studies. X-ray beams can be described as electromagnetic waves which will interact with electron clouds of an atom. Hence the scattering factor of an atom is related to its atomic number Z, *i.e.* the number of electrons in the atom. As a result it is difficult to distinguish neighbouring atoms in the periodic table since they have similar scattering powers, and also light atoms are hard to locate, particularly in the presence of heavy atoms, as they only scattered weakly. As the electron cloud of an atom is large, the scattered X-rays from different electrons around the atom are not in phase and the scattered intensity is reduced rapidly with increasing scattering angle.

Laboratory X-ray Diffractometer Brucker D8

The most commonly used source of X-rays in a laboratory diffractometer is an X-ray tube where electrons are accelerated and bombard a metal target such as copper or molybdenum to generate X-rays. The wavelength characteristic to the metal target is selected using a single crystal monochromator.

In this thesis laboratory X-ray powder diffraction was performed with a Bruker D8 advance diffractometer. The D8 diffractometer uses Cu-Kα_1 radiation with

λ = 1.540598 Å and a Ge (111) monochromator. All samples were measured in flat plate mode. A scan range of 5 ° < 2θ < 98 ° and a scan length of two hours were used for structure characterisation and refinement. Diffraction patterns obtained from the ICSD (Inorganic Crystal Structure Database) were used for the comparison with obtained products, and as the starting models for the refinements.

2.2.1.4 Synchrotron X-ray Diffraction

With a synchrotron radiation source, high brilliance of the beam and coherence of the electromagnetic waves can be produced, so that very intense X-rays are generated compare to those from a conventional X-ray source. The main constituents of a modern synchrotron radiation source are illustrated in Figure 2.4. The electrons will first be accelerated from a linac (linear accelerator) and then by a booster ring. After a certain energy and velocity (approaching the speed of light) is reached the electron beam will be injected into the storage ring which is operated at ultrahigh vacuum conditions. The electron beam will be confined in a circular orbit, which is about the width of a needle, with a large radius by a succession of bending magnets. The beam will be deflected from a straight path by some degrees when passing

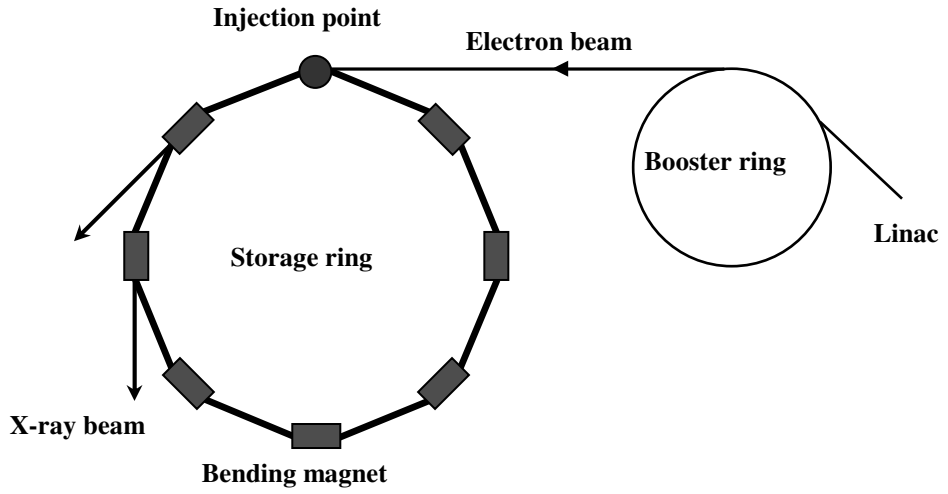

Figure 2.4 Schematic diagram of main constituents of a synchrotron radiation source[7].

through bending magnets, consequently synchrotron radiation will be emitted tangentially to the electron orbit. The emitted radiation has not only extremely high brilliance but also a very broad spectral range with high intensity which easily allows a desired wavelength to be selected for different experiment requirements. In addition, insertion devices such as undulators, wigglers and focusing magnets, which consist of periodically arranged magnets, can be employed at the straight sections of the ring to improve the intensity and brilliance of the radiation.

European Synchrotron Radiation Facility, ESRF

The European Synchrotron Radiation Facility, ESRF, located at Grenoble, France, is a third generation synchrotron source and also one of the brightest synchrotron sources in the world. The energy and maximum current of the electron beam in the storage ring is 6 GeV and 200 mA, respectively. The ESRF storage ring

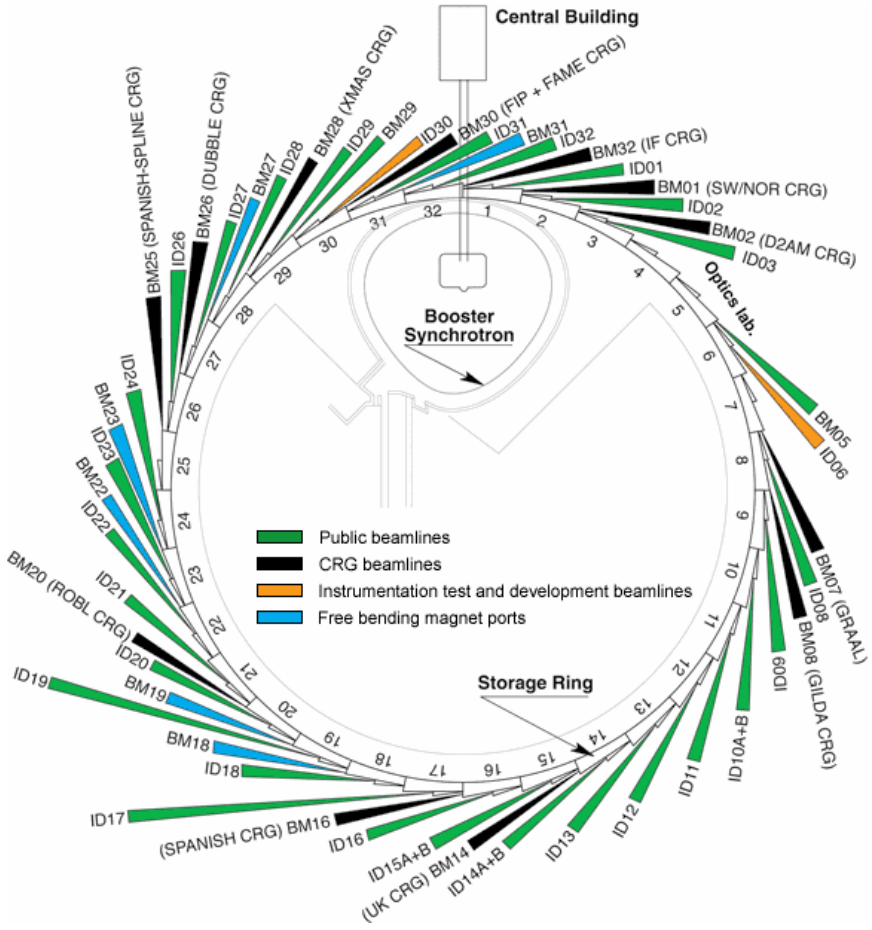

Figure 2.5 The layout of the experiment beamlines of ESRF[8].

has a circumference of 844m and 31 beamlines which are shown in Figure 2.5. These beamlines are operational for public users and cover a wide range of research areas. The instruments for synchrotron X-ray diffraction used in this work were ID31 and BM01B.

ID31

ID31 is the high resolution powder diffraction beamline in ESRF. The X-rays for ID31 are generated by three undulators which give a very intense beam with energy range from 5-60 keV (wavelength 2.48 - 0.21 Å). The beam is then monochromated by a double-crystal monochromator using Si (111) reflections. The diffractometer can accept either spinning capillary or flat plate specimens. A multianalyser detector stage, which consists of a bank of nine scintillation detectors where each detector is equipped with a Si (111) analyser crystal, is scanned vertically to measure the intensities of diffraction as a function of 2θ (Figure 2.6). The detector channels are offset approximately 2 º from each other thus the movement of the detector arm needs no more than about 2.3 º to measure an angular range of 18 º in 2θ. The diffraction peaks have not only accurate and reproducible positions but also the angular resolution is good in terms of the full width at half maximum (FWHM) of around 0.003 º in 2θ. The diffraction can be carried out under a wide range of conditions by using different ancillary equipments such as a cryostat for a spinning capillary to a temperature as low as 3 K or a mirror furnace for Pt capillary heated as high as ~1500 ºC.

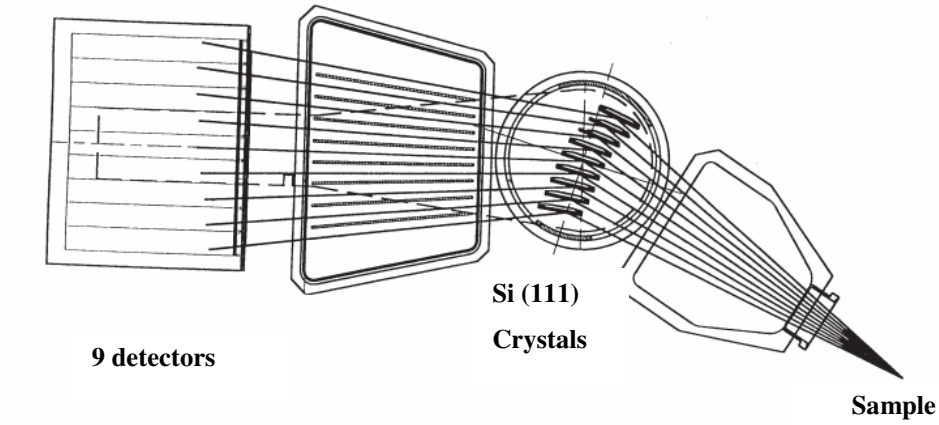

Figure 2.6 The multianalyser detector system used for ID31[8].

The ID31 diffraction data in this thesis was collected using a spinning glass capillary of 0.3 mm diameter with a wavelength of 0.39825 Å in an angular range of $3° \leq 2\theta \leq 30°$. The patterns were collected at room temperature and also a hot-air blower was used to obtain the high temperature data, with a counting time of 1 hour for each pattern.

BM01B

BM01, the so-called Swiss-Norwegian Beam Line (SWBL), is a Collaborating Research Group beamline. The beamline is installed on a bending magnet source and the incoming beam is split into two independently operated beamlines. There are four different experimental techniques provided on the separated two beamlines at BM01, where high resolution powder diffraction is available at BM01B. BM01B has a spectral range of 5 - 41 keV and a typically used wavelength range of 0.4 – 1.2 Å. A similar diffractometer to ID31 is used at BM01B but only six instead of nine detectors with an angular offset of about 1 ° between each other are used. Each detector is mounted with a Si (111) analyser crystal, which results in a resolution (FWHM) of about 0.01 °. A cryostat or a furnace can be used for capillary measurements which allowed the diffraction to be carried out at a condition from 5 to 1273 K.

The high temperature BM01B diffraction experiments were conducted with a 0.7 mm quartz capillary and a wavelength of 0.50010 Å in an angular range of $1° \leq 2\theta \leq 30°$. A series of temperatures and a collecting time of 3 hours was used for each pattern.

2.2.1.5 Neutron Diffraction

The neutron is a powerful tool to study the structure of crystalline materials as an alternative diffraction source to X-rays. By the de Broglie equation, $\lambda = h / p$, the wavelength λ of its corresponding quantum mechanical wave can be related to the momentum p of a free particle, where h is Planck's constant. Thus a thermal neutron

which has approximate velocity of 2.2 km/s can be a useful crystallographic probe since its wavelength is comparable to interatomic distances.

There are several advantages of neutron diffraction in comparison to X-ray sources which makes neutron diffraction an important technique in the field of structure determination. Neutrons, unlike X-rays, interact with nuclei of atoms rather than electron clouds. Thus the fall-off of the scattering power in the case of X-ray diffraction, which is due to the finite size of the electron cloud, is not seen. The scattering power of nuclei, on the other hand, is approximately constant since the neutrons interact with point scatterer atom nuclei. The scattering power, which is represented by neutron scattering length b_i, is generally independent of scattering angle and as a result, strong reflections can be observed at both long and short *d*-spacings.

In addition, neutron scattering lengths b_j vary as an irregular function of atomic number Z as shown in Figure 2.7. Therefore not only can neighbouring atoms in the periodic table be distinguished from each other, but also light atoms can be detected in the presence of heavier atoms. The ability to scatter both light and heavy atoms in a material plays an important role, for example, in the completion of metal oxide structure determinations.

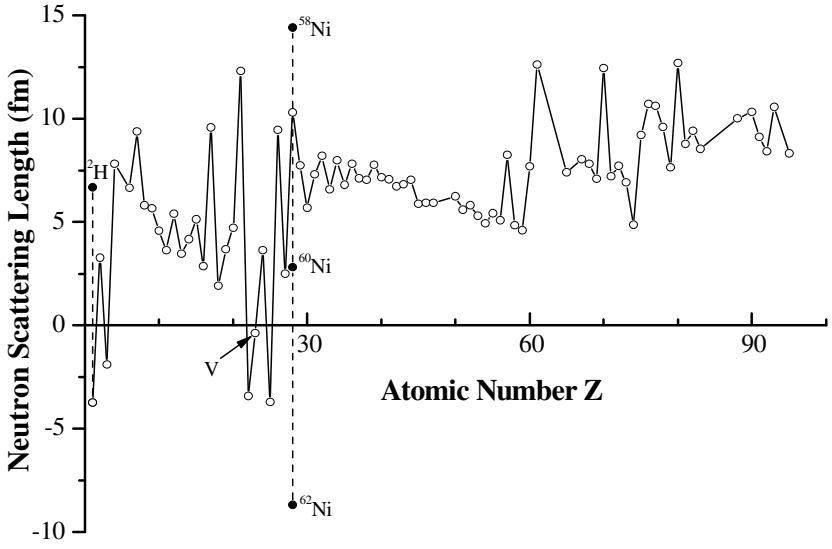

Figure 2.7 The irregular function of neutron scattering length against atomic number. The full markers demonstrate the difference of scattering length among isotopes[9].

Furthermore, the neutron has a spin quantum number ½, and the possession of a magnetic moment allows the neutron to interact with unpaired electron spins. This makes neutron diffraction a powerful tool to determine magnetic structures of materials. The magnetic scattering power of neutron diffraction, which can be termed as a form factor f_m, is similar to the X-ray scattering factor. The total intensity scattered by unpolarised neutrons which contain all directions of spins will be the sum of both nuclear and magnetic scattering, as shown below:

$$F_{hkl}^{Tot^2} = F_{hkl}^{nuc^2} + F_{hkl}^{mag^2} \qquad \textbf{(2.9)}$$

where F_{hkl}^{nuc} and F_{hkl}^{mag} are respectively structure factors of nuclear and magnetic structures. The term F_{hkl}^{nuc} is described in Equation 2.2 and the magnetic structure factor F_{hkl}^{mag} can be defined as:

$$F_{hkl}^{mag} = \sum_{j=1}^{N} q_j p_j \exp\left[2\pi i\left(hx_j + ky_j + lz_j\right)\right] \qquad \textbf{(2.10)}$$

where q_j is the magnetic interaction vector which depends on magnetic moment and scattering vector of atom j, and p_j is the magnetic scattering length which is calculated from the magnitude of the magnetic moment and the magnetic form factor f_m.

When a material possesses magnetic moments which are orientated in all directions as in a paramagnet, the incident neutron is scattered incoherently so that the background intensity increases. The magnetic Bragg peaks can be observed, on the other hand, if magnetic ordering appears in a material. For ferromagnetic structures, the magnetic ordering and the nuclear cell will have the same periodicity, hence the reflections of nuclear and magnetic structure will be superimposed. For commensurate antiferromagnetic structures, extra reflections from magnetic ordering will be observed in addition to nuclear reflections. This is due to the supercell of the magnetic structure, which has a periodicity greater than that of the nuclear cell in one or more directions. For incommensurate magnetic structures, satellite peaks which surround the nuclear Bragg reflections are commonly observed. Therefore with information of nuclear and magnetic reflections, neutron diffraction is a powerful tool that enables both nuclear structure and magnetic ordering of a material to be determined simultaneously.

The weak interactions of neutrons with atom nuclei provide a highly penetrating and non-destructive probe, which enables experimental configurations with complex sample environments such as cryostats, furnaces and pressure cells to be used. Compared to X-rays, however, a relatively large amount of sample is required for neutron diffraction due to the weak interaction and the low intensity generated by neutron sources.

To produce sufficient fluxes of neutrons, two types of sources are built for research use. They are nuclear reactors and spallation sources which respectively allow diffraction studies by constant wavelength and time-of-flight techniques.

2.2.1.5.1 Constant Wavelength Neutron Diffraction

Neutron flux is conventionally generated from a nuclear reactor where fast neutrons are produced continuously in time by nuclear fission. In order to maintain the process of nuclear fission and also to have a suitable range of wavelengths to study atomic structure, a moderator which normally contains a large amount of low mass nuclei is used to slow down the produced fast neutrons. The moderated thermal neutrons have a wide range of energy *i.e.* a white spectrum, hence a monochromator is required to select neutrons with a desired wavelength for the experiments.

Institut Laue-Langevin (ILL)

The High Flux Reactor at Institut Laue-Langevin (ILL) located at Grenoble, France is the most intense constant wavelength neutron source in the world. The high flux research reactor delivers a flux of 1.5×10^{15} thermal neutrons per second per cm^2 with a thermal power of 53.8 MW. Several moderators at various temperatures are used in order to provide high flux neutrons with a wide range of wavelengths for different studies. There are more than 50 measuring stations as shown in Figure 2.8. The instruments used in this thesis are Super-D2B and CRG instrument D1B where the thermal neutrons used are sourced from the main ambient D_2O moderator.

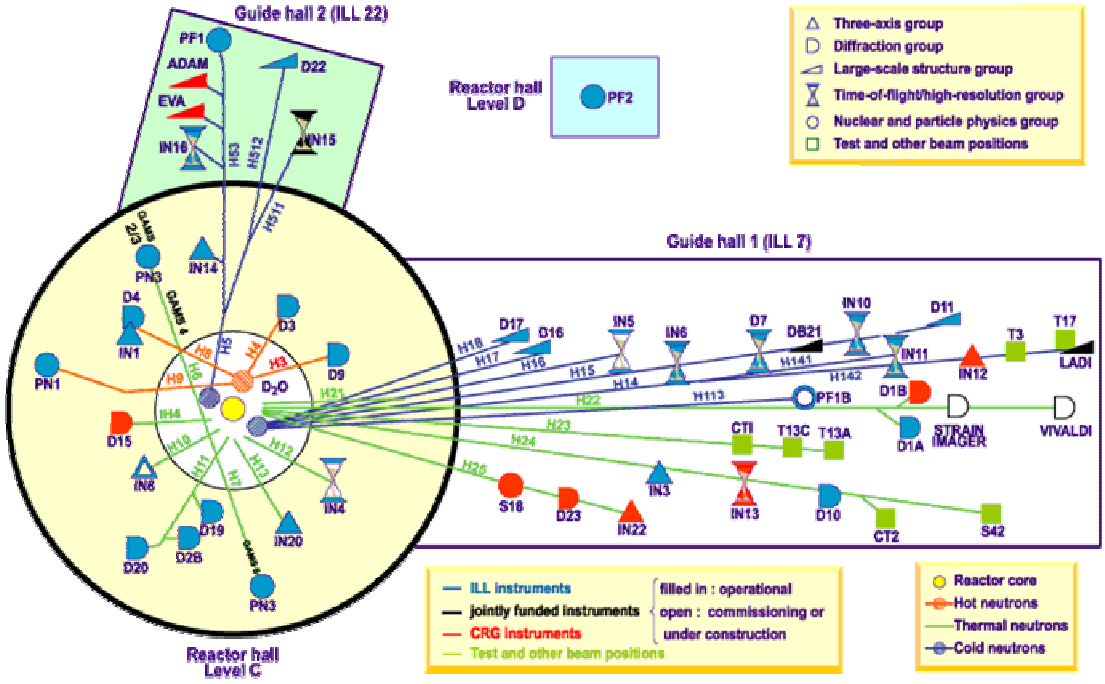

Figure 2.8 The layout of experiment instruments in Institut Laue-Langevin[10].

Supre-D2B

Super-D2B is a high resolution two-axis powder diffractometer designed to achieve high resolution. The diffractometer is located in the reactor hall at ILL where the geometry of instrument layout is shown in Figure 2.9. The optimum neutron flux on the sample is enabled by both vertical and horizontal focussing of the monochromator and the high monochromator take-off angle (135 °). A range of neutron wavelengths from 1.051 to 3.152 Å is available by using different (*hkl*) of a Ge crystal monochromator, and the optimum flux is achieved with a neutron wavelength of 1.594 Å. The detector array consists of high resolution collimators and 128 resistive wire detectors that are 300 mm in height. The detectors have an interval of 1.25 ° so that a complete pattern with the angular range $5\ ^\circ \leq 2\theta \leq 165\ ^\circ$ can be obtained after 25 steps of 0.05 ° in 2θ. The scans are usually repeated several times to improve statistics. A choice of cryostat, cryofurnace or furnace used allows sample temperature to be as low as 1.5 K or as high as 1000 K, and data collection under high pressure can be also achieved by using a pressure cell.

The neutron powder diffraction data of polycrystalline samples obtained from Super-D2B in this thesis were collected with an 8mm diameter vanadium can at 10 and 300 K. Data were collected in the angular range $5° \leq 2\theta \leq 155°$ for about 50 minutes per scan with a neutron wavelength of 1.594 Å without collimation.

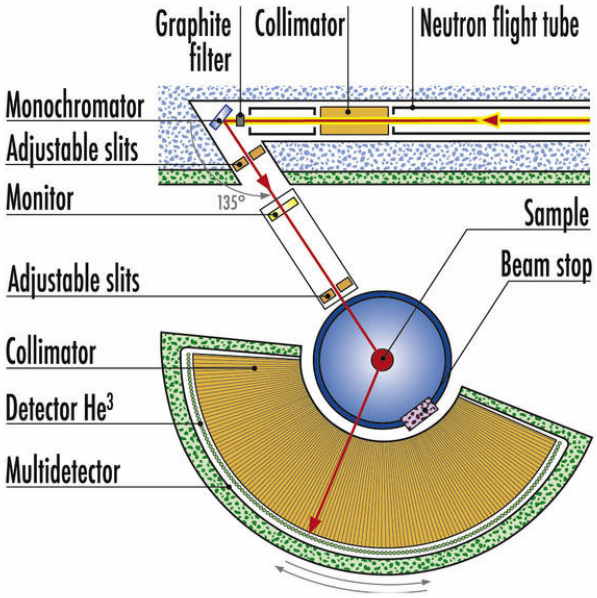

Figure 2.9 The instrument layout and geometry of D2B diffractometer[10].

D1B

D1B is a high intensity two-axis powder diffractometer located in guide hall 1 at ILL, the layout of the instrument is shown in Figure 2.10. High neutron flux with a wavelength of 2.52 Å is achieved with the pyrolitic graphite monochromator, while the Ge monochromator is also available to provide 1.28 Å neutrons but with much lower flux. The multidetector system with 400 cells allows a complete diffraction pattern covering a 2θ range of 80 ° to be collected simultaneously, or a pattern with an angular range $2° \leq 2\theta \leq 130°$ can be obtained by moving the detectors. Due to the high neutron flux and position sensitive detector (PSD), D1B is an ideal diffractometer to efficiently study temperature-dependent magnetic properties, as the main magnetic reflections are expected at high *d*-spacing/low 2θ angle.

High temperature neutron powder diffraction data were collected on instrument D1B using 2.52 Å wavelength neutrons. Diffraction patterns were collected in 1 °C steps from room temperature to 400 °C in the angular range $5\,^{\circ} \leq 2\theta \leq 85\,^{\circ}$ with a ramping rate of 0.8 °C per minute and a counting time for 1.25 minute per scan.

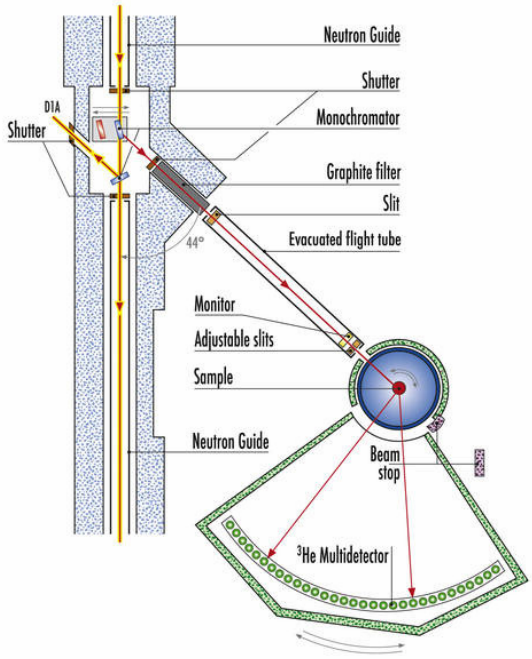

Figure 2.10 The instrument layout and geometry of D1B diffractometer[10].

2.2.1.5.2 Time of Flight method

One of the disadvantages of a reactor-based neutron source is its relatively low neutron flux since a suitable energy range has to be selected in order to perform structure studies. In comparison, a spallation source can generate neutrons with much higher flux. An accelerator-based, or spallation neutron source can produce a flux of greater than 10^{17} $n{\cdot}s^{-1}{\cdot}cm^{-2}$ while the flux of a reactor-based source is about 10^{15} $n{\cdot}s^{-1}{\cdot}cm^{-2}$. A modern spallation neutron source consists of a linear accelerator usually with a synchrotron ring where a beam of protons can be accelerated to high energy, and a heavy metal target (tantalum, uranium or tungsten) which is bombarded by the accelerated proton beam with short pulses. The pulse of neutrons with a range of energies will then be produced by the bombardment and is used for time-of-flight (TOF) techniques.

From Bragg's Law $\lambda = 2d \sin\theta$, there can be two different approaches to determine atomic spacing d from the diffraction. A constant wavelength λ can be selected and varying the detector angle θ performs angle-dispersive diffraction. This can be achieved with monochromated neutrons produced continuously from a reactor source. Alternatively, a fixed detector angle θ can be adopted and using neutrons with a range of wavelengths performs wavelength-dispersive *i.e.* TOF diffraction. Unlike the angle-dispersive diffraction, no specific wavelength selection is needed and neutrons with many energies produced from a pulsed source will be used to complete a diffraction pattern from each pulse.

Considering TOF diffraction, the neutron wavelength can be obtained from the de Broglie equation $\lambda = h / p$ where the momentum $p = mv$ and the velocity $v = L / t$ with neutron mass m, known flight path from source to detector L and the total time of flight t. Combining with Bragg's Law, the total time of flight of the diffracted neutron can be derived as

$$t = \frac{mL}{h} 2d \sin\theta \qquad \textbf{(2.11)}$$

Instrumental resolution can be improved by using a high detector angle and a long neutron flight path. One of the advantages of TOF diffraction is the ability to measure very small d-spacings. In a conventional diffraction, the minimum d-spacing is limited as $d_{min} = \lambda / 2$ when $2\theta = 180$ °. On the other hand, the measurement of very low d-spacings can be achieved by TOF diffraction using high energies *i.e.* short wavelengths neutrons. In order to simultaneously collect diffraction patterns, a series of detector banks which consist of a large number of detectors is often provided on a TOF diffractometer at different set angles.

ISIS

ISIS is the leading pulsed neutron source in the world and is the main facility at the Rutherford Appleton Laboratory located near Oxford. The neutrons are produced by a spallation process which involves the bombarding a tantalum target with pulses of accelerated protons, shown in Figure 2.11. An array of hydrogenous moderators is placed around the target to produce neutrons suitable for condensed matter studies.

The ambient temperature water (43 °C), liquid methane (100 K) and liquid hydrogen (20 K) moderators allow different spectrally distributed neutrons to be used for different types of experiment.

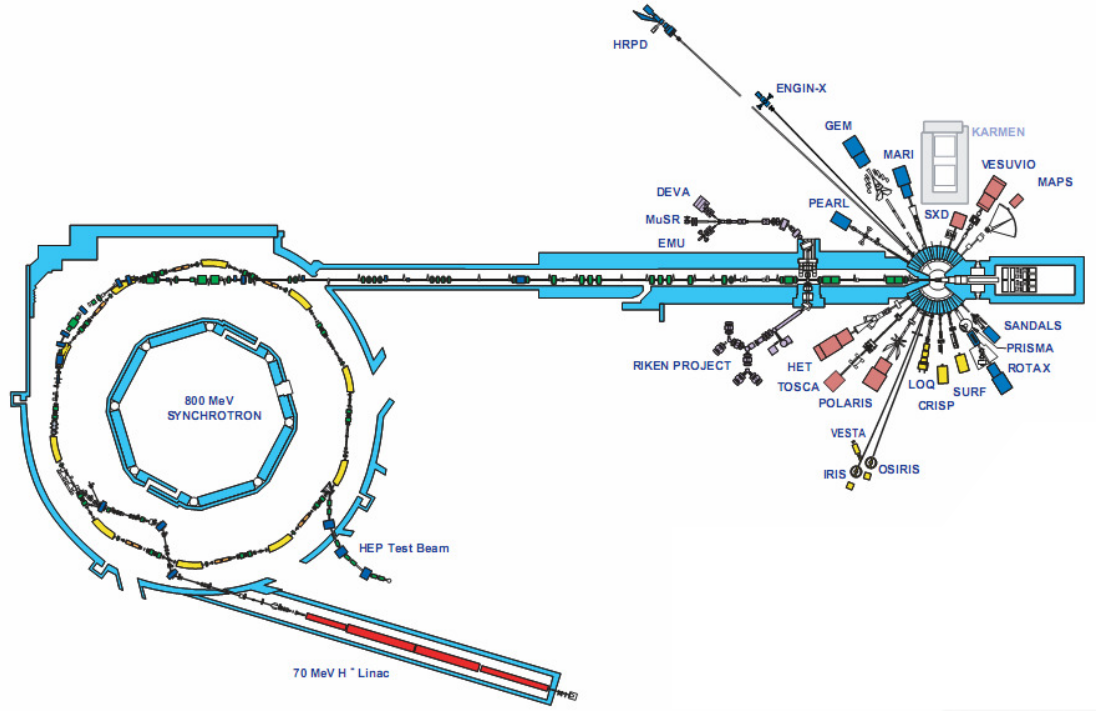

Figure 2.11 The layout of the Linac, proton synchrotron and experiment instruments at ISIS[11].

General Materials Diffractometer, GEM

The General Materials Diffractometer (GEM) is a neutron diffractometer designed for structural studies of disordered materials and crystalline powders. The high intensity, high resolution properties of GEM are provided by high neutron flux and a length of incident beam path 17m from the liquid methane moderator to the diffractometer. The single-frame bandwidth is defined to be 4.2 Å by a series of choppers to prevent frame overlap, and the beam-defining apertures can be set to minimise the background intensity. A very wide range of 1.1 ° to 169.3 ° in scattering angle is covered by the detector banks consisting of more than 7000 ZnS scintillator elements, where the installation of detector banks is shown in Figure 2.12. Study at low temperature can be achieved by using a top-loading Closed-Cycle Refrigerator (CCR).

The materials studied in the thesis were measured within a vanadium can at different temperatures using a CCR on GEM. The diffraction patterns at each temperature were collected from 6 detector banks for 5 to 6 hours. Multi-histogram refinements combining patterns from different detector banks were performed by the GSAS software package with Rietveld method.

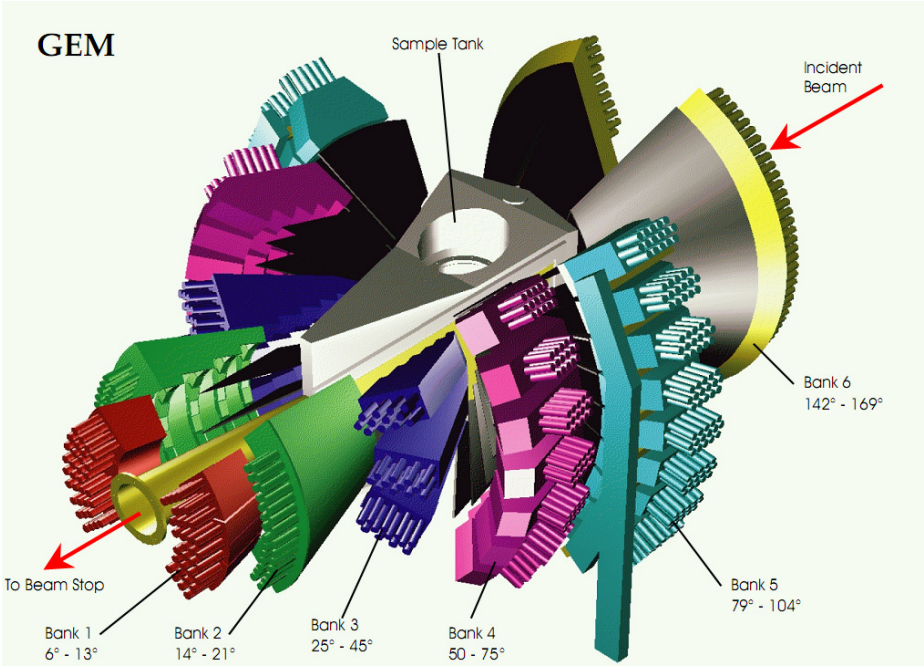

Figure 2.12 The different detector banks at GEM[11].

HiPr: The PEARL High Pressure Facility

HiPr, the PEARL (Pressure and Engineering Advanced Research Line) High Pressure facility, is a medium resolution high-flux diffractometer designed for high pressure studies using the Paris-Edinburgh pressure cell. There are eleven detector modules equipped for the diffractometer allowing two different scattering geometries to be used. The schematic drawing of the instrument is shown in Figure 2.13. The main detector bank which consists of nine of the detector modules is used for the standard transverse (through-anvil) scattering of Paris-Edinburgh cell and covering an angular range of $83^\circ < 2\theta < 97^\circ$ giving access to a *d*-spacing range of~0.5 - 4.1 Å.

The rest of the detector modules are used for longitudinal (through-gasket) scattering which covers angular ranges of $20^\circ < 2\theta < 40^\circ$ and $100^\circ < 2\theta < 120^\circ$ respectively allowing *d*-spacing ranges of ~1 - 10 Å and ~0.5 - 3.5 Å to be studied. The material can be pressurised up to 10 GPa with standard tungsten carbide anvils, and the temperature can be as low as 90 K with liquid nitrogen or up to 1200 K using a graphite heater with the sample cell.

Only the main detector modules (longitudinal scattering) were used for the high pressure studies in this thesis. Diffraction patterns with various pressures and temperatures were collected for 6 hours.

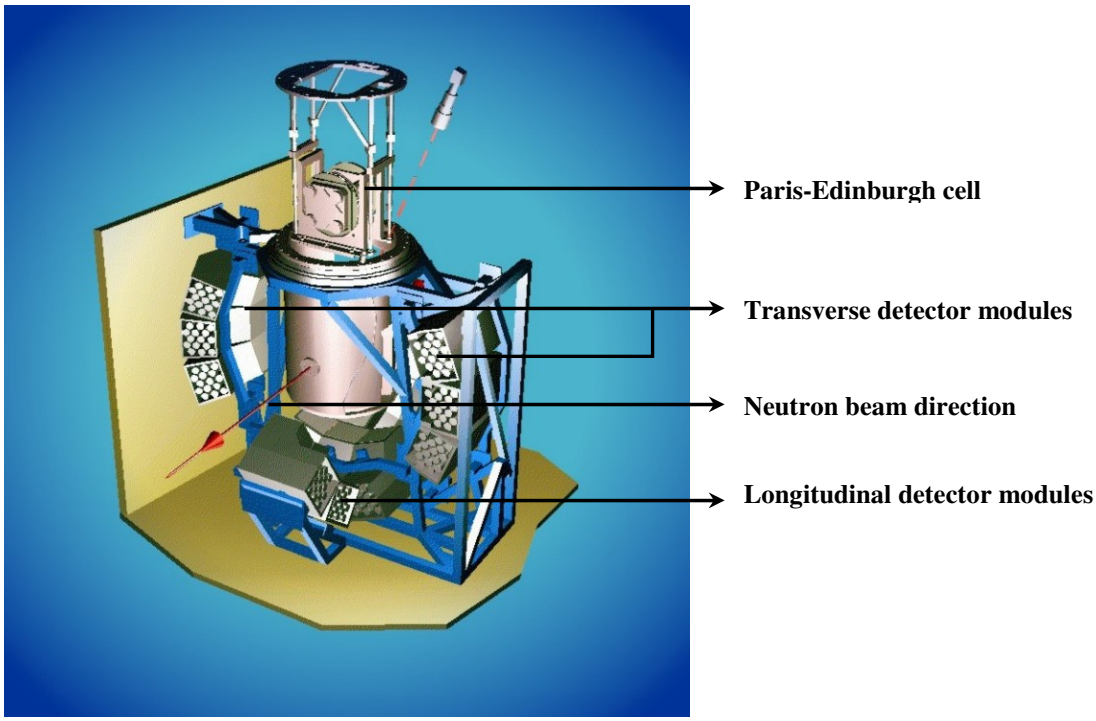

Figure 2.13 The beam direction and the two sets of detector arrays of PEARL[11].

2.2.1.6 Paris-Edinburgh Pressure Cell

High pressure for neutron powder diffraction in this thesis was achieved by the Paris-Edinburgh cell (PE cell), which was developed in 1992 to allow large sample volumes for neutron diffraction to be studied under high pressure[12]. A standard PE cell weighs ~50 kg and consists of a portable hydraulic press and a gasket between

two opposite tungsten carbide anvils. A schematic diagram of the PE cell is shown in Figure 2.14 (a). The hydraulic press can apply 200 tonnes to the studied material, where a material volume of ~100 mm^3 can be pressurised up to 10 GPa. The entire gasket, which the studied material is sealed into, is machined from null-scattering titanium-zirconium alloy, and is encapsulated to avoid contact between the pressure-transmitting medium (usually a mixture of methanol and ethanol) and the anvils. With a PE cell the diffraction pattern can be collected with minimum signal from the pressure cell or the anvils by restricting the diffraction angle to ~90 °, consequently it is ideal for data collection with the TOF method.

When performing a high pressure study with low temperatures the PE cell is sprayed with liquid nitrogen to give temperatures as low as ~90 K. To determine the pressure inside the gasket, a pressure marker is loaded along with the sample. The pressure marker is usually NaCl or Pb which have a cubic space group F*m*-3*m* and a known high-pressure equation of state. Hence from the unit cell parameter of the pressure marker obtained by refinement of the diffraction pattern and the temperature of the system, the pressure in the gasket can be calculated using its equation of state.

A different design of the gasket is adopted, shown in Figure 2.14 (b), to perform high-pressure experiments under high-temperatures[13,14]. A graphite furnace is placed in the modified gasket and the high temperature environment is achieved by passing an electrical current. The temperature can be determined by neutron resonance spectroscopy (NRS) of a metallic foil such as Hf or Ta along with the sample[15]. With the temperature from NRS and the unit cell information from refinement of the pressure callibrant, usually NaCl or MgO powder, the pressure of the sample can be calculated from the P/T equation of state.

The standard PE cell is an ideal equipment for high pressure studies with spallation neutron source and has been widely used for many applications. However it is not suitable for a reactor-based neutron source due to the four tie rods and small azimuthal window from its original design. Recently, an adapted version, VX-type PE cell[16,17], has been designed in order to overcome such disadvantages by having two large equatorial opening angles of 140 ° of the cell, shown in Figure 2.14 (c).

This allows the angle-dispersive experiment to be performed using constant wavelength neutrons with a multidetector array covering wide angular range.

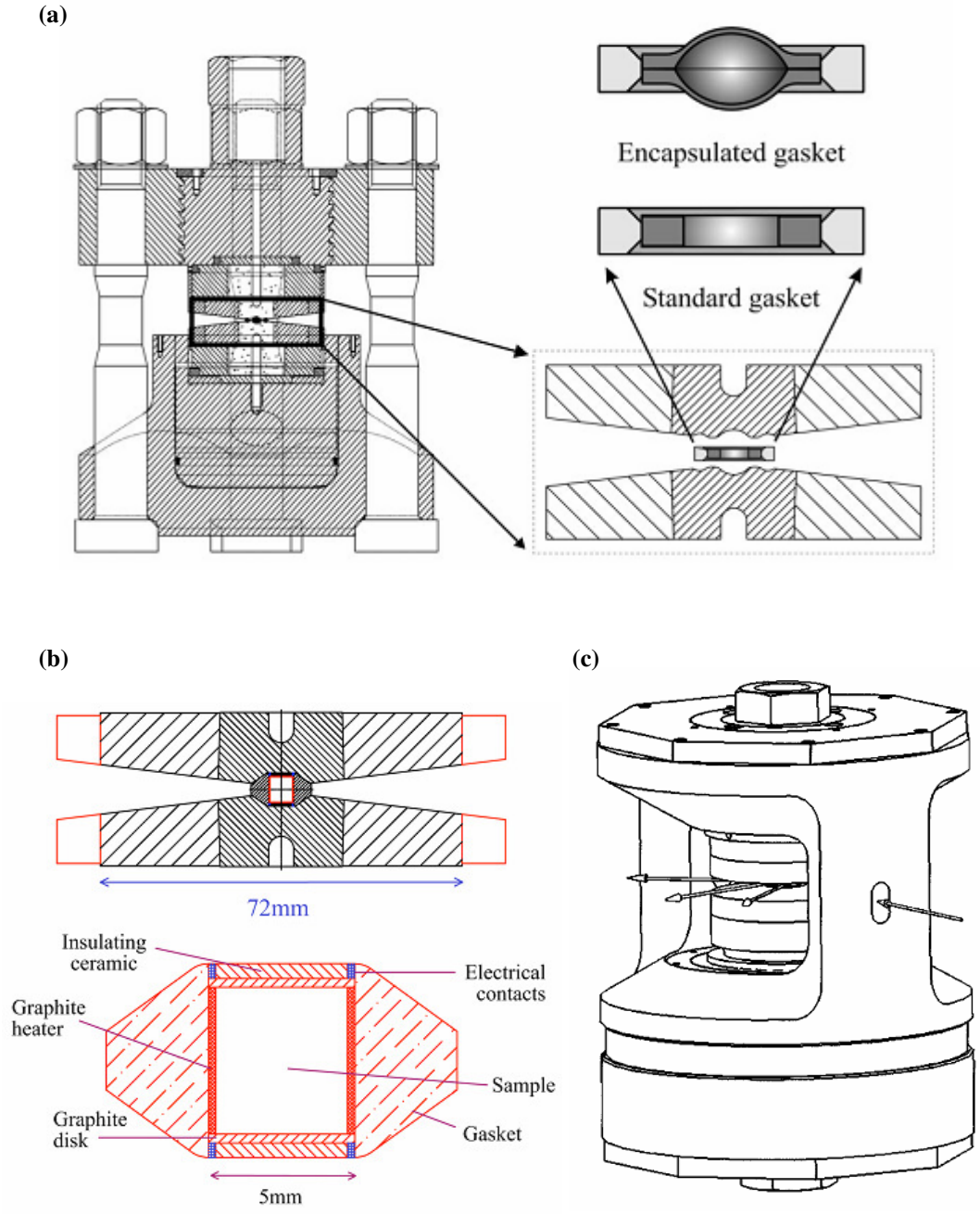

Figure 2.14 (a) a schematic diagram of a standard PE cell and the encapsulated gasket between two opposite anvils[18]. (b) the modification of the gasket and anvils for high temperature experiments[13,14]. (c) a drawing of a VX-type PE cell which allows angle-dispersive experiments[16,17].

2.2.2 Transmission Electron Microscopy

Electron microscopy is a useful tool to study material structures on a small region of a sample, whereas X-ray and neutron diffraction study the bulk crystallographic properties of materials. Electrons are charged particles which can be scattered by both the electron cloud and nuclei of the sample. Electrons have a greater atomic scattering amplitude compared with X-rays. However the penetration of the sample is limited for electrons, therefore a thin material is required for electron studies. Through a series of electromagnetic lenses the electron beam is focused and passes through the studied material. The resultant electron distribution can be displayed as either a real-space lattice image or a reciprocal-space diffraction pattern by selecting the intermediate lenses, as shown in Figure 2.15.

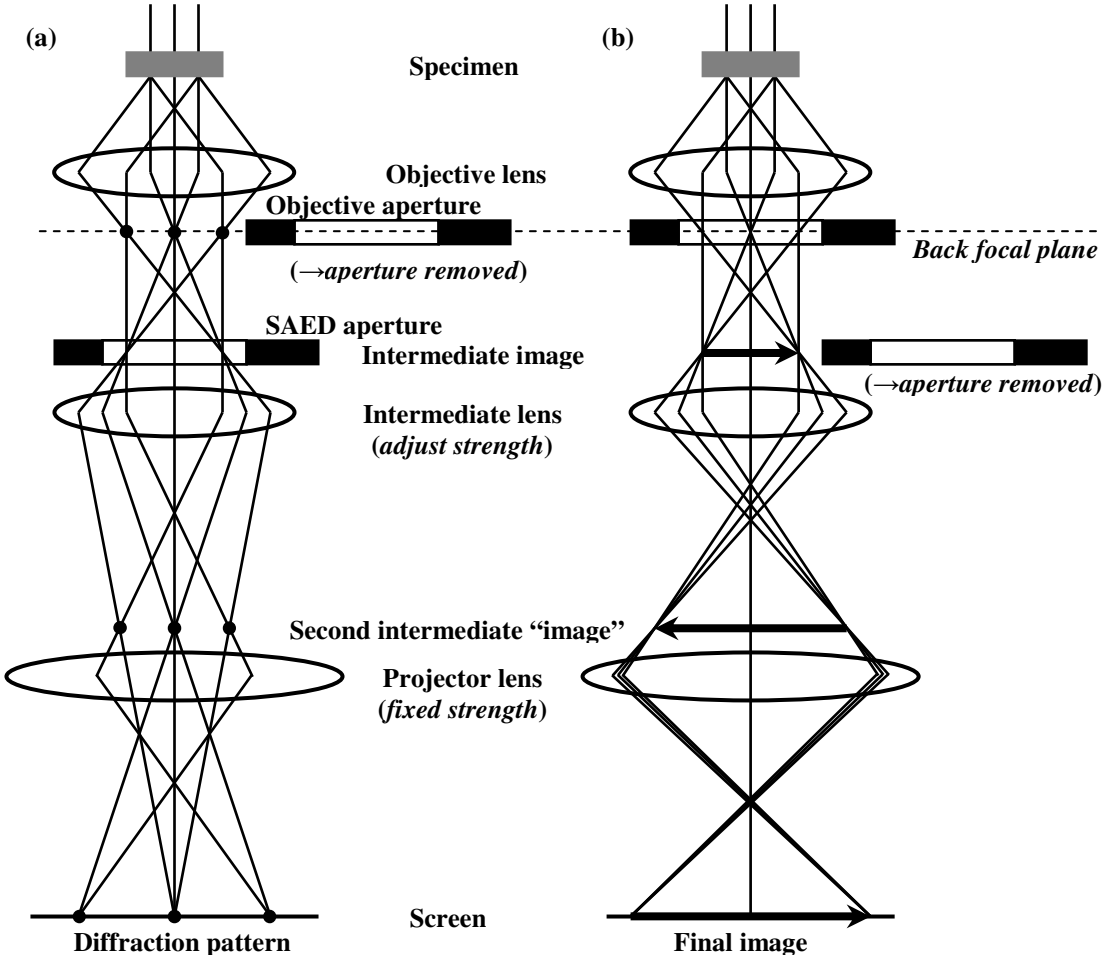

Figure 2.15 The formation of (a) diffraction pattern and (b) lattice image of the specimen[19].

The TEM data collection in this thesis was performed by Dr. W. Zhou and R. Blackley, University of St. Andrews. A copper grid with a holey carbon film was used to mount a small amount of the sample powder. A JEOL JEM 2011 electron microscope was employed to collect both selected area electron diffraction (SAED) patterns and high resolution transmission electron microscopic (HRTEM) images of the studied samples at room temperature.

2.2.3 Bond Valence Sums

In a charge ordered metal oxide, the metal ions can be distinguished from each other by comparing the average metal-oxygen bond distances for each crystallographically distinct metal site. The bond valence sum (BVS) calculation is a useful tool to provide a more accurate estimate of the oxidation states of different metal ions. The BVS method was based on Pauling's concept of valence from the ionic radii and coordination numbers of metal ions[20,21], which was later extended to include metal oxides[22,23].

The relationship between the bond valence V_i of a given cation, which can be obtained from the sum of the individual bond valences v_i surrounding the cation, and the observed bond distances then can be derived[24]:

$$V_i = \sum v_i = \sum \exp(\frac{R_0 - R_i}{B}) \qquad \textbf{(2.12)}$$

where R_i is the observed bond distance, R_o is the bond valence parameter determined and tabulated from known structures of that cation, and B is an empirically derived constant which equals 0.37 Å.

Different bond valence parameters R_o can be found for given cation oxidation states. Therefore intermediate valence states V can be estimated for cations, from BVS by using following formula[25]:

$$V = \frac{L(V_H - V_L) - (H - L)V_L}{(V_H - V_L) - (H - L)} \qquad \textbf{(2.13)}$$

where H and L represent the higher and lower formal oxidation state, and V_H and V_L are the bond valence calculated from BVS for cations with higher and lower oxidation states, respectively.

2.3 Magnetisation Measurement

The Quantum Design Magnetic Property Measurement System (MPMS), which contains a Superconducting Quantum Interference Device (SQUID), is the most sensitive device available for measuring magnetic fields. The SQUID detection system consists of a superconducting ring with a weak link which is capable of amplifying any small changes in magnetic field into large electrical signals. The ring is coupled with a superconducting sensing coil, which surrounds the sample, by superconducting circuitry. The sample moves through the detection coils in discrete steps and the high uniform magnetic field in the magnetometer is generated by a superconducting magnet. The configuration of the MPMS is shown in Figure 2.16. The magnetic flux through the sensing coil is changed by the movement of a sample with any magnetisation within, inducing a supercurrent which in turn changes the flux through the SQUID and consequently produces a change in the output signal of the SQUID.

Quantum Design MPMS and MPMS XL were employed for the SQUID measurements in this thesis. The studied powder materials were placed in a plastic capsule with inverse capsule configuration to prevent sample movement within the capsule which would consequently disturb the measurement. Certain magnetic fields were applied to study temperature-dependent behaviour at a temperature range of 5 - 300 K, and variations in the applied magnetic field of ±10 kOe and ±70 kOe, from MPMS and MPMS XL respectively, were adopted for the hysteresis studies.

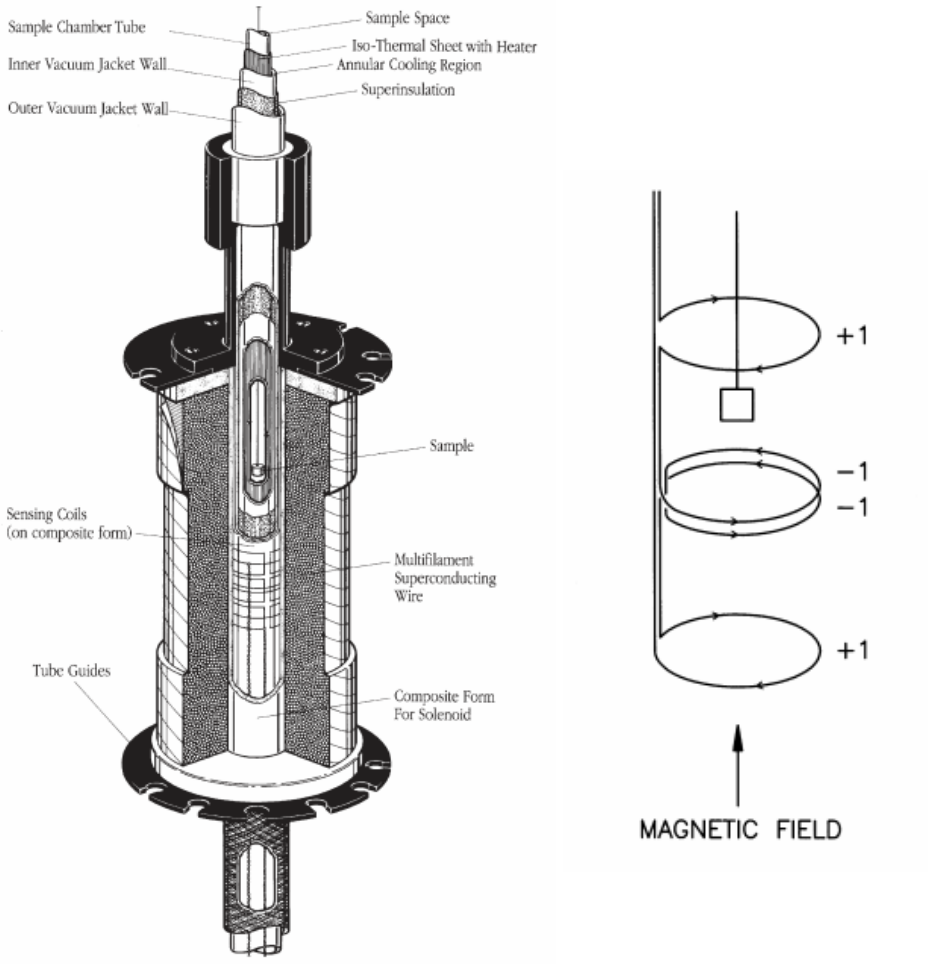

Figure 2.16 (a) The configuration of the magnet, detection coils and sample chamber. (b) The schematic diagram of the detection coils[26].

2.4 Electronic Transport Property Measurement

The transport property measurements of a solid material may provide information which can be related to its electronic nature. An electronic structure model may be suggested from the transport measurements, and the prediction of the model may be checked by other information such as magnetic measurements or crystal structure determination.

In a typical four probe configuration of resistivity measurement, four electrical contacts were attached to the rectangular sample bar as shown in Figure 2.17. The measurement is carried out by passing an electrical current along the sample with a

cross sectional area A between I^+ and I^-, whilst the voltage is measured across the contact with a length L between V^+ and V^-. The resistivity ρ then can be obtained with the measured resistance R in ohms from the formula below:

$$\rho = \frac{R \cdot A}{L} \tag{2.14}$$

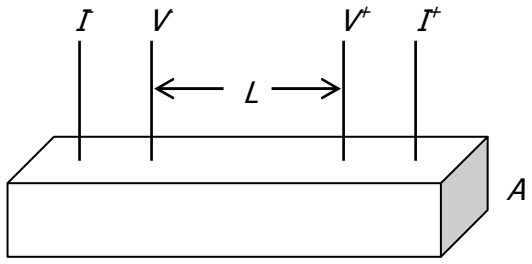

Figure 2.17 A typical four probe configuration of the resistivity measurement.

A Quantum Design PPMS (Physical Properties Measurement System) was used for transport measurements. The resistance of bars which were cut from sample pellets was measured with a standard four probe configuration over the temperature range 280 - 350 K. Wires were attached with silver epoxy resin and baked at 200 °C to reduce contact resistance. The measurement was carried out on three sample bars simultaneously each time.

2.5 References

1. J. A. Rodgers, A. J. Williams, and J. P. Attfield, *Z. Naturforsch., B,* **61**, 1515 (2006).
2. D. Walker, M. A. Carpenter, and C. M. Hitch, *Am. Mineral.,* **75**, 1020 (1990).
3. H. Huppertz, *Z. Kristall.,* **219**, 330 (2004).
4. High-Pressure Laboratory, Department of Chemistry LMU-Munich, http://www.cup.uni-muenchen.de/ac/huppertz/hd.html
5. H. M. Rietveld, *J. Appl. Crystallogr.,* **2**, 65 (1969).

6. A. C. Larson and R. B. V. Dreele, "General Structure Analysis System (GSAS)," pp. 86-748. In *Los Alamos National Laboratory Report LAUR***.** Los Alamos National Laboratory, 2004.
7. V. K. Pecharsky and P. Y. Zavalij,"*Fundamentals of Powder Diffraction and Structural Characterization of Materials*", Springer, (2005).
8. The European Synchrotron Radiation Facility, ESRF, *http://www.esrf.eu/*
9. NIST Center for Neutron Research, *http://www.ncnr.nist.gov/*
10. The Institut Laue-Langevin, *http://www.ill.eu/*
11. ISIS at Rutherford Appleton Laboratory, *http://www.isis.rl.ac.uk/*
12. J. M. Besson, R. J. Nelmes, G. Hamel, J. S. Loveday, G. Weill, and S. Hull, *Phys. B: Condens. Matter,* **180-181**, 907 (1992).
13. Y. Le Godec, M. T. Dove, S. A. T. Redfern, M. G. Tucker, W. G. Marshall, G. Syfosse, and J.-M. Besson, *High Pressure Res.,* **21**, 263 (2001).
14. Y. Le Godec, M. T. Dove, D. J. Francis, S. C. Kohn, W. G. Marshall, A. R. Pawley, G. D. Price, S. A. T. Redfern, N. Rhodes, N. L. Ross, P. F. Schofield, E. Schooneveld, G. Syfosse, M. G. Tucker, and M. D. Welch, *Mineral. Mag.,* **65**, 737 (2001).
15. H. J. Stone, M. G. Tucker, F. M. Meducin, M. T. Dove, S. A. T. Redfern, Y. L. Godec, and W. G. Marshall, *J. Appl. Phys.,* **98**, 064905 (2005).
16. S. Klotz, G. Hamel, and J. Frelat, *High Pressure Res.,* **24**, 219 (2004).
17. S. Klotz, T. Strassle, G. Rousse, G. Hamel, and V. Pomjakushin, *Appl. Phys. Lett.,* **86**, 031917 (2005).
18. W. G. Marshall and D. J. Francis, *J. Appl. Crystallogr.,* **35**, 122 (2002).
19. D. B. Williams and C. B. Cater,"*Transmission Electron Microscopy I: Basics*", Plenum Publishing Corporation, (1996).
20. L. Pauling, *J. Am. Chem. Soc.,* **51**, 1010 (1929).
21. L. Pauling, *J. Am. Chem. Soc.,* **69**, 542 (1947).
22. A. Byström and K.-A. Wilhelmi, *Acta Chem. Scand.,* **5**, 1003 (1951).
23. W. Zachariasen, *Acta Crystallogr.,* **16**, 385 (1963).
24. I. D. Brown and D. Altermatt, *Acta Crystallogr. B,* **41**, 244 (1985).
25. J. P. Attfield, *Solid State Sci.,* **8**, 861 (2006).
26. Quantum Design, *http://www.qdusa.com/*

Chapter 3

Structural and Property Studies of $Bi_xCa_{1-x}FeO_3$ Solid Solutions

3.1 Introduction

Perovskite-type transition metal oxides ABO_3 are of great interest due to their magnetic, dielectric and transport properties that emerge from the coupling of spin, charge and orbital degrees of freedom[1]. Ferromagnetism and ferroelectricity are useful properties which do not often occur simultaneously in perovskites. The "multiferroic" material which consisting of different ferroic properties can arise, however, when a polar cation such as Bi^{3+} or Pb^{2+} is present in the *A* site of the perovskite and a magnetic cation is at the *B* site[2]. The off-centre *A*-cation displacement often leads to polar superstructures with appreciable ferroelectricity while ferro/antiferromagnetic coupling of the transition metal cation spins leads to long-range magnetic order.

$BiFeO_3$ and $BiMnO_3$ are much studied perovskites which show both magnetic and dielectric properties[3-6]. $BiMnO_3$ is a heavily distorted perovskite with a structural phase transition to tetragonal symmetry at 760 K[7], and is ferroelectric with $T_{C\text{-}FE}$ = 450 K[8]. The ferroelectricity persists to low temperatures through the ferromagnetic transition at $T_{C\text{-}FM}$ = 105 K[6,9,10]. Spin, charge and orbital order have been studied extensively in strontium[10,11] and calcium[12,13] substituted bismuth manganites.

$BiFeO_3$ has a rhombohedrally distorted structure (space group *R*3*c*), and shows G-type antiferromagnetic order with a long-periodicity spiral below the Néel temperature $T_{N\text{-}AFM}$ = 643 K[14] and ferroelectricity below the Curie temperature $T_{C\text{-}FE}$ = 1103 K[15]. The ferroelectricity of $BiFeO_3$ is due to Bi^{3+} $6s^2$ lone pair while the residual moment of the canted Fe^{3+} spin structure results in weak ferromagnetism[4] (canted antiferromagnetic). *A*-site substitutions of trivalent (La^{3+}, Nd^{3+} or Sm^{3+})[16-21]

or divalent (Ba^{2+}, Pb^{2+}, Sr^{2+} or Ca^{2+})[22-25] cations for Bi^{3+}, and *B*-sublattice dopings with V^{5+}, Nb^{5+}, Mn^{4+}, Ti^{4+}, Cr^{3+} have recently been investigated in order to improve the magnetoelectric properties[26-31].

Solid solutions of $BiFeO_3$ with $CaFeO_3$ or $SrFeO_3$ may be of particular interest as these perovskites also have notable properties although high oxygen pressures are required to synthesise stoichiometric materials. $SrFeO_3$ has a cubic perovskite structure and is antiferromagnetically ordered below 130 K[32,33], while $CaFeO_3$ has a $GdFeO_3$-type orthorhombic perovskite structure and shows charge disproportionation below 290 K and antiferromagnetic order at $T_{N\text{-}AFM}$ = 116 K[34]. Strontium substituted solid solutions $Bi_{1-x}Sr_xFeO_3$ where x = 0.20 - 0.67 have been reported[23], in this region the materials have cubic cells and show weak ferromagnetism. In the $Bi_{1-x}Ca_xFeO_3$ system, weak ferromagnetism was observed at small dopings x = 0.05 and 0.1[25], and studies of $Bi_{0.8}Ca_{0.2}FeO_3$[24] and some compositions in the series[35] were recently reported, but no systematic study of the entire series has been presented. The intention of the experiments in this chapter is to synthesise the solid solutions of calcium substituted bismuth ferrites $Bi_xCa_{1-x}FeO_3$, and investigate possible structural or magnetic phase transitions, charge ordering and physical properties of the prepared samples.

3.2 Experimental

Sample Preparation

$Bi_xCa_{1-x}FeO_3$ materials were prepared by high temperature solid state reactions in air. Initial attempts to prepare calcium-rich samples where x = 0.0 and 0.2 gave multiphase mixtures of brownmillerite $Ca_2Fe_2O_5$ and perovskite phases, where the appearance of $Ca_2Fe_2O_5$ is because high oxygen pressure is required to prepare the parent compound $CaFeO_3$. Single phase perovskites were obtainable for $x \geq 0.4$ and 10g samples with x = 0.4, 0.5, 0.6, 0.67, 0.8, 0.9 and 1.0 were prepared from stoichiometric amounts of Bi_2O_3, Fe_2O_3 and $CaCO_3$ (all Aldrich, >99.9 % pure). The reactants were weighed, ground and mixed into a fine homogeneous powder which

was pressed into pellets. The pellets were then loaded on an alumina boat and heated at 5 °C per minute to an appropriate sintering temperature with a furnace. The x = 1.0 sample was calcined at 810 °C for one hour, while x = 0.9 to 0.4 samples were calcined for 72 hours at temperatures increasing from 900 to 960 °C to avoid melting. In order to obtain well-crystallised products, the x = 1.0 and 0.9 samples were furnace-cooled but the x = 0.8, 0.67, 0.6, 0.5 and 0.4 samples were quenched to room temperature to prevent formation of the brownmillerite phase. The pellets were then ground, pressed to pellets and calcined several times to complete the reaction until phase-pure samples were confirmed by laboratory X-ray powder diffraction.

Laboratory X-ray Powder Diffraction

Laboratory X-ray powder diffraction data collected for characterisation and Rietveld refinement were obtained using flat plate mode with a Bruker D8 Advance diffractometer. The diffraction data were collected in a range of $15\ ° \leq 2\theta \leq 60\ °$ with an integration time of 5 seconds per 0.01355 ° step with Ge (111) monochromated $\lambda = 1.540598$ Å Cu-Kα_1 radiation at room temperature.

Synchrotron X-Ray Diffraction

High resolution synchrotron X-ray diffraction data from samples in 0.3 mm glass and 0.7 mm quartz capillaries were collected on instruments ID31 and BM01B, respectively, at the ESRF, Grenoble. ID31 data were collected with a wavelength of 0.39825 Å in the angular range $3\ ° \leq 2\theta \leq 30\ °$ from x = 0.4 - 1.0 at room temperature and for x = 0.6, 0.67, 0.8 at high temperatures. High temperature data from BM01B in 50 °C steps up to 400 °C were collected with wavelength 0.50010 Å in the angular range $1\ ° \leq 2\theta \leq 30\ °$, counting for 3 hours for each pattern.

Neutron Powder Diffraction

Neutron powder diffraction data from polycrystalline samples packed in 8mm diameter vanadium cans were collected on instruments Super-D2B and D1B at the ILL, Grenoble. Super-D2B data were collected in the angular range $5\ ° \leq 2\theta \leq 155\ °$ for 50 minutes per scan with a neutron wavelength of 1.594 Å at 10 and 300 K.

Temperature-dependent neutron powder diffraction data were collected on instrument D1B using a 2.52 Å neutron wavelength. Data were collected in 1 °C steps from room temperature to 400 °C in the angular range $5\ ° \leq 2\theta \leq 85\ °$ with a ramping rate of 0.8 °C per minute and counting for 1.25 minute per scan. The X-ray and neutron diffraction data were analysed by the Rietveld method using the GSAS software package.

Transmission Electron Microscopy

A copper grid with a holey carbon film was used to mount the sample for transmission electron microscopy. Selected area electron diffraction (SAED) patterns and high resolution transmission electron microscopic (HRTEM) images of $Bi_{0.8}Ca_{0.2}FeO_3$ and $Bi_{0.67}Ca_{0.33}FeO_3$ samples were collected on a JEOL JEM 2011 electron microscope at room temperature.

Electron Transport Measurements

Electronic transport measurements were carried out using a standard Quantum Design PPMS system between 350 and 280 K, below which the resistivities were too large to be measured reliably. A standard four-probe DC configuration was used and the contacts were attached with silver epoxy resin and baked at 200 °C to reduce contact resistances.

Magnetism measurements

Magnetic properties of the series were measured with a Quantum Design MPMS SQUID magnetometer. The temperature-dependent DC susceptibility was collected with temperature range 5 - 300 K in a zero-field-cooling (ZFC) and a field-cooling (FC) mode with an applied field of 500 Oe and 10 kOe. The field-dependent magnetisation and the hysteresis loop measurements were carried out at 5 K and varied magnetic field of -10 to 10 kOe.

Permittivity measurements

The permittivity analysis was performed by Drs. D. C. Sinclair and M. Li, Department of Engineering Materials, The University of Sheffield. The dielectric properties of ceramics were investigated over the frequency range 10^0 -10^6 Hz using an Impedance analyser (Model E4980A, Agilent, USA) with an applied voltage of 100 mV and Au sputtered electrodes. Low temperature measurements (10 - 320 K) were performed in an Oxford Cryocooler (Model CC 1.5 Oxford Instruments, Oxfordshire, UK). All data were corrected for sample geometry and analysed using the commercial software package Z-View (Scribner Associates, Inc., Charlottesville, VA, Version 2.9c).

3.3 Results

3.3.1 Room Temperature Crystal Structure

Laboratory X-ray powder diffraction patterns of $Bi_xCa_{1-x}FeO_3$ materials show single phase perovskites with $0.4 \leq x \leq 1.0$ (Figure 3.1). The replacement of trivalent Bi by divalent Ca leads to a decrease in the unit cell with decreasing bismuth content x of $Bi_xCa_{1-x}FeO_3$ series. $BiFeO_3$ is a rhombohedrally distorted perovskite and rhombohedral peak splittings or broadenings can be found in undoped and slight calcium doped $BiFeO_3$ samples. The patterns of x = 1.0 and 0.9 samples can be described in a hexagonal setting of space group *R*3*c* (No. 161) with a $\sqrt{2} \times \sqrt{2} \times 2\sqrt{3}$ supercell of the primitive cubic perovskite cell and atom positions Bi/Ca (0, 0, z=0), Fe (0, 0, z) and O (x, y, z). The rhombohedral distortion is suppressed and a cubic structure is obtained with further calcium doping, where the patterns for x = 0.4, 0.5, 0.6, 0.67 and 0.8 are all well fitted by the cubic symmetry with space group $Pm\bar{3}m$ (No. 221) and atom positions Bi/Ca (½,½,½), Fe (0, 0, 0), O (½, 0, 0).

However further structural complexities are revealed by the attempts to fit the neutron and synchrotron data, particularly in the cubic $Bi_xCa_{1-x}FeO_3$ samples. Subtle peak splittings and shoulders are observed in high resolution synchrotron X-ray data

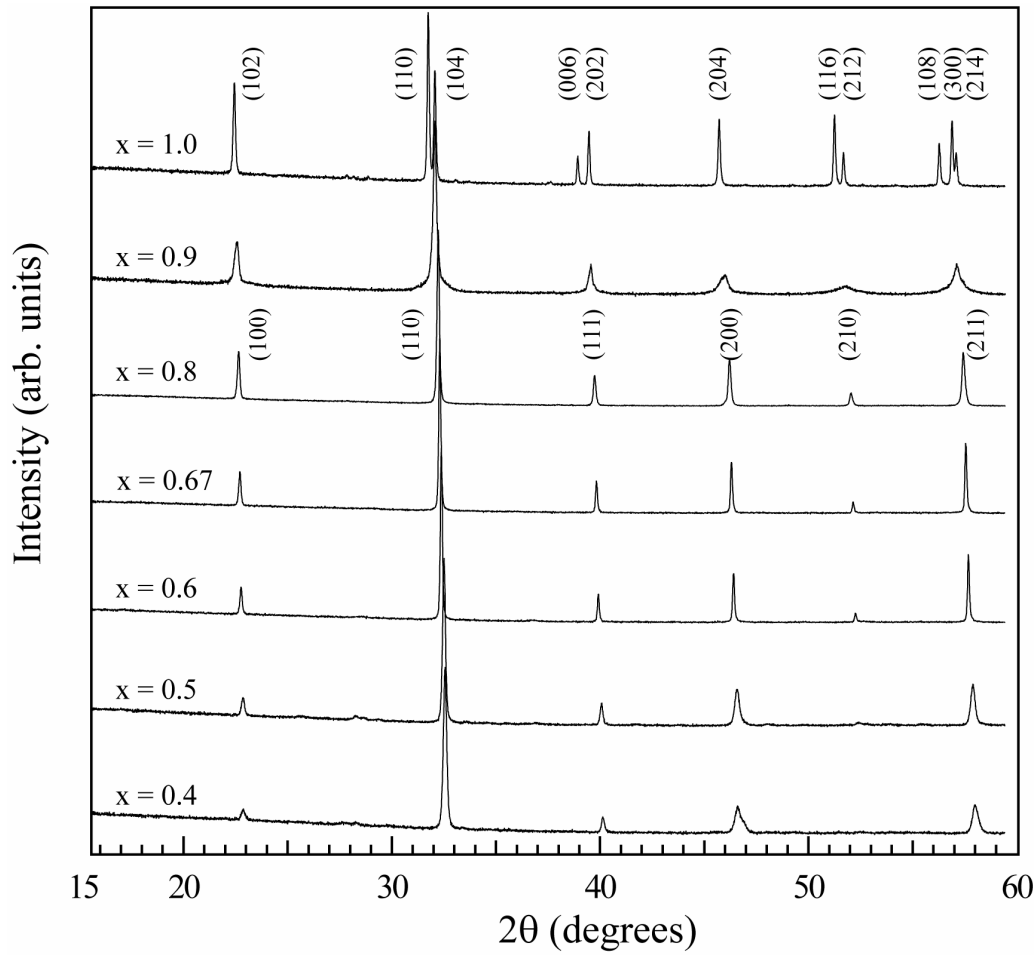

Figure 3.1 Laboratory X-Ray patterns for $Bi_xCa_{1-x}FeO_3$ materials where x = 0.4 - 1.0 collected at room temperature. The indexing of rhombohedral and cubic structures are shown for x = 1.0 and 0.8 samples, respectively.

of $Bi_{0.8}Ca_{0.2}FeO_3$ at room temperature, indicating that two phases are present in the material. The refinements with a multiphase model consisting of both cubic and rhombohedral phases were performed to fit synchrotron and neutron patterns for x = 0.8 and 0.9, considering the rhombohedral and cubic symmetry adopted for undoped and calcium-rich materials, respectively.

Although good fits are provided by the XRD refinements of the materials with x = 0.4 - 0.8, poor results are obtained when the ideal cubic perovskite structure was used to fit the nuclear peaks of Super-D2B neutron diffraction patterns. No splittings or superlattice peaks (except those from the magnetic superstructure described later) are observed, and attempts to fit rhombohedral and other perovskite superstructures

were unsuccessful. The absence of superstructure or structure anomalies implies that the potential long range charge ordering is not shown in $Bi_{0.67}Ca_{0.33}FeO_3$.

The refinements of the neutron data are greatly improved with the introduction of positional disorder in the cubic perovskite model. The variable x_A is introduced to give ($½+x_A$, $½+x_A$, $½+x_A$) position which allowed *A* cations to have [111] off-centre displacements, while y_O gives a (½, y_O, y_O) position for oxygen to have local bending of the Fe-O-Fe bridges. The Rietveld fits of room temperature synchrotron X-ray and neutron diffraction data of $Bi_{0.67}Ca_{0.33}FeO_3$ are shown in Figure 3.2, the fits to other samples are shown in Appendix I. The refinement results of the structures and phase fractions from both synchrotron X-ray and neutron diffraction data are listed in Table 3.1, while the detailed atomic information is listed in Table 3.2 and selected bond distances and angles are shown in Table 3.3. Acceptable fits are provided by the refinements of neutron data with the disordered cubic model, however, the uniformly high χ^2 values and also residual intensity differences observed in the profiles of the series indicate that such a model is only an approximation to the complex local microstructures observed by HRTEM (section 3.3.3).

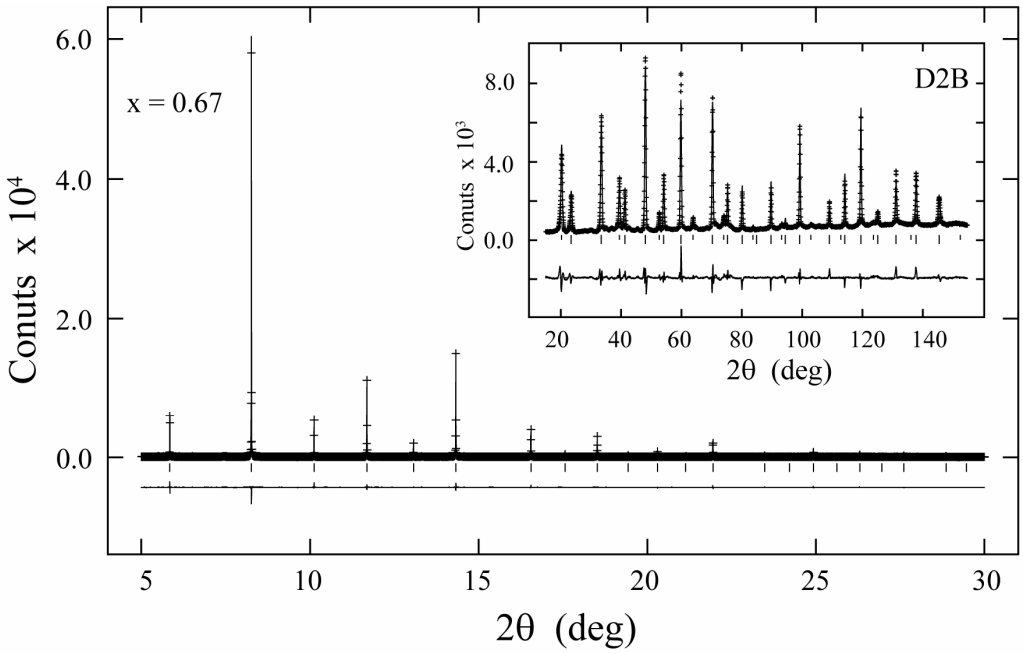

Figure 3.2 Fits of the disordered cubic model refinements of ID31 and D2B (inset) data at room temperature for $Bi_{0.67}Ca_{0.33}FeO_3$.

Table 3.1 Refinement results for $Bi_xCa_{1-x}FeO_3$ series fitting with cubic disordered and rhombohedral models to room temperature ID31 SXD (in bold font) and Super-D2B NPD data. Lattice parameters, cell volume, phase fractions (for x = 0.8 and 0.9 samples), the reliability factors R_{wp} and χ^2 are listed.

x		*a* (Å)	*c* (Å)	*V/f.u.* (Å^3)	phase fraction (%)	R_{wp} (%)	χ^2
0.4	C	**3.89012(5)**		**58.869(2)**		**15.73**	**5.16**
		3.8889(1)		58.815(6)		8.47	6.46
0.5	C	**3.99917(3)**		**59.281(1)**		**12.90**	**5.14**
		3.8980(1)		59.228(5)		9.13	6.41
0.6	C	**3.916436(4)**		**59.756(1)**		**11.41**	**1.70**
		3.91531(5)		59.708(2)		9.27	7.73
0.67	C	**3.909564(5)**		**60.072(1)**		**8.99**	**1.71**
		3.90851(5)		60.020(2)		8.85	7.22
0.8*	**C**	**3.92158(2)**		**60.309(1)**	**59.3**	**7.40**	**1.88**
	R	**5.53921(4)**	**13.5798(2)**	**60.141(1)**	**40.7**		
	C	3.91912(7)		60.196(3)	58.6	7.38	4.63
	R	5.54134(9)	13.5933(17)	60.247(9)	41.4		
0.9*	**C**	**3.9401(1)**		**61.166(7)**	**49.7**	**13.93**	**6.33**
	R	**5.5546(4)**	**13.7707(19)**	**61.148(6)**	**50.3**		
	C	3.9357(4)		60.964(20)	22.0	8.53	6.07
	R	5.56694(11)	13.7581(22)	61.542(12)	78.0		
1.0	R	**5.58000(1)**	**13.87252(3)**	**62.345(3)**		**16.97**	**5.89**
		5.58418(1)	13.8822(2)	62.483(1)		7.61	4.07

***The multiphase refinements with both cubic (C) and rhombohedral (R) phases were performed for x = 0.8 and 0.9 samples, while for x = 0.4 – 0.67 and x = 1.0 samples only cubic disordered and rhombohedral phase were refined, respectively.**

Table 3.2 Refinement results for $Bi_xCa_{1-x}FeO_3$ series, atomic positions, isotropic thermal factors, magnetic moments from ID31 (bold font) and D2B data are listed*.

x		0.4	0.5	0.6	0.67	0.8 C	0.8 R	0.9 C	0.9 R	1.0
Bi/Ca	x	**0.4457(7)**	**0.4486(6)**	**0.4594(9)**	**0.4585(10)**	**0.4569(4)**		**0.4368(3)**		
		0.448(1)	0.457(3)	0.456(2)	0.455(2)	0.488(9)		0.459(2)		
	U_{iso} (Å^2)	**0.006(2)**	**0.011(1)**	**0.027(2)**	**0.030(1)**	**0.0306(3)**		**--**		**0.0069(1)**
		0.008(3)	0.0057(1)	0.0041(1)	0.018(4)	0.041(2)		0.004(1)		0.0048(4)
Fe	z						**0.251(1)**		**0.2251(3)**	**0.22080(9)**
							0.251(1)		0.2217(3)	0.2792(1)
	U_{iso} (Å^2)	**0.0208(5)**	**0.0127(4)**	**0.0170(3)**	**0.0155(2)**	**0.0087(2)**		**--**		**0.0047(3)**
		0.0175(5)	0.0060(4)	0.0082(3)	0.0066(3)	0.0072(2)		0.0072(7)		0.0022(3)
	m_z (μ_B)	3.65(3)	3.68(4)	3.73(3)	3.79(3)	3.90(4)		3.94(3)		4.10(3)
O	x						**0.416(2)**		**0.423(4)**	**0.437(1)**
							0.427(1)		0.4423(9)	0.4275(3)
	y	**0.0811(10)**	**0.0855(9)**	**0.0765(6)**	**0.0767(8)**	**0.077(1)**	**-0.050(3)**		**0.039(4)**	**0.018(1)**
		0.0806(5)	0.0754(4)	0.0756(4)	0.0751(4)	0.0732(5)	0.025(2)		0.0160(9)	-0.0194(3)
	z						**1.020(1)**		**0.961(1)**	**0.9495(4)**
							0.984(2)		0.9554(5)	1.0484(1)
	U_{iso} (Å^2)	**0.016(2)**	**0.029(2)**	**0.034(2)**	**0.030(1)**	**0.014(1)**		**--**		**0.016(1)**
		0.0370(10)	0.0010(1)	0.0323(9)	0.0317(9)	0.0225(7)		0.0025(5)		0.0046(3)

*** For the disordered cubic model, atom positions are Bi/Ca, 8(g), (½+x_A, ½+x_A, ½+x_A); Fe, 1(a), (0, 0, 0); O, 12(j), (½, y_O, y_O) in space group *Pm*$\bar{3}$*m* (No. 221). Rhombohedral positions are Bi/Ca, 6(a), (0, 0, z = 0); Fe, 6(a), (0, 0, z); O, 18(b), (x, y, z) in space group *R*3*c* (No. 161).**

Table 3.3 Selected bond distances and angles and BVS results for $Bi_xCa_{1-x}FeO_3$ series from D2B data refinements, where ranges of distances and angles are shown for the disordered cubic model.

x	0.4	0.5	0.6	0.67	0.8 C	0.8 R	0.9 C	0.9 R	1.0
Bi/Ca-O (Å)	2.030(8) | 3.485(9)	2.10(2) | 3.43(2)	2.11(1) | 3.43(1)	2.11(1) | 3.44(1)	2.30(5) | 3.24(5)	3.06(2)×3 2.567(8) ×3 2.311(8) ×3 3.254(7) ×3	2.15(1) | 3.42(1)	3.209(3) ×3 2.495(5) ×3 2.3025(6)×3 3.378(6) ×3	3.215(1) ×3 2.534(1) ×3 2.263(2) ×3 3.457(2) ×3
Fe-O (Å)	1.9944(6)	1.9961(6)	1.9978(5)	2.0019(5)	2.0011(6)	2.07(1)×3 1.99(1)×3	2.0091(13)	2.086(4) ×3 1.955(4) ×3	2.110(2) ×3 1.956(2) ×3
Fe-BVS	3.22	3.20	3.18	3.14	3.15	2.85	3.06	3.01	2.91
O-Fe-O (º)	70.7(1) | 109.4(1) 154.3(2) | 180	71.2(1) | 108.8(1) 155.1(2) | 180	72.0(1) | 108.0(1) 156.0(1) | 180	71.9(1) | 108.1(1) 155.9(1) | 180	72.5(1) | 107.5(1) 156.6(2) | 180	81.0(4) ×3 165.2(5) ×3 89.2(2) ×3 86.5(1) ×3 101.4(4) ×3	72.6(3) | 107.4(3) 156.7(4) | 180	81.6(2) ×3 167.1(3) ×3 89.4(1) ×3 88.0(1) ×3 99.5(2) ×3	79.5(1) ×3 164.6(1) ×3 89.6(1) ×3 88.0(1) ×3 100.9(1) ×3

The same disordered cubic model is used for the refinements of synchrotron diffraction data which is less sensitive to the oxygen distribution. Although good fits are observed and similar x_A and y_O shifts values are obtained for x = 0.6 - 0.8 samples, additional peak broadening contributions result in poorer fits to the rhombohedral samples x = 0.9 and 1.0 and also those at the limit of cubic phase x = 0.4 and 0.5. Similar observation is evident in the laboratory data shown in Figure 3.1, which implies that further structural and microstructural inhomogeneities exist in these samples. The agreement of cubic/rhombohedral ratios between the refinement results of synchrotron and neutron diffraction (both 59:41) indicates that the model consisting of two phases was realistic for x = 0.8 sample. However, very different R/C ratios are observed between synchrotron (50:50) and neutron results (22:78) for x = 0.9 sample from the same procedure, showing that this structural model is rather approximate.

The variations of lattice constants and unit cell volumes with x in $Bi_xCa_{1-x}FeO_3$ series are shown in Figure 3.3. The expansion of the cell with increasing bismuth content was expected as Bi^{3+} and Fe^{3+} are respectively larger than Ca^{2+} and Fe^{4+}. A change from rhombohedral to cubic symmetry at x = 0.8 was also observed in the $Bi_xSr_{1-x}FeO_3$ phase diagram[23].

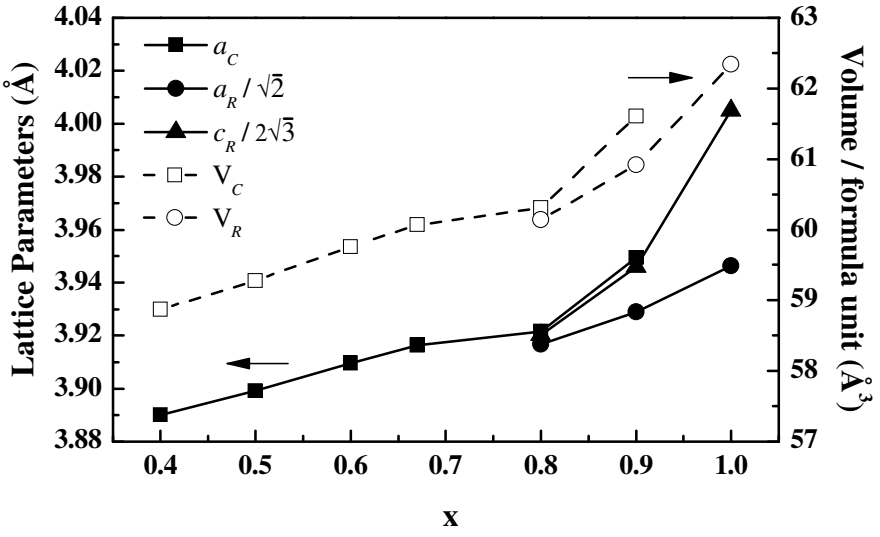

Figure 3.3 The variation of the lattice parameters and volume for the cubic (C-subscripts) and rhombohedral (R-subscripts) phases with x in the $Bi_xCa_{1-x}FeO_3$ series from ID31 data.

3.3.2 Temperature-dependent Crystal Structure

Variable temperature synchrotron X-ray powder diffraction data were collected for x = 0.6, 0.67 and 0.8 samples in $Bi_xCa_{1-x}FeO_3$ from room temperature to 400 °C. The $Bi_{0.8}Ca_{0.2}FeO_3$ sample, which was prepared by quenching from 950 °C, contains 59 % cubic and 41 % rhombohedral phases at room temperature. When heating was applied to the sample, the cubic phase fraction decreased to 45 % at 250 °C and then dropped to 5 % at 350 °C, as shown in Figure 3.4. Above 350 °C, the sample underwent an irreversible chemical phase separation into two perovskite-like phases (Figure 3.5). Thus the relative metastabilities of the two phase components in x = 0.8 sample are demonstrated from these observations. The disordered cubic phase was able to relax into the rhombohedral superstructure through a displacive transition by the initial heating. Further heating, however, led to an irreversible reconstructive change into an equilibrium mixture of several phases. The high temperature behaviour of x = 0.6 and 0.67 samples was also investigated, but only a normal thermal expansion of the cubic phase without any relaxation to the rhombohedral structure was observed for these samples (Figure 3.6).

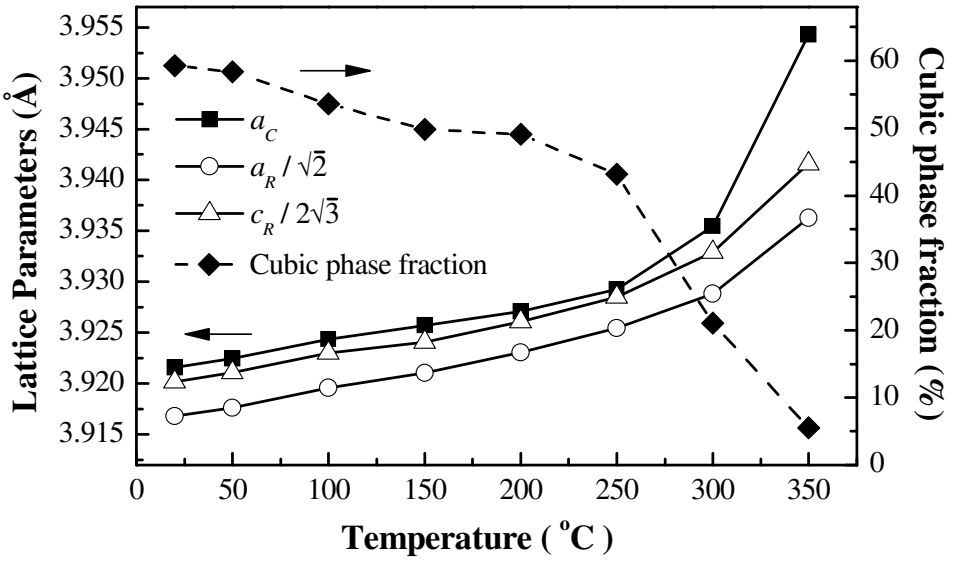

Figure 3.4 The evolution of the lattice parameters and cubic phase fraction with temperature for the $Bi_{0.8}Ca_{0.2}FeO_3$ sample from ID31 data.

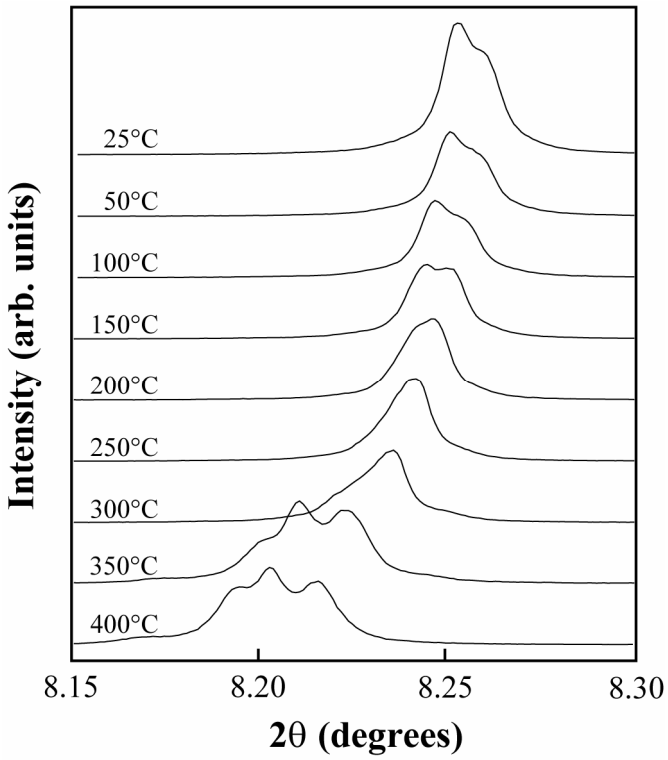

Figure 3.5 The evolution of main peak of x = 0.8 observed from temperature dependent data collection from ID31. An irreversible phase separation occurred above 350 ºC.

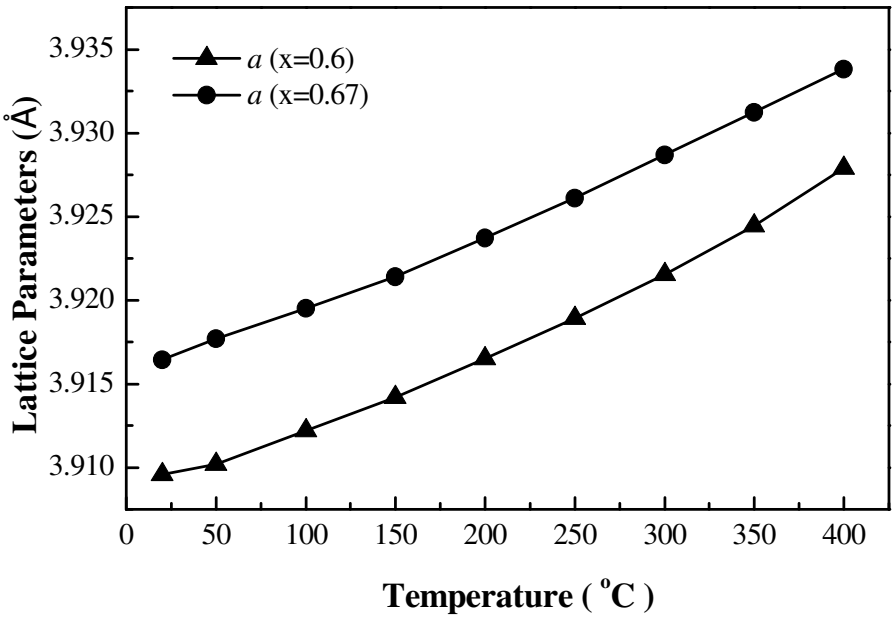

Figure 3.6 Thermal expansion of x = 0.6 and 0.67 samples in the temperature range from room temperature to 400 ºC, no structural phase transition was observed.

3.3.3 Electron Microscopy Study

Although the $Bi_xCa_{1-x}FeO_3$ system appears to be a wide solid solution, the large atom shifts originating mainly from the size differences and coordination environments of Bi^{3+} and Ca^{2+} can lead to complex local superstructures, as observed previously in similar materials[36-38]. SAED patterns and HRTEM images of the x = 0.67 and 0.8 samples have been collected and superstructures and domain patterns are observed as shown in the representative images in Figure 3.7 and Figure 3.8. A five-fold superstructure along the [100] direction in $Bi_{0.67}Ca_{0.33}FeO_3$ sample is observed and shown in Figure 3.7 (a), where this superstructure appeared in both [100] and [010] zone axis in many crystallites and formed a domain structure, as shown in Figure 3.7 (b).

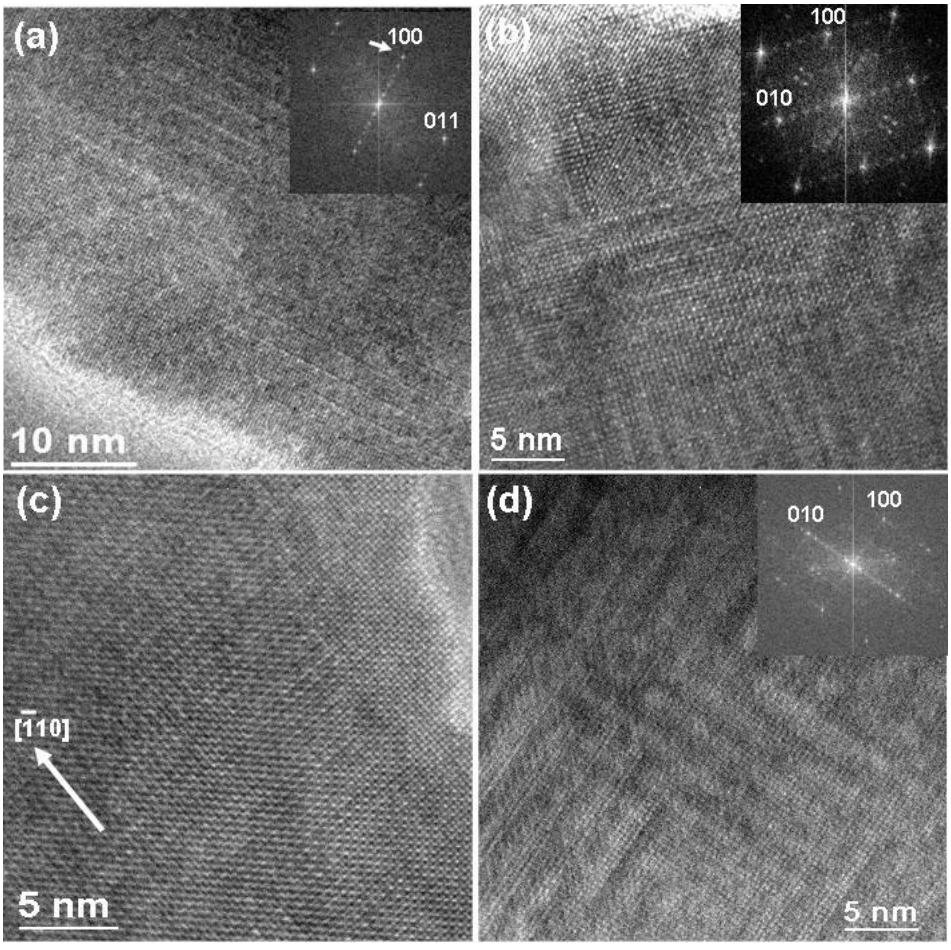

Figure 3.7 HRTEM images of (a) (b) x = 0.67 and (c) (d) x = 0.8, where viewed down (a) the [01-1] and (b) (c) (d) the [001] zone axes of the perovskite-type basic unit cells. The corresponding FFT diffraction patterns were shown in the insets of (a) (b) and (d).

Complex superstructures of the $Bi_{0.8}Ca_{0.2}FeO_3$ sample are observed by SAED patterns, shown in Figure 3.8. Instead of the five-fold superstructure, an eight-fold commensurate superstructure is observed along the [100] and [010] directions in x = 0.8 sample (Figure 3.8 (a)), which indicates a domain structure and is confirmed by HRTEM images (Figure 3.7 (d)). However, an incommensurate superstructure along the [-110] direction is also observed (Figure 3.8 (b)) where the corresponding HRTEM image is shown in Figure 3.7 (c). Furthermore, some particles contain a two-fold superstructure on the [100] zone axis (Figure 3.8 (c)), while poor ordering is also shown by the diffuse reflections along the [010] direction on others (Figure 3.8 (d)).

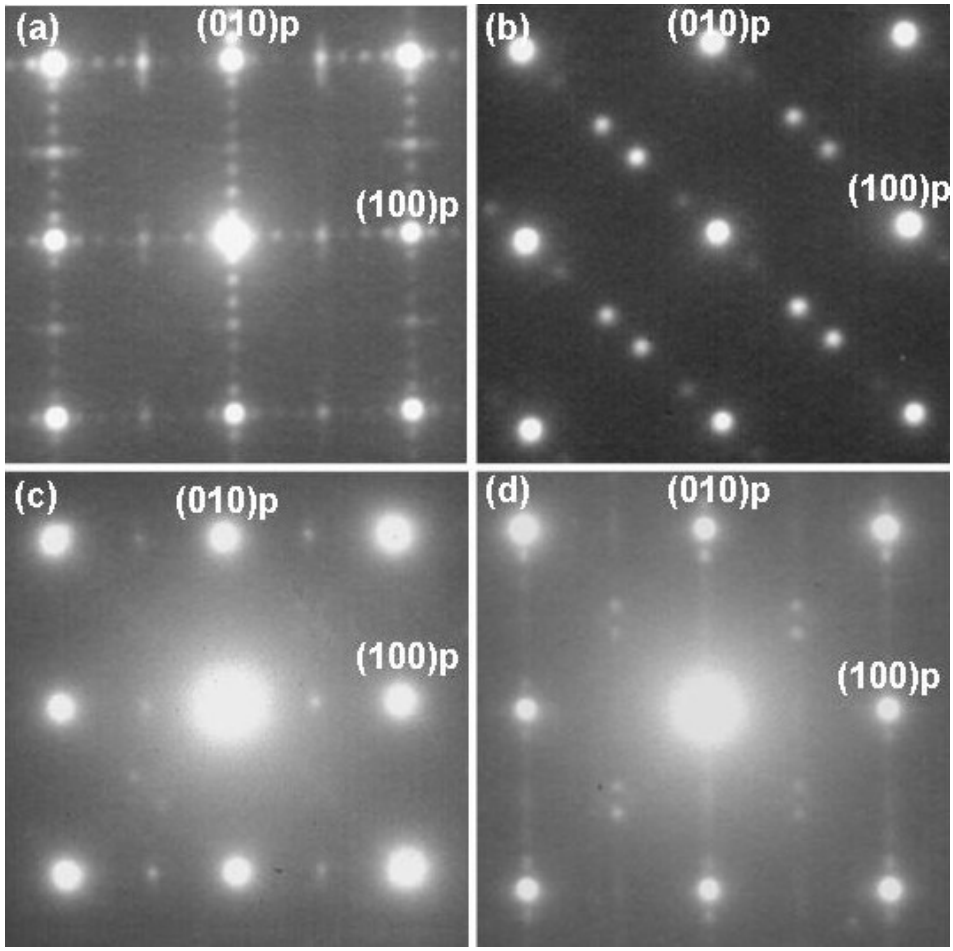

Figure 3.8 Different superstructures observed in the SAED patterns of [001] projections of the perovskite-type basic unit cell for the x = 0.8 sample.

Initial simulations indicate that the superstructures in $Bi_{0.67}Ca_{0.33}FeO_3$ and $Bi_{0.8}Ca_{0.2}FeO_3$ samples are mainly due to the Bi^{3+}/Ca^{2+} ordering accompanied by the ordering of oxygen displacements and vacancies, but further work will be needed to understand the detailed local structures of the $Bi_xCa_{1-x}FeO_3$ system.

3.3.4 Magnetic Structure

In addition to the nuclear reflections, a series of strong magnetic diffraction peaks are observed for all the $Bi_xCa_{1-x}FeO_3$ samples in the Super-D2B neutron diffraction patterns, and these peaks can be indexed by a (½ ½ ½) propagation vector of the cubic cell. Comparing 10 K and room temperature diffraction patterns, the magnetic intensities are unchanged, which implies that the ordering temperatures for the samples are >> 300 K, and only thermal expansion is observed, which indicates that no structural and magnetic phase transition occurred over the interval. The magnetic peaks are fitted by a G-type antiferromagnetic model in which each Fe moment is antiparallel to the six nearest neighbours, and the moments are parallel to the c-axis in the rhombohedral phases. The refined magnitudes for all samples in the series are shown in Figure 3.10.

The evolutions of the magnetic structures of the $Bi_xCa_{1-x}FeO_3$ perovskites at high temperature were investigated by temperature-dependent D1B neutron powder diffraction. The magnetic peak intensities decrease to zero at very similar Néel temperatures for all samples with $T_{N\text{-}AFM}$ = 350 - 370 °C. The evolution of $Bi_{0.67}Ca_{0.33}FeO_3$ patterns is shown in Figure 3.9, these are representative of the series. The temperature evolution of the magnetic moments across the series is shown in Figure 3.10. The ordered magnetic moment decreases with decreasing x, from 4.1 μ_B at x = 1 to 3.6 μ_B at x = 0.4 (Figure 3.10) but the curvature and $T_{N\text{-}AFM}$ values are remarkably constant across the $Bi_xCa_{1-x}FeO_3$ series. The reduction of the magnetic moments by 0.5 μ_B from x = 1.0 to 0.4 conforms to the ideal change of 0.6 μ_B, which is expected from the difference between the ordered moments of Fe^{3+} (S = 5/2, term ^6A) to high spin Fe^{4+} (S = 2, term ^5E) as both states have quenched orbital angular

momentum. This provides indirect evidence of the near-stoichiometric oxygen content in the solid solution.

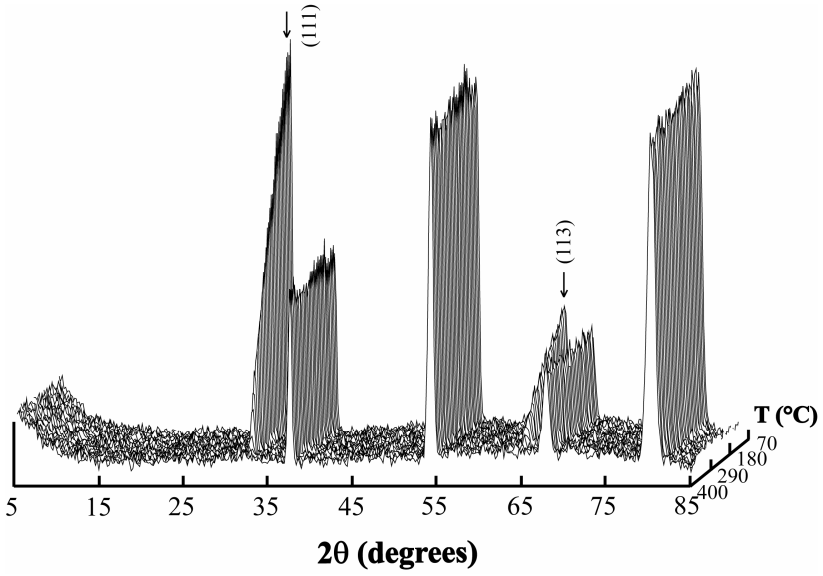

Figure 3.9 Temperature dependent neutron diffraction patterns for $Bi_{0.67}Ca_{0.33}FeO_3$, collected on the instrument D1B over a temperature range of 70 - 400 °C. The magnetic peaks are marked by arrows.

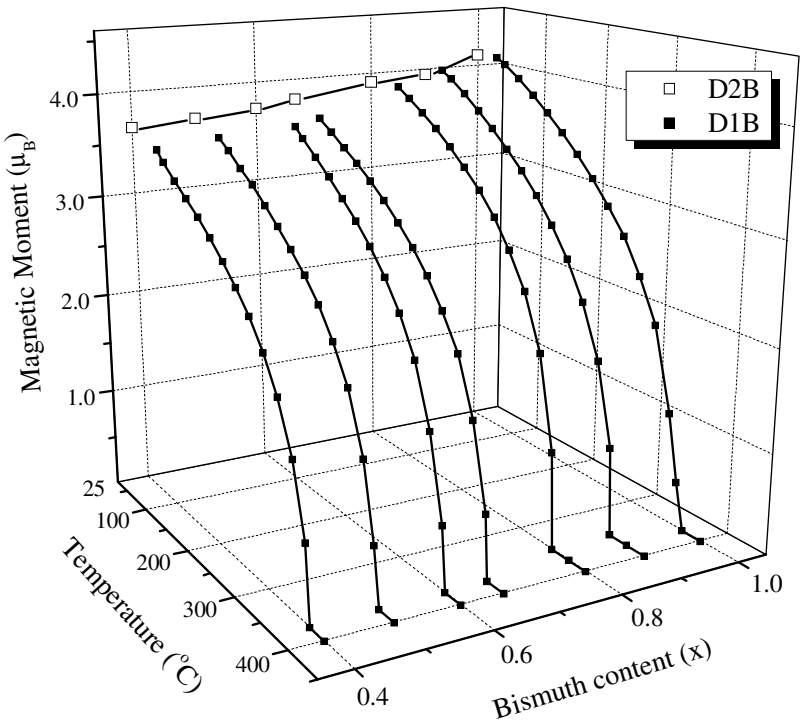

Figure 3.10 The evolution of magnetic moment in the $Bi_xCa_{1-x}FeO_3$ series as functions of bismuth content x and temperature.

3.3.5 Magnetisation Properties

The temperature dependent DC magnetic susceptibilities of the $Bi_xCa_{1-x}FeO_3$ samples were measured at 5 - 300 K in a field of 10 kOe (Figure 3.11). An almost flat response is observed for the series, which is consistent with the neutron result that all the samples are antiferromagnetically ordered at and below room temperature. The field dependent magnetisation measurements were performed from -10 to 10 kOe at 5 K (Figure 3.12). A small net magnetisation is shown for the sample with x = 0.8 - 1.0 which is consistent with the canting in the acentric rhombohedral phases observed with the composition range. For x = 0.4 - 0.67 samples a linear M(H) response is observed, which is in an agreement with the antiferromagnetic ordering confirmed from neutron data. A small anomalous magnetisation, however, is shown at low field for the x = 0.6 sample which is most probably contributed by a small ferromagnetic impurity phase such as $Ca_2Fe_2O_5$, although the reason why this is only apparent in x = 0.6 sample is unclear.

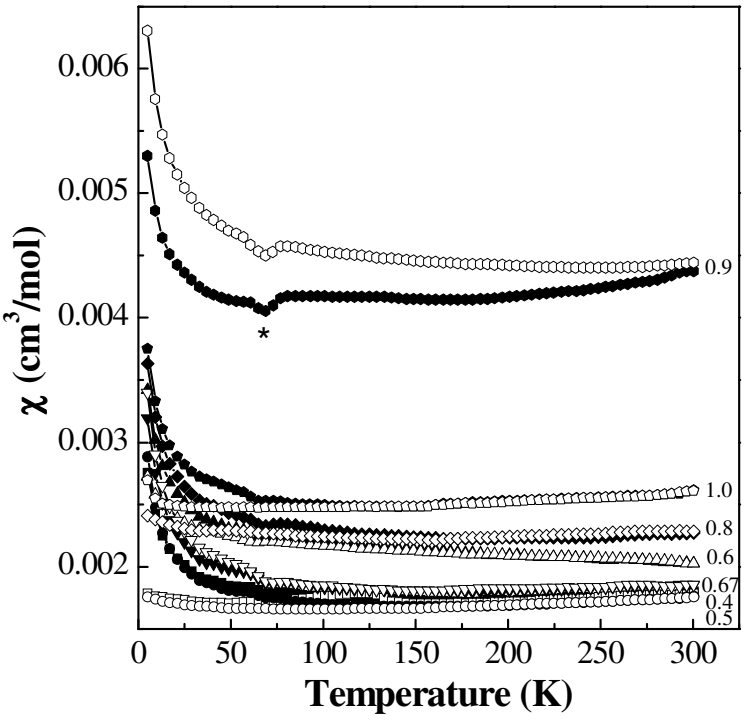

Figure 3.11 Temperature dependent DC magnetic susceptibility measurements for the series of $Bi_xCa_{1-x}FeO_3$. ZFC and FC (closed and open symbols repectively) data were collected with a field of 10 kOe. An unidentified response in the x = 0.9 material was marked by asterisk.

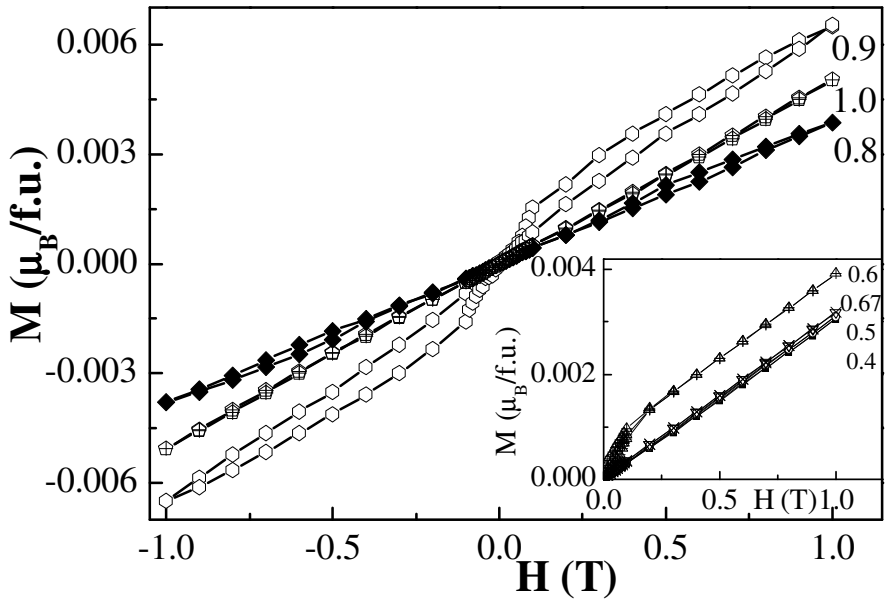

Figure 3.12 Field dependent magnetisation loops at 5 K with a field range of -1.0 to 1.0 T for x = 0.8 - 1.0 and (inset) x = 0.4 - 0.67 samples.

3.3.6 Transport Properties and Permittivity Measurement

The initial electrical resistivity measurements of $Bi_xCa_{1-x}FeO_3$ series have been performed from 280 - 350 K. All the samples in the series show insulating behaviour and the resistivity became too high to measure below 325 K. Further analysis was performed for detailed studies of A.C. permittivity and conductivity properties of the samples. The presence of a large semicircular arc at high frequencies with an associated resistance of ~ 50 - 500 kΩcm and capacitance of ~ 2 - 5 $pFcm^{-1}$ is revealed by the complex Z* plane plots of impedance at 300 K (Figure 3.13). This arc could be modelled on a single parallel Resistor-Capacitor (RC) element and the associated capacitance is consistent with a bulk (intra-grain) response.[39] An Arrhenius plot of the bulk conductivity for the $Bi_xCa_{1-x}FeO_3$ series is shown in Figure 3.14. The behaviour of leaky dielectrics with a single activation energy over the measured temperature range for all the samples is observed. A consistent trend is shown as the bulk conductivity decreased with increasing bismuth content x, while the activation energy E_a increased (Figure 3.15). However, x = 0.8 and 0.9 samples which contained cubic and rhombohedral phases are out of the trend, and relatively

high conductivities and low activation energies are observed. This suggests that the lower level of structural disorder in the doped rhombohedral phase gives a higher conductivity than that of the cubic phases.

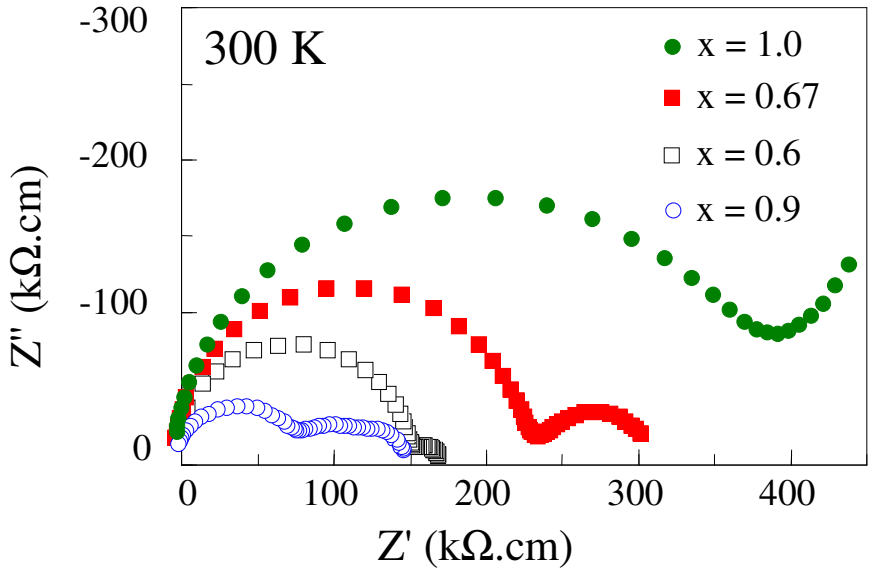

Figure 3.13 Impedance complex plane for representative $Bi_xCa_{1-x}FeO_3$ samples at 300 K.

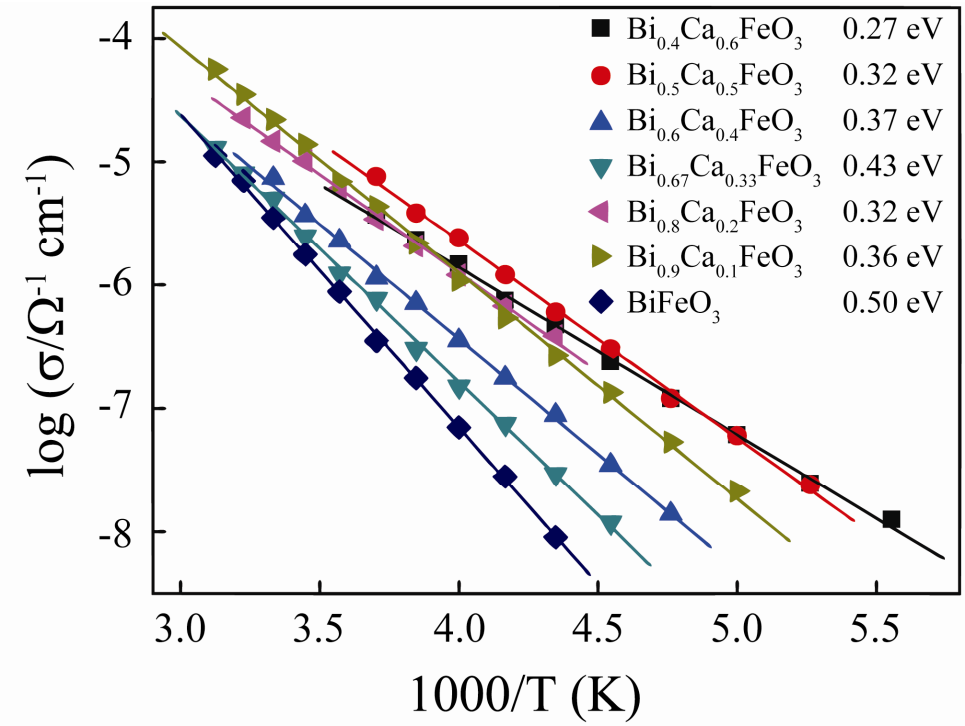

Figure 3.14 Arrhenius plots of the bulk AC conductivity for the $Bi_xCa_{1-x}FeO_3$ series.

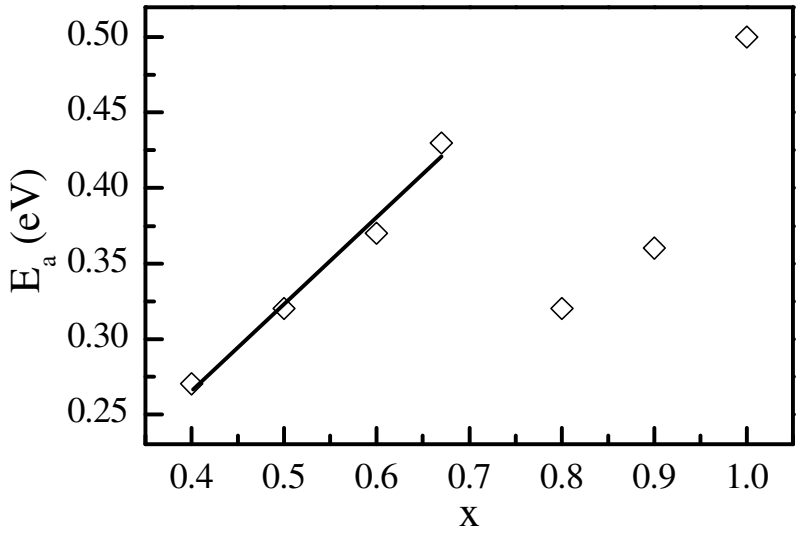

Figure 3.15 The variation of activation energy of $Bi_xCa_{1-x}FeO_3$ series, where a linear fit was performed in the region of x = 0.4 - 0.67.

The presence of a second and smaller arc is observed at lower frequencies for the samples in Figure 3.13, while two low frequency arcs are shown only for the x = 0.9 sample. The magnitude of the low frequency arc increased dramatically when the electrodes were changed from Au to InGa alloy, although the bulk response was unchanged, showing that the low frequency arc is associated with a non-ohmic contact between the metal electrode and these leaky dielectrics. This arises from a mismatch between the Fermi-energy level of the ceramics and the work function of the metal electrode. The further additional arc in the x = 0.9 sample was not investigated, but is most probably related to the biphasic nature of this composition.

Similar trends are observed for the bulk permittivity which increases both with temperature and with x from 0.4 to 0.67 in the cubic regime (Figure 3.16). This is consistent with replacement of Ca^{2+} by the more polarisable Bi^{3+} ion on the *A* site of the perovskite lattice. Almost identical, anomalously high permittivities are observed for biphasic x = 0.8 and 0.9 samples, whereas the permittivity of the x = 1, $BiFeO_3$ sample is lower than expected. This is probably related to the low ceramic density of the sample which was sintered at a significantly lower temperature than the other $Bi_xCa_{1-x}FeO_3$ samples.

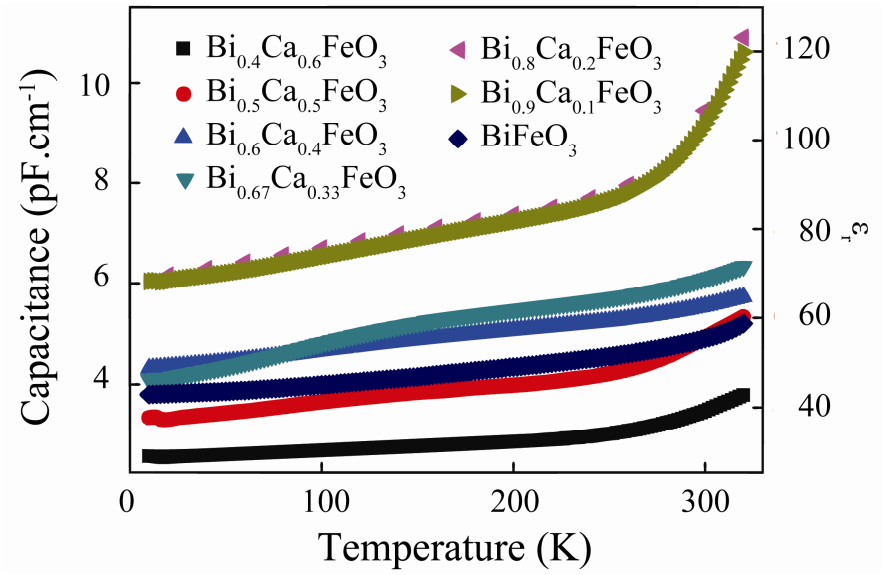

Figure 3.16 The plot of permittivity against temperature for the $Bi_xCa_{1-x}FeO_3$ series.

3.4 Discussion

This investigation demonstrates that $Bi_xCa_{1-x}FeO_3$ solid solutions (x = 0.4 - 1.0) can be synthesised by a standard ceramic method firing the oxides in air. When doped with high calcium content, mixtures of brownmillerite and perovskite phases were obtained. The variations in oxygen content have not been studied in detail, but near-stoichiometric oxygen contents are suggested from the present results for the series.

The structure evolution of the $Bi_xCa_{1-x}FeO_3$ series appears straightforward from standard laboratory X-ray diffractometry which showed a structural transition from rhombohedral *R*3*c* to cubic *Pm*$\bar{3}$*m* symmetry when the bismuth content decreased to 0.8. This is comparable with the reported $Bi_xSr_{1-x}FeO_3$ series in which a similar transition occurred as bismuth content decreases below ≈ 0.8[23]. However, the complexities of the structural transition and the cubic structure itself are revealed from the high resolution provided by synchrotron X-ray diffraction and the sensitivity to oxygen displacement of neutron diffraction. Phase coexistence is observed in the x = 0.8 and 0.9 samples which is associated with enhanced magnetic and dielectric responses. The x = 0.8 sample can be described well by the model

consisting of rhombohedral and cubic phases, however such a model is more approximate for the x = 0.9 sample. This may arise from the differences in their preparation, the x = 0.8 sample was quenched while x = 0.9 was furnace-cooled to room temperature which perhaps allowed the formation of a structural continuum between rhombohedral and cubic. Substantial disordered displacements of Bi/Ca from the *A* sites, and perpendicular shifts of the oxide anions are observed in all of the cubic $Bi_xCa_{1-x}FeO_3$ phases. The Fe-O bond distances slightly decrease from 2.01 to 1.99 Å as Fe is oxidised with decreasing x, and the Fe-O-Fe bridges are bent away from the ideal value of 180 to ~155 °. In the disordered cubic model the range of Bi/Ca-O distances (2.1 - 3.4 Å) is comparable to the distribution of Bi-O distances (2.26 - 3.46 Å) observed in the ordered rhombohedral structure of $BiFeO_3$, which indicates that the characteristic local lone pair distortions of Bi^{3+} play a key role in the disorder.

No long-range ordering of the local displacements is observed for the cubic phases from synchrotron X-ray or neutron diffraction patterns, even for x = 0.67 which was synthesised in case of any charge ordering superstructure. However, a wealth of microstructures is shown in HRTEM studies for x = 0.67 and 0.8 samples. Commensurate and incommensurate superstructure spots and diffuse scattering are observed from different domains and the real space images show modulated twinned and tweeded microstructures. To characterise the local structures in the $Bi_xCa_{1-x}FeO_3$ series further detailed studies will be needed.

Doped $BiFeO_3$ materials are of particular interest for multiferroic properties, as $BiFeO_3$ is one of very few materials to show ferroelectric and magnetic ordering well above room temperature. Although $BiFeO_3$ has a long-range spiral spin modulation, the doped $Bi_xCa_{1-x}FeO_3$ materials display a simple collinear antiferromagnetic arrangement. The suppression of the modulation was observed for various *A*-site doping of $BiFeO_3$ including isovalent (*e.g.* La^{3+}) and non-isovalent (*e.g.* Ca^{2+}, Sr^{2+}, Pb^{2+}, Ba^{2+}) systems[16,22-24,40] or *B*-site (e.g. Mn^{3+}) substitutions[41]. A remarkable robustness of the antiferromagnetic order is demonstrated by the $Bi_xCa_{1-x}FeO_3$ solid solution. A 60 % replacement of the Bi by Ca only leads to a slight decrease in the Néel temperature from 643 to 623 K, and the antiferromagnetically ordered moment

at room temperature decreases only as expected for the replacement of S = 5/2 Fe^{3+} by high spin S = 2 Fe^{4+}. However the ferroelectric order which accompanies the rhombohedral lattice distortion is rapidly suppressed in those calcium-rich samples (x = 0.4 - 0.67) in which only a single disordered cubic phase exists. The observed phase coexistence in x = 0.8 and 0.9 samples, and the relaxation of cubic to rhombohedral phase in the x = 0.8 sample at high temperatures, shows that the sample properties are very sensitive to thermal treatments in the x = 0.8 - 1.0 range.

The $Bi_xCa_{1-x}FeO_3$ samples are leaky dielectrics, with conductivity generally increasing with x, as expected for hole-doping from the oxidation of Fe^{3+} to Fe^{4+}. Enhanced magnetisations and permittivities are observed for x = 0.8 - 1.0, in particular in the x = 0.9 sample. An appreciable magnetic hysteresis is shown although the loop collapses close to H = 0, suggests that the induced magnetisation is of metamagnetic rather than spontaneous origin. x = 0.8 and 0.9 samples have relative permittivities of ~ 100 at room temperature. Further processing of the x = 0.8 and 0.9 compositions to reduce conductivity through oxygen content control could lead to improved $BiFeO_3$-based multiferroics.

In summary, the $Bi_xCa_{1-x}FeO_3$ series have been successfully synthesised at ambient pressure in air by a standard solid state method. From synchrotron X-ray and neutron diffraction results, a disordered cubic model is adopted for x = 0.4 - 0.67 samples and the coexistence of rhombohedral and cubic phases is observed for x = 0.8 and 0.9 samples. Temperature dependent synchrotron X-ray diffraction reveals that the x = 0.8 sample is located at the phase boundary and a transformation from cubic to rhombohedral phases is observed at high temperatures. A robust antiferromagnetic order is shown for all samples however the ferroelectric order is suppressed in the disordered cubic structure (x = 0.4 - 0.67).

3.5 References

1. J. B. Goodenough, *Rep. Prog. Phys.,* **67**, 1915 (2004).
2. D. I. Khomskii, *J. Magn. Magn. Mater.,* **306**, 1 (2006).

3. C. Blaauw and F. v. d. Woude, *J. Phys. C: Solid State Phys.,* **6**, 1422 (1973).
4. P. Fischer, M. Polomska, I. Sosnowska, and M. Szymanski, *J. Phys. C: Solid State Phys.,* **13**, 1931 (1980).
5. I. Sosnowska, T. P. Neumaier, and E. Steichele, *J. Phys. C: Solid State Phys.,* **15**, 4835 (1982).
6. F. Sugawara, S. Iiida, Y. Syono, and S.-I. Akimoto, *J. Phys. Soc. Jpn.,* **25**, 1553 (1968).
7. H. Faqir, H. Chiba, M. Kikuchi, Y. Syono, M. Mansori, P. Satre, and A. Sebaoun, *J. Solid State Chem.,* **142**, 113 (1999).
8. A. Moreira dos Santos, S. Parashar, A. R. Raju, Y. S. Zhao, A. K. Cheetham, and C. N. R. Rao, *Solid State Commun.,* **122**, 49 (2002).
9. V. A. Bokov, I. E. Myl'nikova, S. A. Kizhaev, M. F. Bryzhina, and N. A. Grigoryan, *Sov. Phys. Solid State,* **7**, 2993 (1966).
10. H. Chiba, T. Atou, and Y. Syono, *J. Solid State Chem.,* **132**, 139 (1997).
11. R. J. Goff and J. P. Attfield, *J. Solid State Chem.,* **179**, 1369 (2006).
12. H. Chiba, M. Kikuchi, K. Kusaba, Y. Muraoka, and Y. Syono, *Solid State Commun.,* **99**, 499 (1996).
13. I. O. Troyanchuk, O. S. Mantytskaya, and A. N. Chobot, *Phys. Solid State,* **44**, 2266 (2002).
14. G. A. Smolenskii and V. M. Yudin, *Sov. Phys. Solid State,* **6**, 2936 (1965).
15. Y. E. Roginskaya, Tomashpo.Yy, Venevtse.Yn, V. M. Petrov, and G. S. Zhdanov, *Sov. Phys. Jetp,* **23**, 47 (1966).
16. S.-T. Zhang, L.-H. Pang, Y. Zhang, M.-H. Lu, and Y.-F. Chen, *J. Appl. Phys.,* **100**, 114108 (2006).
17. G. L. Yuan, S. W. Or, and H. L. W. Chan, *J. Phys. D: Appl. Phys.,* **40**, 1196 (2007).
18. V. L. Mathe, K. K. Patankar, R. N. Patil, and C. D. Lokhande, *J. Magn. Magn. Mater.,* **270**, 380 (2004).
19. G. L. Yuan, S. W. Or, J. M. Liu, and Z. G. Liu, *Appl. Phys. Lett.,* **89**, 052905 (2006).
20. V. L. Mathe, *J. Magn. Magn. Mater.,* **263**, 344 (2003).
21. G. L. Yuan and S. W. Or, *J. Appl. Phys.,* **100**, 024109 (2006).
22. D. H. Wang, W. C. Goh, M. Ning, and C. K. Ong, *Appl. Phys. Lett.,* **88**, 212907 (2006).
23. J. Li, Y. Duan, H. He, and D. Song, *J. Alloys Compd.,* **315**, 259 (2001).
24. V. A. Khomchenko, D. A. Kiselev, J. M. Vieira, A. L. Kholkin, M. A. Sa, and Y. G. Pogorelov, *Appl. Phys. Lett.,* **90**, 242901 (2007).
25. D. Kothari, V. R. Reddy, A. Gupta, V. Sathe, A. Banerjee, S. M. Gupta, and A. M. Awasthi, *Appl. Phys. Lett.,* **91**, 202505 (2007).

26. B. Yu, M. Li, J. Liu, D. Guo, L. Pei, and X. Zhao, *J. Phys. D: Appl. Phys.,* **41**, 065003 (2008).
27. Y.-K. Jun, W.-T. Moon, C.-M. Chang, H.-S. Kim, H. S. Ryu, J. W. Kim, K. H. Kim, and S.-H. Hong, *Solid State Commun.,* **135**, 133 (2005).
28. C. H. Yang, T. Y. Koo, and Y. H. Jeong, *Solid State Commun.,* **134**, 299 (2005).
29. I. A. Santos, H. L. C. Grande, V. F. Freitas, S. N. de Medeiros, J. A. Paesano, L. F. Cótica, and E. Radovanovic, *J. Non-Cryst. Solids,* **352**, 3721 (2006).
30. X. Qi, J. Dho, R. Tomov, M. G. Blamire, and J. L. MacManus-Driscoll, *Appl. Phys. Lett.,* **86**, 062903 (2005).
31. M. R. Suchomel, C. I. Thomas, M. Allix, M. J. Rosseinsky, A. M. Fogg, and M. F. Thomas, *Appl. Phys. Lett.,* **90**, 112909 (2007).
32. J. B. MacChesney, R. C. Sherwood, and J. F. Potter, *J. Chem. Phys.,* **43**, 1907 (1965).
33. P. Adler, A. Lebon, V. Damljanovic, C. Ulrich, C. Bernhard, A. V. Boris, A. Maljuk, C. T. Lin, and B. Keimer, *Phys. Rev. B,* **73**, 094451 (2006).
34. P. M. Woodward, D. E. Cox, E. Moshopoulou, A. W. Sleight, and S. Morimoto, *Phys. Rev. B,* **62**, 844 (2000).
35. I. Troyanchuk, D. Karpinsky, M. Bushinskii, O. Prokhnenko, M. Kopcevicz, R. Szymczak, and J. Pietosa, *J. Exp. Theor. Phys.,* **107**, 89 (2008).
36. W. Zhou, D. A. Jefferson, and J. M. Thomas, *Proc. R. Soc. London, A,* **406**, 173 (1986).
37. W. Zhou, *J. Solid State Chem.,* **76**, 290 (1988).
38. W. Zhou, *J. Solid State Chem.,* **101**, 1 (1992).
39. D. C. S. John T. S. Irvine, Anthony R. West,, *Adv. Mater.,* **2**, 132 (1990).
40. I. Sosnowska, M. Loewenhaupt, W. I. F. David, and R. M. Ibberson, *Mater. Sci. Forum,* **133-136**, 683 (1993).
41. I. Sosnowska, W. Schaffer, W. Kockelmann, K. H. Andersen, and I. O. Troyanchuk, *Appl. Phys. A: Mater. Sci. Process.,* **74**, S1040 (2002).

Chapter 4

Studies of Lanthanum Doped Bismuth Manganites $Bi_xLa_{1-x}MnO_3$

4.1 Introduction

Manganese-based oxide perovskites have been found to display a wide variety of fascinating physical phenomena including the colossal magnetoresistance (CMR) effect, and metal-insulator (MI), antiferromagnetic-ferromagnetic and structural transitions[1]. This diversity of properties has provoked great enthusiasm in the scientific community stimulating numerous studies about these compounds. Most of these properties arise from the presence of mixed valence states at the manganese sites, that is, the d^3 Mn^{4+} (t_{2g}^3) cation and the Jahn-Teller active d^4 Mn^{3+} ($t_{2g}^3 e_g^1$). Mixed-valence manganite systems were first reported in the 1950s with the discovery of $T_{1-x}D_xMnO_3$ class of compounds, where T and D represent trivalent rare earth cations and divalent alkaline cations, respectively[2]. Varying the composition of these manganites causes the Mn sites to adopt mixed valence states, allowing for the mentioned physical phenomena to be observed. These phenomena can be attributed to the interactions between double-exchange, antiferromagnetic superexchange, cooperative Jahn-Teller distortions, orbital ordering (OO) and charge ordering (CO) effects.

$BiMnO_3$ is a well-known, widely investigated multiferroic manganite material. $BiMnO_3$ has a ferromagnetic Curie temperature $T_{C\text{-}FM}$ 103 K[3], a ferroelectric $T_{C\text{-}FE}$ 450 K[4] and a structural phase transition from monoclinic to tetragonal symmetry at 760 K[5]. $BiMnO_3$ is a heavily distorted perovskite at room temperature with monoclinic symmetry; this can be attributed to the steric effect of the $6s^2$ lone pair electrons characteristic of Bi^{3+}. The cooperative ordering of these lone pairs, or dipoles, below $T_{C\text{-}FE}$ gives rise to the reported ferroelectric behaviour[6]. The space group of this compound is still under debate, as both acentric (*C*2) and centric (*C*2/*c*)

symmetry have been proposed[7]. The centrosymetric space group has been proposed mainly on the basis of electron diffraction (selected area (SAED) and convergent beam (CBED))[8]. The latter proposition, however, is not compatible with the observed ferroelectric properties. The origin of the ferromagnetism in $BiMnO_3$ has been proposed to be due to a specific arrangement of MnO_6 octahedra, *i.e.* the ordering of the d_{z^2} orbitals of the Mn^{3+} (Figure 4.1 (a))[7]. This is a consequence of characteristic axial elongation as a result of Jahn-Teller distortion. When Bi^{3+} is substituted by divalent cations such as Ca^{2+} and Sr^{2+} it results in the appearance of Mn^{4+} in the manganese sites. The formed mixed valent state destroys the ferromagnetic order but no metal-insulator transition is observed[9,10].

The observed orbital ordering behaviour of $BiMnO_3$ differs from that of $LaMnO_3$, which is an antiferromagnetic insulator with a $T_{N\text{-}AFM} = 140$ K and has an orthorhombic structure with space group *Pnma*[11]. The Jahn-Teller distortion in $LaMnO_3$ leads to a d_{z^2} orbital ordering (Figure 4.1 (b)), resulting in an *A*-type antiferromagnetic ordering and *O'*-type orthorhombic crystal structure. The transition from antiferromagnetic insulating state to ferromagnetic metallic state in $LaMnO_3$ can be observed when the La^{3+} at the *A* site is doped with divalent cations (*e.g.* Ca^{2+}, Sr^{2+})[12,13]. This transition can be explained by the double exchange (DE)

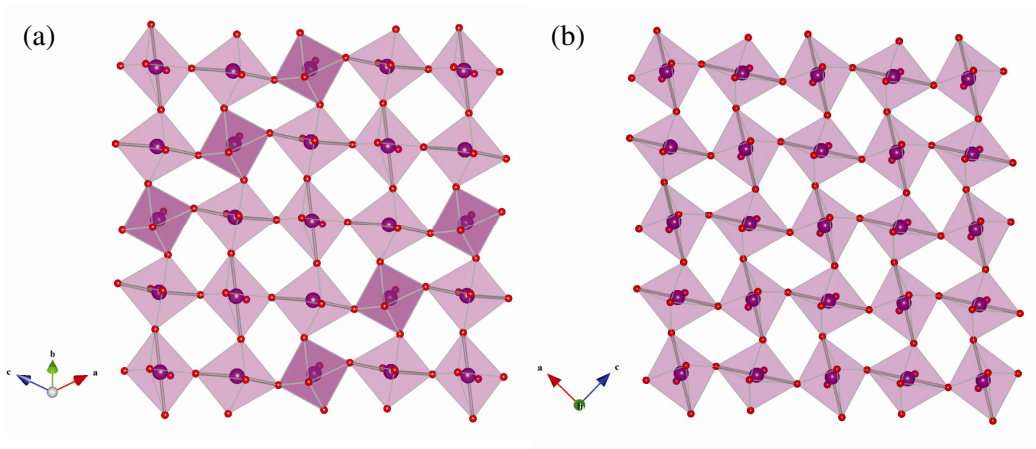

Figure 4.1 The schematic diagram of the orbital ordering in (a) $BiMnO_3$, where the bold bonds present the elongation Mn-O bonds, *i.e.* occupied d_{z^2} orbital. Note that the long Mn-O bonds in the darker octahedra are perpendicular to the plane; (b) $LaMnO_3$, where the long Mn-O bonds ordered antiferrodistortively. Figures adapted from the work of E. Montanari *et al.*[7]

interaction between the Mn^{3+} and the Mn^{4+} cations[14]. This same behaviour can be found in the oxygen non-stoichiometric phase $LaMnO_{3+\lambda}$. The oxygen excess leads to the $LaMn^{3+}_{1-2\lambda}Mn^{4+}_{2\lambda}O_{3+\lambda}$ valence formula. Again in this case, the appearance of Mn^{3+}/Mn^{4+} mixed valence states alters the structure and magnetic properties of the material[15,16].

The ionic radii for Bi^{3+} and La^{3+} are fairly similar (1.17 and 1.16 Å for 8-coordination, respectively[17]). Hence a replacement of Bi^{3+} by isovalent La^{3+} in the material allows the manganese ions to maintain the same valence state whilst the mismatch of the *A* site cations caused by the substitution is small. An intermediate solid solution of $Bi_xLa_{1-x}MnO_3$ is therefore an interesting material based on the very different natures of the orbital ordering and magnetic structures of the parent compounds. Several interesting effects have already been observed in the solid solution $Bi_xLa_{1-x}MnO_3$ ($0 < x < 1$): ferromagnetism and a transition to spin-glass state, a metal-insulator transition and even a colossal magnetoresistance effect. It has been suggested that these properties are due to an oxygen non-stoichiometry and the consequent generation of Mn^{4+} in the material when La is introduced[18,19]. These effects can be linked to those observed in the extensive studies of $LaMnO_{3+\lambda}$ where the oxygen content played an important role in the properties observed in the materials[15,16]. The structures of the oxygen stoichiometric materials were reported to remain orthorhombic for La-rich samples as in $LaMnO_3$, while the monoclinic symmetry observed in $BiMnO_3$ arises when the Bi content reaches 0.9. Additionally, La-rich samples exhibit antiferromagnetic behaviour whereas a mixed-phase consisting of antiferromagnetic and ferromagnetic regions with high Bi content has also been observed[20,21].

Recently, the investigation of the multiferroic properties of a thin film with composition $Bi_xLa_{1-x}MnO_3$ ($x = 0.9$) has been reported[22-24]. The $Bi_{0.9}La_{0.1}MnO_3$ epitaxial layers were grown by pulsed laser deposition using a stoichiometric mixture of sintered oxide starting materials. The films were found to be both ferromagnetic and ferroelectric, and retain the multiferroic properties to a thickness of 2 nm. The ferromagnetism was explained by the Bi-site deficiency, which introduced Mn^{4+} into the films following the formula: $Bi_{0.9-\delta}\square_\delta La_{0.1}Mn^{3+}_{1-3\delta}Mn^{4+}_{3\delta}O_3$ rather than by

oxygen non-stoichiometry. In this case the ferroelectricity is linked to the directional $6s^2$ lone pair of the Bi^{3+} ion.

It is hence of interest to have a comprehensive understanding, of not only the interplay of the properties due to the combination of two distinct parent compounds in $Bi_xLa_{1-x}MnO_3$, but also in the aspects of the multiferroic property exhibited by La-stabilised $BiMnO_3$ thin films. Unlike other manganite perovskite families, relatively few studies have been published about $Bi_xLa_{1-x}MnO_3$ solid solutions. The phase transition over the range of substitutions[20], behaviour of the magnetic ordering[21], transport properties of the materials[18] and also colossal magnetoresistance effect[19] have been reported but some discrepancies exist between the existing literature. Various reasons have been invoked to explain these differences, such as the presence of an oxygen excess or cation vacancies on *A* and/or *B* sites as an analogue to the extensively studied $LaMnO_{3+\lambda}$, which will cause the introduction of Mn^{4+}. However without more detailed information the factors responsible to these properties remain unclear.

Although the research into $Bi_xLa_{1-x}MnO_3$ solid solution has been previously reported, the slight La-doped $BiMnO_3$ bulk materials have not been studied in detail. Recently thin films of La-substituted $BiMnO_3$ on $SrTiO_3$ and $NdGaO_3$ substrates using a pulsed laser deposition technique have been studied by Drs. F. Sher and N. Mathur (University of Cambridge). The aim of this study is to continue their research examining the bulk structural and magnetic properties of lightly La doped $BiMnO_3$, in order to extend and complement the $Bi_xLa_{1-x}MnO_3$ thin film studies.

4.2 Experimental

Sample Preparation

Since high-pressure synthesis is required for the preparation of bismuth manganite, $BiMnO_3$, the multi-anvil technique with a Walker module was used for the preparation of $Bi_xLa_{1-x}MnO_3$ (x = 0.8, 0.9 and 1.0) samples. Initial oxide reagents

Bi_2O_3, La_2O_3 (overnight preheat treatment is required) and Mn_2O_3 (all 99.999 %, Aldrich) were weighed carefully in stoichiometric amounts and ground thoroughly. The well mixed starting materials were sealed into a gold capsule, which was placed in a BN container and pressure cell assemblies. High pressure was applied hydrostatically by a uniaxial force through steel wedges and WC anvils to the assembled cell by a Walker-type press. After the target pressure was reached, a heating period was applied, and the sample was then quenched. The applied pressure was then released slowly (see section 2.1.2 for details).

It has been reported that heating at 1110 °C for 60 minutes under 6 GPa is sufficient to synthesis pure $BiMnO_3$ perovskite[8], although stoichiometric $LaMnO_3$ can be made with ambient pressure solid state synthesis[25]. Different conditions were applied to synthesise the target materials. In each case a gold capsule to contain the starting materials is crucial in order to prevent reaction with the BN container. Experiments with various pressures, temperatures and heating periods were performed to minimise impurity phases in final products. It was found that the optimal heating period was 60 minutes for a complete reaction. The optimised conditions for the samples are listed in Table 4.1. Each synthesis produced a bulk, dark grey cylinder product of mass ~20 mg. The obtained bulk samples were then ground to a black powder. A laboratory X-ray powder diffractometer was used to characterise the products. Syntheses with optimised conditions were repeated several times in order to generate suitable quantities of materials for neutron scattering measurements.

Table 4.1 Optimised synthesis conditions for $Bi_xLa_{1-x}MnO_3$ series. Samples were pressurised in the time shown, heated up to the indicated temperature in 10 minutes and quenched after a heating period of 60 minutes.

	Pressurisation time	Pressure	Temperature
x = 1.0	2.0 hr	6.0 GPa	1100 °C
x = 0.9	1.5 hr	4.5 GPa	900 °C
x = 0.8	1.0 hr	3.0 GPa	800 °C

Laboratory X-ray Powder Diffraction

The obtained samples were characterised by a Bruker D8 Advance X-ray diffractometer using flat plate mode. The XRD patterns were collected in the range of $5° \leq 2\theta \leq 98°$ with an integration time of 5 seconds per 0.01355 ° step with Ge (111) monochromator and Cu-Kα_1 radiation ($\lambda = 1.540598$ Å) at ambient conditions.

Neutron Powder Diffraction

Time-of-flight (TOF) neutron powder diffraction data of the samples were collected at 20 K and 150 K on the General Materials Diffractometer (GEM) instrument in the ISIS pulsed neutron source facility, Rutherford Appleton Laboratory, UK. Samples (~100 mg) were loaded in a 3.0 mm diameter vanadium can and diffraction data at each temperature were collected by 6 detector banks for ~5 hours. The XRD and NPD patterns were analyzed by the Rietveld method with the GSAS program package.

Magnetic studies

Magnetic properties of the samples were measured with a Quantum Design MPMS XL SQUID magnetometer. The temperature-dependent DC susceptibility was collected in the temperature range 5 - 300 K in a zero-field-cooling (ZFC) and a field-cooling (FC) mode with an applied field of 100 Oe. The field-dependent magnetisation and the hysteresis loop measurements were carried out at 5 K and a varying magnetic field of -70 to 70 kOe.

The impedance and ferroelectricity measurements of the synthesised materials are currently in progress in collaboration with Dr. F. Morrison (University of St. Andrews), in order to investigate the multiferroic properties.

4.3 Results

4.3.1 Crystal Structure

The obtained $Bi_xLa_{1-x}MnO_3$ materials were initially examined by laboratory X-ray diffraction. A starting monoclinic structure model of $BiMnO_3$ from the work of E. Montanari *et al.*[7] was used for data analysis, with the atomic positions as: Bi, 8*f*, (x, y, z); Mn1, 4*e*, (0, y, ¾); Mn2, 4*d*, (¼,¼, ½); O, 8*f*, (x, y, z) in space group *C*2/*c* (No. 15). The Rietveld fit resulted in the following lattice parameters: $a = 9.5384(3)$ Å, $b = 5.6103(2)$ Å, $c = 9.8565(3)$ Å and $\beta = 110.639(1)$ °. The high-pressure phase α-Bi_2O_3 was observed as a minor impurity and was included in the refinement. Reasonable fits with $R_{wp} = 4.60$ % were obtained. The XRD Rietveld fits are shown in Figure 4.2 (a) and the refinement results listed in Table 4.2 are comparable with the reported values[7].

Compared to the neutron diffraction data collected at 150 K on the GEM instrument, the 20 K data did not reveal the presence of new structural peaks, hence the room temperature monoclinic model was used for the NPD refinements. Multi-histogram refinements were carried out for GEM data collected from detector banks 1 - 5. The profiles from selected data banks are shown in Figure 4.2. Refined lattice parameters, atom positions and resulting selected bond distances are listed in Table 4.2. The stoichiometric oxygen content was confirmed from the refinement of site occupancies. A shrinkage of the unit cell with decreasing temperature was observed from the decrease of lattice parameters and cell volume. The Jahn-Teller distortion of the oxide octahedron around Mn cation is evident in the Mn-O distances.

The similar XRD patterns of $Bi_{0.9}La_{0.1}MnO_3$ and $BiMnO_3$ suggest that these materials adopt the same crystal structure. Thus the monoclinic space group *C*2/*c* model from the previous $BiMnO_3$ results was used to fit the $Bi_{0.9}La_{0.1}MnO_3$ data. The Rietveld fit is shown in Figure 4.3 and the refinements results are listed in Table 4.3. The resulting lattice parameters show the shrinking of the cell compared to $BiMnO_3$, which indicates that Bi^{3+} has been successfully substituted by relatively smaller La^{3+} (8-coordinated ionic radius 1.17 and 1.16 Å, respectively[17]).

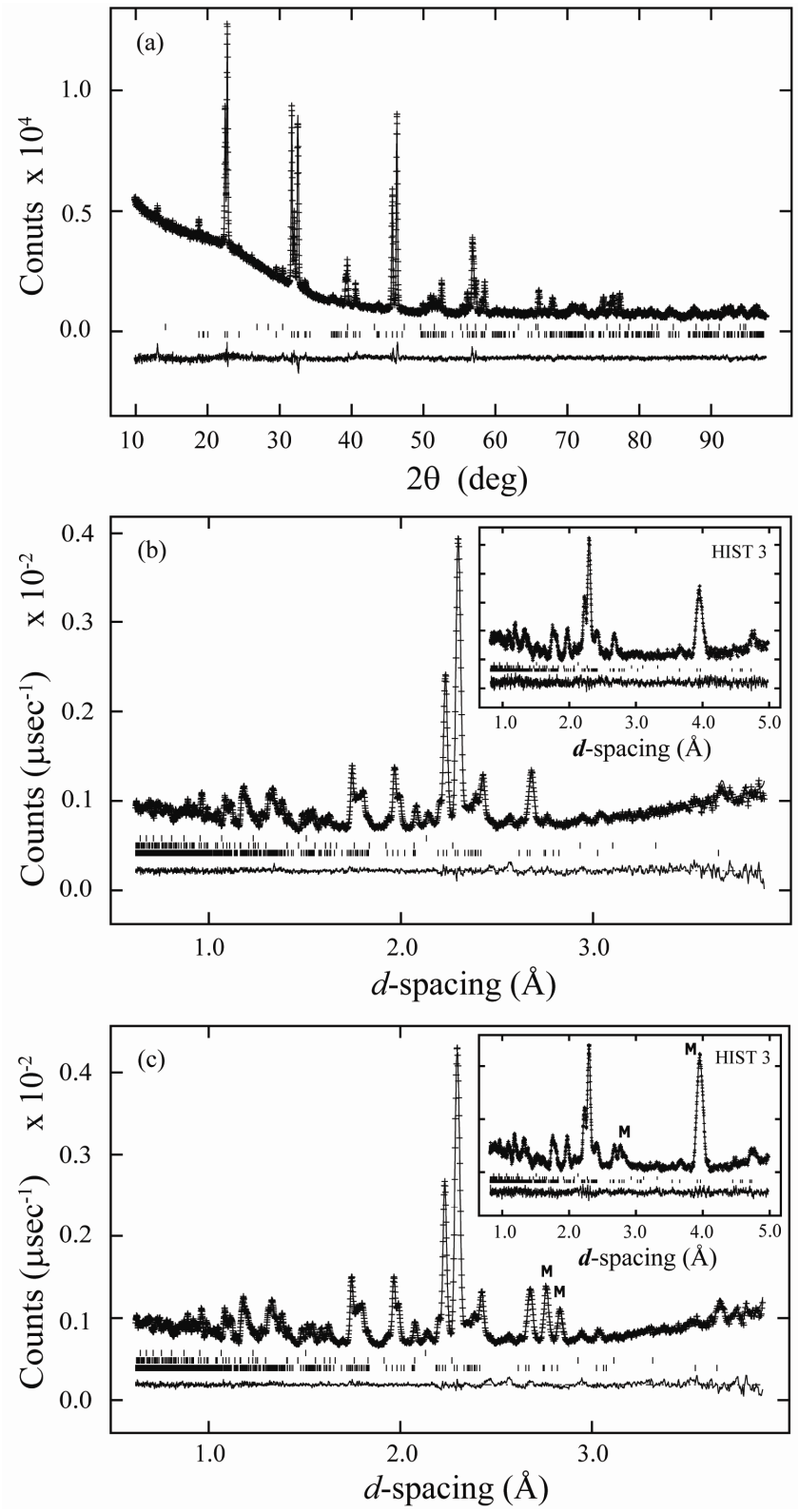

Figure 4.2 The Rietveld fits of $BiMnO_3$ for (a) D8 XRD pattern at room temperature, (b) GEM NPD pattern from bank 4 and bank 3 (inset) at 150 K and (c) GEM NPD pattern from bank 4 and bank 3 (inset) at 20 K, while the magnetic reflections are marked by "M". The index markers from the bottom represent the reflections of $BiMnO_3$ (99(7) %), α-Bi_2O_3 (1(7) %), and V container (GEM data only), respectively.

Table 4.2 Refinement results for $BiMnO_3$ fits at 300 K, 150 K and 20 K. Lattice parameters, cell volume, atomic positions, isotropic thermal factors, magnetic moments, refinement reliability R_{wp} and χ^2 and selected bond distances, and BVS results from the refinements are listed.

$BiMnO_3$		20 K[a]	150 K[a]	300 K[b]
a (Å)		9.5236(1)	9.5262(2)	9.5386(2)
b (Å)		5.5996(1)	5.6029(1)	5.6105(1)
c (Å)		9.8387(1)	9.8453(2)	9.8570(2)
β (º)		110.578(1)	110.634(2)	110.640(1)
V (Å^3)		491.20(1)	491.78(1)	493.65(2)
Bi	x	0.1363(1)	0.1362(1)	0.1357(2)
	y	0.2171(2)	0.2184(2)	0.2187(2)
	z	0.1266(1)	0.1266(1)	0.1254(2)
	U_{iso} (Å^2)	0.0008(2)	0.0006(2)	0.0006
Mn1	y	0.2100(5)	0.2099(6)	0.224(1)
	m_y (μ_B)	3.83(2)	--	--
	U_{iso} (Å^2)	0.0008(2)	0.0006(2)	0.0006
O1	x	0.0978(2)	0.0982(2)	0.090(2)
	y	0.1734(3)	0.1725(4)	0.196(4)
	z	0.5807(2)	0.5803(2)	0.571(2)
O2	x	0.1462(2)	0.1456(2)	0.152(3)
	y	0.5687(2)	0.5702(3)	0.552(4)
	z	0.3670(2)	0.3675(2)	0.375(3)
O3	x	0.3535(2)	0.3535(2)	0.351(3)
	y	0.5463(3)	0.5465(3)	0.539(4)
	z	0.1636(2)	0.1641(2)	0.162(2)
	U_{iso} (Å^2)	0.0048(2)	0.0043(2)	0.0043
Mn1-O (Å)		2.185(1)	2.193(2)	2.23(2)
		1.916(2)	1.910(3)	1.99(2)
		1.974(3)	1.974(3)	2.02(2)
Mn1-BVS		3.06	3.07	2.60
Mn2-O (Å)		1.930(1)	1.927(2)	1.91(2)
		2.228(1)	2.235(2)	2.11(2)
		1.936(2)	1.939(2)	1.95(2)
Mn2-BVS		3.07	3.06	3.30
R_{wp} (%)		2.25	2.51	3.13
χ^2		1.71	1.43	1.96

[a] GEM NPD data. [b] D8 XRD data. For the monoclinic structure model atom positions are Bi, 8*f*, (x, y, z); Mn1, 4*e*, (0, y, ¾); Mn2, 4*d*, (¼,¼, ½); O, 8*f*, (x, y, z) in space group *C*2/*c* (No. 15). R_{wp} values for 150 and 20 K data are total R_{wp} for 5 histograms (GEM detector banks 1-5) refined simultaneously. The magnetic component m_y for Mn1 and Mn2 at 20 K were constrained to be the same. The isotropic thermal factors of Bi/Mn and oxygen were constrained separately at 20 and 150 K, while the U_{iso} values of 300 K were adopted from 150 K data without refining.

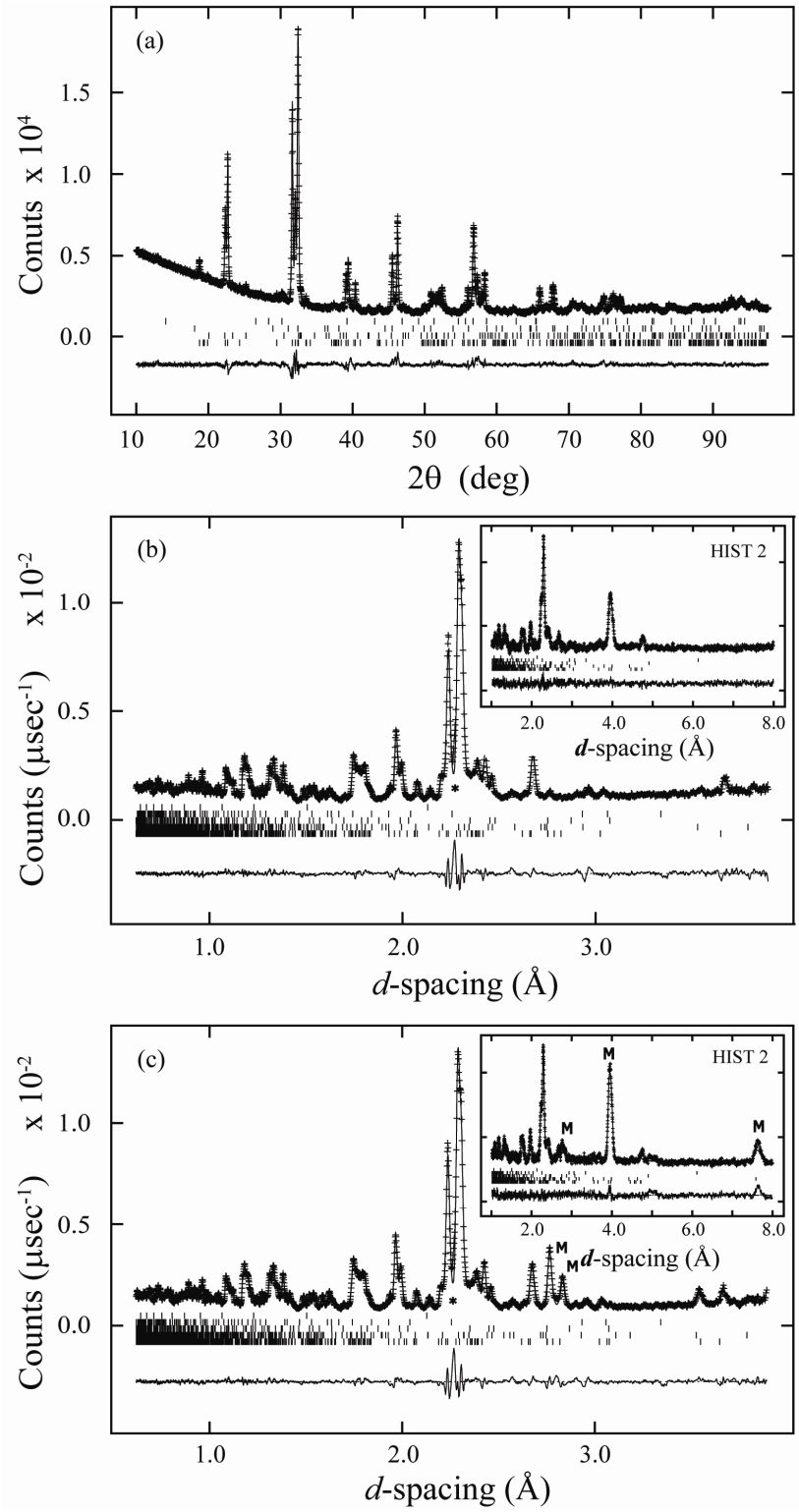

Figure 4.3 The Rietveld fits of $Bi_{0.9}La_{0.1}MnO_3$ for (a) D8 XRD pattern at room temperature, (b) GEM NPD pattern from bank 4 and 2 (inset) at 150 K and (c) GEM NPD pattern from bank 4 and 2 (inset) at 20 K, the magnetic reflections are marked by "M". The index markers from the bottom represent the reflections of $Bi_{0.9}La_{0.1}MnO_3$ (90(2) %), Bi/$LaMnO_3$ orthorhombic phase (5.0(2) %), Mn_3O_4 (1.1(1) %), α-Bi_2O_3 (4.1(1) %), and V container (GEM data only), respectively.

Table 4.3 Refinement results for $Bi_{0.9}La_{0.1}MnO_3$ fits at 300 K, 150 K and 20 K. Lattice parameters, cell volume, atom positions, isotropic thermal factors, magnetic moments, refinement reliability R_{wp} and χ^2 and selected bond distances, and BVS results from the refinements are listed.

$Bi_{0.9}La_{0.1}MnO_3$		20 K[a]	150 K[a]	300 K[b]
a (Å)		9.542(2)	9.547(2)	9.5508(3)
b (Å)		5.5846(9)	5.588(1)	5.5913(2)
c (Å)		9.840(2)	9.850(2)	9.8513(3)
β (º)		110.507(2)	110.566(2)	110.615(2)
V (Å^3)		491.1(2)	492.0(3)	492.39(3)
Bi/ La	x	0.1356(2)	0.1358(2)	0.1340(2)
	y	0.2224(2)	0.2236(2)	0.2248(3)
	z	0.1283(2)	0.1284(2)	0.1264(4)
	U_{iso} (Å^2)	0.0016(2)	0.0038(3)	0.0038
Mn1	y	0.2213(7)	0.2198(7)	0.300(2)
	m_y (μ_B)	3.73(2)	--	--
	U_{iso} (Å^2)	0.0019(4)	0.0022(5)	0.0022
O1	x	0.0938(2)	0.0949(3)	0.099(3)
	y	0.1816(4)	0.1812(5)	0.187(3)
	z	0.5806(2)	0.5810(2)	0.595(2)
O2	x	0.1464(2)	0.1465(2)	0.158(3)
	y	0.5585(3)	0.5590(3)	0.558(4)
	z	0.3661(2)	0.3656(3)	0.386(3)
O3	x	0.3552(3)	0.3558(3)	0.369(3)
	y	0.5420(4)	0.5434(4)	0.567(4)
	z	0.1633(3)	0.1636(3)	0.165(2)
	U_{iso} (Å^2)	0.0072(1)	0.0093(3)	0.0093
Mn1-O (Å)		2.162(2)	2.167(2)	2.07(2)
		1.911(3)	1.913(3)	1.95(2)
		1.993(4)	1.990(4)	2.07(2)
Mn1-BVS		3.07	3.06	2.90
Mn2-O (Å)		1.956(2)	1.951(2)	2.01(3)
		2.184(2)	2.189(2)	2.17(2)
		1.952(2)	1.951(3)	1.92(2)
Mn2-BVS		3.00	3.01	3.00
R_{wp} (%)		5.68	5.41	4.09
χ^2		5.65	4.95	4.06

[a] GEM NPD data. [b] D8 XRD data. For the monoclinic structure model atom positions are Bi, 8*f*, (x, y, z); Mn1, 4*e*, (0, y, ¾); Mn2, 4*d*, (¼,¼, ½); O, 8*f*, (x, y, z) in space group *C*2/*c* (No. 15). R_{wp} values for 150 and 20 K data are total R_{wp} for 5 histograms (GEM detector banks 1-5) refined simultaneously. The magnetic component m_y for Mn1 and Mn2 at 20 K were constrained to be the same. The isotropic thermal factors of Bi/Mn and oxygen were constrained separately at 20 and 150 K, while the U_{iso} values of 300 K were adopted from 150 K data without refining.

Consistent with $BiMnO_3$, no phase transition was observed for the low temperature GEM data of $Bi_{0.9}La_{0.1}MnO_3$, therefore the *C*2/*c* model was also used for the low temperature refinements. A second (Bi/La)MnO_3 phase, which was fixed with the same composition as the main phase for refinement, exists in the material and can be indexed with an orthorhombic *Pnma* structure, showing the weight fraction 4.96 % from the refinement. Two minor phases were observed and can be indexed as Mn_3O_4 and α-Bi_2O_3 with the weight fractions 1.12 % and 4.06 %, respectively. The shrinkage of the unit cell with decreasing temperature and the Jahn-Teller distortion in MnO_6 octahedron can be found as observed in the $BiMnO_3$ sample.

Compared to the x = 1.0 and 0.9 samples in $Bi_xLa_{1-x}MnO_3$, $Bi_{0.8}La_{0.2}MnO_3$ has a very different diffraction profile, which is more similar to those observed for $LaMnO_3$. The orthorhombic structure of $LaMnO_3$ was hence used as an initial model, with atomic positions Bi/La, 4*c*, (x, ¼, z); Mn, 4*b*, (0, 0, ½); O1, 4*c*, (x, ¼, z); O2, 8*d*, (x, y, z) in space group *Pnma* (No. 62)[16]. The structure was fitted with lattice parameters a = 5.8648(1) Å, b = 7.6128(2) Å, c = 5.4548(1) Å showing an *O′*-type orthorhombic relationship ($b/\sqrt{2} < c < a$). The Rietveld fits are shown in Figure 4.4 and the refinements results are listed in Table 4.4.

When the temperature was decreased to 20 K, no splittings or superlattice peaks (except those from the magnetic superstructure described later) were observed, indicating that no structural phase transition has occurred (Figure 4.4 (b) and (c)). Therefore the same space group was used for the low temperature refinements. A second (Bi/La)MnO_3 phase, which was fixed to have the same composition as the main phase for refinement, is present and is indexed with the monoclinic *C*2/*c* structure, showing the weight fraction 10.3(3) % from the refinement. As in the previous cases two minor phases were observed which can be indexed as Mn_3O_4 and α-Bi_2O_3 with weight fractions of 2.8(1) % and 1.6(1) %, respectively. M-O distances (Table 4.4) indicated Jahn-Teller distorted MnO_6 octahedra in the sample.

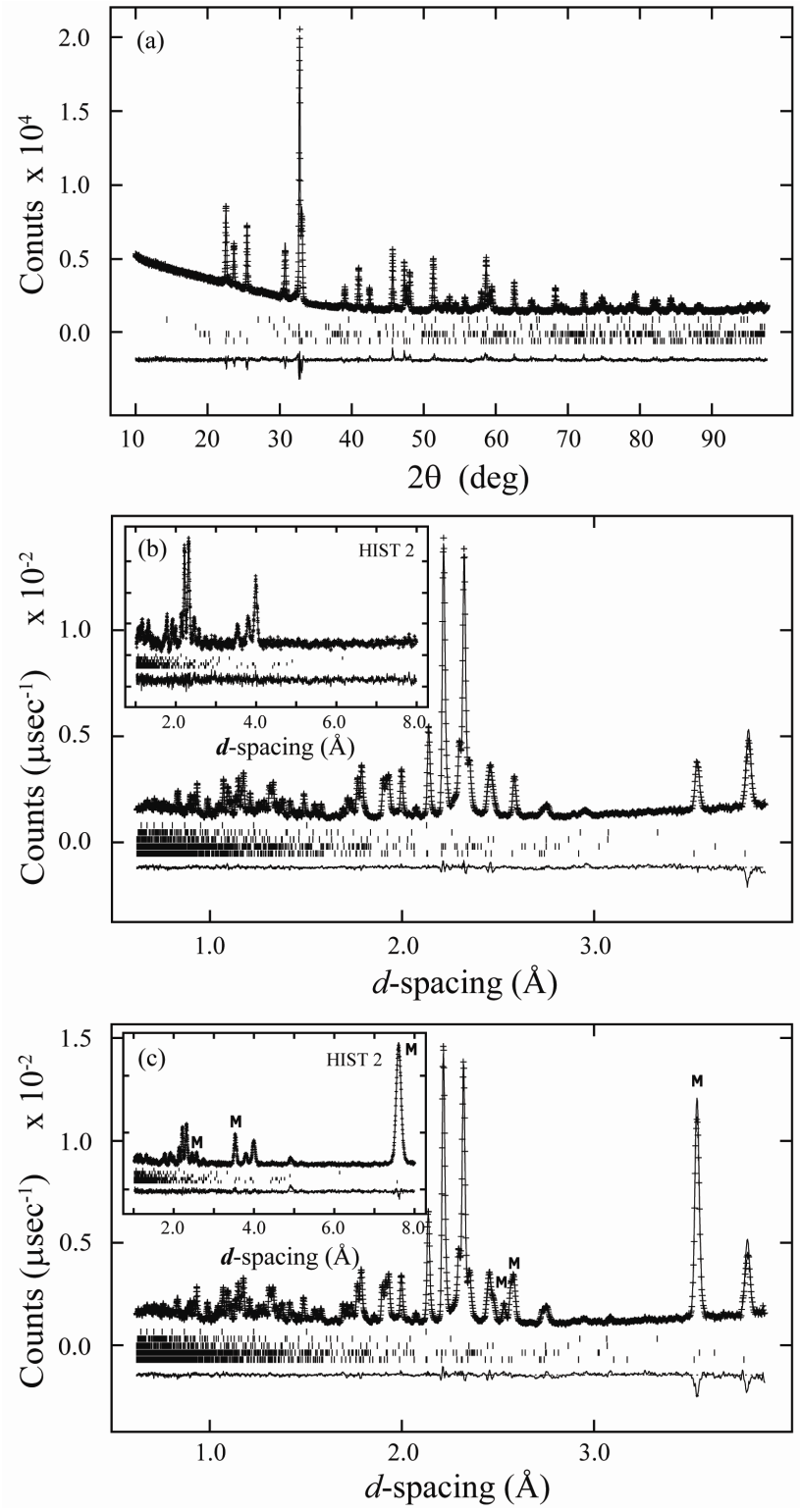

Figure 4.4 The Rietveld fits of $Bi_{0.8}La_{0.2}MnO_3$ for (a) D8 XRD pattern at room temperature, (b) GEM NPD pattern from bank 4 and 2 (inset) at 150 K and (c) GEM NPD pattern from bank 4 and 2 (inset) at 20 K, while the magnetic reflections are marked by "M". The index markers from the bottom represent the reflections of $Bi_{0.8}La_{0.2}MnO_3$ (85(2) %), Bi/$LaMnO_3$ monoclinic phase (10.3(3) %), Mn_3O_4 (2.8(1) %), α-Bi_2O_3 (1.6(1) %), and V container (GEM data only), respectively.

Table 4.4 Refinement results for $Bi_{0.8}La_{0.2}MnO_3$ orthorhombic fits at 300 K, 150 K and 20 K. Lattice parameters, cell volume, atom positions, isotropic thermal factors, magnetic moments, refinement reliability R_{wp} and χ^2 and selected bond distances, and BVS results from the refinements are listed.

$Bi_{0.8}La_{0.2}MnO_3$		20 K[a]	150 K[a]	300 K[b]
a (Å)		5.8578(4)	5.8618(4)	5.8648(1)
b (Å)		7.5877(5)	7.5977(5)	7.6128(2)
c (Å)		5.4508(4)	5.4466(4)	5.4548(1)
V (Å^3)		242.27(5)	242.57(5)	243.55(1)
Bi/ La	x	-0.0656(1)	-0.0657(1)	-0.0668(2)
	z	0.9935(2)	0.9929(1)	0.9952(7)
	U_{iso} (Å^2)	0.0079(2)	0.0078(2)	0.0078
Mn	m_x (μ_B)	3.89(1)	--	--
	U_{iso} (Å^2)	0.0010(2)	0.0017(2)	0.0017
O1	x	0.5253(2)	0.5244(1)	0.518(2)
	z	0.0843(2)	0.0856(2)	0.078(2)
O2	x	0.1838(1)	0.1822(1)	0.198(2)
	y	0.0401(1)	0.0401(1)	0.039(2)
	z	0.7857(1)	0.7861(1)	0.784(2)
	U_{iso} (Å^2)	0.0059(2)	0.0063(1)	0.0063
Mn-O (Å)		1.9574(3)	1.9610(2)	1.953(3)
		1.9177(8)	1.9135(7)	1.96(1)
		2.2107(8)	2.2184(7)	2.15(1)
Mn-BVS		3.07	3.06	3.05
Mn-O1-Mn (º)		151.45(5)	151.21(5)	154.2(8)
Mn-O2-Mn (º)		151.35(4)	150.98(3)	154.5(6)
R_{wp} (%)		3.60	2.97	3.74
χ^2		2.61	2.07	3.18

[a] GEM NPD data. [b] D8 XRD data. For the orthorhombic structure model atom positions are Bi/La, 4*c*, (x, ¼, z); Mn, 4*b*, (0, 0, ½); O1, 4*c*, (x, ¼, z); O2, 8*d*, (x, y, z) in space group *Pnma* (No. 62). R_{wp} values for 20 K and 150 K data are total R_{wp} for 5 histograms (GEM detector banks 1-5) refined simultaneously. The isotropic thermal factors of Bi/Mn and oxygen were constrained separately at 20 and 150 K, while the U_{iso} values of 300 K were adopted from 150 K data without refining.

4.3.2 Magnetic Structures

The 20 K neutron powder diffraction data of $BiMnO_3$ did not show any extra peaks compared with the data taken at 150 K although the intensities of some peaks at low *d*-spacing showed additional intensities of magnetic origin. The superposition of the magnetic reflections and nuclear peaks indicates that the magnetic ordering is of ferromagnetic type, the magnetic transition occurring between 150 and 20 K (Figure 4.2(b) and (c)). In the refinement of the magnetic structure at 20 K the magnetic components of two crystallographic Mn^{3+} sites were constrained to be the same, resulting in refined moments of 3.77(2) μ_B along the *b* axis. This value is slightly smaller than the fully aligned spin value of 4 μ_B for Mn^{3+} ($3d^4$). The nuclear structure and the magnetic ordering of $BiMnO_3$ are illustrated at Figure 4.5.

The $Bi_{0.9}La_{0.1}MnO_3$ material exhibits similar behaviour to the $BiMnO_3$ sample, showing the superposition of the magnetic reflections on nuclear peaks below the transition temperature (Figure 4.3 (b) and (c)). However an extra peak at *d*-spacing ~ 7.6 Å, which was not observed in $BiMnO_3$ and is not indexed by the *C*2/*c* structure model, indicating that either a different magnetic model is required or that the contribution was from another phase. The attempts to index the extra peak by a superstructure of the main phase were not successful, implying that the $Bi_{0.9}La_{0.1}MnO_3$ phase is not responsible for the reflection. A magnetic model for the orthorhombic (Bi/La)MnO_3 minor phase was found to best account for the additional reflection. The proposed magnetic model agreed with the observed profiles, although the contribution of the pronounced magnetic reflection from the minor (Bi/La)MnO_3 phase was underestimated, which is possibly due to the difficulty of refining a phase with a small fraction. The refined magnetic component in $Bi_{0.9}La_{0.1}MnO_3$ material was 3.73(2) μ_B along *b* axis, which is similar to the refined moment of $BiMnO_3$.

The diffraction profile of $Bi_{0.8}La_{0.2}MnO_3$ at 20 K exhibits a very intense reflection at *d*-spacing ~7.6 Å and also other extra peaks, which were not observed in the 150 K NPD pattern (Figure 4.4 (b) and (c)). These extra reflections cannot be indexed by the nuclear structure *Pnma*, indicating that $Bi_{0.8}La_{0.2}MnO_3$ has a superlattice of magnetic ordering, which is consistent with $LaMnO_3$. The additional

low temperature peaks can be described well by an *A*-type antiferromagnetic structure with a magnetic group $Pn'ma'$[16], where the spins are ordered ferromagnetically in the *ac* plane and antiferromagnetically along the *b* axis. The nuclear structure and the magnetic ordering are illustrated at Figure 4.6. The refined

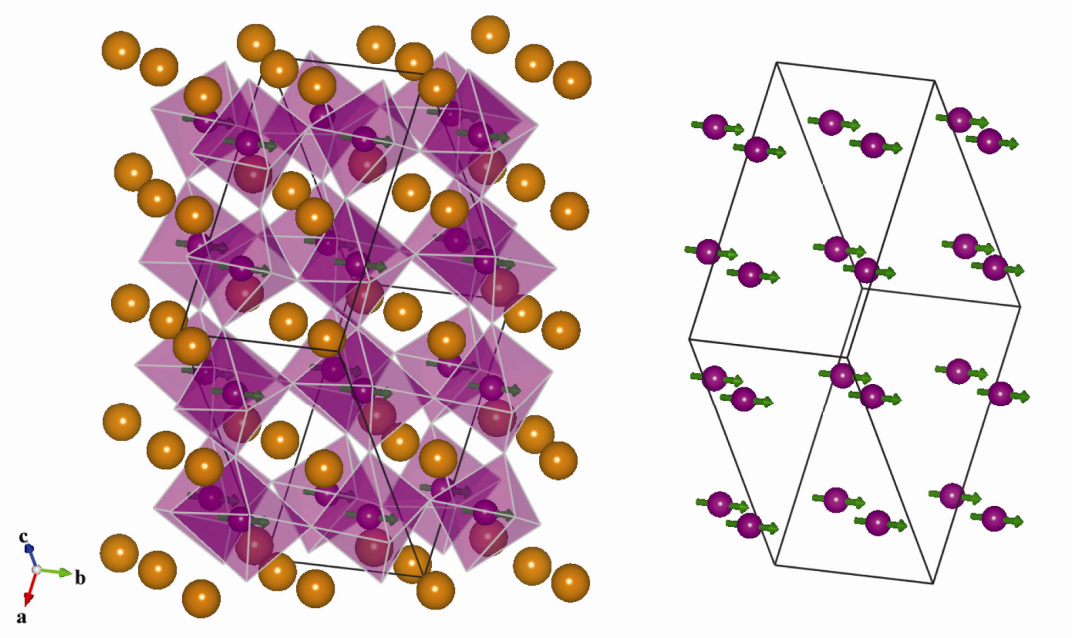

Figure 4.5 The crystal structure and ferromagnetic ordering of $BiMnO_3$ and $Bi_{0.9}La_{0.1}MnO_3$. The arrows show the magnetic moment along *b* axis.

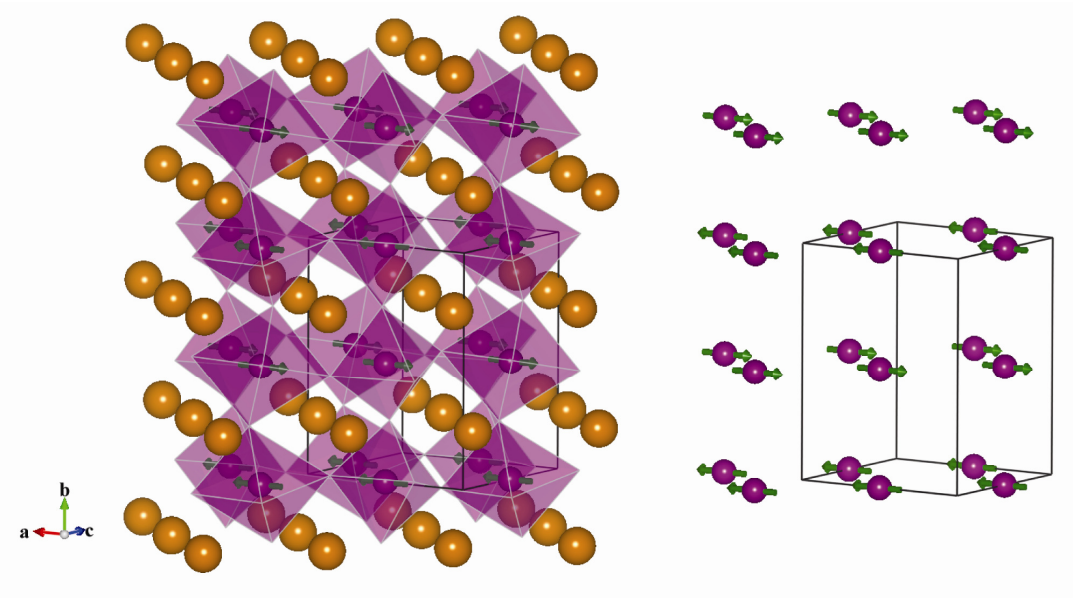

Figure 4.6 The crystal structure and antiferromagnetic ordering of $Bi_{0.8}La_{0.2}MnO_3$.

magnetic moments of Mn^{3+} cation were 3.89(1) μ_B at 20 K along *a* axis, which is higher than the reported value of 3.65(3) μ_B for $LaMnO_3$ at 14 K[16] or 3.87(3) μ_B at 1.4 K[26].

4.3.3 Magnetisation Properties

The zero-field-cooled (ZFC) and field-cooled (FC) temperature-dependent magnetisation curves from 5 K to 300 K with an applied field of 100 Oe are shown in Figure 4.7. It can be observed that the x = 1.0 and 0.9 compounds of the $Bi_xLa_{1-x}MnO_3$ series show typical ferromagnetic behaviour with a pronounced divergence of the FC and ZFC curves around 100 and 90 K, respectively. The observed transition temperature T_C = 101 K for $BiMnO_3$ is comparable to the previously reported values of 99 - 105 K[8]. The ferromagnetic ordering temperature T_C is reduced upon doping to 94 K for $Bi_{0.9}La_{0.1}MnO_3$. As shown in Figure 4.7 the inverse of the magnetic susceptibility above T_C can be fitted with a Curie-Weiss law. The fitted Curie and Weiss constants for $BiMnO_3$ are C = 3.53 $cm^3 \cdot K \cdot mol^{-1}$ and θ = 114 K respectively, giving the effective magnetic moment μ_{eff} = 5.32 μ_B per Mn^{3+} for the paramagnetic region. In comparison, the $Bi_{0.9}La_{0.1}MnO_3$ material has C = 3.12 $cm^3 \cdot K \cdot mol^{-1}$ and θ = 110 K, corresponding to a slightly smaller effective magnetic moment of μ_{eff} = 5.00 μ_B.

By contrast, a cusp at ~80 K was found in the ZFC curve of the $Bi_{0.8}La_{0.2}MnO_3$ sample, which is similar to the reported magnetic behaviour of $LaMnO_3$[27]. The noticeable strong divergence between the FC and the ZFC curves below the critical temperature indicates the presence of ferromagnetic contributions in this compound. From the fit of the high temperature magnetisation data to the Curie-Weiss equation the following parameters were obtained: C = 3.28 $cm^3 \cdot K \cdot mol^{-1}$ and θ = 41 K, giving the effective magnetic moment μ_{eff} = 5.13 μ_B.

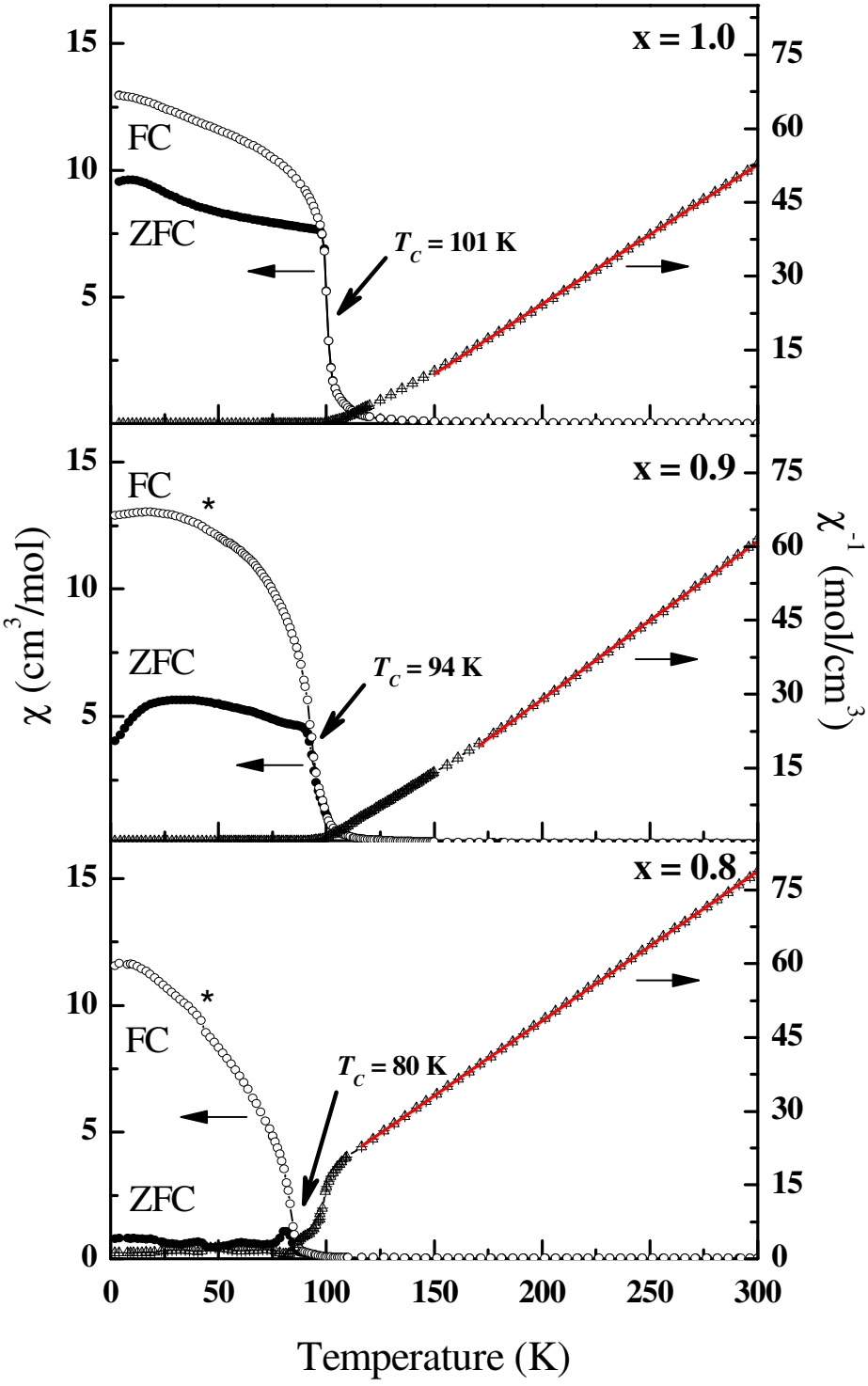

Figure 4.7 The temperature-dependent magnetisation (ZFC and FC) and inverse magnetic susceptibility (ZFC) plots measured from 5 to 300 K in a field of 100 Oe of $Bi_xLa_{1-x}MnO_3$ series. The transition of minor Mn_3O_4 phase was marked by asterisk.

The field-dependent magnetisation data for -70 to 70 kOe at 5 K for all samples is shown in Figure 4.8. A very small hysteresis was observed for the x = 1.0 sample with the coercive field (H_c) ~ 30 Oe and the remnant magnetisation (M_r) ~ 0.07 μ_B per Mn^{3+} cation, while for $Bi_{0.9}La_{0.1}MnO_3$ a wider hysteresis with H_c ~ 120 Oe and M_r ~ 0.26 μ_B per Mn^{3+} cation was observed. The hysteresis loops showed saturated magnetic moments of 3.67 and 3.17 μ_B at high field for the samples with x = 1.0 and 0.9, respectively, which are close to the ideal value of 4 μ_B for Mn^{3+} but smaller than the moments obtained from NPD refinements at 20 K. The hysteresis behaviour of $Bi_{0.8}La_{0.2}MnO_3$ indicates there is a substantial ferromagnetic contribution, in which the parameters obtained from the curves are H_c ~ 350 Oe and M_r ~ 0.24 μ_B. The saturation magnetisation take from the field dependence of the magnetisation is 0.97 μ_B, this is far from the expected 4 μ_B for an ideally ferromagnet but typical of weak ferromagnetic samples where antiferromagnetic interactions are dominant.

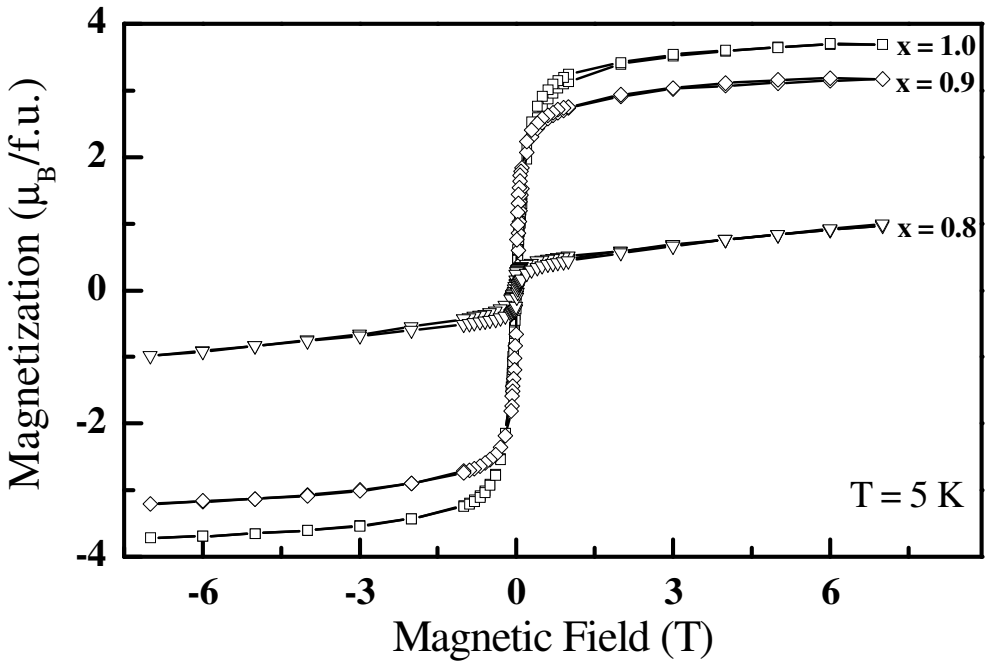

Figure 4.8 The field-dependent magnetisation at 5 K for $Bi_xLa_{1-x}MnO_3$ series with a field range from -70 to 70 kOe at 5 K.

4.4 Discussion

The compounds with x = 0.8, 0.9 and 1.0 of the $Bi_xLa_{1x}MnO_3$ solid solution have been successfully synthesised by high-pressure techniques. The oxygen stoichiometry of $BiMnO_3$ has been confirmed from the refinement of neutron data. The material has the *C2/c* crystal structure and shows ferromagnetic behaviour with a Curie temperature of T_C = 101 K, which is consistent with reported information[7,8].

The x = 0.9 sample has been reported to have a monoclinic structure and two-phase magnetic states, but there was a lack of detailed information. The obtained $Bi_{0.9}La_{0.1}MnO_3$ is fairly similar from a structural and magnetic point of view to the parent $BiMnO_3$ compound. It can also be described by the monoclinic space group *C2/c* and also shows ferromagnetic behaviour at low temperatures. A small lattice volume shrinkage was found for the x = 0.9 sample compared to the undoped $BiMnO_3$, which is due to the slight discrepancy between the ionic radii of La^{3+} and Bi^{3+}. This also indicates that the La^{3+} ions have entered into the crystal lattice. The symmetry of the structure remains unchanged with slight La doping, indicating the absence of Mn^{4+}, which has a considerably smaller ionic radius and would be likely to cause a structural transition of the material. Moreover, the similar magnetic behaviour implies no Mn^{4+} in the material, since distinct magnetic behaviour can be caused by this different electronic state. A comparable ferromagnetic ordering to $BiMnO_3$ was observed for the x = 0.9 sample, and the transition temperature T_C = 94 K was obtained from the magnetic susceptibility measurement.

In contrast, $Bi_{0.8}La_{0.2}MnO_3$ possesses an orthorhombic structure. This means that there is a structural transition as a result of the substitution at the *A* site. It has been reported that the oxygen content in the material plays a key role to the lattice structure from the x = 0.4 - 0.6 materials in the series[21]. The materials have an *O*-type orthorhombic lattice ($b/\sqrt{2} \approx c \approx a$) with excess oxygen content, and an *O'*-type orthorhombic lattice ($b/\sqrt{2} < c < a$) when the oxygen content is stoichiometric. The lattice parameters of $Bi_{0.8}La_{0.2}MnO_3$ in this work follow the *O'*-type orthorhombic lattice relationship, indicating the samples are oxygen stoichiometric.

Not only does the structure change drastically between x = 0.9 to 0.8, but the characteristic ferromagnetic ordering of $BiMnO_3$ is also lost with the increased La doping level. Although the two-phase magnetic states was reported[20], the x = 0.8 material is characterised to be an orbitally ordered *A*-type antiferromagnet, showing weak ferromagnetism as observed in $LaMnO_3$[16,21]. From the magnetic susceptibility measurement T_C = 80 K was obtained, which is in agreement with the $Bi_xLa_{1-x}MnO_3$ series[20], while $LaMnO_3$ has a transition temperature of 140 K[16].

The obtained Curie constant for $Bi_{0.8}La_{0.2}MnO_3$ is 3.28 $cm^3 \cdot K \cdot mol^{-1}$. The Curie constant corresponds to the effective magnetic moment μ_{eff} = 5.13 μ_B, which is close to the spin-only effective magnetic moment for Mn^{3+} (d^4, S = 2) μ_{eff} = 4.90 μ_B. The fitted Weiss constant θ is 41 K. The obtained values are comparable with reported single-crystal $LaMnO_3$: C = 3.41 $cm^3 \cdot K \cdot mol^{-1}$, θ = 52 K and μ_{eff} = 5.22 μ_B[28].

In $Bi_xLa_{1-x}MnO_3$ solid solutions, both the nuclear structure and the magnetic properties are affected by the substitution of bismuth by lanthanum. Amounts up to 10% of La in the Bi position seem to slightly affect the structure and magnetism but for La contents higher than 10% the ferromagnetism is destroyed and the crystal structure becomes less distorted. As a consequence, $Bi_{0.8}La_{0.2}MnO_3$ adopts the crystal structure and exhibits the magnetic properties of the end member of the solid solution, $LaMnO_3$ (orthorhombic and A-type antiferromagnetic).

A recent investigation of $Bi_{0.9}La_{0.1}MnO_3$ thin films demonstrated multiferroic properties[22-24]. The Bi-site deficiency was reported to be responsible for the exhibited ferromagnetism due to the induced Mn^{4+} in the films. However in the bulk $Bi_{0.9}La_{0.1}MnO_3$ and $Bi_{0.8}La_{0.2}MnO_3$ materials prepared in this work neither bismuth deficiency nor oxygen non-stoichiometry was observed, hence no Mn^{4+} cations are introduced into the material. Further comparisons of the obtained bulk materials with thin films are needed.

In summary, the bismuth-rich $Bi_xLa_{1-x}MnO_3$ materials were synthesised by HTHP techniques and the stoichiometric oxygen content was confirmed. For samples with bismuth content x = 1.0 and 0.9 a highly distorted perovskite structure with a space group *C2/c* was adopted and ferromagnetic behaviour was observed. In

contrast, $Bi_{0.8}La_{0.2}MnO_3$ showed an *O′*-type orthorhombic structure with space group *Pnma*. *A*-type antiferromagnetic ordering at low temperature was observed, which is comparable with stoichiometric $LaMnO_3$. The impedance and ferroelectricity measurements of the synthesised materials will be conducted in the near future to investigate their multiferroic properties.

4.5 References

1. S. Jin, T. H. Tiefel, M. McCormack, R. A. Fastnacht, R. Ramesh, and L. H. Chen, *Science,* **264**, 413 (1994).
2. G. H. Jonker and J. H. Van Santen, *Physica,* **16**, 337 (1950).
3. F. Sugawara, S. Iiida, Y. Syono, and S.-i. Akimoto, *J. Phys. Soc. Jpn.,* **25**, 1553 (1968).
4. A. Moreira dos Santos, S. Parashar, A. R. Raju, Y. S. Zhao, A. K. Cheetham, and C. N. R. Rao, *Solid State Commun.,* **122**, 49 (2002).
5. H. Faqir, H. Chiba, M. Kikuchi, Y. Syono, M. Mansori, P. Satre, and A. Sebaoun, *J. Solid State Chem.,* **142**, 113 (1999).
6. A. Moreira dos Santos, A. K. Cheetham, T. Atou, Y. Syono, Y. Yamaguchi, K. Ohoyama, H. Chiba, and C. N. R. Rao, *Phys. Rev. B,* **66**, 064425 (2002).
7. E. Montanari, G. Calestani, L. Righi, E. Gilioli, F. Bolzoni, K. S. Knight, and P. G. Radaelli, *Phys. Rev. B,* **75**, 220101 (2007).
8. A. A. Belik, S. Iikubo, T. Yokosawa, K. Kodama, N. Igawa, S. Shamoto, M. Azuma, M. Takano, K. Kimoto, Y. Matsui, and E. Takayama-Muromachi, *J. Am. Chem. Soc.,* **129**, 971 (2007).
9. H. Woo, T. A. Tyson, M. Croft, S. W. Cheong, and J. C. Woicik, *Phys. Rev. B,* **63**, 134412 (2001).
10. J. L. García-Muñoz, C. Frontera, M. A. G. Aranda, A. Llobet, and C. Ritter, *Phys. Rev. B,* **63**, 064415 (2001).
11. E. O. Wollan and W. C. Koehler, *Phys. Rev.,* **100**, 545 (1955).
12. P. Schiffer, A. P. Ramirez, W. Bao, and S. W. Cheong, *Phys. Rev. Lett.,* **75**, 3336 (1995).
13. A. Urushibara, Y. Moritomo, T. Arima, A. Asamitsu, G. Kido, and Y. Tokura, *Phys. Rev. B,* **51**, 14103 (1995).
14. P. G. de Gennes, *Phys. Rev.,* **118**, 141 (1960).

15. J. Töpfer and J. B. Goodenough, *J. Solid State Chem.,* **130**, 117 (1997).
16. Q. Huang, A. Santoro, J. W. Lynn, R. W. Erwin, J. A. Borchers, J. L. Peng, and R. L. Greene, *Phys. Rev. B,* **55**, 14987 (1997).
17. R. Shannon, *Acta Crystallogr. Sect. A,* **32**, 751 (1976).
18. Y. D. Zhao, J. Park, R. J. Jung, H. J. Noh, and S. J. Oh, *J. Magn. Magn. Mater.,* **280**, 404 (2004).
19. T. Ogawa, H. Shindo, H. Takeuchi, and Y. Koizumi, *Jpn. J. Appl. Phys.,* **45**, 8666 (2006).
20. I. O. Troyanchuk, O. S. Mantytskaja, H. Szymczak, and M. Y. Shvedun, *Low Temp. Phys.,* **28**, 569 (2002).
21. V. Khomchenko, I. Troyanchuk, O. Mantytskaya, M. Tovar, and H. Szymczak, *J. Exp. Theor. Phys.,* **103**, 54 (2006).
22. M. Gajek, M. Bibes, A. Barthelemy, M. Varela, and J. Fontcuberta, *J. Appl. Phys.,* **97**, 103909 (2005).
23. M. Gajek, M. Bibes, S. Fusil, K. Bouzehouane, J. Fontcuberta, A. Barthelemy, and A. Fert, *Nat. Mater.,* **6**, 296 (2007).
24. M. Gajek, M. Bibes, F. Wyczisk, M. Varela, J. Fontcuberta, and A. Barthelemy, *Phys. Rev. B,* **75**, 174417 (2007).
25. G. Matsumoto, *J. Phys. Soc. Jpn.,* **29**, 606 (1970).
26. F. Moussa, M. Hennion, J. Rodriguez-Carvajal, H. Moudden, L. Pinsard, and A. Revcolevschi, *Phys. Rev. B,* **54**, 15149 (1996).
27. V. Skumryev, F. Ott, J. M. D. Coey, A. Anane, J. P. Renard, L. Pinsard-Gaudart, and A. Revcolevschi, *Eur. Phys. J. B,* **11**, 401 (1999).
28. J. S. Zhou and J. B. Goodenough, *Phys. Rev. B,* **60**, R15002 (1999).

Chapter 5

Charge Disproportionation and Charge Transfer in $BiNiO_3$ Perovskite

5.1 Introduction

Transition metal oxide perovskites exhibit a wide variety of fascinating electronic and magnetic phenomena such as ferromagnetism, spin-glass like behaviour, superconductivity and colossal magnetoresistance (CMR). The rare earth nickelate perovskite RNiO$_3$ family has unusual properties for a metal oxide, in that they exhibit metallic behaviour. Due to this behaviour, the relationship between conductivity and crystal structure has been widely studied[1-3]. Excepting LaNiO$_3$, which shows rhombohedral structure and metallic character down to 1.5 K, a metal-insulator transition is found in all RNiO$_3$ compounds. The transition temperature T_{MI} is strongly dependent on the R^{3+} cation[1,2], as shown in Figure 5.1. Orthorhombic distorted structures with *Pbnm* symmetry are observed for RNiO$_3$ materials above the T_{MI} with R^{3+} cation smaller than La^{3+}. With reduction of the size of R cation in the family, the degree of RNiO$_3$ orthorhombicity increases. This results in the superexchange Ni-O-Ni angle becoming smaller and an accompanying systematic increasing of T_{MI} occurs[1,3]. The metal-insulator transition across T_{MI} is usually associated with a structural transition, as observed in RNiO$_3$ with smaller R^{3+} (R = Ho, Y, Er, Lu)[1,4,5]. When the temperature decreases below T_{MI}, a further distortion of the symmetry to $P2_1/n$ is observed. This reduction in symmetry arises from B-site Ni charge disproportionation which results in insulating behaviour. For those RNiO$_3$ materials with a relatively large R^{3+} (R = Pr, Nd, Sm, Eu, Gd, Dy), it was initially reported that the metal-insulator transition resulted in no lowering of the *Pbnm* symmetry[3,6-9]. However, recent synchrotron studies of PrNiO$_3$ revealed that the above-mentioned monoclinic distortion to $P2_1/n$ symmetry should be adopted for the structure below T_{MI}[10,11]. This implies the insulating RNiO$_3$ phases all adopt $P2_1/n$ structure below T_{MI}, while the earlier reported *Pbnm* symmetry of the

insulating phases holds true only due to an approximation of the monoclinic angle to 90° (*e.g.* β = 90.059(2) ° for $PrNiO_3$[11]).

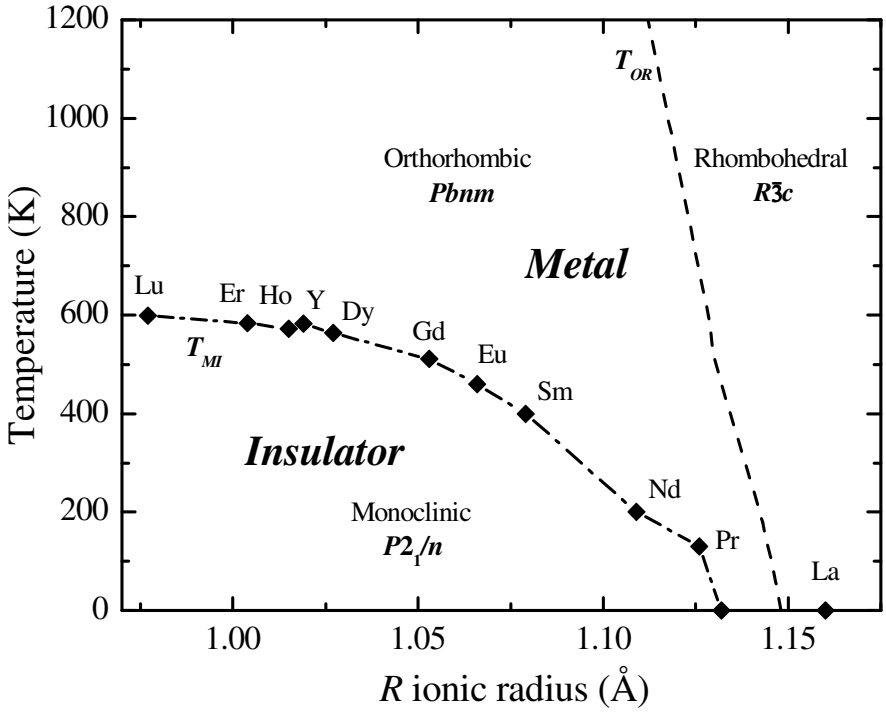

Figure 5.1 The metal-insulator phase diagram of RNiO$_3$ as a function of the ionic radius of rare earth R^{3+}. The figure is adapted from the works of M. L. Medarde and J. B. Torrance *et al.*[1,2].

Considering the rhombohedral structure of metallic $LaNiO_3$ and also the tendency of the RNiO$_3$ family to exhibit high conductivity, a less distorted structure and enhanced metallic behaviour is expected when substituting La^{3+} by the slightly larger Bi^{3+} cation. Bismuth nickelate perovskite $BiNiO_3$, however, exhibits unique behaviours under ambient pressure[12,13]. Similar to $BiCrO_3$[14], $BiMnO_3$[15], $BiCoO_3$[16] and Bi_2NiMnO_6[17] materials, $BiNiO_3$ requires high-pressure and high-temperature synthesis conditions[12]. However, in contrast to these other bismuth transition metal perovskites, $BiNiO_3$ shows an unusual *A*-site bismuth charge disproportionation to Bi^{3+} and Bi^{5+}[12]. In this charge disproportionation phase, $BiNiO_3$ adopts a triclinic structure with two inequivalent Bi (Bi^{3+}/Bi^{5+}) and four Ni^{2+} sites [12,13]. This is a considerable distortion compared with to the rest of the RNiO$_3$

phases (with both trivalent R^{3+} and Ni^{3+}) that exhibit only rhombohedral or orthorhombic symmetries[3]. As a consequence of the additional charge ordering, $BiNiO_3$ shows insulating behaviour from 300 down to 5 K[13], in contrast to $LaNiO_3$ and $RNiO_3$ which are metallic down to 1.5 K[3] and above T_{MI}[2,3], respectively. Furthermore, $BiNiO_3$ also shows a pressure-induced insulator-metallic transition around 3 GPa[18], and a structural phase transition between 2.1 and 4.7 GPa at room temperature has been observed[19]. The structural transition from the triclinic symmetry to a $GdFeO_3$-type orthorhombic phase entails a reorganisation of the charges to $Bi^{3+}Ni^{3+}O_3$ as evident by the bond valence sum (BVS) calculations[19]. It was concluded that the transition results in the melting of the Bi^{3+}/Bi^{5+} charge disproportionation and also a charge transfer between the Ni and Bi sites. A similar phase change to an orthorhombic structure with metallic behaviour can also be induced by partial La or Pb substitution at the bismuth site[20-22].

In consideration of the possible varieties of Bi and Ni charge distributions in $BiNiO_3$, four distinct electronic ground states of the material have been proposed and they are summarised in Figure 5.2[19]. These states include the ambient Phase I $(Bi^{3+}_{0.5}Bi^{5+}_{0.5})Ni^{2+}O_3$ and also the high pressure Phase III $Bi^{3+}Ni^{3+}O_3$. Since $BiNiO_3$ Phase III displays an orthorhombic metallic phase which is similar to $RNiO_3$ phase above T_{MI}, the appearance of Ni charge disproportionated phase like that observed in $RNiO_3$ family is proposed. This $Bi^{3+}(Ni^{2+}_{0.5}Ni^{4+}_{0.5})O_3$ phase (Phase IV) is expected to

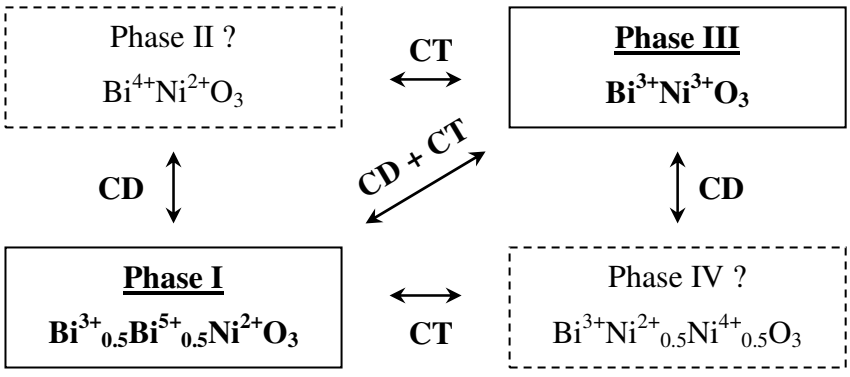

Figure 5.2 Four possible Bi and Ni charge distributions in $BiNiO_3$ material, showing the transitions between phases via intermetallic charge transfer (CT) and/or charge disproportionation (CD)[19].

be observed on cooling of Phase III. A $Bi^{4+}Ni^{2+}O_3$ Phase II is also suggested with the melting of the Bi charge disproportionation in Phase I ($Bi^{3+} + Bi^{5+} \rightarrow 2\ Bi^{4+}$). It has been reported that Bi^{4+} and Ni^{2+} electronic states can be stabilised by Pb doping, resulting in a substituted form $(Bi_{0.8}Pb_{0.2})^{4+}Ni^{2+}O_3$[22] of the bismuth nickel oxide. However pure $BiNiO_3$ Phase II has not been observed under ambient pressure due to decomposition below the transition.

Recent studies of $BiNiO_3$ suggest the existence of different phases which have derived from the known Phases I and III, however the experimental data was insufficient to identify the observed phases. The temperature-dependent conductivity measurements of $BiNiO_3$ under varying pressure revealed a metal-insulator transition below 250 K at 4 GPa, while the transition is suppressed at 5 GPa and no transition is observed above 6 GPa (Figure 5.3)[23]. Although the resultant insulating phase might imply the existence of Ni charge disproportionated Phase IV, the possibility of a transition from Phase III to insulating Phase I cannot be ruled out.

Phase II $Bi^{4+}Ni^{2+}O_3$ is suggested to be present at elevated temperature, however at ambient pressure the material decomposed before the transition occurs. A recent

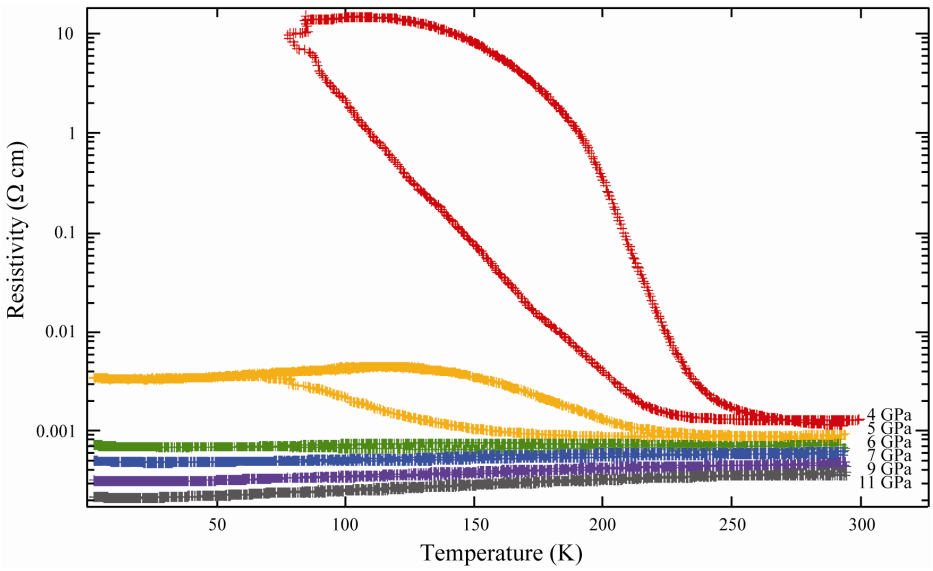

Figure 5.3 The resistivity measurements of $BiNiO_3$ under different pressure applied[23], where an insulating phase takes place below around 250 K under 4 GPa. The same transition is suppressed under 5 GPa and the material remains metallic down to low temperature when pressurised above 6 GPa.

orthorhombic phase at 573 K and 1 GPa[24], demonstrating the suppression of the decomposition with moderate applied pressure (Figure 5.4 (a)). Moreover, the structural transition is accompanied by a change of conductivity (Figure 5.4 (b)), indicating the melting of Phase I Bi charge disproportionation. However whether the obtained orthorhombic phase is Phase II $Bi^{4+}Ni^{2+}O_3$ or Phase III $Bi^{3+}Ni^{3+}O_3$ remained unclear.

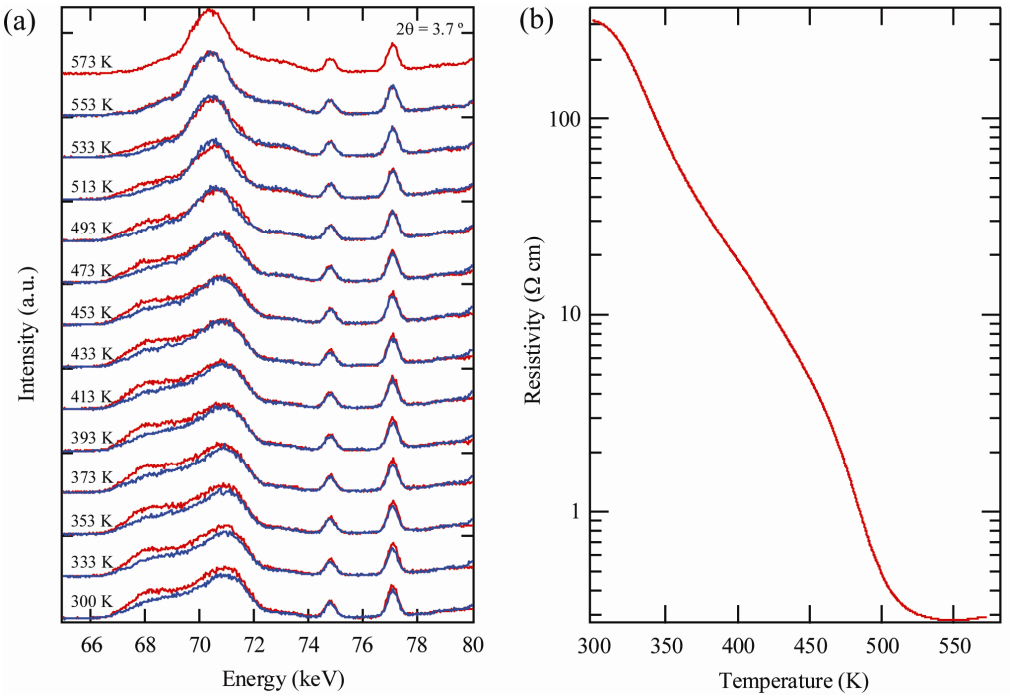

Figure 5.4 Temperature-dependent measurement with applied pressure 1 GPa of (a) energy dispersive SXRD, where the patterns in red and blue represent the measurements with temperature increasing and decreasing, respectively; (b) resistivity of $BiNiO_3$ material[24].

Therefore it is worth exploring different pressure and temperature regions to ascertain whether the suggested electronic states of $BiNiO_3$ exist. The aim of this work is to study both the structure and the charge distribution of observed high pressure low temperature (HPLT) and high temperature (HT) phases of $BiNiO_3$. This has been carried out by neutron diffraction experiments that were performed with various pressure and temperature conditions, in order to investigate not only different $BiNiO_3$ states but also the phase boundary in between them. With the Bi-O and Ni-O bond distances information obtained from neutron diffraction, the valence states of $BiNiO_3$ can be determined using BVS method.

5.2 Experimental

Sample Preparation

High pressure techniques are required to synthesise polycrystalline $BiNiO_3$ samples. The sample used in this study was prepared by Dr. S. Ishiwata at the Institute for Chemical Research, Kyoto University, Japan[12]. Stoichiometric amounts of Bi_2O_3 and Ni were dissolved in nitric acid and heated at 750 °C in air for 12 h as a precursor. The obtained fine powder was mixed with oxidising agent $KClO_4$ with weight ratio of 4:1 and then sealed into a gold capsule. This capsule was then placed in a cubic anvil-type high pressure apparatus under 6 GPa and 1000 °C for 30 minutes. After the treatment the resulting sample was removed from the capsule, ground and washed with distilled water to dissolve the accompanying KCl by-product.

High Pressure Neutron Powder Diffraction at Hi-Pr: PEARL

Time-of-flight (TOF) neutron powder diffraction data was collected on the PEARL High Pressure instrument at the ISIS facility. The sample (~90 mm^3) was loaded into a Paris-Edinburgh cell[25] which provided a high-pressure environment. A pressure transmission medium of methanol/ethanol mixture and a pressure calibrant lead pellet was sealed into the gasket with the sample for low temperature study. A modified gasket with a graphite heater and Ta/Hf metal sheets as temperature probe was used in the high temperature experiment (see 2.2.1.6 for detail). The diffraction data was collected with the transverse geometry of the P-E cell giving access to the scattering angle range 83 ° $\leq 2\theta \leq$ 97 °.

High Pressure Synchrotron Diffraction at BL22XU, SPring-8

The high resolution SPring-8 synchrotron X-ray powder diffraction experiments were carried out by Drs. O. Smirnova and M. Azuma, Kyoto University. The data were collected with a wavelength of 0.49690 Å in the angular range 3.5 ° $\leq 2\theta \leq$ 21.1 ° from room temperature to 50 K under 4.3 GPa.

5.3 Results

5.3.1 Pressure-induced phase transition at 300 K

It has been shown that a room temperature pressure-induced metal-insulator transition of $BiNiO_3$ occurs, accompanied with a structural phase transition from triclinic $P\bar{1}$ to a $GdFeO_3$-type *Pbnm* symmetry at around 3 GPa[18,19]. Previous work has demonstrated the determination of bismuth and nickel valence states by BVS method, showing the transition $(Bi^{3+}_{0.5}Bi^{5+}_{0.5})Ni^{2+}O_3 \rightarrow Bi^{3+}Ni^{3+}O_3$[19]. As phase coexistence is expected around the first order metal-insulator transition, the reported transition pressure can only be taken to be approximate. The precise transition pressure and any phase coexistence have not been observed in previous neutron work.

The sample of $BiNiO_3$ was pressurised up to 5.5 GPa at 300 K (Figure 5.5). The obtained diffraction patterns are similar to the ambient profile during the initial

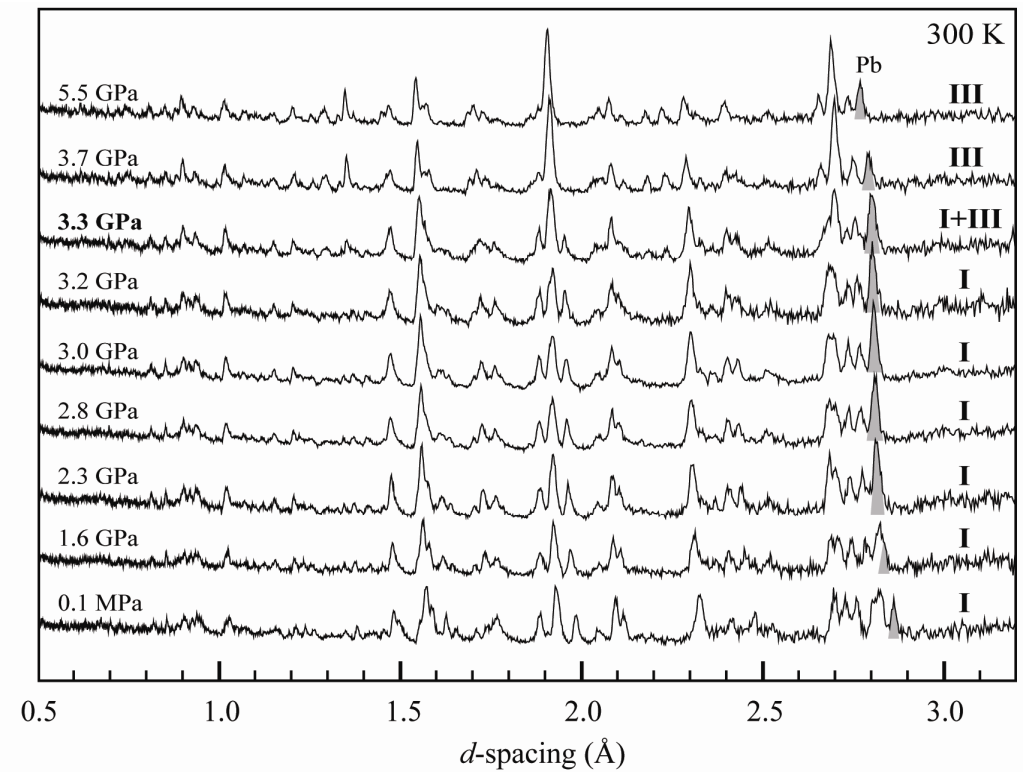

Figure 5.5 Pressure-dependent neutron diffraction data collected at 300 K, showing the pressure induced phase transition where the coexistence of Phase I and III occurs at 3.3 GPa. A shaded peak shows one of the reflections of the lead calibrant.

pressurisation, thus a triclinic structure of space group $P\bar{1}$ (No. 2) with a $\sqrt{2}\times\sqrt{2}\times 2$ superstructure of the primitive cubic perovskite was used for the Phase I refinement[11,18]. The results show that the sample consists of 84 % $BiNiO_3$, 4 % NiO and 12 % Pb (pressure calibrant) by weight, while the small contribution of WC and Ni from the anvils is also taken into account for the fits. $BiNiO_3$ remains Phase I up to 3.2 GPa at room temperature. The Rietveld fit of the pattern at 3.2 GPa is shown in Figure 5.6 (a). The coexistence of two phases was observed when the sample was pressurised to 3.3 GPa, where the ratio of triclinic:orthorhombic phases 72(1) %:28(1) % is obtained from the refinement (Figure 5.6 (b)). It should be noted that the Phase I and III coexistence was also examined for the pattern at 3.2(2) GPa, however the refinement became unstable due to the low fraction obtained for Phase III (~ 1 %), thus the existence of Phase III was not demonstrated in the refinement. A drastic change of the diffraction pattern occurred when $BiNiO_3$ was further pressurised, where a $GdFeO_3$-type *Pbnm* (No. 62) perovskite superstructure is adopted for the high pressure Phase III[18,23]. No evidence of Phase I was found in the 3.7(2) GPa pattern, indicating the completion of the transition to orthorhombic Phase III (Figure 5.6 (c)). Therefore at room temperature the $BiNiO_3$ material remains Phase I up to 3.2 GPa, exhibits a Phase I and III coexistence at 3.3 GPa and transforms to Phase III completely beyond 3.7 GPa. In addition, no intermediate phase was found between the two phases, confirming that the direct first order transition takes place with pressure. The results are in good agreement with previously reported synchrotron X-ray and neutron studies[12,19,20]. The evolution of structure parameters, valence states from BVS results and also phase fractions are plotted in Figure 5.7, showing the pressure-induced phase transition. With these observations it can be concluded that the first order transition between Phase I and III occurs within a rather narrow pressure range of 3.2(2) to 3.7(2) GPa.

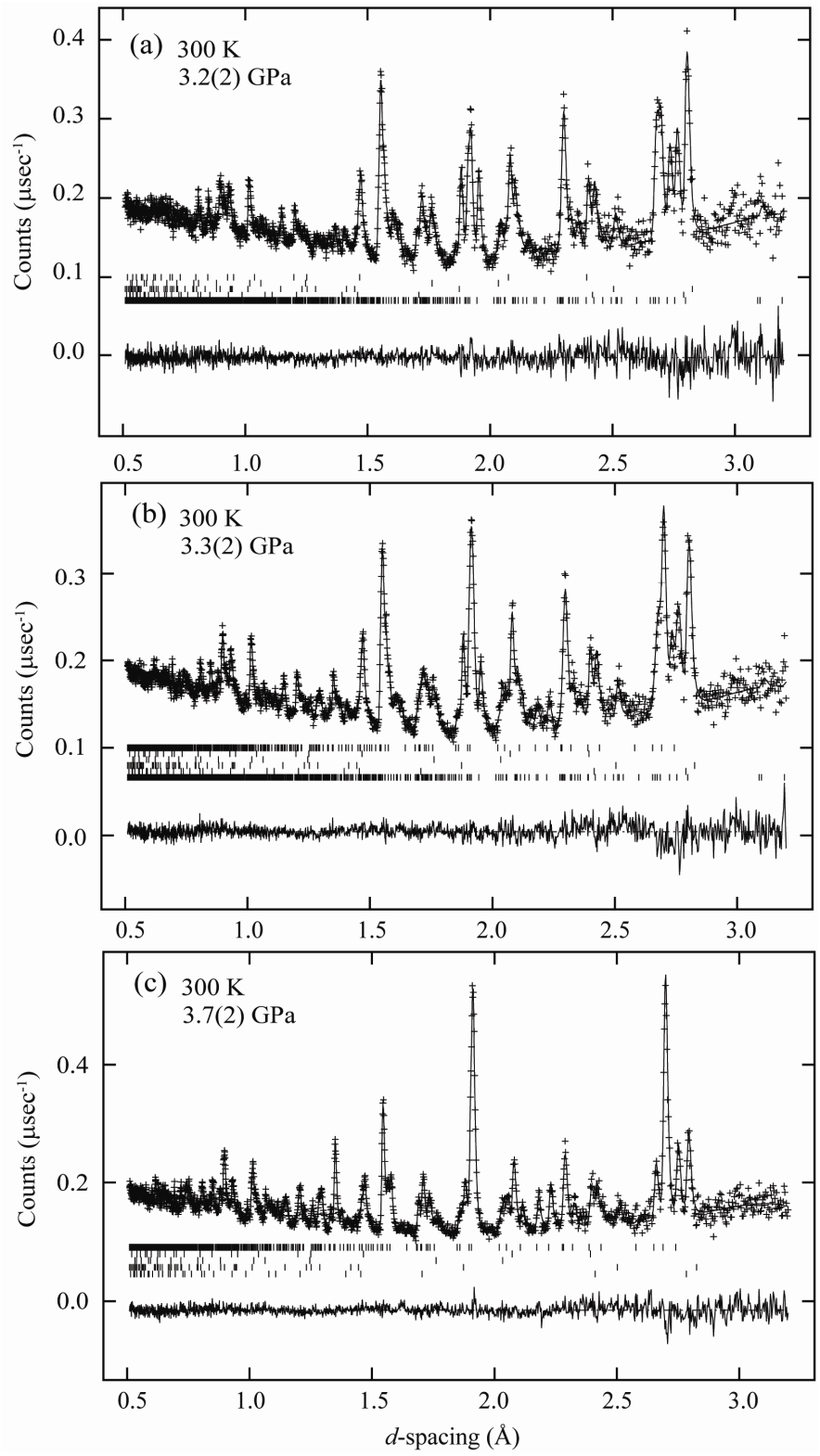

Figure 5.6 The room temperature Rietveld fits of $BiNiO_3$ at (a) 3.2(2) GPa which shows triclinic $P\bar{1}$ Phase I before the transition and (b) 3.3(2) GPa which shows the coexistence of two phases, and (c) 3.7(2) GPa where the transition to orthorhombic Phase III completed. The index markers from the bottom represent the reflections of $BiNiO_3$ Phase I, Pb calibrant, WC, Ni, NiO and $BiNiO_3$ Phase III ((b) and (c) only).

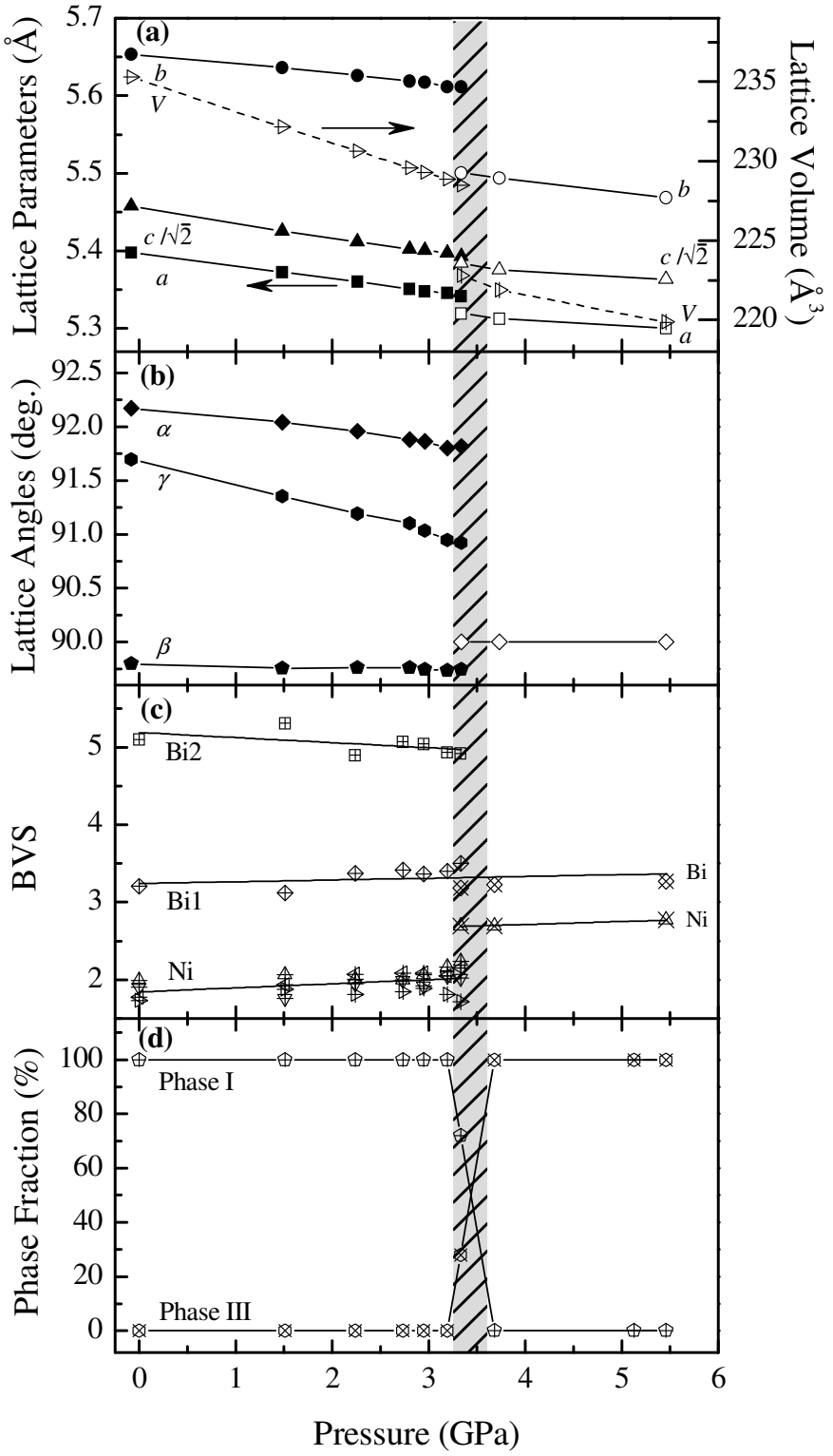

Figure 5.7 The pressure-induced evolution from Phase I to III of (a) lattice parameters and cell volume, (b) lattice angles, (c) BVS calculated valences, (d) phase fractions of Phase I and III at various pressures and 300 K, where shaded area shows the transition pressure range.

5.3.2 Phase transition at high pressure low temperature

New high pressure low temperature (HPLT) phase

Low temperature neutron diffraction patterns were collected at ~ 5.2 GPa, and the evolution of diffraction profiles with temperature is shown in Figure 5.8 (a). No substantial changes are observed in the profile down to 233 K. A distinct diffraction profile was obtained when the temperature decreased to 193 K, showing that a new phase was present. However, the characteristic *Pbnm* (2 0 2) and (0 2 2) reflections of Phase III were observed (Figure 5.8 (a), marked with arrows), showing the coexistence of a high pressure low temperature (HPLT) phase and orthorhombic Phase III at 193 K. With further cooling the Phase III peaks decrease but are still observed, indicating that the transformation was not complete down to 133 K. The observed structural transition occurs between 233 and 193 K, which is in agreement with the recent conductivity measurements of $BiNiO_3$ conducted by Takajo *et al.*[23]. The measurement showed the metal-insulator transition takes place around 220 K under 5 GPa (Figure 5.3), indicating the insulating character of obtained HPLT phase. In addition, the suppression of transition found at 5 GPa from the conductivity measurements can be explained by the existence of metallic Phase III down to 133 K.

Comparing the metal-insulator transition from conductivity measurements under different pressures, the observed behaviour shows that no transition occurs above 6 GPa. The measurement also implies that the metallic phase transforms to the insulating phase completely at low temperature under 4 GPa. Therefore a further neutron investigation was carried out in order to obtain the fully transformed HPLT phase, and the temperature-dependence data are shown in Figure 5.8 (b). The sample was pressurised to 4.6 GPa and then cooled. Diffraction patterns were collected at 150 and 100 K. The single HPLT phase below 150 K is evident by the absence of characteristic Phase III *Pbnm* (2 0 2) and (0 2 2) reflections. The observed temperature of the structural transition is comparable with that suggested by the conductivity measurements at 4 GPa (Figure 5.3). These show that the metal-insulator transition takes place at around 250 K and reaches a maximum resistivity at around 120 K, indicating the completion of the transition.

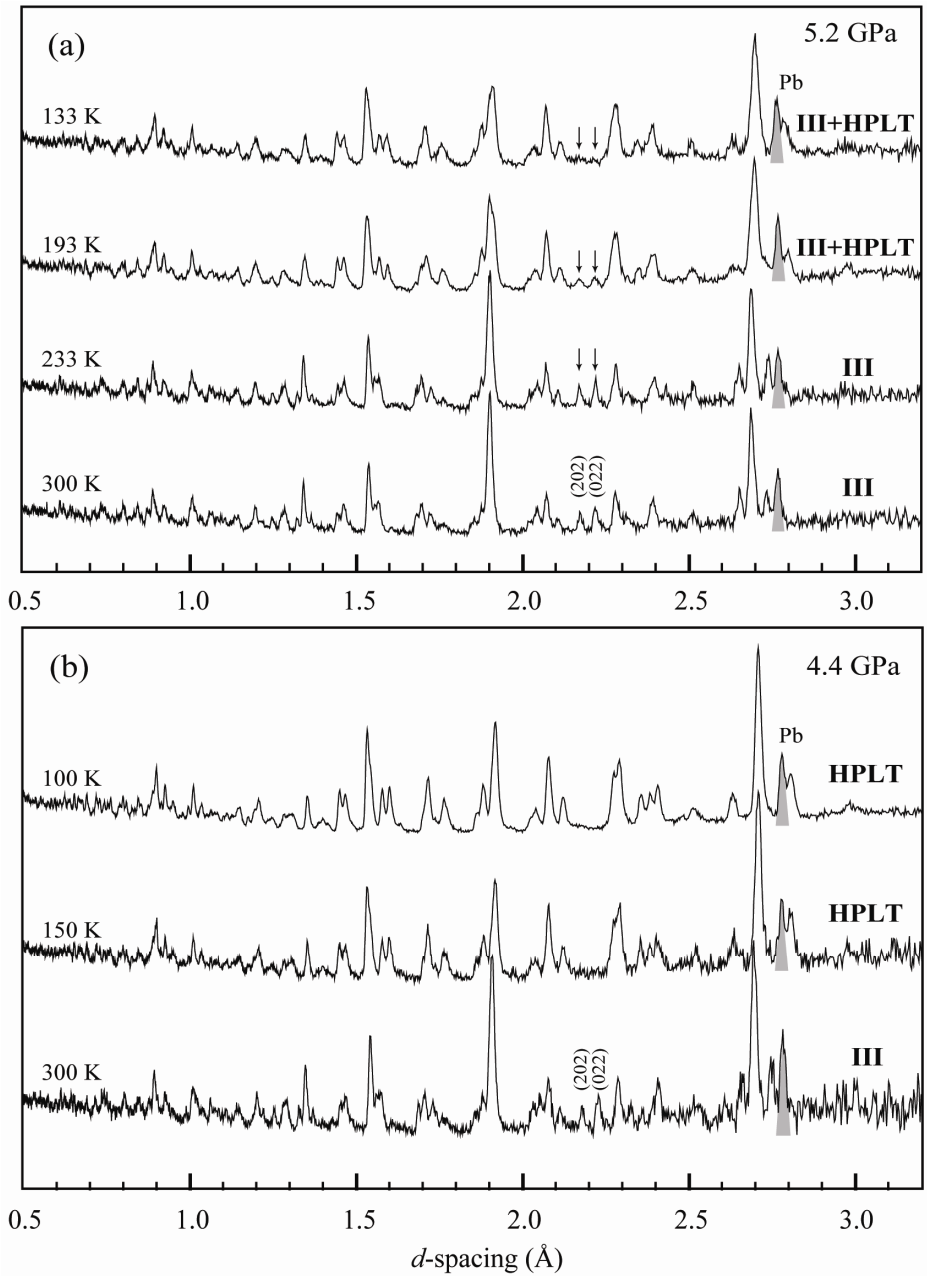

Figure 5.8 Temperature-dependent NPD collected at (a) 5.4 GPa, showing phase coexistence at low temperature, where *Pbnm* (202) and (022) reflections of Phase III are marked by arrows, and (b) 4.3 GPa, showing single high pressure low temperature phase below 150 K. A shaded peak shows one of the reflections of lead calibrant.

Synchrotron X-ray diffraction

Initial attempts to refine the new HPLT structure were unsuccessful due to the low resolution of the instrument used. The $BiNiO_3$ HPLT phase was firstly analysed

with *Pbnm* and $P2_1/n$ symmetry from $RNiO_3$ materials[4,11,26], however clear splittings of the peaks were revealed from recent high resolution SPring-8 synchrotron data obtained by Drs. O. Smirnova and M. Azuma, Kyoto University. It was shown that *Pbnm* or $P2_1/n$ symmetry is insufficient to index the observed splittings, indicating that other monoclinic space groups or even lower symmetry is required to fit the data. Three monoclinic subgroups ($P2_1/b11$, $P12_1/n1$ and $P112_1/m$) of *Pbnm* were examined, but the observed splittings could only be indexed by

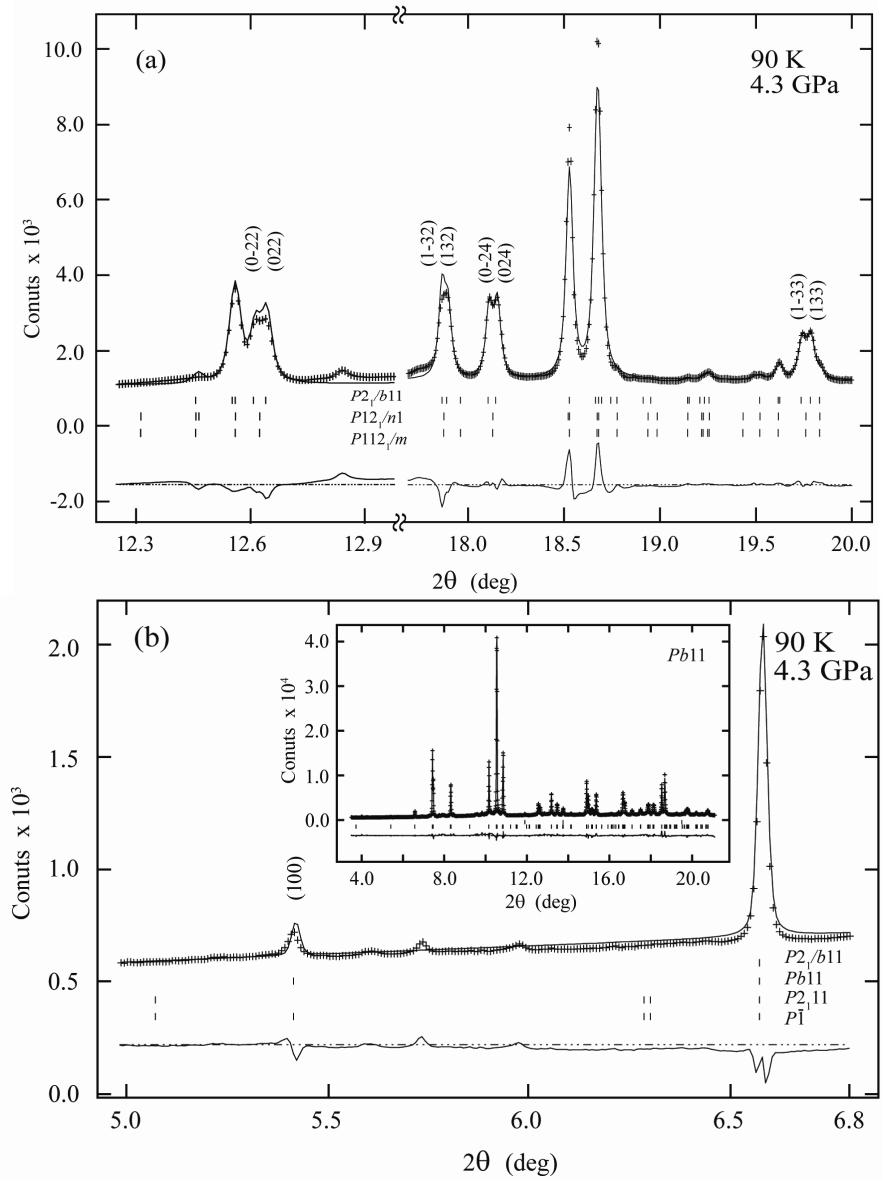

Figure 5.9 The selected *2θ* areas of SXRD data showing (a) the splittings and the fits of $P2_1/b11$ to the profile and also the reflection markers of $P12_1/n1$ and $P112_1/m$, and (b) the fits of *Pb*11 and also reflection markers of $P2_1/b11$, $P2_111$ and $P\bar{1}$, where the inset shows the *Pb*11 Rietveld fits of SXRD data with an angular range of $3.5 < 2\theta < 21$.

$P2_1/b11$ (Figure 5.9 (a)). Moreover, the presence of an unindexed peak at *d*-spacing ~ 5.25 Å highlights the limitation of $P2_1/b11$ model, in which the (1 0 0) reflection is absent. Thus three subgroups of $P2_1/b11$ symmetry, namely $Pb11$, $P2_111$ and $P\bar{1}$, were further examined. The weak (1 0 0) reflection can be well-fitted by $Pb11$, while the (1 0 0) reflection is absent with $P2_111$ symmetry, and $P\bar{1}$ symmetry results in the generation of peaks at (0 1 0) and (0 1 1) which are absent in the data (Figure 5.9 (b)). It should be noted that there are several minor unidexed peaks, indicating the existence of unidentified impurities. The (1 0 0) reflection gives evidence for the further distortion, so $Pb11$ (No. 7) is concluded to be the best candidate space group for the observed insulating phase.

Neutron data analysis

The $Pb11$ model derived from SXRD was adopted as an initial structure to analyse the obtained NPD patterns. Reasonable fits were achieved, with R_{wp} = 2.10 % and χ^2 = 3.78. The $Pb11$ Rietveld fit of the 4.3 GPa and 100 K pattern is shown in Figure 5.10 and the crystal structure is illustrated in Figure 5.11. The refinement results and selected distances and angles of the material at approximately

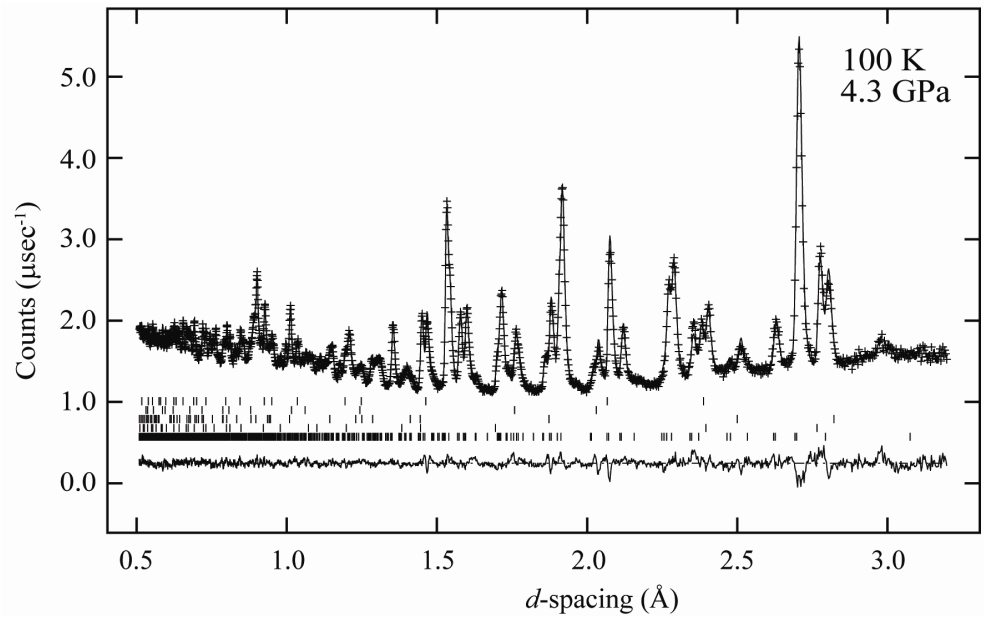

Figure 5.10 The Rietveld fits of *Pb*11 model to the neutron data collected at 4.3 GPa, 100 K. The reflection markers from the bottom represent the reflections of the HPLT Phase, Pb calibrant, WC and Ni from the anvils, and impurity NiO, respectively.

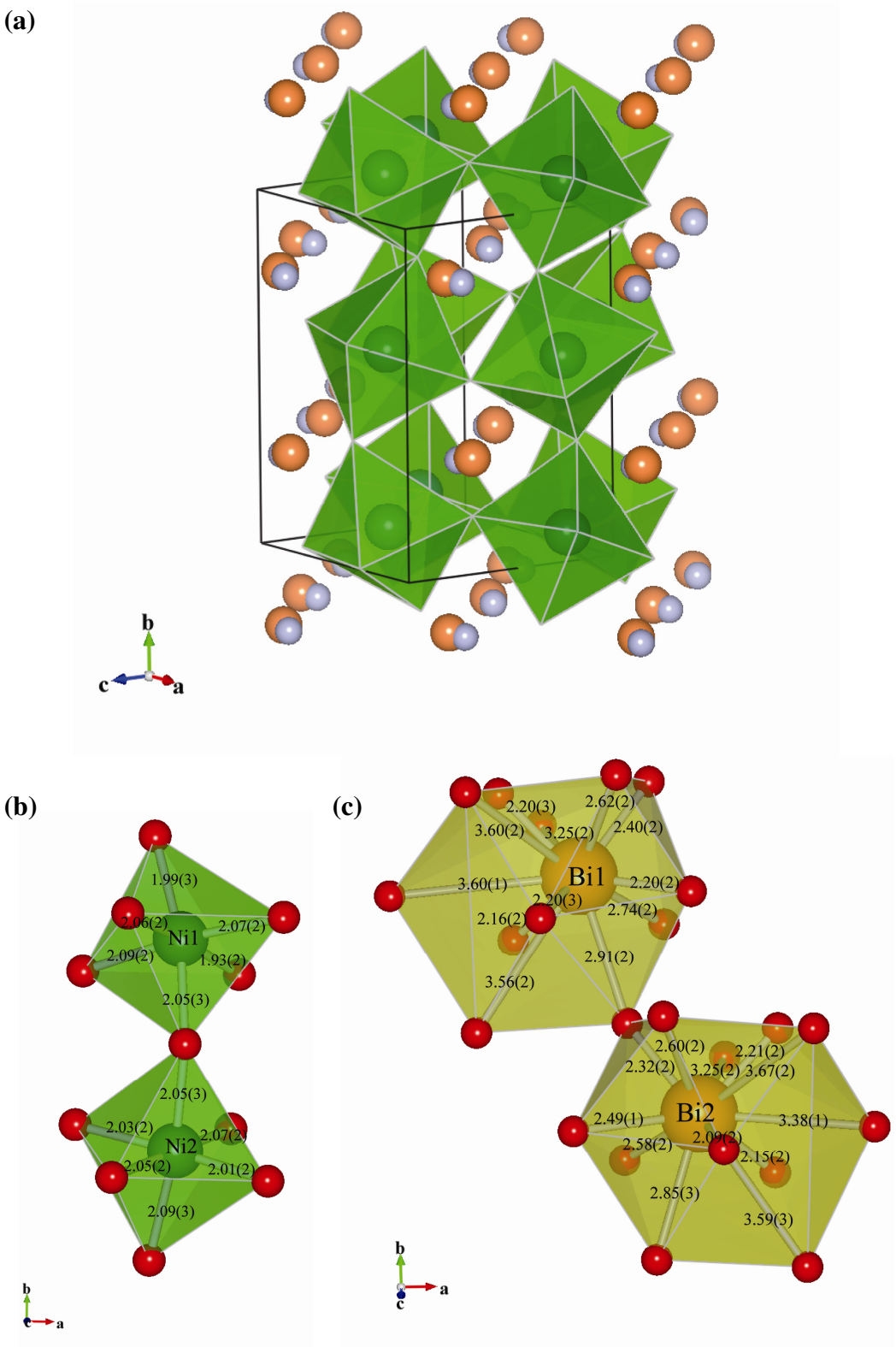

Figure 5.11 The high-pressure low-temperature $BiNiO_3$ phase, showing (a) the *Pbnm* symmetry of the structure, where the orange and cyan spheres represent Bi atom and $6s^2$ electrons, respectively, (b) NiO_6 octahedra and Ni-O bond distances, and (c) BiO_{12} polyhedra and Bi-O distances.

5.2 and 4.4 GPa are listed in Table 5.1 and Table 5.2[#]. The similarity of Ni-O bonds indicates the absence of Jahn-Teller distortion of the NiO_6 octahedra, as shown in Figure 5.11 (b). The Bi-O distances show a bismuth displacement in the BiO_{12} polyhedra, which is due to the Bi $6s^2$ lone-pair electrons (Figure 5.11 (c)).

The refined structural parameters, BVS results and phase fractions from the data collected at 4.4 GPa, which shows the single HPLT phase, are illustrated at Figure 5.12. The phase fractions of 5.2 GPa data are also plotted in Figure 5.12 (c) as a reference. Drastic changes of the structure were observed between the Phase III and HPLT phase, where the lattice parameters and cell volume increase with the decreasing temperature. However the obtained metal-insulator transition temperature is very approximate with the present data. When the sample is pressurised to 5.2 GPa, the Phase III fraction decreases to 35(1) % at 193 K and reaches 10(1) % at 133 K, while the single HPLT phase was obtained at 150 K and 4.2 GPa. This indicates that the phase boundary exists between 150 and 200 K at 4.2 GPa, which is comparable with the conductivity results (Figure 5.3)[23]. Although there are two crystallographic sites for each bismuth and nickel given by the space group *Pb*11, the BVS calculation of the HPLT phase shows only Bi^{4+} and Ni^{2+} (Figure 5.12 (b)). In this sense, charge disproportionation was not observed for either bismuth or nickel cations.

 # It should be noted that although under the same applied force, the pressure on the sample varies with temperature due to the complex changes of the environment provided from the Paris-Edinburgh cell.

Table 5.1 Refined results of $BiNiO_3$ orthorhombic and monoclinic phases at different pressure and temperature conditions, lattice parameters, cell angle, cell volume, refinement reliability R_{wp} and χ^2 are listed.

	5.2 GPa				**4.4 GPa**		
	Pbnm		***Pb*11**[a]		***Pbnm***	***Pb*11**	
T (K)	300	233	193	133	300	150	100
P (GPa)	5.5(2)	5.1(2)	5.2(1)	5.3(2)	4.6(3)	4.5(2)	4.3(1)
a (Å)	5.3008(4)	5.2977(4)	5.2534(4)	5.2562(4)	5.3053(5)	5.2521(4)	5.2515(2)
b (Å)	5.4687(5)	5.4742(5)	5.5931(5)	5.5780(6)	5.4810(6)	5.6000(6)	5.6012(3)
c (Å)	7.5848(5)	7.5816(5)	7.6019(8)	7.6002(8)	7.5919(7)	7.6176(7)	7.6202(4)
β (°)			90.22(2)	90.19(2)		90.20(2)	90.20(1)
V (Å)	219.87(1)	219.87(2)	223.36(3)	222.83(3)	220.76(3)	224.05(3)	224.14(1)
x	-0.006(2)	-0.001(1)	0.739(3)	0.739(3)	-0.007(2)	0.735(5)	0.736(2)
Bi1 y	0.0500(6)	0.0506(6)	0.078(2)	0.074(3)	0.0510(8)	0.079(3)	0.072(2)
z			0.346(2)	0.343(3)		0.337(3)	0.342(2)
x			0.219(3)	0.222(3)		0.224(4)	0.223(2)
Bi2 y			0.463(2)	0.463(3)		0.468(3)	0.457(2)
z			0.831(3)	0.838(3)		0.836(3)	0.838(2)
U_{iso} (Å^2)	0.0061(7)	0.0040(8)	0.0010(5)	0.0018(6)	0.006(1)	0.0008(7)	0.0009(4)
x			0.239(3)	0.246(4)		0.242(5)	0.242(2)
Ni1 y			0.010(4)	0.008(4)		0.013(4)	0.026(2)
z			0.083(2)	0.084(3)		0.088(3)	0.087(1)
x			0.257(4)	0.244(4)		0.252(5)	0.250(3)
Ni2 y			0.013(4)	0.014(4)		0.007(4)	0.018(2)
z			0.585(3)	0.584(3)		0.590(3)	0.586(2)
U_{iso} (Å^2)	0.0002(5)	0.0012(5)	0.0010(5)	0.0018(6)	0.0018(8)	0.0008(7)	0.0009(4)
x	0.6977(9)	0.6973(9)	0.422(6)	0.426(6)	0.699(1)	0.432(7)	0.424(4)
O1 y	0.2967(8)	0.3003(8)	0.341(4)	0.329(6)	0.301(1)	0.339(5)	0.348(3)
z	0.0384(7)	0.0383(7)	0.146(3)	0.150(4)	0.039(1)	0.148(5)	0.139(2)
x	0.087(1)	0.085(1)	0.982(4)	0.980(4)	0.090(2)	0.963(6)	0.961(4)
O2 y	0.477(1)	0.478(1)	0.233(3)	0.238(4)	0.476(2)	0.225(5)	0.223(3)
z			0.006(3)	0.150(4)		0.012(5)	0.011(3)
x			0.078(5)	0.087(6)		0.091(6)	0.080(4)
O3 y			0.705(4)	0.700(5)		0.701(4)	0.705(3)
z			0.634(3)	0.634(3)		0.641(5)	0.647(3)
x			0.563(5)	0.562(5)		0.551(7)	0.552(4)
O4 y			0.819(4)	0.835(5)		0.815(5)	0.809(3)
z			0.514(3)	0.523(4)		0.518(6)	0.515(3)
x			0.870(3)	0.879(4)		0.871(4)	0.867(2)
O5 y			0.435(2)	0.441(3)		0.450(3)	0.444(2)
z			0.349(3)	0.337(5)		0.324(4)	0.330(3)
x			0.386(3)	0.380(4)		0.395(4)	0.389(2)
O6 y			0.047(2)	0.043(3)		0.048(3)	0.041(2)
z			0.837(4)	0.828(5)		0.836(6)	0.837(3)
U_{iso} (Å^2)	0.0049(6)	0.0046(6)	0.0004(5)	0.001(1)	0.0076(9)	0.003(1)	0.0029(6)
R_{wp} (%)	3.80	3.88	2.29	2.86	5.49	3.89	2.12
χ^2	1.31	1.29	2.90	1.51	1.25	2.31	3.84

[a] the coexistence of orthorhombic and monoclinic phases were refined, showing the ratio of phase fraction 35(1)/65(1) and 10(1)/90(1) % at 193 and 133 K, respectively. For the *Pbnm* (No. 62) model atom positions are Bi, 4*c*, (x, y, ¼); Ni, 4*b*, (½, 0, 0); O1, 8*d*, (x, y, z) ; O2, 4*c*, (x, y, ¼). For the *Pb*11 (No. 7) model all atom positions are 2a, (x, y, z).

Table 5.2 The selected distances and angles of $BiNiO_3$ orthorhombic and monoclinic phases at different pressure and temperature conditions.

	~5.2 GPa				~4.4 GPa		
	Pbnm		*Pb*11[a]		*Pbnm*	*Pb*11	
T (K)	300	233	193	133	300	150	100
P (GPa)	5.5(2)	5.1(2)	5.2(1)	5.3(2)	4.6(3)	4.5(2)	4.3(1)
Bi1-O (Å)	2.619(7)×2	2.617(7)×2	2.70(3)	2.63(4)	2.62(1) ×2	2.60(4)	2.74(2)
	2.350(6)×2	2.332(6)×2	2.18(3)	2.18(4)	2.343(8)×2	2.15(4)	2.16(2)
	2.580(6)×2	2.579(6)×2	3.01(3)	2.97(3)	2.580(9)×2	2.88(4)	2.91(2)
	3.350(6)×2	3.348(6)×2	3.54(3)	3.47(3)	3.346(9)×2	3.54(4)	3.56(2)
	3.170(8)	3.176(8)	3.52(3)	3.55(4)	3.19(1)	3.65(4)	3.60(2)
	2.389(8)	2.392(8)	2.50(3)	2.49(3)	2.39(1)	2.58(4)	2.62(2)
	3.106(10)	3.072(10)	2.15(3)	2.13(4)	3.12(2)	2.24(5)	2.20(3)
	2.256(10)	2.286(9)	2.44(3)	2.54(3)	2.26(1)	2.43(4)	2.40(2)
			3.66(2)	3.61(2)		3.59(2)	3.59(1)
			2.11(2)	2.18(2)		2.21(2)	2.20(1)
			3.30(3)	3.33(3)		3.26(4)	3.25(2)
			2.20(3)	2.14(3)		2.19(4)	2.20(2)
Bi1-BVS	3.27	3.27	4.20	4.20	3.30	4.00	4.00
Bi2-O (Å)			2.71(3)	2.71(4)		2.71(5)	2.60(2)
			3.70(3)	3.64(4)		3.63(5)	3.67(2)
			2.24(3)	2.23(3)		2.35(4)	2.32(2)
			2.27(3)	2.28(3)		2.20(4)	2.21(2)
			2.15(3)	2.16(4)		2.10(4)	2.15(2)
			2.59(3)	2.68(3)		2.68(4)	2.58(2)
			3.61(3)	3.64(4)		3.56(5)	3.59(3)
			2.78(3)	2.74(3)		2.83(5)	2.85(3)
			2.49(2)	2.49(2)		2.52(2)	2.49(1)
			3.38(2)	3.34(2)		3.37(2)	3.38(1)
			3.21(2)	3.20(3)		3.28(3)	3.25(2)
			2.13(2)	2.14(3)		2.05(4)	2.09(2)
Bi2-BVS			4.00	3.90		4.10	4.10
Ni1-O (Å)	1.953(5)×2	1.969(5)×2	2.14(4)	2.09(4)	1.982(7)×2	2.13(4)	2.07(2)
	1.972(5)×2	1.963(5)×2	2.07(3)	2.06(4)	1.954(7)×2	2.02(5)	2.06(2)
	1.956(2)×2	1.952(2)×2	1.93(3)	1.98(4)	1.961(3)×2	1.98(4)	1.93(2)
			2.02(3)	2.00(3)		2.02(4)	2.09(2)
			2.14(3)	2.07(5)		1.92(4)	1.99(3)
			2.04(3)	2.07(5)		2.09(5)	2.05(3)
Ni1-BVS	2.88	2.81	2.10	2.10	2.76	2.20	2.20
Ni2-O (Å)			2.00(3)	1.97(4)		1.95(4)	2.03(2)
			2.10(4)	2.06(4)		2.14(4)	2.07(2)
			2.01(3)	2.00(4)		1.98(4)	2.05(2)
			2.03(3)	2.12(4)		2.09(4)	2.01(2)
			1.96(3)	2.02(5)		2.15(4)	2.09(3)
			2.04(4)	2.00(5)		2.03(5)	2.05(3)
Ni2-BVS			2.30	2.30		2.10	2.10
Ni-O-Ni (º)	151.9(2)	151.3(2)	137.0(16)	137.4(19)	151.38(35)	139.6(22)	141.1(12)
	151.6(4)	152.4(4)	143.9(15)	146.8(16)	150.9(6)	142.3(22)	140.7(12)
			143.6(18)	140.0(18)		140.8(20)	138.8(12)
			139.0(19)	140.8(20)		140.4(25)	142.6(13)
			136.8(12)	136.5(13)		139.3(15)	137.5(8)
			136.9(13)	137.9(14)		134.2(15)	136.7(8)

[a] **the coexistence of orthorhombic and monoclinic phases were refined.**

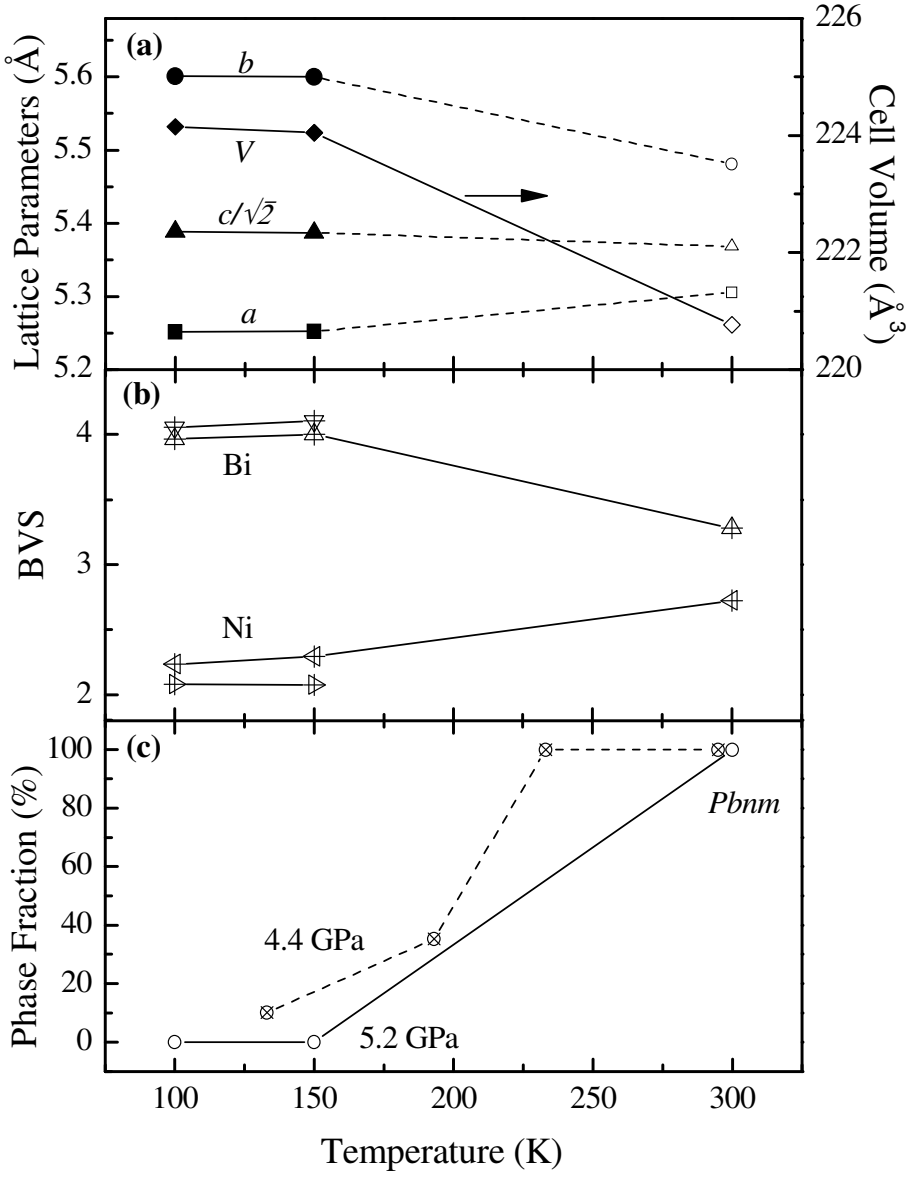

Figure 5.12 Temperature-dependent refinement results at 4.4 GPa of (a) lattice parameters and cell volume of *Pnma* and *Pb*11 phases, (b) Bi and Ni BVS calculated from refined Bi-O and Ni-O distances, and (c) the phase fraction of *Pnma* and *Pb*11 phases (open marker), where the data collected at 5.2 GPa (crossed open marker) are also shown for reference.

5.3.3 High temperature moderate pressure phase of $BiNiO_3$

The $BiNiO_3$ sample was pressurised to 1.8 GPa and neutron diffraction patterns were collected from room temperature to 560 K, as shown in Figure 5.13 (a). The profiles remain unchanged up to 400 K, hereafter the evolution of the patterns suggested the presence of the second phase above 440 K. The characteristic (2 $\bar{2}$ 0) reflection of triclinic Phase I was observed (Figure 5.13 (a), marked arrow), showing a phase coexistence until 510 K. From the obtained patterns, it can be inferred that the completion of transition occurs at 1.8 GPa and 560 K giving a high-temperature (HT) phase, which is comparable with the previous SXRD result (Figure 5.4)[24]. It should be noted that no pressure transmission medium was used in the high-pressure high-temperature experiment, hence a considerable pressure gradient may exist within the sample cell. An orthorhombic structure *Pbnm* from the refinement of Phase III was adopted as an initial model. Due to the low resolution provided in the instrument, only $BiNiO_3$ phase was refined as the main phase, while the contribution from the sample capsule/pressure calibrant MgO, capsule assembly alumina disc Al_2O_3 and the temperature indicator Ta foil were also taken into the account to the fits. A reasonable fit was obtained with the assuming *Pbnm* symmetry to the profile as shown in Figure 5.14, giving a result of $R_{wp} = 5.35$ % and $\chi^2 = 8.75$, while the refinement results, selected distances and angles are listed in Table 5.3.

In order to clarify whether the obtained HT phase differs from the known Phase III, a pressure-dependent neutron diffraction experiment was also performed to explore the phase boundary. The patterns collected at around 440 K from 1.8 up to 5.2 GPa are shown in Figure 5.13 (b). The characteristic reflection of Phase I was observed at 2.7 GPa but disappeared above 3.7 GPa, consistent with the transition to a single orthorhombic phase. At this pressure the orthorhombic phase is stable down to 375 K, which shows no change in the powder diffraction profile.

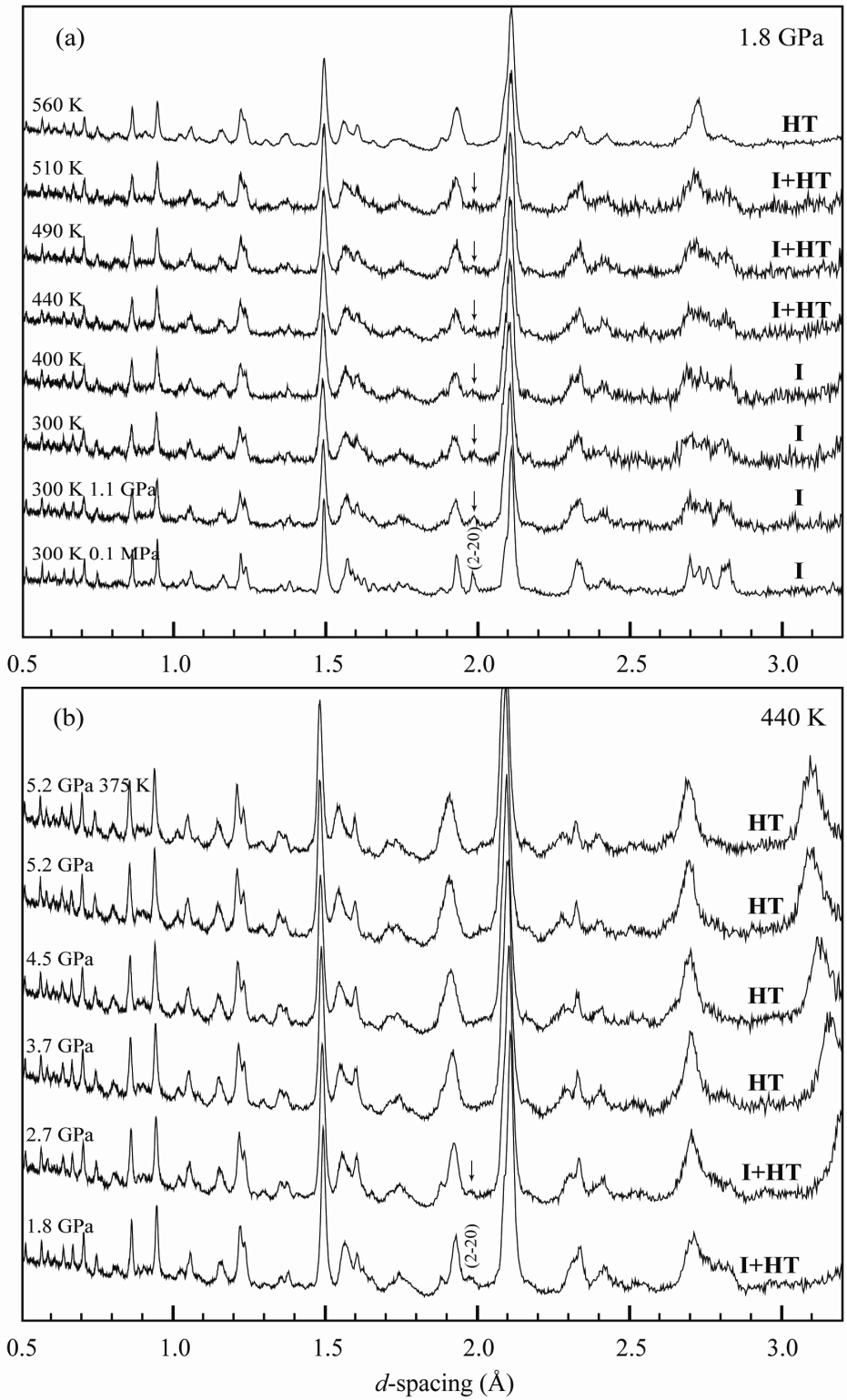

Figure 5.13 The evolution from Phase I to the HT phase: (a) temperature-dependent NPD collected at 1.8 GPa. The two patterns at the bottom were collected at 300 K and 1.1 and ambient pressure. (b) pressure-dependent neutron diffraction data collected at around 440 K, where the top pattern was collected at 375 K and 5.2 GPa. The characteristic ($2\bar{2}0$) reflection of Phase I is marked by arrows.

Table 5.3 Refined results of $BiNiO_3$ high-temperature orthorhombic phase, lattice parameters, cell angle, cell volume, refinement reliability R_{wp} and χ^2, selected bond distances and angles, and BVS results are listed.

T (K)	560	440			375
P (GPa)	1.8	3.7	4.5	5.2	5.2
a (Å)	5.345(1)	5.306(2)	5.293(2)	5.283(2)	5.281(2)
b (Å)	5.585(2)	5.564(2)	5.559(2)	5.551(3)	5.553(3)
c (Å)	7.663(1)	7.600(3)	7.582(3)	7.570(3)	7.566(3)
V (Å)	228.71(9)	224.4(1)	223.1(1)	222.0(1)	221.9(1)
Bi1 x	0.021(2)	0.035(2)	0.030(2)	0.022(3)	0.023(2)
Bi1 y	0.054(1)	0.048(2)	0.051(2)	0.055(2)	0.055(1)
Bi1 U_{iso} (Å^2)	0.010(3)	0.020(4)	0.018(4)	0.014(3)	0.008(3)
Ni U_{iso} (Å^2)	0.025(3)	0.017(2)	0.014(2)	0.019(3)	0.016(2)
O1 x	0.670(2)	0.658(2)	0.660(3)	0.665(2)	0.664(2)
O1 y	0.313(2)	0.320(2)	0.312(2)	0.309(2)	0.306(2)
O1 z	0.035(2)	0.037(2)	0.027(2)	0.022(2)	0.021(2)
O2 x	0.099(3)	0.108(4)	0.113(4)	0.118(4)	0.122(4)
O2 y	0.468(3)	0.471(5)	0.481(4)	0.485(4)	0.488(4)
O2 U_{iso} (Å^2)	0.039(3)	0.072(3)	0.046(3)	0.038(3)	0.033(3)
Bi1-O (Å)	2.88(2) ×2	2.98(1) ×2	2.97(2) ×2	2.92(2) ×2	2.92(2) ×2
	2.36(1) ×2	2.30(2) ×2	2.37(2) ×2	2.41(2) ×2	2.43(2) ×2
	2.44(2) ×2	2.40(1) ×2	2.34(2) ×2	2.32(2) ×2	2.32(2) ×2
	3.42(1) ×2	3.41(2) ×2	3.34(2) ×2	3.33(2) ×2	3.31(2) ×2
	3.30(2)	3.24(3)	3.20(3)	3.20(2)	3.19(2)
	2.35(2)	2.39(3)	2.43(2)	2.44(2)	2.46(2)
	3.34(2)	3.44(3)	3.43(2)	3.40(3)	3.43(2)
	2.09(2)	1.94(3)	1.93(3)	1.94(3)	1.91(2)
Bi1-BVS	3.60	4.10	4.10	4.00	4.10
Ni1-O (Å)	1.99(1) ×2	1.99(1) ×2	1.94(1) ×2	1.93(1) ×2	1.91(1) ×2
	2.07(1) ×2	2.09(1) ×2	2.09(1) ×2	2.07(1) ×2	2.08(1) ×2
	1.995(5) ×2	1.992(7) ×2	1.991(6) ×2	1.995(6) ×2	1.999(6) ×2
Ni1-BVS	2.32	2.28	2.43	2.50	2.52
Ni-O-Ni (º)	144.7(6)	140.9(6)	144.3(7)	146.6(7)	147.0(6)
	147.6(10)	145.1(13)	144.5(11)	143.1(11)	142.2(10)
R_{wp} (%)	5.35	5.45	5.42	5.45	5.39
χ^2	8.75	5.44	5.36	4.38	4.71

The coexistence of orthorhombic and monoclinic phases were refined, showing the ratio of phase fraction 35(1)/65(1) and 10(1)/90(1) % at 193 and 133 K, respectively. For the *Pbnm* (No. 62) model atom positions are Bi, 4*c*, (x, y, ¼); Mn, 4*b*, (½, 0, 0); O1, 8*d*, (x, y, z) ; O2, 4*c*, (x, y, ¼).

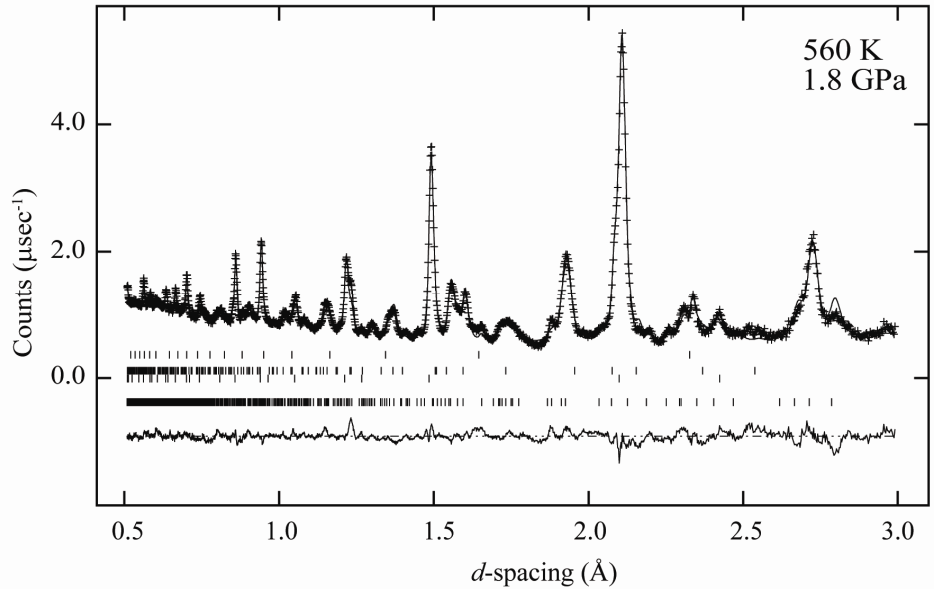

Figure 5.14 The orthorhombic *Pbnm* Rietveld fits of $BiNiO_3$ collected at 1.8 GPa and 560 K.

Although the characteristic *Pbnm* (2 0 2) and (0 2 2) reflections of Phase III (Figure 5.8) were not observed in the HT phase, uncertainty remains due to the poor resolution, which is owing to the strain broadening from temperature and pressure gradients in the sample. The lattice parameters and cell volume of $BiNiO_3$ HT phase and also the Phase III at 5.2 GPa are shown in Figure 5.15. A drastic change was observed at high temperature in comparison with the known Phase III, indicating that the HT phase differs from known Phase III.

However, from pressure-dependent experiment the disappearance of the characteristic (2 $\bar{2}$ 0) Phase I reflection occurred between 2.7 and 3.7 GPa, which is comparable with Phase I and III boundary (3.2(2) to 3.7(2) GPa). The pressure-dependent evolution of cell volume is shown in Figure 5.16, where a similar tendency between HT phase and Phase III is displayed. In addition, the cell volume difference between two phases may be eliminated when taking the thermal expansion into account. Although the BVS calculation shows Bi^{4+} and Ni^{2+} valence states for the HT phase, which is different from Phase III ($Bi^{3+}Ni^{3+}O_3$), the big error indicates that the obtained BVS result are only approximate.

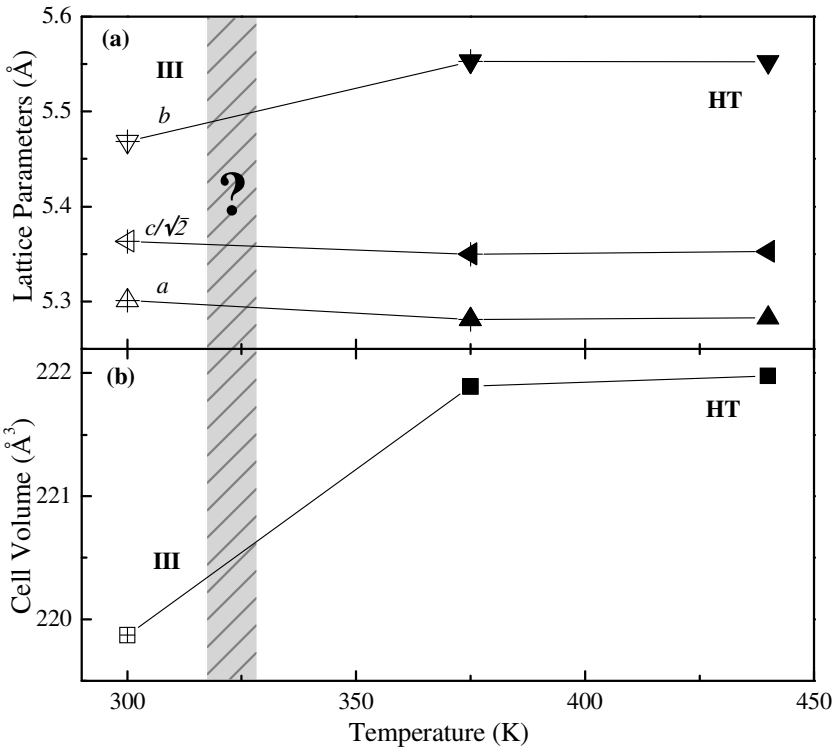

Figure 5.15 Temperature dependence evolution of the data collected at ~5.2 GPa of (a) the lattice parameters, and (b) cell volume, where the steep changes indicating the existence of different HT phase. The uncertain transition temperature range was shown in shaded area.

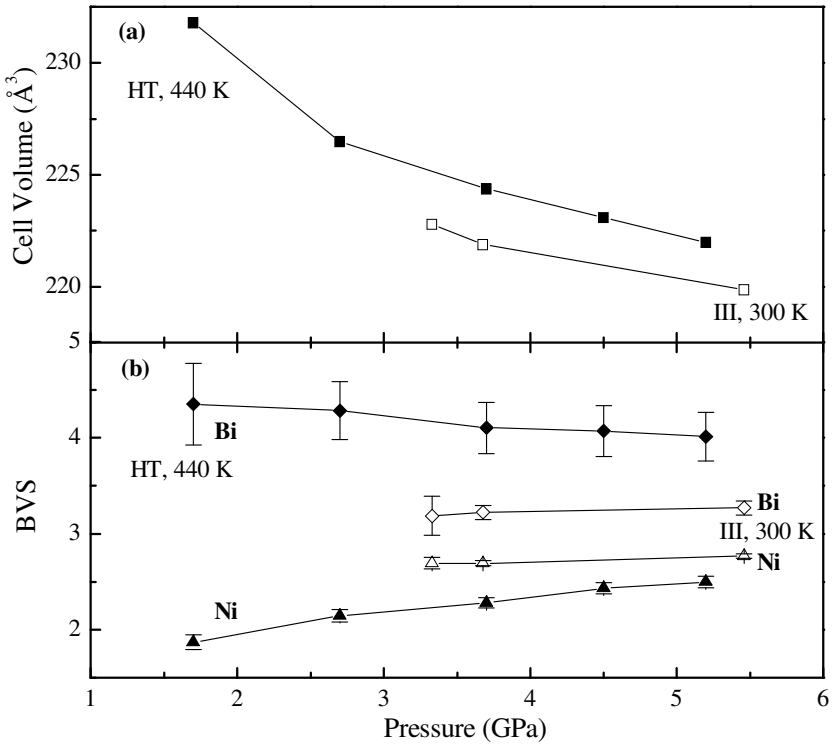

Figure 5.16 Pressure dependence evolution of (a) the cell volume of HT phase, and (b) Bi and Ni BVS calculated from refined Bi-O and Ni-O distances, in comparison with Phase III.

5.4 Discussion

An approximate pressure-temperature phase diagram is proposed based on the present and previous work (Figure 5.17). The pressure-induced structural phase transition from triclinic Phase I to orthorhombic Phase III has been studied[19]. The transition has been reported to occur at about 3 GPa from resistivity measurements[18] and within the range of 2.1 to 4.7 GPa from a previous neutron experiment[19]. Data collected during the present study has allowed the observation of phase coexistence, which was not seen before. The relatively narrow transition occurs in the pressure range of 3.2(2) to 3.7(2) GPa. Phases I and III coexist at 3.3(2) GPa, and no intermediate phase is observed to be present between these two phases, demonstrating that the first order transition takes place directly with pressurisation.

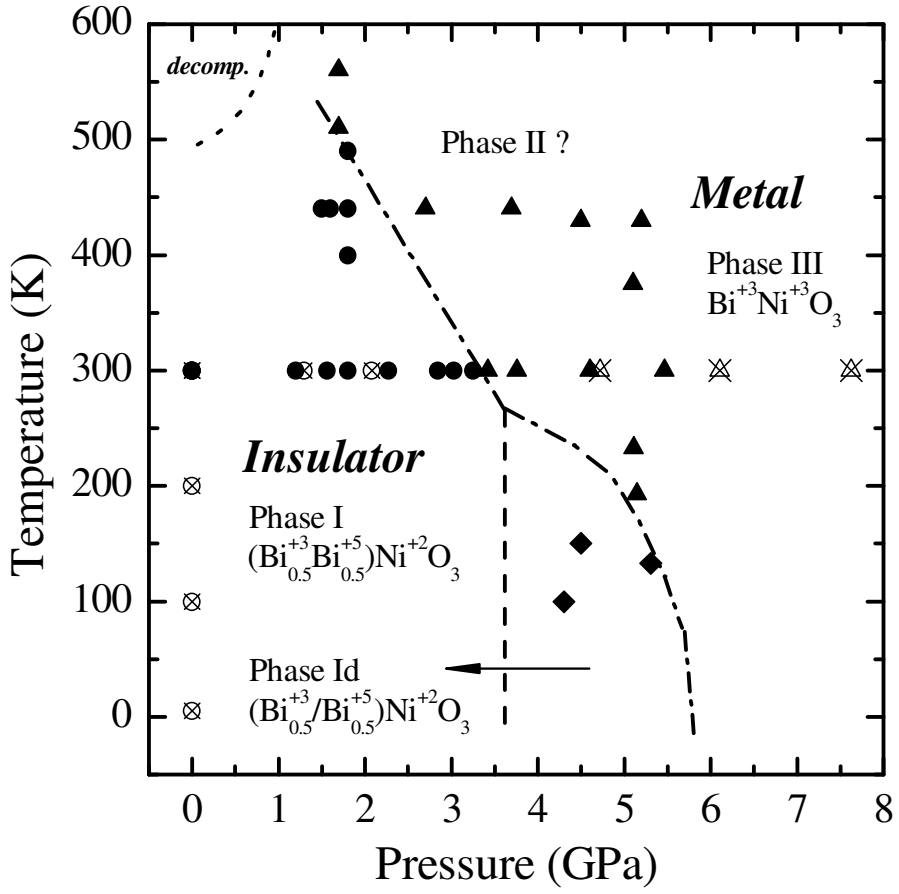

Figure 5.17 The present proposed P-T phase diagram for $BiNiO_3$ states, showing the approximate boundary between regions of insulating Phase I, metallic Phase III, and also the HPLT phase. The crossed open markers represent the data from M. Azuma *et al.*[19] and S. Carlsson *et al.*[13].

The BVS calculation confirms that the valence states of charge disproportionated Phase I remained as $(Bi^{3+}_{0.5}Bi^{5+}_{0.5})Ni^{2+}O_3$ up to 3.3 GPa. Above the transition the oxidation states are as $Bi^{3+}Ni^{3+}O_3$, the orthorhombic Phase III. These observations are in good agreement with previous studies.

It has been reported that with the metal-insulator transition, RNiO$_3$ materials display a structural phase transition from a $GdFeO_3$-type orthorhombic phase to a Ni charge disproportionated monoclinic $P2_1/n$ phase[1,4,5,10,11]. However $BiNiO_3$ shows rather different behaviour compared to the RNiO$_3$ family. A distorted monoclinic $Pb11$ symmetry for the HPLT phase was revealed by synchrotron X-ray diffraction. The BVS calculation shows that the obtained monoclinic HPLT phase has the valence states of Bi^{4+} and Ni^{2+} rather than the Ni charge disproportionated $Bi^{3+}(Ni^{2+}_{0.5}Ni^{4+}_{0.5})O_3$. The observed Bi^{4+} valence state probably results from the structural averaging of disordered Bi^{3+}/Bi^{5+} as in Phase I because a genuine Bi^{4+} phase would be metallic, thus the obtained HPLT phase is labelled Phase Id. The increase of the cell volume also indicates that Phase Id is insulating, so that the Bi^{3+}/Bi^{5+} valences are localised but not ordered. The absence of Jahn-Teller distortion of NiO_6 octahedra is in agreement with the Ni^{2+} (d^8) valence state, which is comparable with the Phase I environments of Ni^{2+}[13]. The Bi-O distances show the effects of Bi $6s^2$ lone pairs, where the displacement of Bi cation in the lattice is illustrated in Figure 5.11 (a). The directional Bi $6s^2$ lone pairs might result in ferroelectric character but these are diluted by 50 % undistorted Bi^{5+} states. A further synchrotron X-ray diffraction experiment is proposed at low temperatures with various pressures, in order to investigate the evolution of the structure from Phase I to Phase Id, which will help to clarify the origin of the insulating behaviour.

For $BiNiO_3$ in the moderate pressure and high temperature region of the phase diagram, the completion of a transition occurs at 1.8 GPa and 560 K to a *Pbnm* HT phase, which is comparable with recent SXRD measurements (Figure 5.4)[24]. However it is unclear whether the observed HT phase is a new metallic orthorhombic phase, or identical to the known $BiNiO_3$ Phase III. From the BVS calculation the different charge distributions between HT phase and Phase III were displayed (Figure 5.16 (b)), but the large errors indicate that the obtained BVS are only

approximate. Although the drastic change implied a phase transition above 300 K at ~ 5.2 GPa (Figure 5.15), the pressure-dependent experiments suggest that the obtained HT phase is possibly identical to the known $BiNiO_3$ Phase III. The difficulty of the experiment is due to the limited resolution of the data, which is caused by strain broadening due to the temperature and pressure gradients in the sample. To clarify the nature of the obtained high temperature orthorhombic phase, an investigation of the structural phase transition between the HT phase and Phase I and a comparison with high pressure Phase III is required. Therefore a detailed synchrotron study of the structural changes (*i.e.* lattice parameters and cell volume) is proposed and will be performed in the near future.

The magnetic behaviour of $BiNiO_3$ Phase I has previously been studied at ambient pressure, showing a *G*-type antiferromagnetic ordering down to 5 K[13], which is quite different to the rather complex magnetic structure of $RNiO_3$ materials[26-28]. Considering the weak intensity of magnetic reflection of $S = 1$ Ni^{2+} demonstrated by this previous study of Phase I[13], and also the subtle splittings revealed by the SPring-8 experiment (Figure 5.18 (a)), the PEARL data alone are insufficient to draw conclusions about Phase Id due to the limited resolution and *d*-spacing range available (Figure 5.18 (b)). The high resolution instrument Super-D2B is ideal to study not only the subtle distortion of the obtained HPLT phase (which will provide more precise information about the charge distribution) but also the evolution of magnetic ordering at high pressure (Figure 5.18 (c)). To achieve the desired experimental conditions, a modified Paris-Edinburgh cell model VX5[21,22] was used on Super-D2B. Due to the small amount of the loaded sample and also the neutron flux provided on Super-D2B, a pattern at 4.4(4) GPa and 78 K was collected for 40 hours, but the obtained poor counting statistics did not provide useful information (Figure 5.19). Either a larger sample cell on Super-D2B to give a stronger signal or the higher flux provided by D20 which gives slightly lower resolution in high resolution mode (Figure 5.18 (d)) will be considered for future experiments.

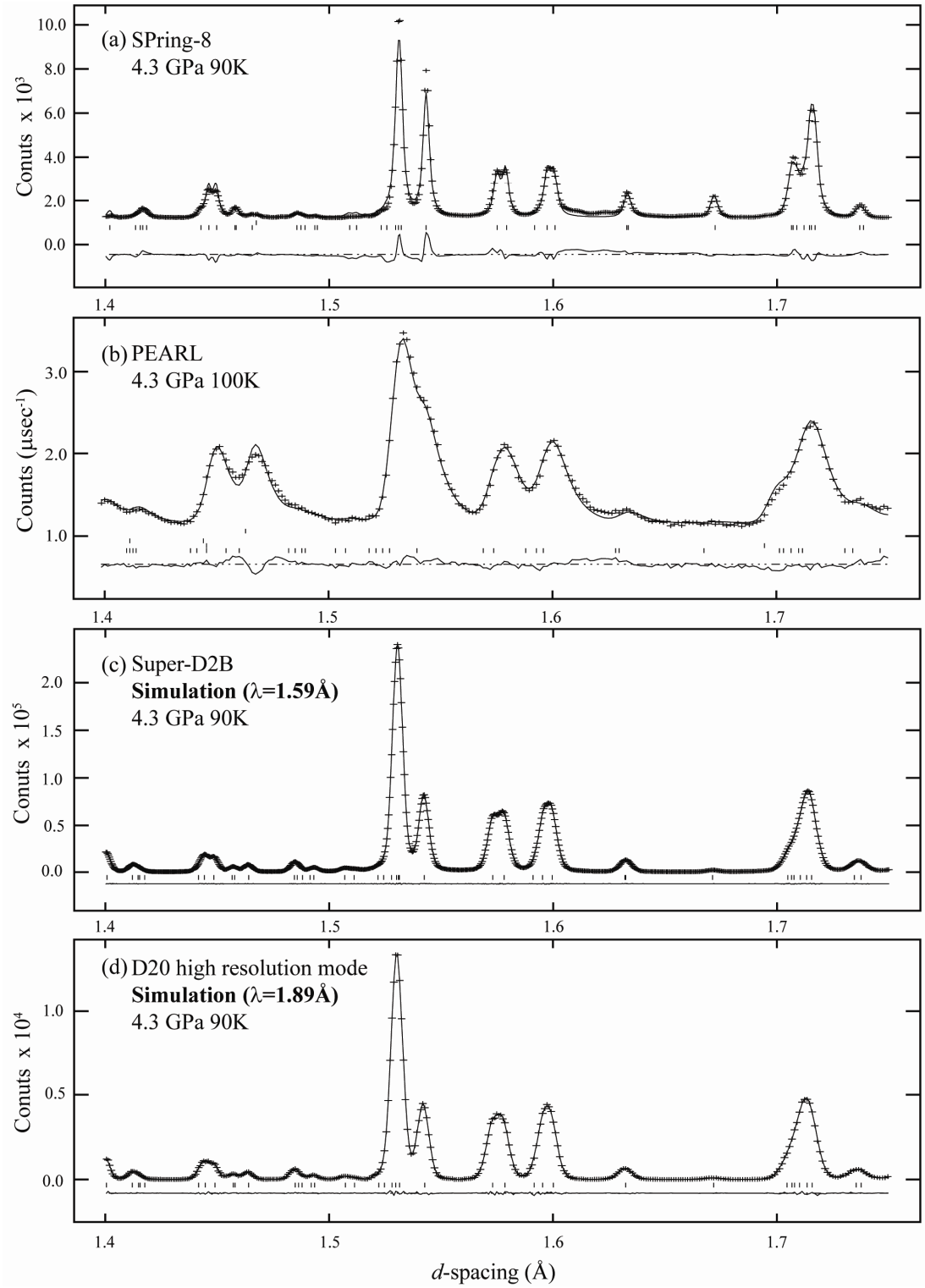

Figure 5.18 Comparison of patterns at 4.3 GPa and 90/100 K with certain *d*-spacing range of (a) synchrotron X-ray diffraction pattern from SPring-8, (b) neutron powder diffraction pattern from PEARL, (c) the simulation pattern for Super-D2B and (d) the simulation pattern for D20 high resolution mode.

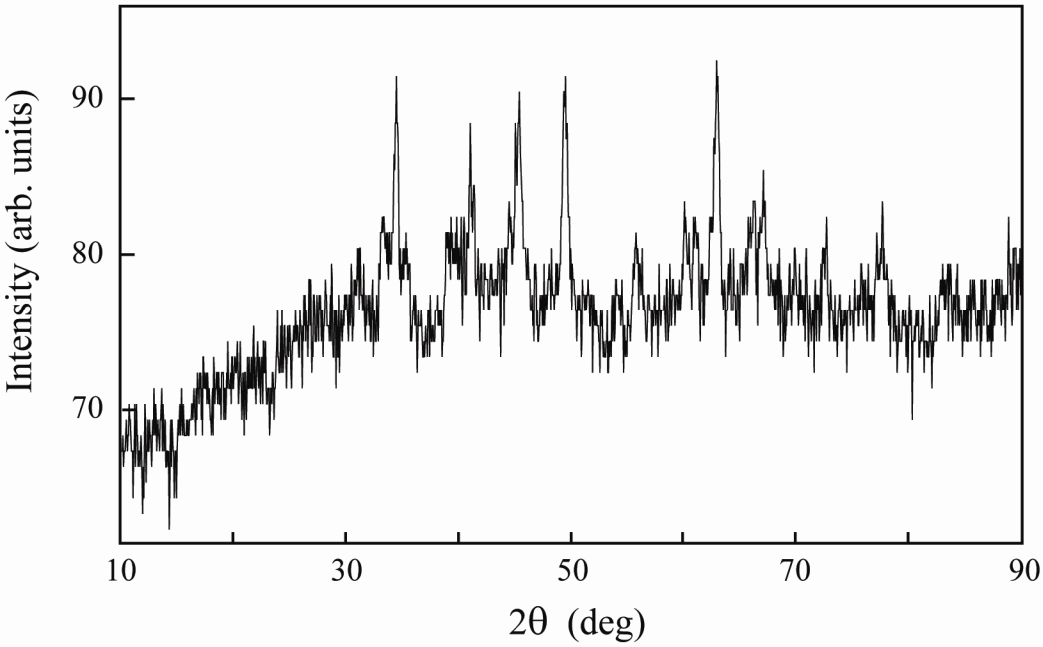

Figure 5.19 The diffraction profile collected at 4.4 GPa and 78 K for 40 hours on the Super-D2B instrument.

In summary, $BiNiO_3$ is a unique material showing a great variety of electronic states. Different pressure-temperature regions have been studied to investigate the possible charge distribution states of $BiNiO_3$. The phase boundary between triclinic insulating Phase I $(Bi^{3+}_{0.5}Bi^{5+}_{0.5})Ni^{2+}O_3$ and orthorhombic metallic Phase III $Bi^{3+}Ni^{3+}O_3$ was found between 3.2(2) and 3.7(2) GPa at room temperature. A new phase, namely Phase Id $(Bi^{3+}_{0.5}Bi^{5+}_{0.5})Ni^{2+}O_3$, was observed in a high-pressure low-temperature region. The obtained insulating phase is derived from Phase I, where the charge disproportionated *A*-site cations becomes disordered. Despite the observation of Pb-stabilized $(Bi_{0.8}Pb_{0.2})^{4+}Ni^{2+}O_3$, the existence of undoped Phase II $Bi^{4+}Ni^{2+}O_3$ at moderate pressure and elevated temperature was not found to be evident, and $Bi^{3+}Ni^{3+}O_3$ Phase III is assumed to be the probable obtained HT orthorhombic phase. Further detailed studies are necessary to investigate the structure and determine more accurate valence states of the $BiNiO_3$ phases and the nature of their transitions across the temperature and/or pressure boundaries.

5.5 References

1. M. L. Medarde, *J. Phys.: Condens. Matter,* **9**, 1679 (1997).
2. J. B. Torrance, P. Lacorre, A. I. Nazzal, E. J. Ansaldo, and C. Niedermayer, *Phys. Rev. B,* **45**, 8209 (1992).
3. J. L. García-Muñoz, J. Rodríguez-Carvajal, P. Lacorre, and J. B. Torrance, *Phys. Rev. B,* **46**, 4414 (1992).
4. J. A. Alonso, M. J. Martínez-Lope, M. T. Casais, J. L. García-Muñoz, and M. T. Fernández-Díaz, *Phys. Rev. B,* **61**, 1756 (2000).
5. J. A. Alonso, M. J. Martínez-Lope, M. T. Casais, J. L. García-Muñoz, M. T. Fernandez-Díaz, and M. A. G. Aranda, *Phys. Rev. B,* **64**, 094102 (2001).
6. P. Lacorre, J. B. Torrance, J. Pannetier, A. I. Nazzal, P. W. Wang, and T. C. Huang, *J. Solid State Chem.,* **91**, 225 (1991).
7. J. L. García-Muñoz, J. Rodríguez-Carvajal, and P. Lacorre, *Phys. B: Condens. Matter,* **180-181**, 306 (1992).
8. J. A. Alonso, M. J. Martínez-Lope, and I. Rasines, *J. Solid State Chem.,* **120**, 170 (1995).
9. J. A. Alonso, M. J. Martinez-Lope, M. T. Casais, J. L. Martinez, G. Demazeau, A. Largeteau, J. L. Garcia-Munoz, A. Munoz, and M. T. Fernandez-Diaz, *Chem. Mater.,* **11**, 2463 (1999).
10. T. Saito, M. Azuma, E. Nishibori, M. Takata, M. Sakata, N. Nakayama, T. Arima, T. Kimura, C. Urano, and M. Takano, *Phys. B: Condens. Matter,* **329-333**, 866 (2003).
11. T. Saito, M. Azuma, H. Kanda, E. Nishibori, M. Sakata, M. Takata, N. Nakayama, C. Urano, A. Asamitsu, T. Arima, and M. Takano, *unpublished,* (2004).
12. S. Ishiwata, M. Azuma, M. Takano, E. Nishibori, M. Takata, M. Sakata, and K. Kato, *J. Mater. Chem.,* **12**, 3733 (2002).
13. S. J. E. Carlsson, M. Azuma, Y. Shimakawa, M. Takano, A. Hewat, and J. P. Attfield, *J. Solid State Chem.,* **181**, 611 (2008).
14. S. Niitaka, M. Azuma, M. Takano, E. Nishibori, M. Takata, and M. Sakata, *Solid State Ionics,* **172**, 557 (2004).
15. A. A. Belik, S. Iikubo, T. Yokosawa, K. Kodama, N. Igawa, S. Shamoto, M. Azuma, M. Takano, K. Kimoto, Y. Matsui, and E. Takayama-Muromachi, *J. Am. Chem. Soc.,* **129**, 971 (2007).

16. A. A. Belik, S. Iikubo, K. Kodama, N. Igawa, S. Shamoto, S. Niitaka, M. Azuma, Y. Shimakawa, M. Takano, F. Izumi, and E. Takayama-Muromachi, *Chem. Mater.,* **18**, (2006).
17. M. Azuma, K. Takata, T. Saito, S. Ishiwata, Y. Shimakawa, and M. Takano, *J. Am. Chem. Soc.,* **127**, 8889 (2005).
18. S. Ishiwata, M. Azuma, and M. Takano, *Solid State Ionics,* **172**, 569 (2004).
19. M. Azuma, S. Carlsson, J. Rodgers, M. G. Tucker, M. Tsujimoto, S. Ishiwata, S. Isoda, Y. Shimakawa, M. Takano, and J. P. Attfield, *J. Am. Chem. Soc.,* **129**, 14433 (2007).
20. S. Ishiwata, M. Azuma, M. Hanawa, Y. Moritomo, Y. Ohishi, K. Kato, M. Takata, E. Nishibori, M. Sakata, I. Terasaki, and M. Takano, *Phys. Rev. B,* **72**, 045104 (2005).
21. H. Wadati, M. Takizawa, T. T. Tran, K. Tanaka, T. Mizokawa, A. Fujimori, A. Chikamatsu, H. Kumigashira, M. Oshima, S. Ishiwata, M. Azuma, and M. Takano, *Phys. Rev. B,* **72**, 155103 (2005).
22. S. Ishiwata, M. Azuma, and M. Takano, *Chem. Mater.,* **19**, 1964 (2007).
23. S. Takajo and Y. Uwatoko, Institute for Solid State Physics, University of Tokyo (*unpublished work*).
24. M. Azuma, Institute for Chemical Research, Kyoto University (*unpublished work*).
25. J. M. Besson, R. J. Nelmes, G. Hamel, J. S. Loveday, G. Weill, and S. Hull, *Phys. B: Condens. Matter,* **180-181**, 907 (1992).
26. J. A. Alonso, J. L. García-Muñoz, M. T. Fernandez-Díaz, M. A. G. Aranda, M. J. Martínez-Lope, and M. T. Casais, *Phys. Rev. Lett.,* **82**, 3871 (1999).
27. J. L. García-Muñoz, J. Rodríguez-Carvajal, and P. Lacorre, *Phys. Rev. B,* **50**, 978 (1994).
28. J. Rodríguez-Carvajal, S. Rosenkranz, M. Medarde, P. Lacorre, M. T. Fernandez-Díaz, F. Fauth, and V. Trounov, *Phys. Rev. B,* **57**, 456 (1998).

Chapter 6

Structural and Magnetic Studies of $BiCu_3Mn_4O_{12}$

6.1 Introduction

Due to high interest in both fundamental properties and technological applications, considerable attention has been paid to the $R_{1-x}A_xMnO_3$ (R = rare earth, A = alkali earth) manganese perovskites, which exhibit colossal magnetoresistance (CMR)[1,2]. The CMR materials can be generally grouped into two types, intrinsic and extrinsic, depending on the origin of their magnetoresistive (MR) properties. Recently, a new structural type of manganese perovskites, of which $CaCu_3Mn_4O_{12}$ is the most known example, have also revealed interesting MR behaviour[3-6]. This material adopts an $AA'_3B_4O_{12}$ structure derived from the simple ABO_3 perovskite, which was studied in the 1970s owing to its high magnetic transition temperature[7,8]. The valence state distribution is $Ca^{2+}Cu^{2+}{}_3Mn^{4+}{}_4O_{12}$, with a 1:3 Ca^{2+}/Cu^{2+} cation ordering at the A and A' sites of the perovskite cell and a tilted three-dimensional network of corner-shared MnO_6 octahedra where the Mn-O-Mn angle is ~ 142 º (Figure 6.1(a)). The ordering of A and A' cations results from the distortion of the cell, in which Ca^{2+} shows an isotropically coordinated AO_{12} configuration while the Cu^{2+} cation sits in a heavily distorted $A'O_{12}$ polyhedron (Figure 6.1 (b) and (c)). There are three sets of Cu^{2+}-O distances exhibited in the $A'O_{12}$ polyhedra, and a typical square-planar coordination for the Cu^{2+} (d^9) cation is formed by the four short Cu-O bonds ~1.9 Å (Figure 6.1 (d))[9,10]. It should be noted that in the $AA'_3B_4O_{12}$ structure, the A' site tends to accommodate a Jahn-Teller distorted ion, *e.g.* Cu^{2+} (d^9) or Mn^{3+} (d^4). Thus in the Mn-substituted $CaCu_{3-x}Mn_{4+x}O_{12}$ materials, the introduction of Mn^{3+} induces mixed-valences $Ca^{2+}(Cu^{2+}{}_{3-x}Mn^{3+}{}_x)(Mn^{4+}{}_{4-x}Mn^{3+}{}_x)O_{12}$[9]. The injection of electrons into the B sites results in an enhancement of the MR effect[10-12].

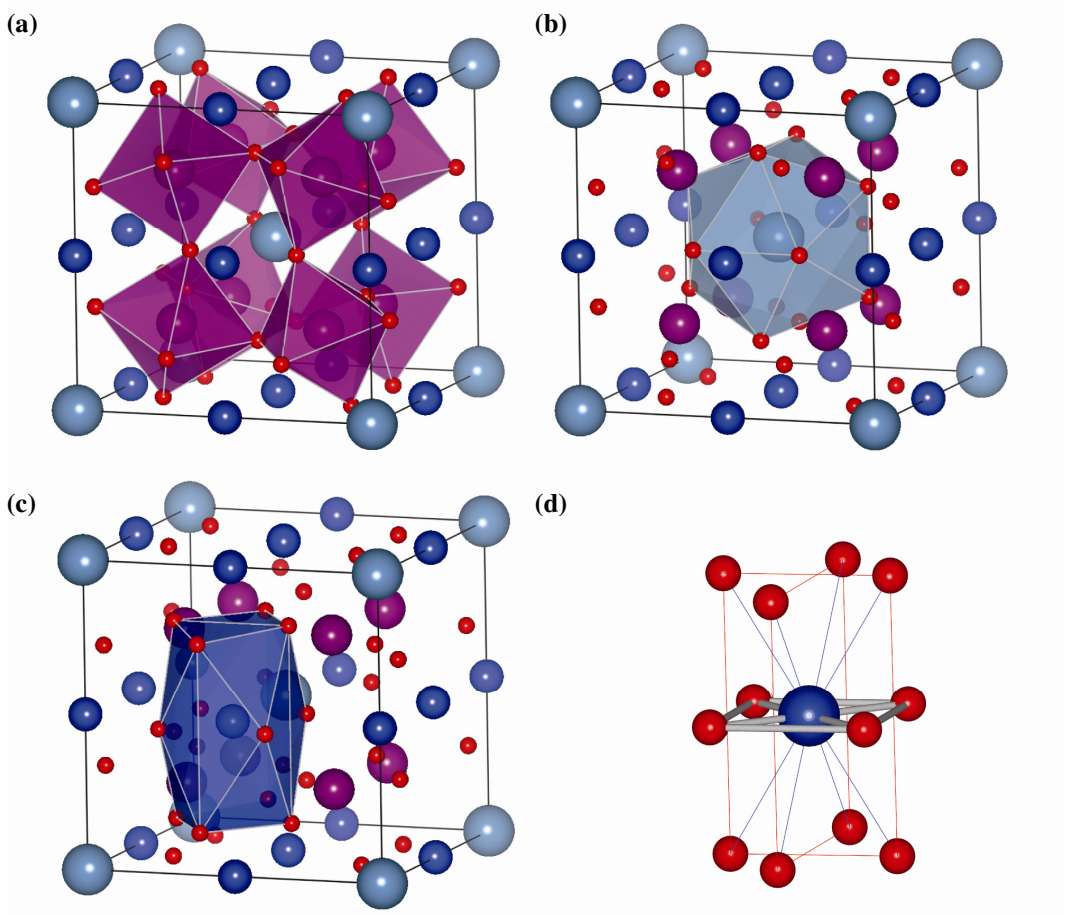

Figure 6.1 The crystal structure of $CaCu_3Mn_4O_{12}$ showing (a) the tilting network of MnO_6 octahedra, (b) the CaO_{12} polyhedra, (c) 12-coordinated polyhedra at Cu site and (d) the short Cu^{2+}-O bonds forming square-planar coordination.

$CaCu_3Mn_4O_{12}$ has a magnetic transition temperature T_C at 355 K[10], which decreases with increasing Mn doping at the Cu site[10,12]. In this phase, magnetic moments of the *B*-site Mn^{3+}/Mn^{4+} are coupled ferromagnetically and are antiparallel to the moments at *A'*-site Cu^{2+} in $YCu_{2.3}Mn_{4.7}O_{12}$[8], resulting in a ferrimagnetic state. The ferrimagnetic configuration of $CaCu_3Mn_4O_{12}$ has been predicted by band structure calculation[6]. The Mn^{3+}/Mn^{4+} mixed-valence state, which is achieved by substitution at the Cu *A*' site, may also be accessed by doping of the Ca^{2+} *A* site with a cation of a different valence. Systematic studies of $RCu_3Mn_4O_{12}$ have been reported where *R* = rare earth with R^{3+}: La^{3+}, Pr^{3+}… to Yb^{3+}[3,11-15] or R^{4+}: Ce^{4+} and Th^{4+}[7,10]. The La^{3+} analogue exemplifies how Mn^{3+}/ Mn^{+4} mixed-valence states may be achieved by doping at both the *A* and *A*' sites[11].

The observed cell volumes of $R Cu_3Mn_4O_{12}$ perovskite materials can be related to two main factors: the sizes of the MnO_6 octahedra and the RO_{12} polyhedra. The cell volume differences between R^{2+}, R^{3+} and R^{4+} series analogues are considerable. This is owing to the large variation in size of the MnO_6 octahedra, which contain Mn^{4+}, $Mn^{3.75+}$ and $Mn^{3.5+}$ as a result of the Mn^{3+} doping at the Mn^{4+} site. However in contrast to $RMnO_3$ perovskites, the size of RO_{12} in $R^{3+}Cu_3Mn_4O_{12}$ is mainly responsible for the cell volume, since the variations of Mn-O distances are rather insignificant across the series[14,15]. It was reported that the ferrimagnetic ordering observed in $CaCu_3Mn_4O_{12}$-type materials is also observed in R analogues[12,13,16]. With the electron doping at B site, enhancement of the MR effect has been reported[12,14].

Recently, a bismuth analogue $BiCu_3Mn_4O_{12}$ has been reported which was prepared by high-pressure synthesis[17]. From the synchrotron X-ray diffraction experiment it was found that the material adopts $Im\bar{3}$ symmetry as observed in the reported $AA'_3B_4O_{12}$ family. Although the Mn substitution on Cu A' site was reported in $CaCu_3Mn_4O_{12}$[16] and $LaCu_3Mn_4O_{12}$[11], such introduction of Mn was not observed in $BiCu_3Mn_4O_{12}$. A spontaneous magnetisation below a relatively high $T_C = 350$ K was observed in the material, which has a saturated magnetic moment of 10.5 μ_B at 5 K and the saturation occurs at approximately 0.5 T. A ferrimagnetic behaviour of the material was suggested based on the magnetic measurements. The material has semiconducting high temperature behaviour and becomes metallic below T_C. $BiCu_3Mn_4O_{12}$ shows a large magnetoresistance under low magnetic fields over a wide temperature range below T_C, which is due to extrinsic effects of the polycrystalline samples. At 5 K, the MR below 1 T is as large as −28 %, and reaches −31 % at 5 T. The calculated band structure is very similar to that reported for $LaCu_3Mn_4O_{12}$[18]. In order to investigate the magnetic behaviour further and obtain an accurate composition, neutron powder diffraction experiments were performed on the high-resolution Super-D2B instrument from 5 to 400 K, that is, above and below the transition.

6.2 Experimental

Sample Preparation

The $BiCu_3Mn_4O_{12}$ sample used in this study was prepared with a high-pressure synthesis technique by Dr. K. Takata *et al.* at the Institute for Chemical Research, Kyoto University, Japan[17]. MnO_2 was prepared by firing MnOOH powder at 300 ºC in air and stoichiometric amounts of Bi_2O_3, CuO, Mn_2O_3 and MnO_2 were then sealed into a gold capsule. The starting materials were treated in 6 GPa and 1000 ºC for 30 minutes with a cubic anvil-type high pressure apparatus. After the treatment the sample was quenched to room temperature before releasing the applied pressure.

Neutron Powder Diffraction

Neutron powder diffraction data from a ~0.4 g polycrystalline sample packed in a vanadium can were collected on instrument Super-D2B at the ILL, Grenoble. The patterns at certain temperature points from 5 to 400 K were collected in the angular range $5\,° \leq 2\theta \leq 155\,°$ for 4 hours per scan with a neutron wavelength of 1.594 Å without collimation. The neutron diffraction data were analysed by the Rietveld method using the GSAS software package.

6.3 Results

Neutron powder diffraction patterns collected on Super-D2B from 5 to 400 K are shown in Figure 6.2. The structural refinements of $BiCu_3Mn_4O_{12}$ were performed by the Rietveld method in the $Im\bar{3}$ (No. 204) space group, with the starting model from reported synchrotron X-ray diffraction data[17]. The material crystallised in an $AA'_3B_4O_{12}$ perovskite-like phase of cubic symmetry with a $2 \times 2 \times 2$ superlattice of the primitive cubic perovskite cell. The doubling of all unit cell parameters is owing to the 1:3 Bi^{3+} and Cu^{2+} ordering at A and A' sites and the tilting of the corner-shared MnO_6 octahedra. In the refinement the atomic positions were taken from the

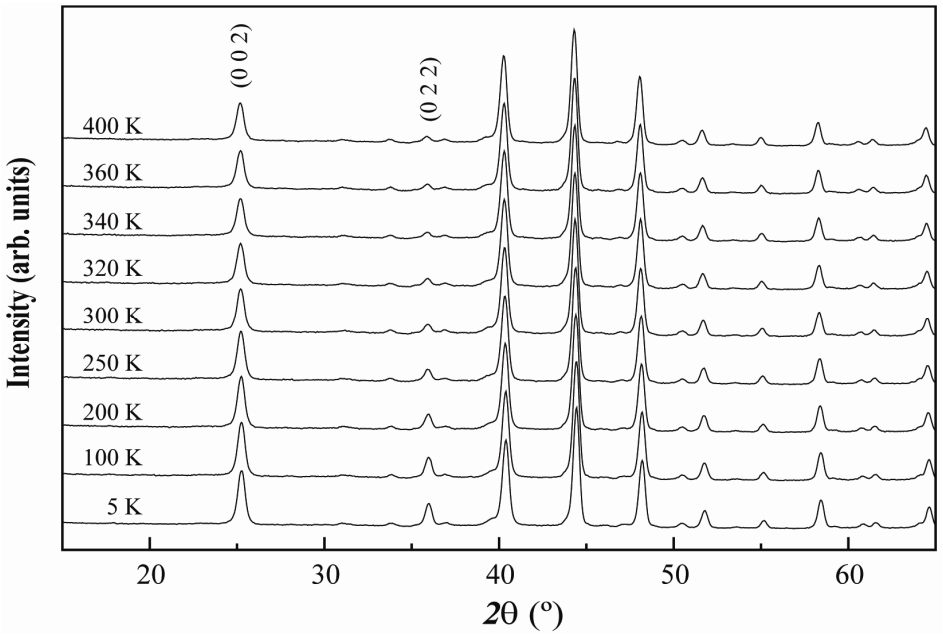

Figure 6.2 The evolution of NPD patterns of $BiCu_3Mn_4O_{12}$ from 5 to 400 K with selected 2θ range, showing the superposed magnetic contributions on (0 0 2) and (0 2 2) reflection.

$CaCu_3Mn_4O_{12}$ model[7], where Bi atoms were placed at *A* site 2*a* (0, 0, 0) positions, Cu at *A′* site 6*b* (0, ½, ½) positions, Mn at *B* site 8*c* (¼, ¼, ¼) positions and O at 24*g* (*x*, *y*, 0) sites. From the refinements no apparent oxygen vacancy was observed, thus the stoichiometric occupancy was fixed. Since the 6*b* crystallographic site is suitable for Jahn-Teller cations such as Cu^{2+} or Mn^{3+} the possibility of Mn substitution in Cu site was considered. The Mn^{3+} substitution consequently introduces Mn^{3+} into 8*c* position, however no extra peaks indicating Cu^{2+}/Mn^{3+} or Mn^{4+}/Mn^{3+} ordering are observed from the patterns. Therefore Mn was introduced into Cu position without ordering and a noticeable improvement of the fits was achieved giving the crystallographic formula $Bi(Cu_{2.50(2)}Mn_{0.50(2)})Mn_4O_{12}$. The indexed impurities CuO and $Bi_2(CO_3)O_2$ were taken into account to the fits with the weight fractions of 8.72 and 0.14 %, respectively. An instrumental peak contribution at $2\theta \sim 120°$ was excluded. A reasonable fit with $R_{wp} = 4.88$ % was achieved for the pattern collected at 300 K, although the high χ^2 is possibly due to the existence of an unidentified impurity at $2\theta \sim 40°$.

Comparing NPD patterns collected from 5 to 400 K, superimposed magnetic contributions on the low angle Bragg reflections (0 0 2) and (0 2 2) were observed (Figure 6.2). The contribution is characteristic for ferromagnetic ordering, in which the magnetic ordering coincides with the crystallographic unit cell. No extra magnetic reflections were observed, implying the absence of any antiferromagnetic ordering. Although the composition $Bi(Cu_{2.5}Mn_{0.5})Mn_4O_{12}$ obtained from nuclear structure refinement gives rise to Mn^{3+} substitution at both *A′* and *B* sites, for the simplicity of refinement, only the Cu^{2+} and Mn^{4+}magnetic scattering factors were used for 6*b* and 8*c* sites, respectively. A weak magnetic moment for Cu^{2+} was obtained at 5 and 100 K from the refinements. At higher temperatures the refinement of the Cu^{2+} magnetic moment becomes unstable, therefore the moment was fixed to be zero from 200 K upwards. A reasonable fit to 5 K data was achieved with R_{wp} = 5.26 %. The representative fits to patterns collected at 5 and 400 K are shown in Figure 6.3. The refinement results of the structure parameters and detailed atomic information are summarised in Table 6.1, while selected bond distances and angles of Bi, Cu and Mn polyhedra are listed in Table 6.2.

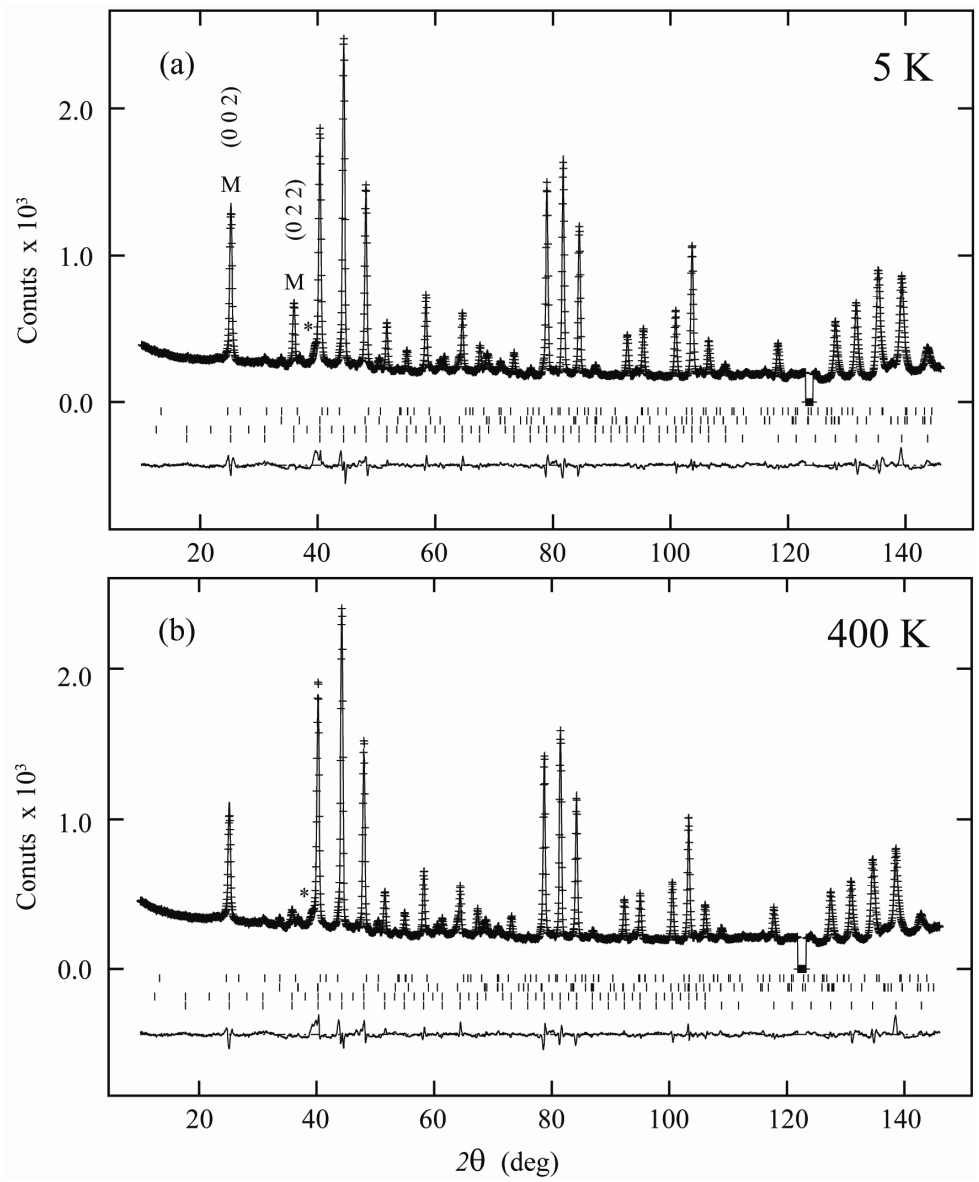

Figure 6.3 The Rietveld fits of $BiCu_3Mn_4O_{12}$ at (a) 5 K, where the magnetic contribution at (0 0 2) and (0 2 2) reflections are marked "M", and (b) 400 K, which is above the magnetic transition temperature showing only nuclear reflections. The unidentified impurity is marked by asterisk, and the instrument peak contribution at 2θ ~120 º was excluded.

Table 6.1 Refined parameters of $BiCu_3Mn_4O_{12}$ with cubic structure at various temperatures, lattice parameter, cell volume, isotropic thermal factor, atomic coordinations, magnetic moment, and reliability factors R_{wp} and χ^2 are listed.

Temperature (K)		5	100	200	250	300	320	340	360	400
a (Å^2)		7.31337(8)	7.31482(8)	7.31871(8)	7.32146(8)	7.32471(8)	7.32623(8)	7.32782(9)	7.32932(9)	7.33237(9)
V (Å^3)		391.16(1)	391.39(1)	392.02(1)	392.46(1)	392.98(1)	393.23(1)	393.48(1)	393.72(1)	394.22(1)
Bi	U_{iso} (Å^2)	0.013(1)	0.0151(9)	0.018(1)	0.019(1)	0.021(1)	0.021(1)	0.022(1)	0.023(1)	0.024(1)
Cu	U_{iso} (Å^2)	0.0074(9)	0.0081(5)	0.0097(5)	0.0104(5)	0.0116(5)	0.0124(5)	0.0124(5)	0.0128(5)	0.0138(5)
	m_z (μ_B)	0.31(6)	0.21(5)	0	0	0	0	0	0	0
Mn	U_{iso} (Å^2)	0.0067(6)	0.0072(6)	0.0077(6)	0.0081(6)	0.0082(6)	0.0078(6)	0.0075(6)	0.0074(6)	0.0076(6)
	m_z (μ_B)	2.76(5)	2.67(5)	2.26(5)	1.97(7)	1.58(10)	0.67(10)	0	0	0
O	x	0.3054(2)	0.3054(2)	0.3054(2)	0.3055(2)	0.3054(2)	0.3055(2)	0.3054(2)	0.3056(2)	0.3055(2)
	y	0.1822(2)	0.1820(2)	0.1821(2)	0.1820(2)	0.1822(2)	0.1823(2)	0.1824(2)	0.1824(2)	0.1825(2)
	U_{iso} (Å^2)	0.0040(6)	0.0043(3)	0.0056(3)	0.0063(3)	0.0070(3)	0.0073(3)	0.0070(3)	0.0075(3)	0.0083(3)
R_{wp} (%)		5.26	5.12	4.99	4.93	4.88	4.90	4.89	4.91	4.80
χ^2		18.32	11.99	11.53	11.31	11.13	11.18	11.24	11.37	16.44

For the cubic model atom positions are Bi, 2*a*, (0, 0, 0); Cu, 6*b*, (0, ½, ½); Mn, 8*c*, (¼, ¼, ¼); O, 24*g*, (*x*, *y*, 0) in space group $Im\bar{3}$ (No. 204). The magnetic moment of Cu and Mn are fixed to 0 above 200 and 340 K, respectively.

Table 6.2 Refined results of $BiCu_3Mn_4O_{12}$ with cubic structure at various temperatures, selected bond distance and angle for Bi, Cu and Mn poluhedra, and BVS results are listed.

Temperature (K)	5	100	200	250	300	320	340	360	400
Bi-O ×12 (Å)	2.6006(17)	2.6004(17)	2.6025(17)	2.6035(17)	2.6047(17)	2.6063(18)	2.6065(18)	2.6086(18)	2.6094(18)
Bi-BVS	3.05	3.05	3.03	3.02	3.02	3.00	3.00	2.99	2.98
Cu-O ×4 (Å)	1.949(1)	1.949(1)	1.950(1)	1.950(1)	1.953(1)	1.953(1)	1.954(1)	1.954(1)	1.955(1)
Cu-O ×4 (Å)	2.726(2)	2.727(2)	2.728(2)	2.729(2)	2.730(2)	2.729(2)	2.730(2)	2.729(2)	2.730(2)
Cu-O ×4 (Å)	3.224(1)	3.225(1)	3.227(1)	3.228(1)	3.228(1)	3.229(1)	3.229(1)	3.230(1)	3.231(1)
O-Cu-O[a] (°)	93.8(1)	93.8(1)	93.8(1)	93.8(1)	93.8(1)	93.7(1)	93.7(1)	93.6(1)	93.7(1)
O-Cu-O[a] (°)	86.2(1)	86.2(1)	86.2(1)	86.2(1)	86.2(1)	86.3(1)	86.3(1)	86.4(1)	86.4(1)
Mn-O ×6 (Å)	1.9373(4)	1.9379(4)	1.9389(4)	1.9399(4)	1.9402(3)	1.9406(4)	1.9408(4)	1.9414(4)	1.9420(4)
Mn-BVS	3.67	3.66	3.65	3.65	3.64	3.64	3.64	3.63	3.63
O-Mn-O (°)	89.47(7)	89.50(7)	89.47(7)	89.47(7)	89.47(7)	89.42(7)	89.44(7)	89.38(7)	89.39(7)
O-Mn-O (°)	90.53(7)	90.50(7)	90.53(7)	90.53(7)	90.53(7)	90.58(7)	90.56(7)	90.62(7)	90.61(7)
Cu-O-Mn (°)	109.13(3)	109.14(3)	109.14(3)	109.16(3)	109.12(3)	109.12(3)	109.10(3)	109.13(3)	109.11(3)
Mn-O-Mn (°)	141.38(6)	141.36(6)	141.35(6)	141.32(6)	141.41(6)	141.41(6)	141.45(6)	141.41(6)	141.45(6)

[a] For the CuO_4 square-plane with short Cu-O distances.

The crystal and magnetic structures of $BiCu_{2.5}Mn_{4.5}O_{12}$ are illustrated in Figure 6.4. As shown, the magnetic structure of this phase consists of *A′* and *B* cations ferromagnetically ordered along the c axis. Refined magnetic moments at 5 K are 2.76(5) and 0.31(6) μ_B for Mn^{4+} and Cu^{2+} sites, respectively. The temperature dependent evolution of the lattice parameters and selected bond distances are displayed in Figure 6.5. The distances increase gradually with increasing temperature, showing a typical thermal expansion in the range of 5 to 400 K, which indicates no structural phase transition occurs over the interval. The Bi^{3+} and $Mn^{3.64+}$ valences are evident from the bond valence sum (BVS) calculation (Figure 6.6). The evolution of refined magnetic moments at *A′* and *B* sites are illustrated in Figure 6.7 (a) and (b), respectively. The observed trend for the Mn atom was fitted with the expression $M(T) = M_0 (1 - T/T_C)^{\beta}$ to determine the transition temperature T_C. This permitted the fit of the critical exponent β, which was found to be 0.22. The fitting gives a maximum saturation magnetic moment of M_0 = 2.79(4) μ_B and a T_C = 320.5(8) K.

The Mn site moment decreases gradually from 5 K to room temperature and drops steeply around 320 K, indicating a magnetic transition at T_C. Additionally, the behaviour of Cu moment implies a low temperature transition between 100 and 200 K, however this was not evident from the reported magnetic measurement[17].

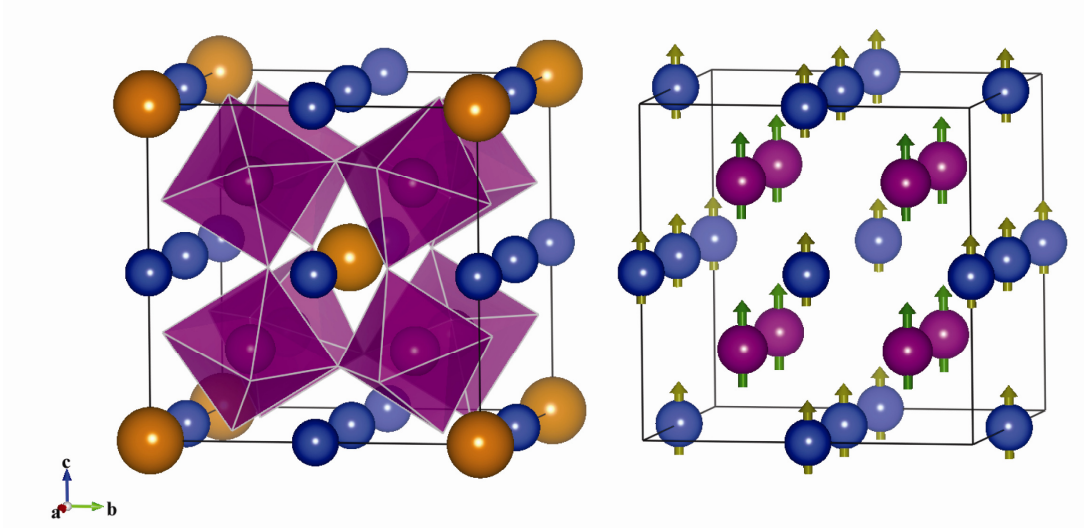

Figure 6.4 Crystal structure and magnetic ordering of $BiCu_{2.5}Mn_{4.5}O_{12}$ at 5 K. The violet octahedra correspond to MnO_6, where Bi, Cu and Mn atoms are represent by orange, blue and violet spheres, respectively. The refined magnetic moments at Cu and Mn sites are shown in olive and green arrows, respectively.

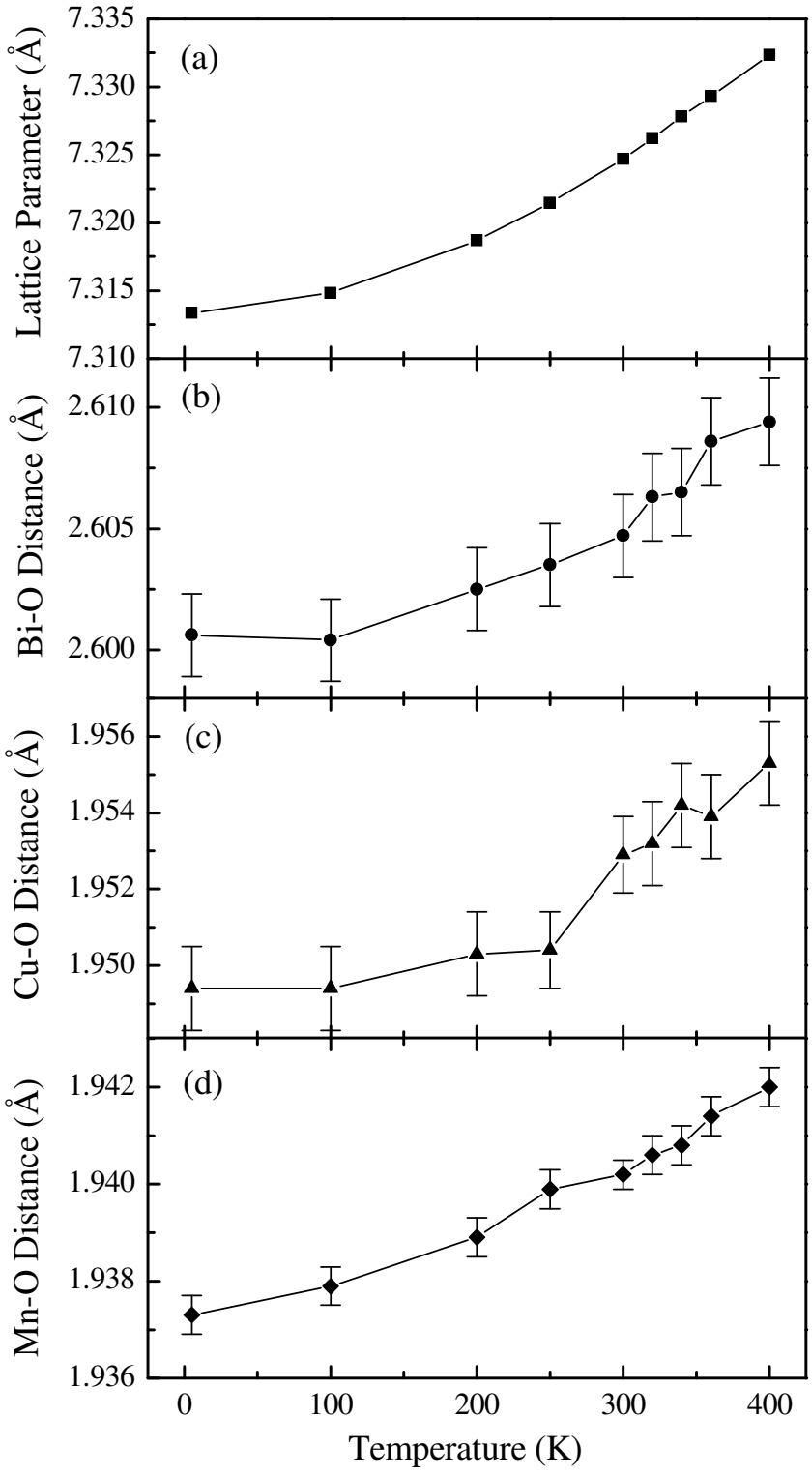

Figure 6.5 Temperature dependent evolution of (a) lattice parameter, where the error bar is smaller than the marker, (b) the *A*-site Bi-O distance, (c) the short *A'*-site Cu-O distance, and (d) the *B*-site Mn-O distance.

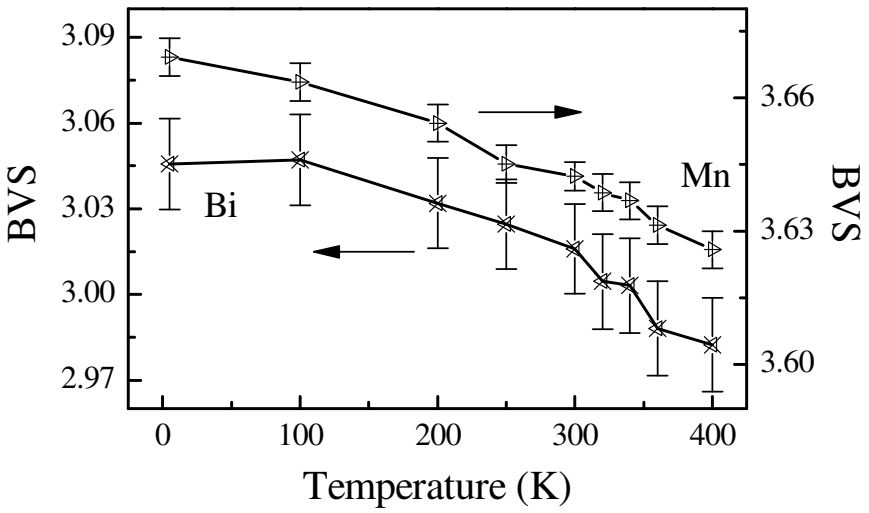

Figure 6.6 Bi and Mn valences from the BVS calculation for $BiCu_{2.5}Mn_{4.5}O_{12}$ material.

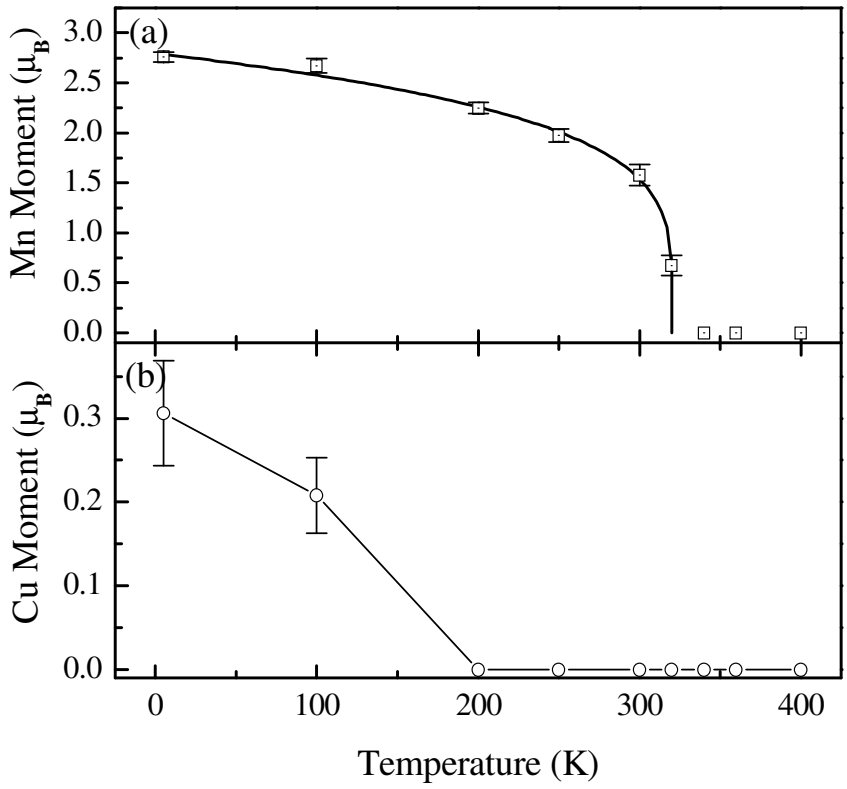

Figure 6.7 Temperature dependent evolution of magnetic moment at (a) Mn 8*c* site which shows a transition at about 320 K, and (b) Cu 6*b* site which indicates a low temperature transition between 100 and 200 K.

6.4 Discussion

The neutron powder diffraction experiment has allowed the complete description of the crystal and magnetic structures of $BiCu_3Mn_4O_{12}$. This material has $AA'_3B_4O_{12}$ cubic symmetry with space group $Im\bar{3}$, as shown in similar perovskites such as $CaCu_3Mn_4O_{12}$[7] and $RCu_3Mn_4O_{12}$ (R = rare earth: La, Pr, Nd…)[12-15]. Unlike the Ca analogue $Ca^{2+}Cu^{2+}{}_3Mn^{4+}{}_4O_{12}$, it was reported that the replacement of divalent Ca^{2+} with trivalent Bi^{3+} introduces Mn^{3+} into B sites, resulting in a $Bi^{3+}Cu^{2+}{}_3(Mn^{3+}Mn^{4+}{}_3)O_{12}$ mixed valence material with the average charge assigned to Mn equal to 3.75+[17].

Temperature-dependent NPD data from 400 down to 5 K indicates that there is no distortion from cubic symmetry. No indication of Mn^{3+}/Mn^{4+} charge and orbital ordering was observed. Unlike similar compounds, some A' and B site substitutional disorder has been found. This is consistent with the A' site being suitable for Jahn-Teller distorted ions, such as Mn^{3+} and Cu^{2+}. As a consequence, the nuclear refinement from NPD shows the crystallographic composition of the material to be $Bi(Cu_{2.5}Mn_{0.5})Mn_4O_{12}$ rather than the reported $BiCu_3Mn_4O_{12}$. This deficiency in Cu leads to the incorporation of extra Mn^{3+} ions in the Cu site, consequently forming the mixed-valence state $Mn^{3.63+}$ that results from $Bi^{3+}(Cu^{2+}{}_{2.5}Mn^{3+}{}_{0.5})(Mn^{3+}{}_{1.5}Mn^{4+}{}_{2.5})O_{12}$. This is in agreement with the Mn valence of 3.64+ at room temperature evident by BVS calculation, while the 3+ valence of Bi over the temperature range was also confirmed by BVS.

The determined structure of $BiCu_{2.5}Mn_{4.5}O_{12}$ from NPD refinement shows isotropically coordinated Bi cations with 12 oxygen ions, which gives the Bi-O bond length of 2.605(2) at 300 K. The reported $LaCu_{2.5}Mn_{4.5}O_{12}$[11] consists of an A cation La^{3+} which has similar ionic radius comparing to Bi^{3+}. In addition, the same $A^{3+}Cu_{2.5}Mn_{4.5}O_{12}$ composition gives rise to the same Mn valence at 8c site. This is evident by the similarity in the lattice parameters 7.32471(8) and 7.3272(4) Å for Bi and La phases, respectively. A thermal expansion of the unit cell was observed from 5 to 400 K, while the changes of Cu-O-Mn and Mn-O-Mn angles are insignificant, confirming that the structure symmetry remains unchanged over the interval. The

refined Cu-O-Mn and Mn-O-Mn angles are similar to those of the R^{3+} analogues[3,9,11-13], and show the insensitivity of MnO_6 tilting as *A* cations and temperature are varied. The refined mean Mn-O distance is 1.9402(3) Å, this is significantly longer than 1.915(1) Å observed for $CaCu_3Mn_4O_{12}$[7] and comparable to 1.940(2) Å for La analogue[11]. This is consistent with the introduction of the larger Mn^{3+} cation into Mn 8*c* sublattice forming the mixed-valence $Mn^{3.63+}$. An expansion of the short Cu/Mn-O distance in square-planar configurations was also observed, with the refined value of 1.953(1) Å compared to 1.942(3) Å of $CaCu_3Mn_4O_{12}$[7], confirming the incorporation of Mn^{3+} into Cu 6*b* sites.

The Mn-O-Mn angle in $BiCu_{2.5}Mn_{4.5}O_{12}$ material is ~142 º, an intermediate value between 180 º where antiferromagnetic ordering of Mn moments is expected and 90 º for which ferromagnetic ordering is predicted from Goodenough-Kanamori rules[19]. For $CaCu_3Mn_4O_{12}$, an antiferromagnetic coupling between Mn and Cu magnetic moments was suggested from band structure calculation[6]. Ferrimagnetic ordering was demonstrated in $CaCu_{3-x}Mn_{4+x}O_{12}$[16] and $RCu_3Mn_4O_{12}$[4,10,11] materials, and was also suggested in Bi analogue by magnetisation measurements[17]. Recent magnetic circular dichroic (MCD) results based on $BiCu_3Mn_4O_{12}$ composition also support this conclusion[20]. However a ferromagnetic ordering of Mn and Cu moments in $BiCu_{2.5}Mn_{4.5}O_{12}$ at low temperatures was revealed by NPD refinement. Furthermore, the observed Cu magnetic behaviour (Figure 6.7) indicates that either a low temperature transition of Cu moments exists between 100 and 200 K, or the Cu moments were induced by Mn magnetic ordering at low temperature. It should be noted that the observation is different from reported Ca and rare earth analogues, which show that the Cu moments ordered spontaneously and remained antiparallel to Mn moments up to room temperature[11,14].

It was reported that in $CaCu_{2.5}Mn_{4.5}O_{12}$[16] a canting angle exists between ordered Mn moments at *A* sites giving an extra (1 1 1) magnetic reflection, and also the incorporated Mn^{3+} at Cu 6*b* site has magnetic moments almost perpendicular to those of Cu. Although the NPD refinements demonstrated the similarity in the composition of $BiCu_{2.5}Mn_{4.5}O_{12}$ material, the extra magnetic reflection, resulting from the canted magnetic moments was not observed. The refined moments at Mn 8*c*

and Cu 6*b* sites in the material at 5 K are 2.76(5) and 0.31(6) μ_B, respectively. This gives a total magnetic moment of 12.0(4) μ_B/f.u. with a ferromagnetic ordering configuration which is comparable to the reported saturated moment 10.5 μ_B/f.u. at 5 K[17]. The magnetic moment of 2.76(5) μ_B at Mn 8*c* position is lower than the expected moment of 3.38 μ_B for $Mn^{3+}_{1.5}Mn^{4+}_{2.5}$, which is possibly due to electronic delocalisation from covalent effects.

In summary, the temperature-dependent neutron powder diffraction study of $BiCu_3Mn_4O_{12}$ material has been performed from 5 to 400 K, and no structural phase transition was observed. The NPD refinement revealed the incorporation of Mn^{3+} into Cu 6*b* site hence giving the composition $BiCu_{2.5}Mn_{4.5}O_{12}$ rather than reported $BiCu_3Mn_4O_{12}$. Although the ferrimagnetic behaviour of the material was reported, a ferromagnetic ordering of Mn and Cu moments was shown in the present work. The Cu magnetic behaviour indicates either a low temperature transition between 100 and 200 K exists, or that the Cu moments were induced by the Mn magnetic ordering at low temperature. Canting between Mn and Cu moments as in $CaCu_{2.5}Mn_{4.5}O_{12}$ was not observed in the Bi analogue.

6.5 References

1. R. von Helmolt, J. Wecker, B. Holzapfel, L. Schultz, and K. Samwer, *Phys. Rev. Lett.,* **71**, 2331 (1993).
2. S. Jin, T. H. Tiefel, M. McCormack, R. A. Fastnacht, R. Ramesh, and L. H. Chen, *Science,* **264**, 413 (1994).
3. I. O. Troyanchuk, L. S. Lobanovsky, N. V. Kasper, M. Hervieu, A. Maignan, C. Michel, H. Szymczak, and A. Szewczyk, *Phys. Rev. B,* **58**, 14903 (1998).
4. Z. Zeng, M. Greenblatt, M. A. Subramanian, and M. Croft, *Phys. Rev. Lett.,* **82**, 3164 (1999).
5. H. Wu, Q.-Q. Zheng, and X.-G. Gong, *Phys. Rev. B,* **61**, 5217 (2000).
6. R. Weht and W. E. Pickett, *Phys. Rev. B,* **65**, 014415 (2001).
7. J. Chenavas, J. C. Joubert, M. Marezio, and B. Bochu, *J. Solid State Chem.,* **14**, 25 (1975).

8. B. Bochu, J. C. Joubert, A. Collomb, B. Ferrand, and D. Samaras, *J. Magn. Magn. Mater.,* **15-18**, 1319 (1980).
9. Z. Zeng, M. Greenblatt, J. E. Sunstrom, M. Croft, and S. Khalid, *J. Solid State Chem.,* **147**, 185 (1999).
10. Z. Zeng, M. Greenblatt, and M. Croft, *Phys. Rev. B,* **58**, R595 (1998).
11. J. A. Alonso, J. Sánchez-Benítez, A. De Andrés, M. J. Martínez-Lope, M. T. Casais, and J. L. Martínez, *Appl. Phys. Lett.,* **83**, 2623 (2003).
12. J. Sánchez-Benítez, J. A. Alonso, A. de Andrés, M. J. Martínez-Lope, M. T. Casais, and J. L. Martínez, *J. Magn. Magn. Mater.,* **272-276**, E1407 (2004).
13. J. Sánchez-Benítez, J. A. Alonso, A. de Andrés, M. J. Martínez-Lope, J. L. Martínez, and A. Muñoz, *Chem. Mater.,* **17**, 5070 (2005).
14. J. Sánchez-Benítez, J. A. Alonso, H. Falcon, M. J. Martínez-Lope, A. D. Andrés, and M. T. Fernández-Díaz, *J. Phys.: Condens. Matter,* **17**, S3063 (2005).
15. J. Sánchez-Benítez,"*Síntesis y caracterización de las perovskitas complejas derivadas de CaCu3Mn4O12 con propiedades magnetorresistivas* " PhD Thesis (2005).
16. J. Sánchez-Benítez, J. A. Alonso, M. J. Martínez-Lope, M. T. Casais, J. L. Martínez, A. de Andrés, and M. T. Fernández-Díaz, *Chem. Mater.,* **15**, 2193 (2003).
17. K. Takata, I. Yamada, M. Azuma, M. Takano, and Y. Shimakawa, *Phys. Rev. B,* **76**, 024429 (2007).
18. X.-J. Liu, H.-P. Xiang, P. Cai, X.-F. Hao, Z.-J. Wu, and J. Meng, *J. Mater. Chem.,* **16**, 4243 (2006).
19. J. B. Goodenough,"*Magnetism and the Chemical Bond*", John Wiley & Sons, (1963).
20. T. Saito, Institute for Chemical Research, Kyoto University (*unpublished work*).

Chapter 7
Conclusions

In this work, several bismuth-containing transition metal perovskites have been synthesised and studied. These materials may possess multiferroism as a consequence of the presence of Bi^{3+} $6s^2$ lone pair, and the magnetism from transition metal cations. The physical properties of the materials can be affected by different factors, such as cation doping, oxygen content, or external pressure application. Substitutions of the well-known multiferroic materials $BiFeO_3$ and $BiMnO_3$ have been conducted. In addition, an undoped transition metal perovskite $BiNiO_3$ and an *A*-cation ordered perovskite $BiCu_3Mn_4O_{12}$ have been investigated. These materials have been structurally characterised and their physical properties have been examined at varying temperatures and pressures.

$Bi_xCa_{1-x}FeO_3$ solid solutions have been synthesised at ambient pressure in air by a standard solid state method. With divalent Ca^{2+} substitution into $BiFeO_3$, Fe^{4+} cations can be introduced into the *B* site and the oxygen deficiency may take place to compensate the charge distribution of the material. In the $Bi_xCa_{1-x}FeO_3$ series, neither charge ordering nor charge disproportionation phenomena are observed. A structural phase boundary was found to occur at x = 0.8. A disordered cubic model is adopted for x = 0.4 - 0.67 samples, where the characteristic local lone pair distortions of Bi^{3+} play a key role in the disorder. The coexistence of rhombohedral and cubic phases is observed for x = 0.8 and 0.9 samples, in which the metastabilities of the two phase components are demonstrated. The robustness of the antiferromagnetic order is displayed in the series. A 60 % replacement of the Bi^{3+} by Ca^{2+} leads to a slight decrease in the transition temperature T_N from 643 K to 623 K. The antiferromagnetically ordered moment at room temperature decreases from 4.1 μ_B for $BiFeO_3$ to 3.6 μ_B for x = 0.4 material, which is in agreement with the replacement of S = 5/2 Fe^{3+} by high spin S = 2 Fe^{4+}.

High-pressure techniques were required for the preparation of $Bi_xLa_{1-x}MnO_3$ with x = 1.0, 0.9 and 0.8. The isovalent La^{3+} substitution for Bi^{3+} in $BiMnO_3$ and preservation of oxygen stoichiometry leads to no introduction of mixed-valent Mn cations. A structural phase boundary is observed to occur at x = 0.9. $Bi_{0.9}La_{0.1}MnO_3$ adopts the highly distorted monoclinic structure shown by $BiMnO_3$, which is due to the characteristic Bi^{3+} lone pair. With higher La^{3+} substitution, the Bi^{3+} lone pair character is suppressed and $Bi_{0.8}La_{0.2}MnO_3$ shows an *O′*-type orthorhombic structure with space group *Pnma* as in stoichiometric $LaMnO_3$. Ferromagnetic behaviour was observed in $BiMnO_3$ and $Bi_{0.9}La_{0.1}MnO_3$, which results from the orbital ordering due to the cooperative Jahn-Teller effects. Unlike the robustness of antiferromagnetism shown in $Bi_xCa_{1-x}FeO_3$ series, a change from ferromagnetism to antiferromagnetism is observed in $Bi_xLa_{1-x}MnO_3$ materials with increasing La^{3+} substitution. The *A*-type antiferromagnetic ordering is displayed in the x = 0.8 sample, where the change of magnetic ordering across the composition results from the transformation of orbital ordering.

$BiNiO_3$ is a unique material that shows a variety of electronic states. The phase boundary between the unusual *A*-site charge disproportionated triclinic insulating Phase I $(Bi^{3+}_{0.5}Bi^{5+}_{0.5})Ni^{2+}O_3$ and the orthorhombic metallic Phase III $Bi^{3+}Ni^{3+}O_3$ was found between 3.2(2) and 3.7(2) GPa at room temperature. Although Ni charge disproportionated rare earth perovskites $R^{3+}(Ni^{2+}_{0.5}Ni^{4+}_{0.5})O_3$ have been widely studied, the suggested Phase IV $Bi^{3+}(Ni^{2+}_{0.5}Ni^{4+}_{0.5})O_3$ was not observed. Instead a newly discovered Bi^{3+}/Bi^{5+} disordered Phase Id, which is derived from Phase I, was proposed to explain the observed "$Bi^{4+}Ni^{2+}O_3$" insulating phase. The characteristic Bi $6s^2$ lone pair effect is demonstrated, which contributes to the monoclinic distortion of Phase Id. The existence of suggested Phase II $Bi^{4+}Ni^{2+}O_3$ was not evidenced, and $Bi^{3+}Ni^{3+}O_3$ Phase III is assumed to be the obtained HT orthorhombic phase.

$BiCu_3Mn_4O_{12}$ adopts the 1:3 *A*-site ordered perovskite structure $AA'_3B_4O_{12}$. The introduction of Mn^{3+} into the Cu^{2+} site is revealed giving the composition $BiCu_{2.5}Mn_{4.5}O_{12}$ rather than reported $BiCu_3Mn_4O_{12}$. This has also been shown in $CaCu_3Mn_4O_{12}$, however the observed substitution is absent in rare earth R^{3+} analogues. Therefore in addition to the presence of trivalent Bi^{3+}, a mixed-valent

B cation $Mn^{3.63+}$ is obtained from $Bi^{3+}(Cu^{2+}_{2.5}Mn^{3+}_{0.5})(Mn^{3+}_{1.5}Mn^{4+}_{2.5})O_{12}$. In the studied temperature range, no distortion from cubic symmetry was found down to 5 K, and no indication of Mn^{3+}/Mn^{4+} charge and orbital ordering was observed. Although ferrimagnetic behaviour of the material was reported, a ferromagnetic ordering of Mn and Cu moments was shown in the present work. The canting between Mn and Cu moments observed in $CaCu_{2.5}Mn_{4.5}O_{12}$ was not observed in this Bi analogue.

In summary, bismuth plays an important role in the structure of Bi-containing materials due to its characteristic $6s^2$ lone pair. Since the properties of the materials are strongly related to their structures, the bismuth can enable them to display fascinating and exceptional characters. This is exhibited by Ca^{2+} doping in the $Bi_xCa_{1-x}FeO_3$ series, La^{3+} substitution without electronic doping in $Bi_xLa_{1-x}MnO_3$, and the distinct properties of $BiNiO_3$ in different pressure-temperature regions. In contrast, the character of the bismuth $6s^2$ lone pair is not pronounced in $BiCu_3Mn_4O_{12}$, since the material exhibits the same structure as other analogues. This may be because Bi is only in 25 % of the *A* sites of the material.

To extend the research carried out in this thesis, Ca-rich materials could be prepared using high-pressure techniques and detailed studies on oxygen contents could be conducted to complete the study of $Bi_xCa_{1-x}FeO_3$ solid solutions. For $Bi_xLa_{1-x}MnO_3$ materials, impedance and ferroelectricity measurements will be performed to investigate their multiferroic properties in comparison with the reported thin film studies. Further detailed studies are needed to investigate the structures, valence states, and temperature/pressure transitions of $BiNiO_3$ phases, due to the limitation of the resolution provided in the performed experiments. To examine the role of Bi in $AA'_3B_4O_{12}$ materials, new Bi-containing analogues should be prepared for comparison with $BiCu_3Mn_4O_{12}$.

Appendix I

Rietveld Refinements of $Bi_xCa_{1-x}FeO_3$

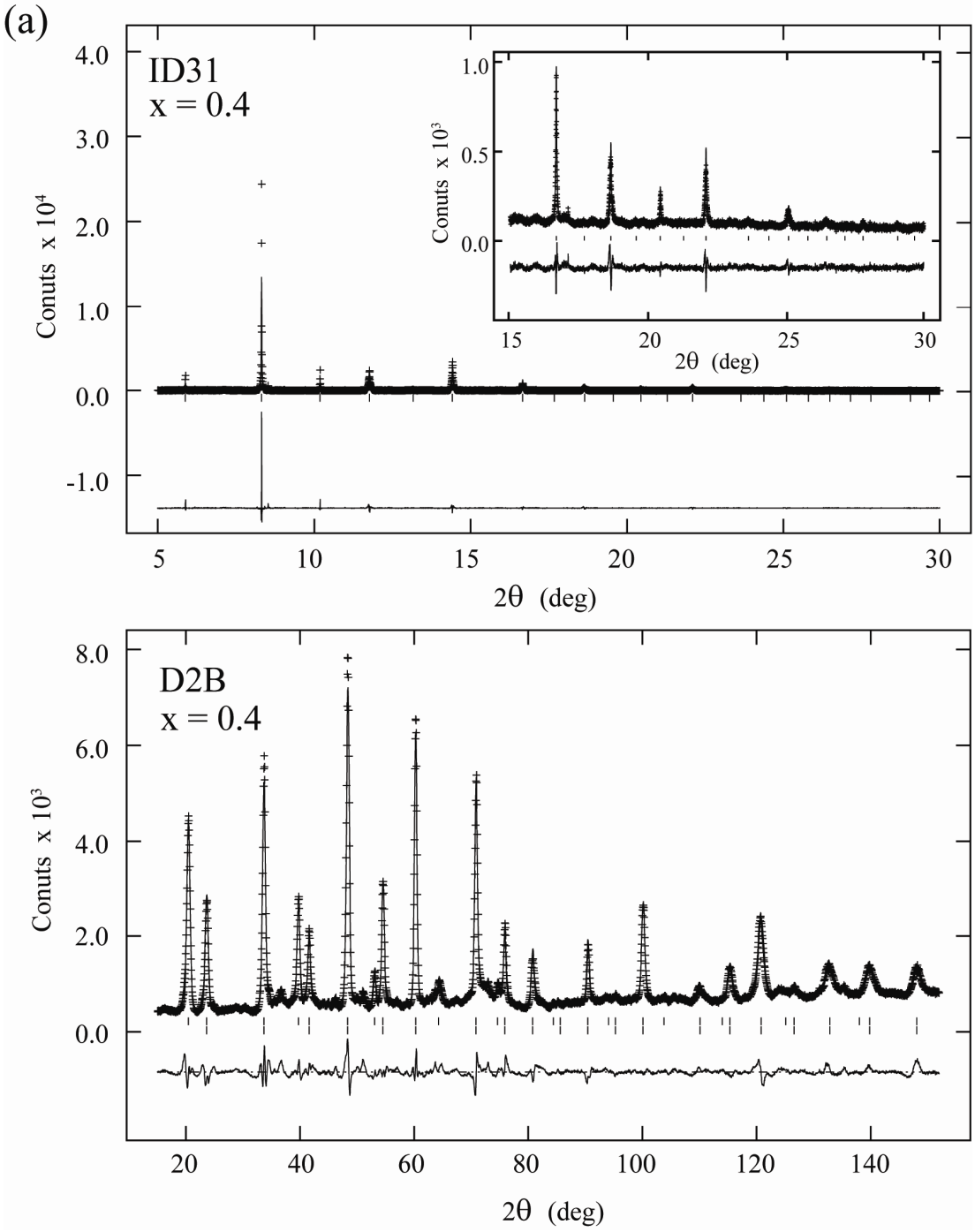

Rietveld fits of the disordered cubic model refinements of ID31 and D2B (inset) data at room temperature for (a) $Bi_{0.4}Ca_{0.6}FeO_3$

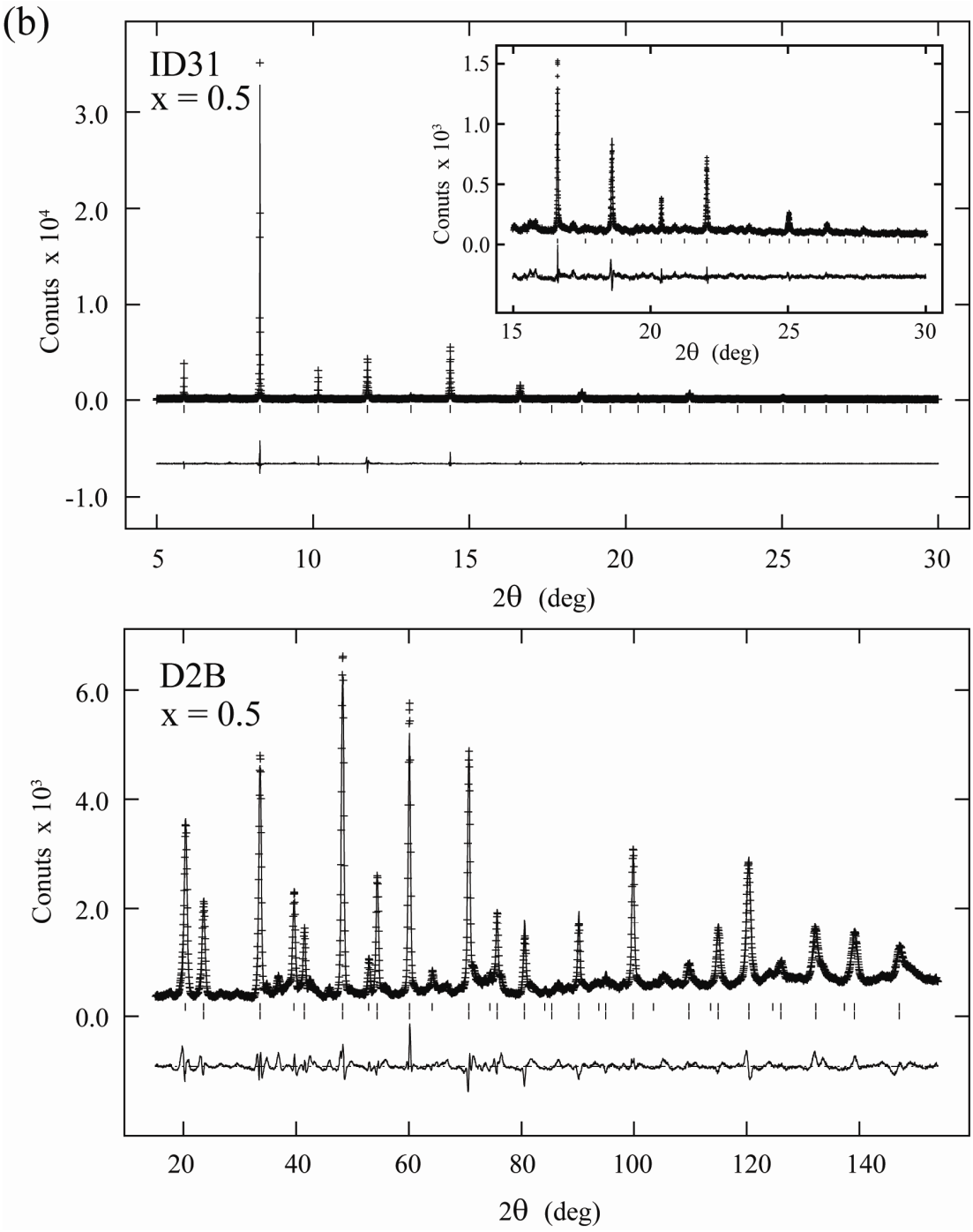

Rietveld fits of the disordered cubic model refinements of ID31 and D2B (inset) data at room temperature for (b) $Bi_{0.5}Ca_{0.5}FeO_3$

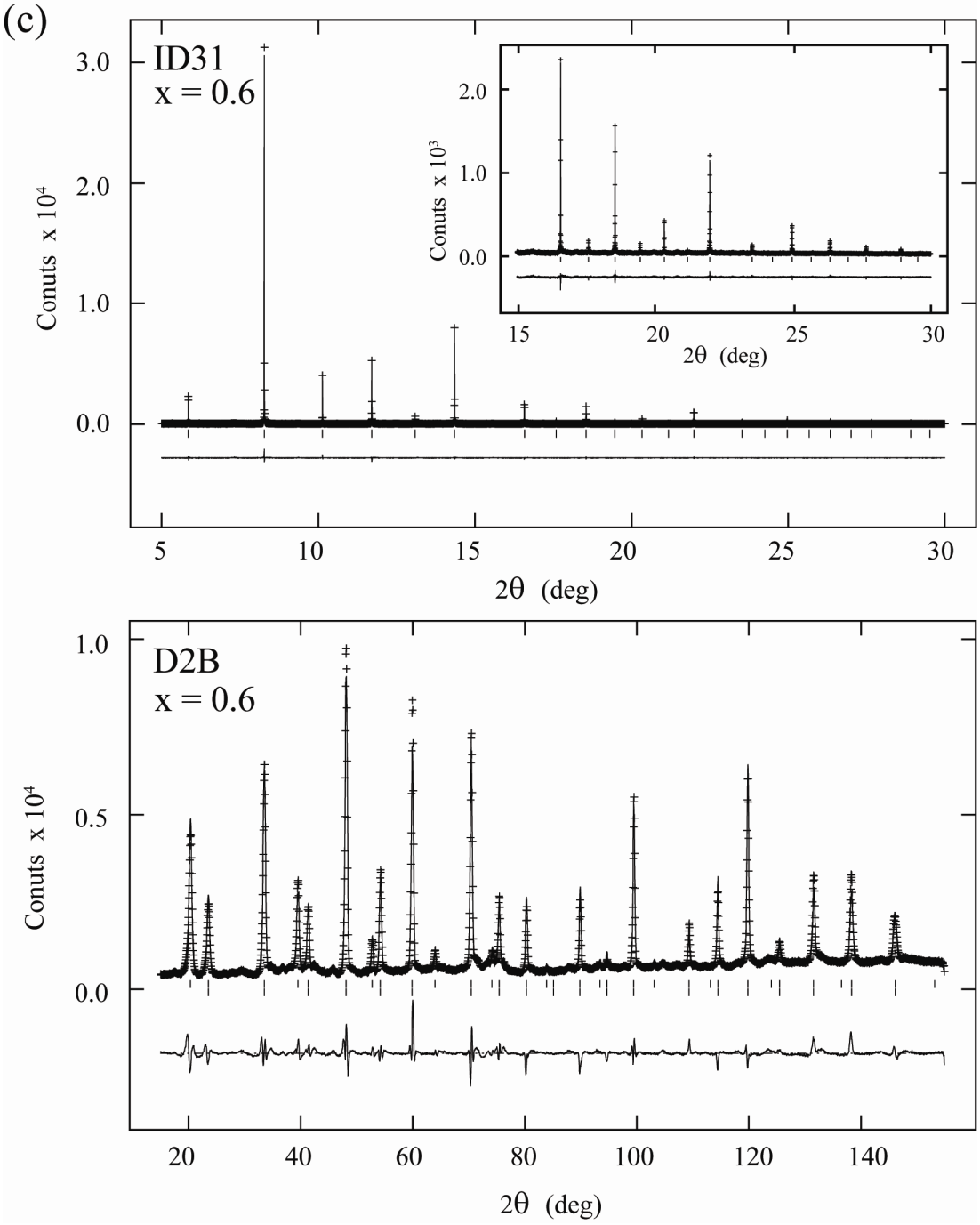

Rietveld fits of the disordered cubic model refinements of ID31 and D2B (inset) data at room temperature for (c) $Bi_{0.6}Ca_{0.4}FeO_3$

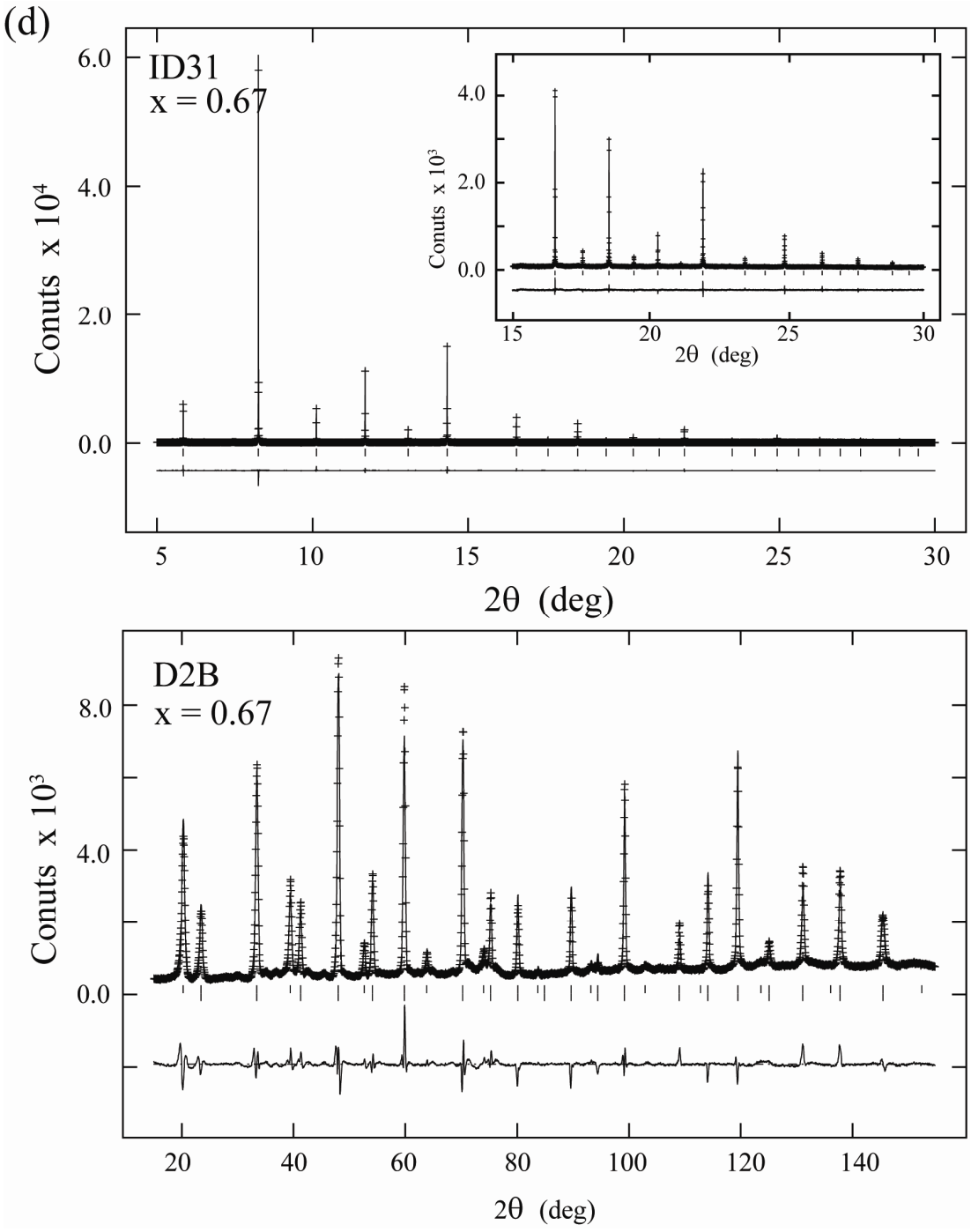

Rietveld fits of the disordered cubic model refinements of ID31 and D2B (inset) data at room temperature for (d) $Bi_{0.67}Ca_{0.33}FeO_3$

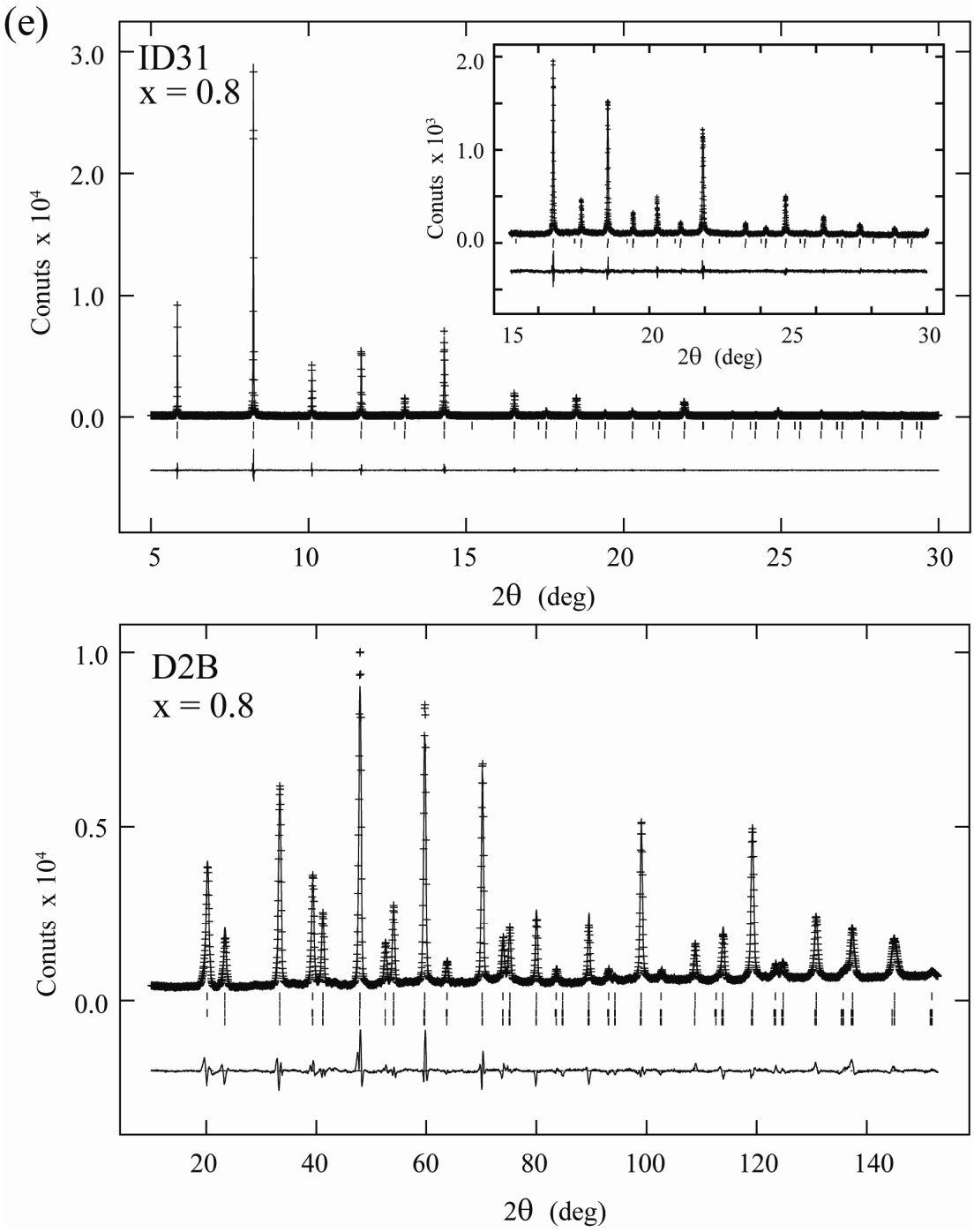

Rietveld fits of the disordered cubic model refinements of ID31 and D2B (inset) data at room temperature for (e) $Bi_{0.8}Ca_{0.2}FeO_3$

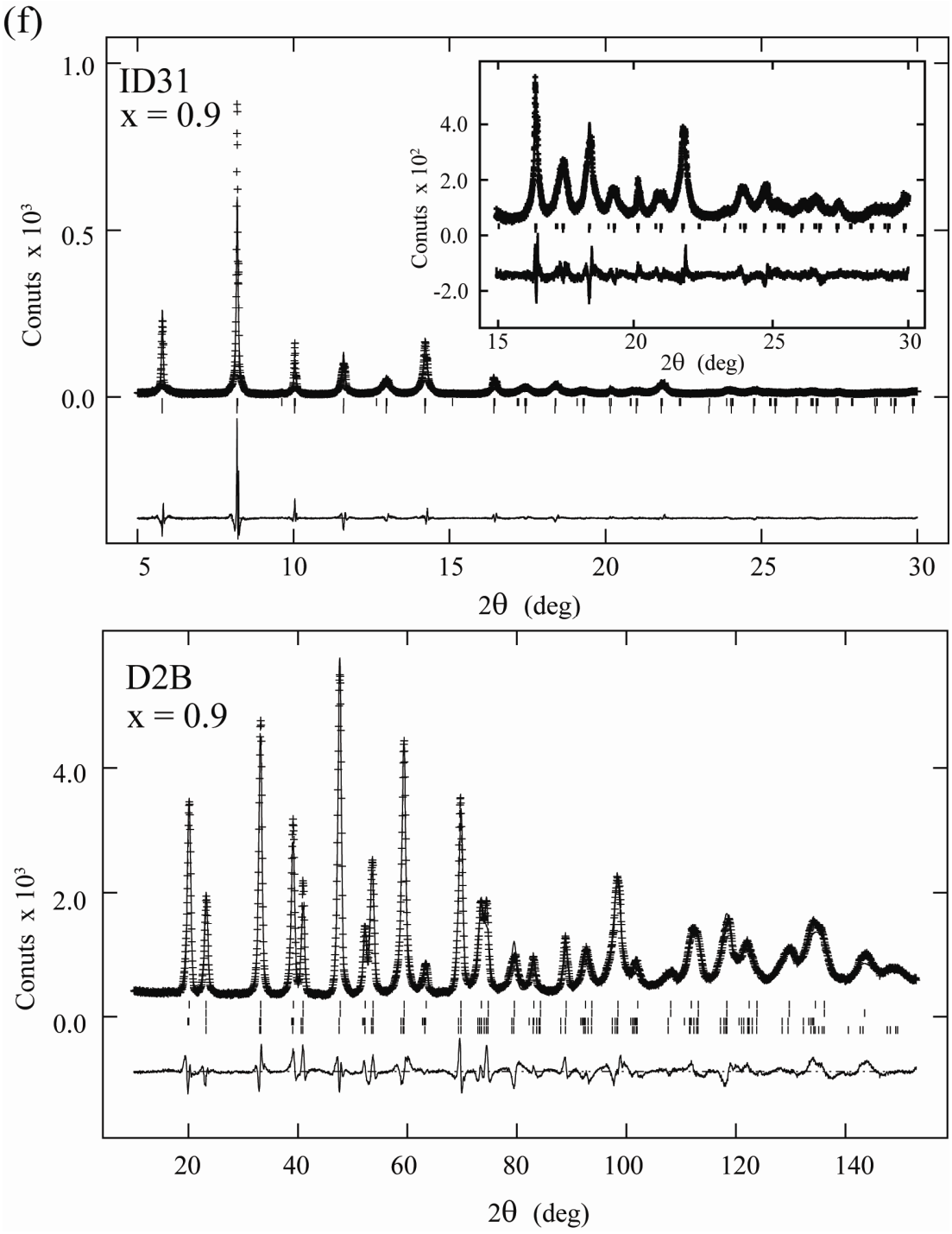

Rietveld fits of the disordered cubic model refinements of ID31 and D2B (inset) data at room temperature for (f) $Bi_{0.9}Ca_{0.1}FeO_3$

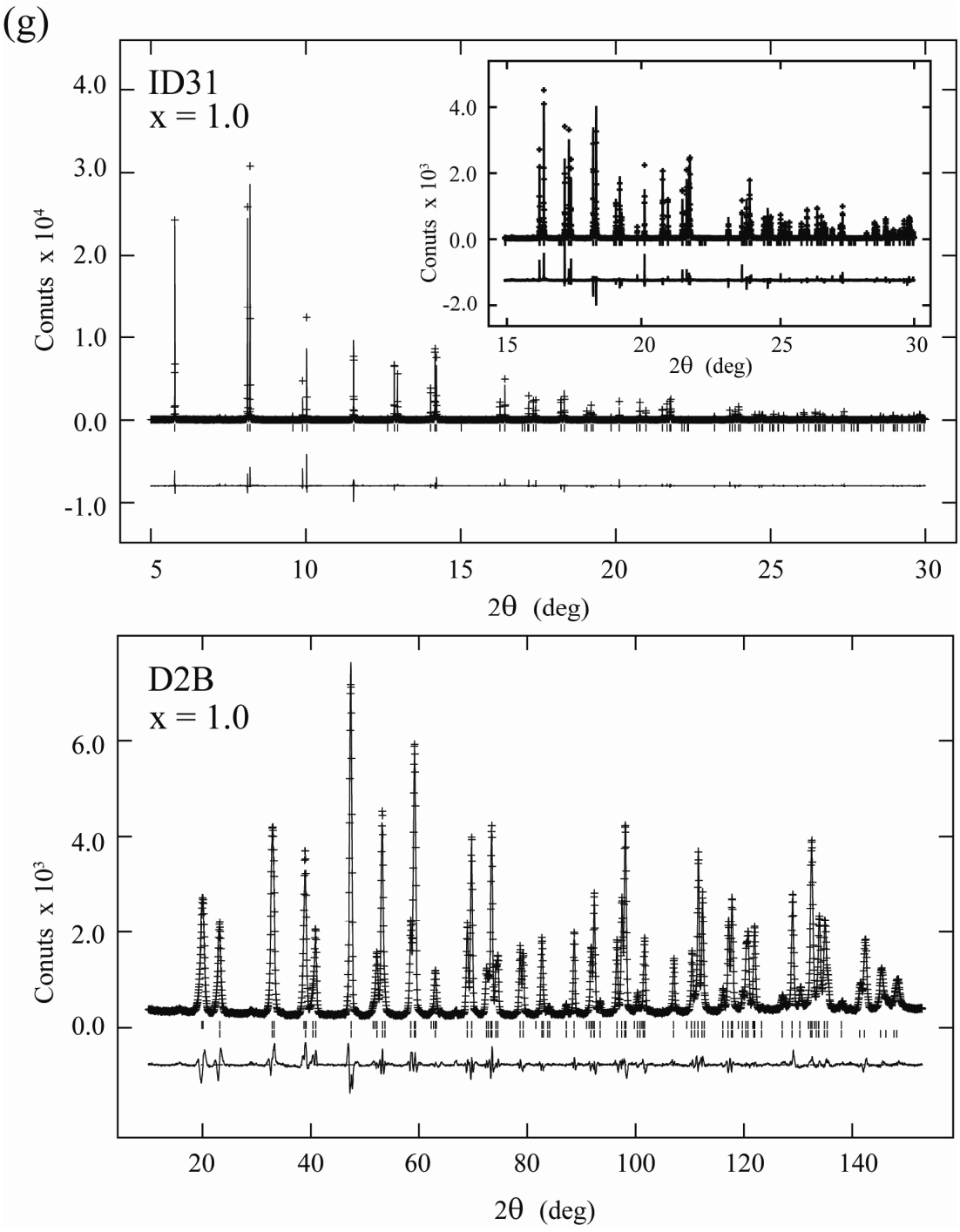

Rietveld fits of the disordered cubic model refinements of ID31 and D2B (inset) data at room temperature for (g) $BiFeO_3$.